

**DOCTORAL THESIS**

# Two-photon Spectroscopy as a New Quantitative Protonation Probe

Matt Rammo

TALLINN UNIVERSITY OF TECHNOLOGY  
DOCTORAL THESIS  
21/2023

# Two-photon Spectroscopy as a New Quantitative Protonation Probe

MATT RAMMO



TALLINN UNIVERSITY OF TECHNOLOGY

School of Science

Department of Cybernetics

This dissertation was accepted for the defense of the degree of Doctor of Philosophy in Applied Physics on 05/05/2023

**Supervisor:** Prof. Aleksander Rebane  
National Institute of Chemical Physics and Biophysics  
Tallinn, Estonia

**Co-supervisor:** PhD Charles William Stark  
National Institute of Chemical Physics and Biophysics  
Tallinn, Estonia

**Opponents:** Prof. Joanna Olesiak-Banska  
Wroclaw University of Science and Technology  
Wroclaw, Poland

Prof. Tõnu Pullerits  
Lund University  
Lund, Sweden

**Defense of the thesis:** 27/06/2023, Tallinn

**Declaration:**

Hereby I declare that this doctoral thesis, my original investigation and achievement, submitted for the doctoral degree at Tallinn University of Technology has not been submitted for doctoral or equivalent academic degree.

Matt Rammo

-----  
signature



European Union  
European Regional  
Development Fund



Investing  
in your future

Copyright: Matt Rammo, 2023

ISSN 2585-6898 (publication)

ISBN 978-9949-83-987-2 (publication)

ISSN 2585-6901 (PDF)

ISBN 978-9949-83-988-9 (PDF)

Printed by Koopia Niini & Rauam

TALLINNA TEHNIKAÜLIKOOL  
DOKTORITÖÖ  
21/2023

# **Kahefotoonne neeldumisspektroskoopia kui uus kvantitatiivne protoneerimise sond**

MATT RAMMO







## Table of contents

|   |    |
|---|----|
| List of publications .....  | 8  |
| Author's contributions to the publications .....  | 9  |
| Introduction .....  | 10 |
| Abbreviations, terms, symbols.....  | 12 |
| 1 Theoretical considerations .....  | 13 |
| 1.1 Probability and cross-sections of one- and two-photon transitions .....                         | 13 |
| 1.1.1 Role of molecular inversion symmetry and Laporte rule .....                                   | 16 |
| 1.1.2 Simplified models of 2PA spectra .....  | 17 |
| 1.1.3 Vibronic structure of 1PA spectra .....   | 18 |
| 1.1.4 Vibronic contribution to 2PA spectra .....  | 20 |
| 1.1.5 Two-level model of 2PA and vibronic 2PA transitions .....                                     | 22 |
| 1.1.6 Estimation of the permanent electric dipole moment change upon<br>electronic transition ..... | 23 |
| 1.1.7 Quantum-chemical calculations and modeling .....  | 23 |
| 2 Experimental methods.....   | 26 |
| 2.1 Overview of experimental techniques for measuring 2PA spectra and 2PA cross-<br>sections.....   | 26 |
| 2.1.1 Two-photon excited fluorescence .....   | 27 |
| 2.2 Chemical solvents and reagents .....  | 28 |
| 2.3 Compounds under study .....   | 28 |
| 2.3.1 Measurement of linear absorbance spectra .....  | 30 |
| 2.3.2 Measurement of linear fluorescence emission spectra .....                                     | 30 |
| 2.3.3 Determination of molar extinction coefficient .....   | 30 |
| 2.3.4 Measurement of fluorescence quantum yield .....   | 31 |
| 2.3.5 Measurement of pH .....   | 31 |
| 2.3.6 Measurement of 1PA titration spectra.....   | 32 |
| 2.4 Measurement of two-photon absorption spectral profiles and 2PA cross-<br>sections.....          | 32 |
| 2.4.1 Wavelength-tunable femtosecond laser system .....   | 32 |
| 2.4.2 Two-photon-excited fluorescence spectrometer .....  | 34 |
| 2.4.3 LabView control software.....   | 39 |
| 2.5 Procedures for evaluating 2PA spectral shape.....   | 39 |
| 2.6 Procedure for measuring 2PA cross-section.....  | 40 |

|       |   |     |
|-------|---|-----|
| 2.7   | Spectral decomposition by multivariate curve resolution-alternating least squares (MCR-ALS) method.....   | 41  |
| 2.7.1 | Decomposition of linear absorption spectra .....  | 41  |
| 2.7.2 | Decomposition of two-photon absorption spectra .....  | 42  |
| 3     | Aim of the study.....   | 45  |
| 4     | 2PA study of protonation effects in novel organic chromophores.....   | 47  |
| 4.1   | Spectroscopic characterization of lipophilic coumarins: Measurement of titration spectra.....   | 47  |
| 4.1.1 | On potential causes of apparent mismatching between the spectral profiles of 1PA and 2PA of $S_0 \rightarrow S_1$ transition in protonated C1–C4..... | 53  |
| 4.1.2 | Fluorescence emission quantum yield and two-photon brightness .....   | 56  |
| 4.1.3 | Preliminary fluorescence microscopy studies .....   | 58  |
| 4.2   | On-off-on control of molecular inversion symmetry via multistage protonation .  | 59  |
| 4.2.1 | Photophysical properties of pyrrolopyrroles.....  | 59  |
| 4.3   | Multi-stage protonation in a novel inversion symmetric pyrrolopyrrole.....  | 61  |
| 4.3.1 | Quantitative relation between 2PA spectra and pH.....   | 76  |
| 5     | Conclusions and outlook.....  | 77  |
|       | List of figures.....  | 79  |
|       | List of tables .....  | 81  |
|       | References .....  | 82  |
|       | Acknowledgements.....   | 89  |
|       | Abstract.....   | 90  |
|       | Lühikokkuvõte.....  | 91  |
|       | Appendix 1 .....  | 93  |
|       | Appendix 2 .....  | 105 |
|       | Appendix 3 .....  | 113 |
|       | Appendix 4 .....  | 127 |
|       | Appendix 5 .....  | 131 |
|       | Appendix 6 .....  | 136 |
|       | Appendix 7 .....  | 138 |
|       | Appendix 8 .....  | 140 |
|       | Appendix 9 .....  | 141 |
|       | Appendix 10 .....   | 143 |
|       | Appendix 11 .....   | 144 |
|       | Appendix 12 .....   | 146 |

|                        |     |
|------------------------|-----|
| Appendix 13 .....      | 150 |
| Appendix 14 .....      | 151 |
| Appendix 15 .....      | 152 |
| Appendix 16 .....      | 153 |
| Appendix 16 .....      | 155 |
| Curriculum vitae ..... | 156 |
| Elulookirjeldus.....   | 158 |

## List of publications

- I. **Rammo, M.**; Trummal, A.; Uudsemaa, M.; Pahapill, J.; Petritsenko, K.; Sildoja, M.-M.; Stark, C. W.; Selberg, S.; Leito, I.; Palmi, K.; Adamson, J.; Rebane, A., "Novel Lipophilic Fluorophores with Highly Acidity-Dependent Two-Photon Response," *Chem. – Eur. J.*, vol. 28, no. 8, p. e202103707, 2022.
- II. Stark, C. W.; **Rammo, M.**; Trummal, A.; Uudsemaa, M.; Pahapill, J.; Sildoja, M.-M.; Tshepelevitsh, S.; Leito, I.; Young, D. C.; Szymański, B.; Vakuliuk, O.; Gryko, D. T.; Rebane, A., "On-off-on Control of Molecular Inversion Symmetry via Multi-stage Protonation: Elucidating Vibronic Laporte Rule," *Angew. Chem. Int. Ed.*, vol. 61, no. 51, Oct. 2022.
- III. Tasior, M.; Kowalczyk, P.; Przybył, M.; Czichy, M.; Janasik, P.; Bousquet, M. H. E.; Łapkowski, M.; **Rammo, M.**; Rebane, A.; Jacquemin, D.; Gryko, D. T., "Going beyond the borders: pyrrolo[3,2-b]pyrroles with deep red emission," *Chem. Sci.*, vol. 12, no. 48, pp. 15935–15946, Dec. 2021.

## **Author's contributions to the publications**

- I. Conducting all measurements, analyzing the results, and participating in writing of the article. Development of hardware and software for the automated sample stage, optimizing the 2PA spectrometer.
- II. Conducting 2PA shape and cross-section measurements, 1PA and 2PA titrations, and determining molar extinction coefficients. Building and optimizing the 2PA spectrometer.
- III. Performing 2PA shape and cross-section measurements, automation of position control SHG crystal in the cross-section measurements.

## Introduction

The process of simultaneous two-photon absorption (2PA) was first theoretically predicted by Maria Goeppert-Mayer in 1931 [1] (Nobel prize in Physics 1963). She considered the quantum-mechanical transition probability from an atom's ground electronic state to an excited electronic state via simultaneous absorption of two photons, where the combined energy of the photons equals the resonance transition energy between the states. The first experimental confirmation of this archetypical nonlinear-optical phenomenon was reported, about 30 years later by W. Kaiser and C. G. Garret [2], following the invention of the pulsed ruby laser. They used this light source to excite the crystal of  $\text{CaF}_2$  containing luminescent  $\text{Eu}^{2+}$  ions to induce emission from ions excited levels possessing twice the energy that of the near-infrared laser photons. This pioneering experiment also confirmed the parity selection rule, according to which 2PA in systems with inversion symmetry is allowed only between states of equal parity. The latter property, often referred to as the Laporte rule, is now widely used to investigate symmetry properties of complex systems and their complex environments.

Interestingly, it has been observed that even nominally inversion symmetric chromophores may sometimes show partial overlap between the 1PA and 2PA spectra [3], [4], [5]. Our approach is to study the extent and the nature of that overlap and use this knowledge to gain new photophysical insights, such as the origin and underlying mechanisms leading to the apparent relaxation of the Laporte rule [5], [6], [7]. One should note, however, that because the efficiency of 2PA is usually relatively low and the experiments often rely upon a very high flux of photons, accurate quantitative 2PA measurements remain a technically demanding task. In the experiments described in this Thesis, we take advantage of recent advances in femtosecond laser technology, producing ultrashort pulses with high instantaneous photon flux and an automated selection of a wide range of excitation wavelengths. Latter characteristics facilitate the collection of quantitative 2PA spectral data with superior accuracy and fidelity.

Because the rate of 2PA in a molecule increases as a square of instantaneous photon flux, i.e., fluence or intensity of the incident light, the excitation may be confined to a small sample volume by utilizing a sharply focused laser. This property facilitates various practical applications encompassing fluorescence excitation microscopy, 3D micro- and nano-fabrications, optical power limiting [8], photonic materials processing, ultrahigh-density optical data storage [9], and photodynamic therapy [10], to name a few.

Additionally, 2PA has entered a rapidly evolving field of super-resolution microscopy, where a combination of two-photon excitation with stimulated emission depletion facilitates significantly increased spatial resolving power, surpassing the diffraction limit [11], [12].

While developing new applications for 2PA materials is outside the scope of the current Thesis, the results described here may be applied in biological two-photon excitation fluorescence microscopy. Compared to 1PA, 2PA techniques offer several added advantages, such as reduced scattering and deeper tissue penetration while, at the same time, lowering photodamage.

One key to progress, through understanding the physics underlying 2PA processes, lies in the accurate characterization of 2PA materials, their 2PA spectral profiles and 2PA cross-section values and determining how these parameters change in response to different molecular environments. Even though there are numerous commercial

wavelength-tunable ultrafast laser systems, there are no commercial instruments for 2PA spectroscopy. Therefore, performing reliable and accurate two-photon measurements at accuracy levels comparable to conventional spectrometers that measure one-photon absorbance spectra remains an important task.

This doctoral Thesis starts with a brief overview of the theory underlying 2PA spectroscopy of organic fluorophores, including a short discussion of the role of inversion symmetry. Our advanced 2PA spectroscopy techniques, some of which were developed as part of this Thesis, are described next. The focus is on two-photon induced fluorescence (2PIF) detection methods. The thesis provides a detailed description of an automated multi-sample 2PA spectrometer, which we used to achieve the required accuracy, high throughput, and expanded spectral range.

In this Thesis, we study two different types of novel proton-sensing 2PA fluorophores with contrasting inversion symmetry properties. First, we address a set of non-centrosymmetric coumarin derivatives augmented with four different phosphazene groups, serving as preferred sites for protonation in low-pH solvents. The fluorophores' neutral and protonated forms are characterized in terms of their 1PA and 2PA spectra. A strong blueshift in both absorbance and fluorescence is noted upon protonation, accompanied by reduced 2PA cross-section and much lower quantum yield values compared to the neutral structures, thus indicating reduced conjugation.

Secondly, we study nominally inversion symmetric diketopyrrolopyrrole fluorophore containing two symmetrically placed potential protonation sites. By gradually increasing the pH of the solution, we observe how the chromophore's 1PA and 2PA spectra change as the symmetry breaks upon single protonation and then, upon double protonation, reverts back to the inversion-symmetric state. These observations are the first demonstration of 2PA spectral behavior as an on-off-on inversion symmetry switch, monitored by the corresponding Laporte rule. Furthermore, for the first time, the 2PA vs. 1PA spectral behavior is related back to the pH of the solvent and  $pK_a$  values of the fluorophore, thus establishing two-photon spectroscopy as a new quantitative protonation probe.



## Abbreviations, terms, symbols

|         |  |
|---------|--|
| 1PA     | One-photon absorption  |
| 2PA     | Two-photon absorption  |
| 2PIF    | Two-photon induced fluorescence  |
| 2PEFM   | Two-photon excited fluorescence microscopy   |
| ACN     | Acetonitrile   |
| AF455   | 2,4,6-tris[9,9-bis(3,7-dimethyloctyl)-7-(diphenylamino)-fluoren-2-yl]-1,3,5-triazine |
| BBO     | Beta Barium Borate   |
| C151    | Coumarin 151   |
| C153    | Coumarin 153   |
| DCM     | Dichloromethane  |
| DMSO    | Dimethylsulfoxide  |
| EEM     | Excitation-emission matrix   |
| MCR-ALS | Multivariate curve resolution-alternating least squares                              |
| MeOH    | Methanol   |
| NICPB   | National Institute of Chemical Physics and Biophysics                                |
| NLT     | Nonlinear transmittance  |
| OPA     | Optical parametric amplifier   |
| PBS     | Phosphate-Buffered Saline  |
| QY      | Quantum yield  |
| Rh6G    | Rhodamine 6G   |
| SDS     | Sodium dodecyl sulfate   |
| SHG     | Second harmonic generator  |
| SOS     | Sum-over-states  |
| TCSPC   | Time-correlated single-photon counting   |
| THF     | Tetrahydrofuran  |
| Tol     | Toluene  |
| TPM     | Two-photon microscopy  |
| Triflic | Trifluoromethanesulfonic acid  |

# 1 Theoretical considerations

## 1.1 Probability and cross-sections of one- and two-photon transitions

Figure 1 shows the ground energy level ( $E_g$ ) and the excited energy level ( $E_e$ ) of a molecule, separated by the energy gap,  $\Delta E = E_e - E_g$ . When the molecule, initially in the ground state, is illuminated with monochromatic light of frequency,  $\nu_{1PA}$  (in Hz), the system may undergo a transition to the excited state, provided that the transition between the energy eigenstates is not prohibited by symmetry, and that the absorbed photon inducing the excitation has the energy,

$$E_{ph} = h\nu_{1PA} = \Delta E, \quad (1)$$

where  $h$  is the Planck constant. This process, called one-photon absorption (1PA), is indicated in Figure 1 by a single vertical blue arrow.

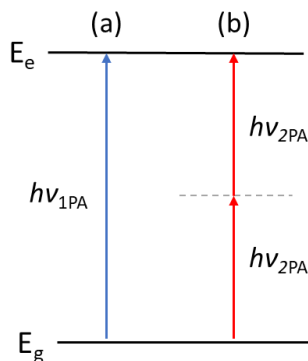


Figure 1: Optically induced transitions from the ground state ( $E_g$ ) to an excited state ( $E_e$ ) are enacted by (a) absorption of one photon (blue vertical arrow) and (b) by simultaneous absorption of two photons (two red arrows). The dashed horizontal line corresponds to the so-called virtual intermediate state.

Alternatively, the same excited state may be reached by the simultaneous absorption of two photons (or in a more general case – any integer number of photons), provided, again, that the transition is not prohibited by symmetry, and that the combined energy of the photons equals the energy difference between the initial and final states. In the case of degenerate 2PA, indicated with two red arrows in Figure 1, the two photons have equal energy:

$$E_{ph} = h\nu_{2PA} = \frac{1}{2}(\Delta E). \quad (2)$$

The dashed horizontal line in Figure 1 shows the so-called virtual intermediate level, located half-way between the two real energy states. However, since the two photons are absorbed strictly simultaneously, no distinction can be made between the arrival times of the photons, even in principle, meaning that no “storage” of energy may occur in the process. Indeed, as will be made clear from the quantum-mechanical calculations shown below, no intermediate state experiences a change of population in the 2PA process. The notion of a virtual intermediate level is more a matter of mathematical convenience and serves illustrative purposes rather than reflects any physical reality.

From a simple phenomenological viewpoint, let us consider a monochromatic laser beam of the photon flux,  $\Phi$ , where every photon has the same angular frequency,  $\omega$ . When the beam passes through a thin cuvette of thickness,  $\Delta z$ , containing a solution with absorbing chromophores at the concentration,  $N_g$ , then the photon flux at the output of the cuvette will be attenuated with respect to that at the input. Neglecting attenuation potentially caused by scattering and reflections by the cuvette walls etc., we may write down an approximate expression for the variation (attenuation) of the photon flux:

$$\Delta\Phi = \Phi - \Phi_0 \simeq -\sigma_{1PA}N_g\Phi_0\Delta z - \sigma_{2PA}N_g\Phi_0^2\Delta z, \quad (3)$$

where  $\Phi_0$  is the incident photon flux,  $\sigma_{1PA}$  is the 1PA cross-section and  $\sigma_{2PA}$  is the 2PA cross-section. Any higher-order multi-photon absorption cross-section may be phenomenologically defined in a similar manner. Typical peak cross-section values for organic dyes and fluorophores are,  $\sigma_{1PA} \sim 10^{-19} - 10^{-16} \text{ cm}^2$ , and,  $\sigma_{2PA} 10^{-50} - 10^{-47} \text{ cm}^4 \text{ s photon}^{-1}$ . The small value of  $\sigma_{2PA}$  suggests that in order for the 2PA to have an attenuation effect comparable to that of 1PA, one would need instantaneous photon flux values on the order of,  $\Phi_0 \simeq \sigma_{1PA}/\sigma_{2PA} \simeq 10^{28} - 10^{34} \text{ photon cm}^{-2} \text{ s}^{-1}$ . Another notable feature that follows from the phenomenological expression Equation (3) is that 2PA may be distinguished from potential concurrent 1PA by its quadratic dependence on  $\Phi_0$ . This property will be extensively used in our experiments described below for distinguishing between 2PA and 1PA.

In Appendix 4, we derive the one-photon absorption cross-section for molecules in a solution using first-order quantum-mechanical time-dependent perturbation theory, leading to the following relation (assuming random orientation of the absorbers):

$$\sigma_{1PA}(\omega) = \frac{\pi\omega}{3nc\varepsilon_0\hbar} |\vec{\mu}_{fg}|^2 \rho_M(\omega), \quad (4)$$

where  $\vec{\mu}_{fg}$  is the transition dipole moment between the initial state,  $g$ , and the final state,  $f$ ,  $n$  is the index of refraction of the solvent and  $\varepsilon_0$  is the electric constant (vacuum permittivity),  $\hbar$  is the reduced Planck constant, and  $c$  is the velocity of light in a vacuum. The  $\rho_M(\omega)$  is the normalized line shape function:

$$\int \rho(\omega)d\omega = 1. \quad (5)$$

The transition dipole moment may be evaluated from the known ground- and excited state wavefunctions,  $\Psi_g(\vec{r})$  and  $\Psi_f(\vec{r})$ , according to the relation:

$$\vec{\mu}_{fg} = \int \Psi_f^*(\vec{r})e\vec{r}\Psi_g(\vec{r})d^3(\vec{r}), \quad (6)$$

where  $e$  is the elementary charge and the integral runs over the coordinates of all electrons,  $\vec{r}$ . The magnitude of the transition dipole moment is commonly expressed in Debye (D) ( $1 \text{ D} = 3.33564 \times 10^{-30} \text{ C}\cdot\text{m}$ ), and electric dipole-allowed transitions in organic dyes have typical values,  $|\mu| \sim 1 - 10 \text{ D}$ . In the SI units, 1PA cross-section is expressed ( $\text{m}^2$ ); however, most literature uses the units of  $\text{cm}^2$ . The larger the transition dipole, the stronger the associated per-molecule attenuation or absorption. Another useful metric of 1PA is the oscillator strength, which is proportional to the square of the magnitude of  $|\vec{\mu}_{fg}|$  and is expressed as [13]:

$$f_{fg} = \frac{2m_e\omega}{3e^2\hbar} |\mu|^2, \quad (7)$$

where  $m_e$  is the electron mass, and  $e$  is the electron charge. Chromophore's ability to absorb light is also often expressed in the molar extinction coefficient units ( $\text{cm}^{-1} \text{ M}^{-1}$ ), which is related to the 1PA cross-section as follows:

$$\varepsilon_M(\omega) = \frac{\sigma_{1PA}(\omega)N_a}{10^3 \ln(10)}, \quad (8)$$

where  $N_a$  is the Avogadro constant and  $\sigma_{1PA}$  is in  $\text{cm}^2$  [14]. Expression for the two-photon absorption cross-section is obtained by means of extending the time-dependent perturbation calculation to the second order (Appendix 4):

$$\sigma_{2PA} = \frac{\pi \omega^2}{\varepsilon_0^2 c^2 \hbar^2 n^2} \left| \sum_m \frac{(\vec{\mu}_{mg} \cdot \vec{e}) \times (\vec{\mu}_{fm} \cdot \vec{e})}{(\omega_{mg} - \omega)} \right|^2 \rho_M(2\omega), \quad (9)$$

where  $\vec{e}$  is the unit polarization vector and the subscript  $m$  refers to any intermediate state and  $\omega_{mg} = \omega_m - \omega_g$ . A commonly used unit for the two-photon cross-section is GM (1 GM is  $10^{-50} \text{ cm}^4 \text{ s photon}^{-1}$ ), named after Maria Goeppert-Mayer.

According to Equation (9), the cross-section is proportional to the modulus square of the sum of terms (generally complex), where each one corresponds to a particular transition probability amplitude. Figure 2 shows, in an illustrative manner, the different dipole moments contributing to these amplitudes. We assume, for simplicity, the lowest-energy excited state to act as the final state. First, we note that the summation over the index  $m$  implies that we need to include contributions from the transition matrix elements between the ground state and all states, i.e., including the state  $g$  itself,  $(\vec{\mu}_{gg})$ , and elements between the final state and any intermediate state, i.e., including the final state itself,  $(\vec{\mu}_{ff})$ . Permanent dipole moment change ( $\Delta\mu$ ) between the ground and final state is expressed as:

$$\Delta\mu_{fg} = \mu_{ff} - \mu_{gg}. \quad (10)$$

Secondly, Equation (9) implies that at any given frequency,  $\sigma_{2PA}$ , includes values of transition dipole moments and transition frequencies for all excited electronic states, so-called sum-over-states (SOS), consisting of a large number of terms. These virtual states can be represented with the sum of individual stationary states  $E_i$ . However, it must be emphasized that the latter representation is purely illustrative in nature as only the overall transition from  $E_g$  to  $E_f$  can be observed.

When the energy difference between the photon energy and the energy of the nearest one-photon allowed state is reduced, dramatic enhancement of the 2PA will be observed [15]. It means that in general, all, except the lowest excited state, 2PA transitions are enhanced. Additionally, when one would use non-degenerate two-photon excitation, i.e.,  $\hbar\omega_1 \neq \hbar\omega_2$ , the 2PA spectra might differ depending on whether  $\hbar\omega_1$  or  $\hbar\omega_2$  is nearing resonance with a 1PA transition. In our experiments, however, we only use degenerate excitation.

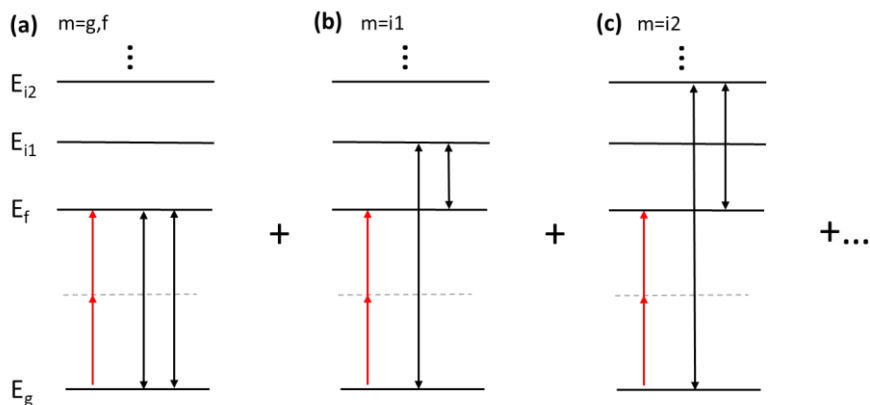


Figure 2: Different transition dipole moments contributions to the molecule's transition from the initial state  $E_g$  to the final state  $E_f$ . Black horizontal lines represent real energy levels, red vertical arrows represent photon energy and black vertical arrows show transition dipole moments. (a) the intermediate energy level is represented by the ground or the final level. (b), (c) the  $g \rightarrow f$  transition involves a higher-lying energy level acting as an intermediate level but without its population.

### 1.1.1 Role of molecular inversion symmetry and Laporte rule

For any centrosymmetric molecule, a Cartesian reference frame of coordinates may be chosen such that for each atom in the position,  $\{x,y,z\}$ , representing the molecule's structure, there is an equivalent atom in the position,  $\{-x, -y, -z\}$ . Similarly, electronic states of an isolated centrosymmetric molecule may be classified as either gerade ( $g$ ) (even) or ungerade ( $u$ ), depending on whether or not the electronic wave function,  $\Psi_m(\vec{r})$ , changes sign upon inversion of the coordinates. Figure 3, is presenting a simplified model of  $u$ -parity (a) and  $g$ -parity (b) wave functions acts and how their sign changes upon inversion.

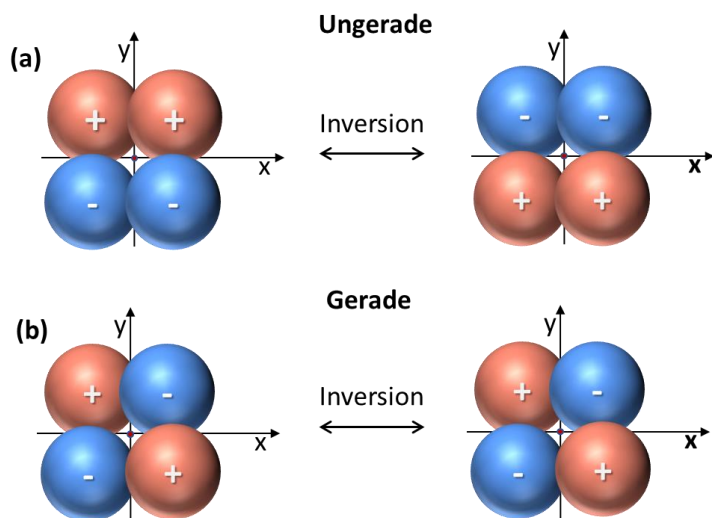


Figure 3: Schematic representation of the effect that inversion of coordinates has on the wavefunction of certain parity. Positive values are colored in red and negative values are colored in blue, (a)  $u$ -parity electronic states, (b)  $g$ -parity electronic states.

The Laporte rule stipulates that, as a result of the antisymmetric nature of individual photon electric fields, an electric dipole-allowed one-photon transition must involve a parity change, either  $g \rightarrow u$  or  $u \rightarrow g$ . Only in this case does the transition dipole moment integral, Equation (6), contain a totally symmetric representation, i.e., it may be different from zero. This constraint means that parity-preserving, purely electronic transitions must be absent from the one-photon absorption spectra of centrosymmetric chromophores. On the other hand, two-photon transitions between opposite parity states,  $g \rightarrow u$  or  $u \rightarrow g$ , are forbidden, while transitions between the same parity states,  $u \rightarrow u$  or  $g \rightarrow g$ , are allowed. Indeed, for the sum in Equation (9) to be different from zero, in the case of a centrosymmetric molecule, every intermediate state  $m$  must have a different parity from  $g$ . Because, at the same time,  $f$  and  $m$  states must also be of opposite parity, it follows that the states  $g$  and  $f$  must be of the same parity. Therefore, in molecules with an inversion center, purely electronic transitions that are one-photon allowed are two-photon forbidden, and vice-versa.

No parity selection rule applies if the molecule lacks inversion symmetry or if the nominal inversion symmetry is broken. Symmetry breaking can result from lower-symmetry conformations, non-symmetric environments, etc. Another common reason why the Laporte rule may appear relaxed in the spectra of nominally inversion-symmetric chromophores is related to electronic-vibrational interactions, which will be discussed below.

### 1.1.2 Simplified models of 2PA spectra

As already discussed above, calculating the 2PA cross-section using Equation (9) implies summation over all contributing probability amplitudes (Figure 2). In practice, such summation is often difficult or even unattainable, especially because of lacking reliable information on the matrix elements connecting initial- and final states to higher energy states. On the other hand, situations exist where the SOS may be approximated by considerably simplified models accounting only for a few so-called essential states. Of particular interest for our studies is a situation when a non-centrosymmetric molecule possesses a strong permanent electric dipole moment difference between the ground and the first excited state ( $\Delta\mu_{fg} = \mu_{ff} - \mu_{gg} \neq 0$ ). In this case, an important simplification can be made regarding the transition to the lowest-energy excited state; we may assume that only the initial and final levels contribute to the 2PA, and all higher energy states contribution is negligible. This is the so-called two-level model of 2PA and is illustrated in Figure 4 (a), where the  $E_g$  and  $E_f$  represent the ground and final energy levels. Expression for the cross-section accounting also for random orientation of chromophores in a solvent may be written as follows:

$$\sigma_{2PA}(\omega) = \frac{\pi L^4}{15 n^2 c^2 \epsilon_0^2 \hbar^2} (2 \cos^2(\beta) + 1) |\vec{\mu}_{fg}|^2 |\Delta\vec{\mu}_{fg}|^2 g_M(2\omega) \quad (11)$$

where  $\beta$  is the angle between vectors,  $\vec{\mu}_{fg}$ , and,  $\Delta\vec{\mu}_{fg}$ , and  $g_M(2\omega)$  is the normalized line shape function. The optical local field correction factor,  $L$ , is introduced in order to account for the fact that the electric field acting on the molecule may differ from the one applied, due to interactions with the solvent. The procedure of isotropic averaging is explained in Appendix 4.

When a molecule is centrosymmetric, then the static dipole moments are equal to zero,  $\vec{\mu}_{gg} = \vec{\mu}_{ff} = 0$ , and the two-level model may contribute only through vibrational coupling (which will be discussed in the next paragraph). Purely electronic contribution to  $\sigma_{2PA}$  requires then accounting for an intermediate energy level, ( $m$ ), which leads to the

so-called three-level model (Figure 4 (b)) and includes the transition dipole moments  $\vec{\mu}_{mg}$  and  $\vec{\mu}_{fm}$ . At this point, it is appropriate to make some important observations:

- i. It has been established empirically [16], [17] that the two-level approximation Equation (11) is often applicable to the lowest-energy electronic transition of molecules with large  $\Delta\mu$ .
- ii. If  $\Delta\mu$  is small or if a high-energy excited state is the final state, then accounting for contributions from essential intermediate states (other than  $g$  and/or  $f$ ) is requisite (three-level model).

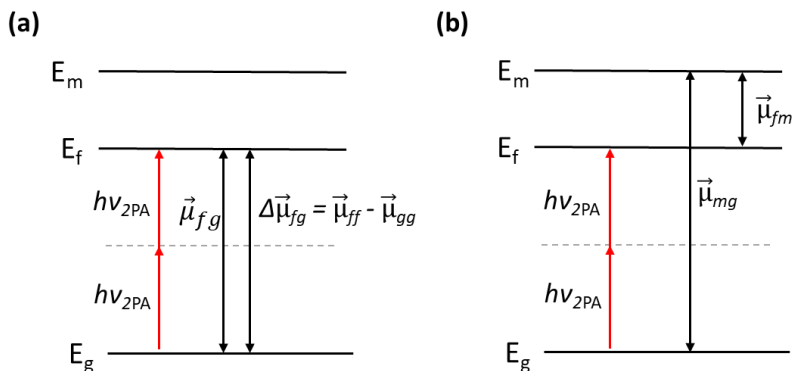


Figure 4: Few essential state models of 2PA; black horizontal lines represent molecule energy levels, red arrows represent photon energy, and black arrows are the transition dipole moments (a) two-level model for non-centrosymmetric chromophore with non-zero permanent dipole moment difference,  $\Delta\mu$  (b) Three-level model for centrosymmetric chromophore that involves transition dipole moments from the ground electronic state to the intermediate energy state,  $\vec{\mu}_{mg}$ , and from the intermediate state to the final state,  $\vec{\mu}_{fm}$ .

### 1.1.3 Vibronic structure of 1PA spectra

In addition to the dependence on the electronic coordinates ( $r$ ), one must also account for the coordinates of the normal mode of the nuclei ( $Q$ ) to obtain a complete wave function for a molecule. In the Born-Oppenheimer approximation, the wavefunction may be presented as the product,

$$\Psi(r, Q) \approx \psi_i(r, Q)\chi_{n(i)}(Q). \quad (12)$$

Where  $\chi_{n(i)}(Q)$  is the vibrational-rotational wavefunction and  $\psi_i(r, Q)$  is the electronic wavefunction depending parametrically on the normal coordinates of the nuclei,  $Q$ . As a consequence, the electronic energy is no longer constant, as was assumed above, but rather varies as a function of ( $Q$ ). This reliance is schematically shown in Figure 5, where the vibrational states (belonging to a particular electronic state) are represented with the numbered oscillating lines. The dashed black line represents the potential energy surfaces,  $E_g(Q)$ , and,  $E_f(Q)$ , of the ground- and excited electronic states, respectively. The horizontal axis represents one (generalized) nuclear or vibrational motion coordinate, and the vertical axis corresponds to the total energy. In Figure 5, the potential energy surfaces, and consequently, the vibrational wave functions, are approximated to be of the same shape (i.e., congruent, and equal scale factors), with minima shifted by  $\Delta Q$  indicating a generalized bond length extension in the excited state. In reality,

the potential surfaces may have different shapes, shifted minima positions and even different sets of normal vibrational coordinates (Duschinsky effect). Even more, different electron distributions in an excited state or close-lying electronic levels may couple, producing multiple energy minima [18].

The transition dipole matrix element between  $m$ 'th vibronic level of the ground electronic state,  $\Psi_{g,n} = \psi_g(r, Q)\chi_n(Q)$ , and  $n$ 'th vibronic level of the excited electronic state,  $\Psi_{f,m} = \psi_f(r, Q)\chi_m(Q)$  can be expressed as:

$$\vec{\mu}_{fg, mn} = \langle \chi_m(Q) | \chi_n(Q) \rangle \overline{M}_{fg}. \quad (13)$$

Where  $\overline{M}_{fg}$  is averaged electronic transition dipole moment evaluated over the nuclear coordinates of the initial and the final vibrational states. Equation (13) expresses the Condon approximation stating that the overall transition dipole  $\vec{\mu}_{fg, mn}$  depends on the overlap integral of the nuclear wave functions,  $\langle \chi_m(Q) | \chi_n(Q) \rangle$ , multiplied by the averaged electronic transition dipole moment. The square of the nuclear overlap integral  $|\langle \chi_m | \chi_n \rangle|^2$ , is called the Franck-Condon factor [19].

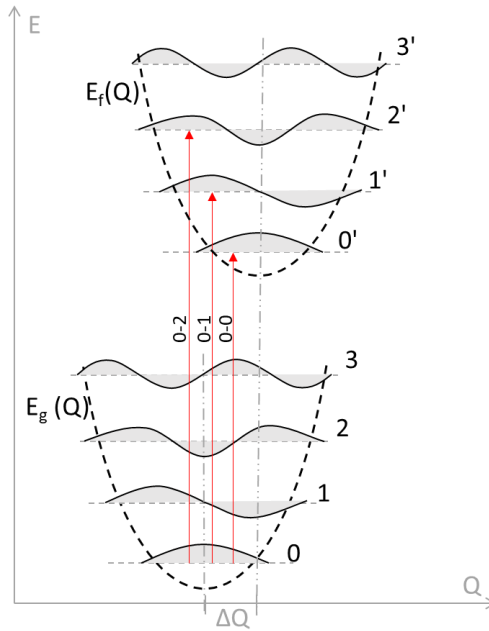


Figure 5: One-photon transitions between a set of vibrational levels in the ground ( $E_g$ ) and excited ( $E_f$ ) electronic state. The vertical axis corresponds to the total energy,  $E$ , and the horizontal axis is the vibrational coordinate,  $Q$ . Dashed lines show corresponding potentials  $E_g(Q)$  and  $E_f(Q)$ .  $\Delta Q$  is the shift between the two potential minima positions. 0-0, 0-1, and 0-2 vibronic transitions are marked with red arrows.

Because quantum-mechanics postulates that transitions between discrete energy states are instantaneous, the transition between  $E_g$  and  $E_f$  may be presented by vertical arrows (vertical transitions, Figure 5). If the potentials had the same shapes and no shift occurred between the equilibrium nuclear coordinates in the ground and the excited electronic states,  $\Delta Q = 0$ , then only transitions without change of the vibrational quantum



number would be non-vanishing, due to orthogonality of the vibrational wave functions. At low temperatures, the molecule would be in the lowest vibrational level ( $n = 0$ ) in the ground state, and only a 0-0' transition would be present. Higher vibrational levels would also be populated with increasing temperature, meaning that transitions would occur between 0-0', 1-1', 2-2', etc. However, as long as perfect harmonic potential vibrational levels have the same energy gaps, the absorption spectrum would consist of a single absorption band, which we call the 0-0 band. In most cases, the vibrational eigenfunctions in the  $g$  and  $f$  electronic states are neither identical nor perfectly harmonic. As a result, the absorption (and emission) spectrum displays a so-called vibronic progression reflecting a non-zero Franck-Condon factors for the transitions, 0-1, 0-2, etc.

#### 1.1.4 Vibronic contribution to 2PA spectra

While the expression, Equation (9), for the 2PA cross-section is applicable regardless of the exact nature of the states  $g$ ,  $f$ , and  $m$ , it would be advantageous to rewrite it in terms of electronic-vibrational wave functions accounting for the Franck-Condon principle. As illustrated in Figure 6, the totality of electronic ( $g$ ,  $m$ ,  $f$ ) and vibronic ( $i$ ,  $j$ ,  $k$ ) quantum numbers are represented in initial-, intermediate- and final energy levels:  $E_{(g,i)}$ ,  $E_{(m,j)}$ ,  $E_{(f,k)}$ , respectively.

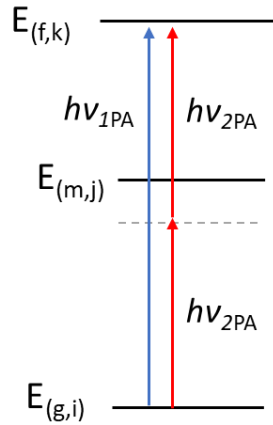


Figure 6: One- and two-photon induced electronic-vibrational transitions. One-photon absorption is marked with a blue arrow, two-photon absorption is marked with red arrows, virtual energy level is marked with a dashed line, initial-, intermediate- and final energy level  $E_{(g,i)}$ ,  $E_{(m,j)}$ ,  $E_{(f,k)}$  are marked with a black horizontal line where indexes ( $g$ ,  $m$ ,  $f$ ) and ( $i$ ,  $j$ ,  $k$ ) represent the totality of electronic and vibronic quantum numbers, respectively, in each electronic state.

The application of the Franck-Condon principle to two-photon spectra was discussed in detail by W.L. Smith [20] and is replicated here, who showed that much of the above description for the vibronic one-photon spectra and the same vibrational overlap integrals could be applied to the corresponding two-photon spectra. In the Born-Oppenheimer approximation, the electric dipole moment matrix element between the states ( $g,i$ ) and ( $f,k$ ) is given by:

$$\begin{aligned} \vec{\mu}_{gi, fk} &= \langle \chi_{f,k}(Q) | \langle \psi_f(r, Q) | \hat{\mu}(r, Q) | \psi_g(r, Q) \rangle | \chi_{g,i}(Q) \rangle \\ &= \langle \chi_{f,k}(Q) | \vec{\mu}_{fg}(Q) | \chi_{g,i}(Q) \rangle. \end{aligned} \quad (14)$$

Where  $\chi_k, \chi_i$  are the vibrational wavefunctions in the initial and final electronic states, respectively,  $\hat{\mu}(r, Q)$  is the dipole moment operator, and where in the second line of the equation, we performed integral over the electron coordinates,  $r$ , which gives the electronic transition moment  $\vec{\mu}_{fg}(Q)$ . The dependence of the electronic transition moment on the nuclear coordinates can be expressed as a Taylor series in the individual normal coordinates  $Q_r$  about the equilibrium position of the initial electronic state:

$$\mu_{fg}(Q) = \mu_{fg}(0) + \sum_r \left\{ \frac{\partial \mu_{fg}}{\partial Q_r} \right\}_0 Q_r + \frac{1}{2} \sum_{r_1, r_2} \left\{ \frac{\partial^2 \mu_{fg}}{\partial Q_{r_1} \partial Q_{r_2}} \right\}_0 Q_{r_1} Q_{r_2} + \dots \quad (15)$$

When looking at only the first two terms of Equation (15) and separating the totally symmetric ( $s$ ) and non-totally symmetric ( $a$ ) modes, we obtain

$$\mu_{fg}(Q) = \mu_{fg}(0) + \mu_{fg}^s Q_s + \mu_{fg}^a Q_a, \quad (16)$$

where

$$\mu_{fg}^s Q_s = \sum_s \left\{ \frac{\partial \mu_{fg}}{\partial Q_s} \right\}_0 Q_s \quad \text{and} \quad \mu_{fg}^a Q_a = \sum_a \left\{ \frac{\partial \mu_{fg}}{\partial Q_a} \right\}_0 Q_a. \quad (17)$$

The corresponding approximate expression for the vibronic transition moment in Equation (14) is:

$$\begin{aligned} \mu_{gi,fk} &= \left\langle \chi_k(Q) \left| \mu_{fg}(0) + \mu_{fg}^s Q_s + \mu_{fg}^a Q_a \right| \chi_i(Q) \right\rangle = \\ &= \mu_{fg}(0) \langle \chi_k | \chi_i \rangle + \mu_{fg}^s \langle \chi_k | Q_s | \chi_i \rangle + \mu_{fg}^a \langle \chi_k | Q_a | \chi_i \rangle = \\ &= \mu_{fg}(0) \langle k | i \rangle + \mu_{fg}^s \langle k | Q_s | i \rangle + \mu_{fg}^a \langle k | Q_a | i \rangle. \end{aligned} \quad (18)$$

Above we are using the abbreviation,  $\langle \chi_k | \chi_i \rangle = \langle k | i \rangle$ , while remembering that  $k$  and  $i$  represent the totality of vibrational quantum numbers in the two states. The first term is the electronic transition moment at the equilibrium position of the initial state multiplied by the vibrational overlap, factor called the Condon integral. The second and third terms, which arise from vibronic interaction, can collectively be called Herzberg-Teller terms. An electronically forbidden transition is one where  $\mu_{gi,fk}$  vanishes for all nuclear configurations having the same symmetry as the equilibrium position of the initial state, e.g., due to the Laporte rule. Symmetric distortions along the axis preserve inversion symmetry on this axis, and the second term in Eq. (18) still obeys the Laporte rule. In this case, only the third term of Equation (18) remains.

Following the calculations presented in [20] and detailed in Appendix 12, assuming absorption of two identical photons i.e.  $\vec{e}$  vectors at the beginning and the end are the same, we reach the equation for the two-photon absorption cross-section for a transition that takes place from the initial electronic state,  $g$ , with vibronic quantum number  $k$ , to the final electronic state,  $f$ , with the vibronic quantum number,  $i$ , through an intermediate state,  $m$ :

$$\begin{aligned} \sigma_{2PA} &= \frac{\pi \omega^2}{\epsilon_0^2 c^2 \hbar^2 n^2} \left\langle \left| \vec{e} \left( \langle k | i \rangle \sum_m \frac{\mu_{fm}(0) \mu_{mg}(0)}{(\omega_{mg} - \omega)} + \langle k | Q_{(i)} | i \rangle \times \right. \right. \right. \\ &\quad \left. \left. \left. \sum_m \left\{ \frac{\mu_{fm}(0) \mu_{mg}(1) + \mu_{fm}(1) \mu_{mg}(0)}{(\omega_{mg} - \omega)} \right\} \right) \vec{e} \right|^2 \right\rangle g_M(2\omega). \end{aligned} \quad (19)$$

where  $\mu_{fm}(0)$  and  $\mu_{mg}(1)$  are zeroth and first-order approximations of electronic transition moment Taylor series expansion and where we have used the fact that the

vibrational terms for the intermediate state are canceled out. Here  $\langle k|i\rangle$  represents the overlap integral of the vibrational wave functions of the initial and final state with the nuclei in the equilibrium positions, whereas the term  $\langle k|Q_{(i)}|i\rangle$  accounts for changes in overlap due to the vibrational displacement of the nuclei. Index ( $i$ ) on the ensemble coordinates of the nuclei represents the initial electronic state.

Similarly, the 1PA cross-section can present by combining Equation (18) and Equation (4):

$$\sigma_{1PA}(\omega) = \frac{\pi\omega}{3nc\varepsilon_0\hbar} \left| \mu_{fg}(0)\langle k|i\rangle + \mu_{fg}^s Q_s \langle k|Q_s|i\rangle + \mu_{fg}^a Q_a \langle k|Q_a|i\rangle \right|^2 g_M(\omega). \quad (20)$$

If we neglect Herzberg-Teller terms:

$$\sigma_{1PA}(\omega) = \frac{\pi\omega}{3nc\varepsilon_0\hbar} \left| \mu_{fg}^2(0)\langle k|i\rangle \right|^2 g_M(\omega). \quad (21)$$

### 1.1.5 Two-level model of 2PA and vibronic 2PA transitions

It was mentioned above that in the case of strongly dipolar molecules, a two-level model of 2PA has often proven to be adequate, particularly for the description of the lowest-energy electronic transition [16]. Let us re-cast Equation (19) by retaining only the sum of initial and final levels, whereby the intermediate level is represented, in turn, by the ground and final levels. We obtain:

$$\sigma_{2PA}(\omega) = \frac{\pi\omega^2}{\varepsilon_0^2 c^2 \hbar^2 n^2} \left\langle \vec{e} \left( \langle k|i\rangle \left( \frac{\mu_{fg}\mu_{gg}}{-\omega} + \frac{\mu_{ff}\mu_{fg}}{\omega} \right) + \langle k|Q_{(i)}|i\rangle \times \left( \frac{\mu_{fg}^m \frac{\partial \mu_{gg}}{\partial Q} + \mu_{gg} \frac{\partial \mu_{fg}}{\partial Q}}{-\omega} + \frac{\mu_{ff}^m \frac{\partial \mu_{fg}}{\partial Q} + \mu_{fg} \frac{\partial \mu_{ff}}{\partial Q}}{\omega} \right) \right) \vec{e} \right\rangle g_M(2\omega). \quad (22)$$

After some re-arrangement (see Appendix 12) this may be written in a more compact form when assuming linearly polarized identical photons (Appendix 4):

$$\sigma_{2PA}(\omega) = \frac{\pi}{15 n^2 c^2 \varepsilon_0^2 \hbar^2} (2 \cos^2(\beta) + 1) \left| \langle k|i\rangle \mu_{fg} \Delta\mu + \langle k|Q_{(i)}|i\rangle \left( \mu_{fg} \frac{\partial(\Delta\mu)}{\partial Q} + \frac{\partial \mu_{fg}}{\partial Q} (\Delta\mu) \right) \right|^2 g_M(2\omega). \quad (23)$$

if we neglect Herzberg-Teller terms, then:

$$\sigma_{2PA}(\omega) = \frac{\pi (2 \cos^2(\beta) + 1)}{15 n^2 c^2 \varepsilon_0^2 \hbar^2} \left| \langle k|i\rangle \mu_{fg} \Delta\mu \right|^2 g_M(2\omega). \quad (24)$$

It can be seen from comparing Equations (21) and (24) that in the case of the two-level system the vibronic intensity distributions in the corresponding progression is determined by  $\langle k|i\rangle$  and are the same for 2PA and 1PA, as is often the case for strongly dipolar chromophores.

### 1.1.6 Estimation of the permanent electric dipole moment change upon electronic transition

If the chromophore is strongly dipolar, then both 2PA and 1PA transitions are allowed, and the main contribution to the 2PA originates from the Frank-Condon term. Such direct relation between the 2PA,  $\mu_{fg}$  and  $\Delta\mu_{fg}$  allows quantitative estimation of the absolute value of the change of the permanent electric dipole moment as follows (for derivation, see Appendix 14):

$$|\overline{\Delta\mu}| = \sqrt{\frac{5}{P(\beta)} \frac{n c \varepsilon_0 \hbar N_a \omega \sigma_{2PA(max)}}{10^3 \ln(10) L^2 \varepsilon_{M(max)}}}. \quad (25)$$

Here the terms  $\varepsilon_{M(max)}$  and  $\sigma_{2PA(max)}$  represent respective peak values in the 0-0 band,  $P(\beta)$  is introduced by isotropic averaging [21] and depends on excitation polarization. For linearly polarized light  $P(\beta) = 2 \cos^2(\beta) + 1$ , whereas for circularly polarized light  $P(\beta) = 1/2(\cos^2(\beta) + 3)$  [14].

### 1.1.7 Quantum-chemical calculations and modeling

When interpreting our experimental findings, we extensively rely on quantum-chemical calculations that provide respective theoretical values of key molecular parameters, such as 1PA oscillator strengths, 2PA cross-section, and corresponding peak wavelengths. The calculations were performed by our NICPB lab group members, Dr. Merle Uudsemaa and Dr. Aleksander Trummal, and also by our collaborator Dr. Denis Jacquemin at the University of Nantes, France. Therefore, even though quantum chemistry is outside the scope of this Thesis, a short description of the calculation methods used is in order.

Gaussian09 [22] or Gaussian16 [23] software was used to obtain relaxed molecular structures and respective linear spectra, while Dalton2020 [24] was used for estimating nonlinear-optical properties. As a common prerequisite, the ground-state conformational search was carried out in the gas phase at B3LYP [25], [26]/6-311G(d,p) [27] DFT level. The lowest energy conformers were re-optimized in the solvent of interest using PCM [28], [29]/B3LYP/6-311G(d,p) method, where the solvent effects were treated in the framework of polarized continuum approximation. The lack of imaginary frequencies in harmonic vibrational spectra was established for each optimized structure to confirm the true minimum conditions on the potential energy hypersurface. The ground-state vibrational eigenvectors displacement patterns were subsequently used for 2PA profiling of selected vibrational modes. For some calculations, the discrete-continuum approach involving one explicit solvent molecule was also implemented to account for the specific solvation contribution of especially in case of hydrogen-bond donation-capable solvents. The resulting lowest energy conformers were selected for the calculation of optical properties. 1PA vertical excited state energies, transition oscillator strengths, and the change of the permanent electric dipole moment ( $\Delta\mu$ ) upon the electronic excitation were obtained from TD-DFT [30] calculations using tuned Coulomb Attenuated Method B3LYP [31] (CAM-B3LYP) functional. The fine-tuning was performed to achieve an optimal match with the experimentally determined counterpart values based on a) the quality of fitting of the measured 1PA line shape using theoretical vibronic approach (see below) and b) the calculated energy of the first vertical singlet transition, which is expected to be close to the energy of experimental absorption maxima. It has been shown that the representative set of internal CAM-B3LYP parameters ( $\alpha = 0.03$ ;  $\beta = 0.97$ ;

$\mu = 0.125$ ) along with slight variations in the range-separation parameter  $\mu$  used in the present study led to satisfactory predictions of the spectroscopic properties.

Theoretical extinction coefficients of the 1PA transitions were obtained by applying a Gaussian broadening function on respective calculated oscillator strengths and excitation energies obtained from TD-DFT calculations. The corresponding experimental values of FWHM were estimated from Gaussian deconvolution of the measured absorption spectra.

The present study also computed the vibrationally-resolved electronic spectra using Franck-Condon and Herzberg-Teller (FCHT) expansion terms for selected  $S_0 \rightarrow S_1$  transitions. The geometries of the ground state and first excited state were optimized, and frequency calculations were performed in a respective solvent under equilibrium conditions. The vibronic 1PA spectra were generated at  $T = 0$  K with convergence levels of over 90%.

The dominant natural transition orbitals [32] (NTOs) were calculated and subsequently visualized using the GaussView software package to characterize the changes in electron density related to a particular electronic transition.

Dalton2018 software suite [33], [24] was used for all single residue quadratic response calculations of two-photon transition probability,  $\delta_{2PA}$  in implicit solvent.

Rotationally averaged 2PA transition probabilities are evaluated in DALTON according to:

$$\langle \delta_{2PA} \rangle = \frac{1}{30} \sum_{ab} (FS_{aa}\bar{S}_{bb} + GS_{ab}\bar{S}_{ab} + HS_{ba}\bar{S}_{ba}), \quad (26)$$

with F, G, and H being equal to 2 in the case of linearly polarized light and  $\bar{S}$  is the complex conjugate of  $S$ .

The corresponding second-order transition moment  $S_{ab}^{if}$  between the initial ( $i$ ) and final ( $f$ ) states is expressed as:

$$S_{ab}^{if}(\omega_1, \omega_2) = \sum_{n \neq i} \left\{ \frac{\langle i|\mu_a|n\rangle\langle n|\bar{\mu}_b|f\rangle}{\omega_{ni}-\omega_1} + \frac{\langle i|\mu_b|n\rangle\langle n|\bar{\mu}_a|f\rangle}{\omega_{ni}-\omega_2} \right\}, \quad (27)$$

where  $\langle i|\mu_a|n\rangle$  is the transition dipole moment between the corresponding electronic states,  $\omega_{ni}$  is the excitation energy,  $\omega_1$  and  $\omega_2$  are the frequencies of photons involved in transition ( $\omega_1$  and  $\omega_2$  are equal in the case of 2PA).

The macroscopic 2PA cross-sections (in GM) for the  $S_0 \rightarrow S_1$  transition was obtained from the relation:

$$\sigma_{2PA} = \frac{4\pi^3\alpha a_0^5}{c} \frac{\omega^2}{\pi\left(\frac{\text{FWHM}}{2}\right)} \langle \delta_{2PA} \rangle \cdot 10^{50}, \quad (28)$$

where  $\alpha$  is the fine structure constant,  $a_0$  is Bohr radius,  $\omega$  is the calculated photon energy (half of the transition energy), and FWHM is the full width at half maximum of the 2PA absorption band.

Theoretical estimation of  $pK_{aH}$  values in methanol was conducted by our collaborators in the group of Prof. Ivo Leito from the University of Tartu. It was based on a correlation established between the computed  $\Delta G_s$  values (Gibbs free energy differences between protonated and deprotonated forms) and experimental  $pK_{aH}$  values [25] of 11 differently substituted pyridines, covering  $pK_{aH}$  range from 2.8 to 10.4. using expression:

$$pK_{aH} = c_1 \frac{\Delta G_s}{N_A k_B T \ln(10)} + c_2. \quad (29)$$

Where  $c_1$  and  $c_2$  are linear regression constants,  $N_A$  is Avogadro's Constant,  $k_B$  is the Boltzmann constant, and  $T$  is the absolute temperature. Likewise, the respective correlation was used for the prediction of dication deprotonation ( $pK_{aH}(2)$ ).

The required  $\Delta G_s$  values were estimated from COSMO-RS calculations at T = 298K and assuming infinite dilution by applying solvent-specific deviations from the ideal conductor state as computed by the statistical thermodynamics approach implemented in COSMOtherm software. The preceding single-point ideal conductor calculations were carried out for all stable conformers at COSMO/BP86/def2-TZVPD level of theory, following sampling of conformational space and identification of relevant conformers using COSMO/BP86/def-TZVP method. TURBOMOLE quantum chemistry suite was used for all calculations in the ideal conductor.

## 2 Experimental methods

### 2.1 Overview of experimental techniques for measuring 2PA spectra and 2PA cross-sections

As was pointed out at the beginning of section 2, the probability of 2PA is much lower than that of the 1PA, under typical excitation conditions. This difference makes the determination of the minor photon flux changes due to 2PA a challenging task.

To further illustrate this circumstance, let us estimate the relative change of the photon flux when a collimated laser beam passes through a cuvette of the path length,  $d$ , and is filled with a solution of 2-photon absorbing chromophores at the molar concentration,  $C_M = \frac{10^3}{N_A} N_g$ . Integration of the second term in Equation (3) gives:

$$T = \frac{\Phi_0 - \Phi(d)}{\Phi_0} = \frac{1}{1 + C_M \cdot 10^3 \cdot N_A \cdot \sigma_{2PA} \cdot \Phi_0 \cdot d}. \quad (30)$$

After inserting typical experimental values,  $C_M = 1 \text{ mM}$ ,  $\sigma_{2PA} = 1 \text{ GM}$ ,  $\Phi_0 = 10^{27} \frac{\text{photons}}{\text{cm}^2 \cdot \text{s}}$ ,  $d = 1 \text{ cm}$ , we arrive at the transmittance change,  $\Delta T \approx 0.994$  or  $0.6\%$ . Measuring such a small change of the transmittance implies that the experimental accuracy of determining the photon flux must be much better than  $1\%$ , both at the input as well as at output side of the sample. Achieving such high accuracy which is often not an easy task, especially due to large pulse-to-pulse energy fluctuations inherent to pulsed lasers. Another potential disadvantage of direct measurement of 2PA is that, in many cases, it requires using a relatively high chromophore concentration ( $\geq 1 \text{ mM}$ ). The latter may cause difficulties due to aggregation and other inter-chromophore interactions. In addition, because of the need to utilize relatively high photon flux ( $10^{27} \frac{\text{photons}}{\text{cm}^2 \cdot \text{s}}$  or higher), there may occur artifacts causing nonlinear side effects such as thermal lensing, self-focusing(-defocusing), sample bleaching, etc. Certainly, there exist well-established experimental techniques for the direct determination of  $\sigma_{2PA}$  such as z-scan [34] and Nonlinear transmittance [35]. Nevertheless, for the purpose of characterizing potential fluorescent probes for microscopy applications, it is advantageous to use a fluorescence detection-based method, which allows the use of lower laser power and much lower sample concentration. A summary of the advantages and disadvantages of direct and indirect methods is further summarized in Table 1.

It should be noted that even though fluorescence serves only as an indirect probe of the 2PA transition rate, and thus determining the 2PA values requires supplementary measurements (see below), it does offer a significant advantage as it allows better discriminations between 2PA and potential artifacts, especially such as non-linear lensing, excited state absorption (ESA) and residual 1PA.

Table 1: Comparison of direct and indirect methods for measuring 2PA spectra and cross-sections.

| Direct techniques  | Indirect techniques   |
|--|---|
| <p><b>Advantages:</b></p> <ul style="list-style-type: none"> <li>• Direct absolute determination of <math>\sigma_{2PA}</math></li> <li>• Broadly applicable to various nonlinear absorbers, including liquids, solids, thin films, etc.</li> <li>• Conceptually straightforward</li> <li>• Relatively simple and low-cost experimental setup.</li> </ul>                     | <p><b>Advantages:</b></p> <ul style="list-style-type: none"> <li>• Potentially background-free signal</li> <li>• Allows use of more diluted solution and/or lower laser power</li> <li>• Allows distinguishing between “pure” 2PA process and potential experimental artifacts such as 1PA, ESA etc.</li> </ul> |
| <p><b>Disadvantages:</b></p> <ul style="list-style-type: none"> <li>• Requires measurement of very small changes of the photon flux typically, &lt;1%</li> <li>• May require highly concentrated samples &gt;1 mM</li> <li>• Susceptible to nonlinear side effects due to high photon flux</li> <li>• Difficulty of distinguishing between 2PA and 1PA, ESA, etc.</li> </ul> | <p><b>Disadvantages:</b></p> <ul style="list-style-type: none"> <li>• Requires samples to be sufficiently fluorescent (or luminescent)</li> <li>• Requires characterization of emission properties</li> <li>• Assumes that the emission follows Kasha’s rule.</li> </ul>  |

### 2.1.1 Two-photon excited fluorescence

As 2PA promotes the molecule to an excited electronic state, the accumulated excitation energy is eventually released to the surrounding environment. This process may proceed by one or more physical pathways, such as the emission of fluorescence and/or phosphorescence, the creation of heat and/or phonons, etc. [36]. Methods of indirect 2PA spectroscopy methods are based on detecting these 2PA-induced secondary effects. However, establishing the required quantitative relation between the detected secondary signal and the number of excited molecules created by each excitation laser pulse may be, again, a demanding task.

The most commonly used indirect method is based on detecting two-photon absorption-induced fluorescence (2PIF). Under conditions where the excitation rate is much less than the excited-state relaxation rate, such that absorption saturation may be ignored, the number of fluorescence photons emitted is proportional to the number of chromophores excited via 2PA. Depending on how the above proportionality ratio is evaluated, the 2PIF methods can be, in turn, divided into absolute and relative 2PIF methods.

The absolute 2PIF method implies accurate characterization of the excitation laser pulse photon flux, i.e., energy (number of photons), and spatial and temporal profiles in the entire range of excitation wavelengths. To determine the 2PA cross-section value, one also needs to evaluate the fluorescence emission quantum yield, which, in turn, may imply knowledge of the efficiency of the fluorescence detection system, thus turning the 2PA measurement, again, into an experimentally rather tedious task. The relative 2PIF



method, on the other hand, may alleviate some of these complications, provided that suitable well-characterized 2PA reference standards can be used. Indeed, by comparing the 2PIF signals obtained for the studied chromophore (sample) to that of the reference sample at identical excitation conditions, one may eliminate the need for accurate characterization of the photon flux.

This allows not only increase of the efficiency and throughput of measuring the 2PA spectra, but also increase of the accuracy and reliability of these measurements. Increased accuracy is due to reduced systematic errors, as the sample spectra are always corrected with respect to a known reference, thus greatly alleviating effects due to potential artifacts caused by changes in the excitation laser pulse shape and duration. The experiments described in this Thesis take extensive advantage of such 2PA reference standards, which have been previously developed by our group [37]. A detailed account of our 2PIF measurement techniques is given below.

## 2.2 Chemical solvents and reagents

This study uses organic chromophores that have been acquired from commercial sources as well as those that were synthesized by our collaborators, especially for this project. Commercial dyes, coumarin 153 (C153) (99%), Rhodamine 6G (Rh6G) (99%), were purchased from Sigma Aldrich, coumarin 151 (7-amino-4-(trifluoromethyl) coumarin) (99%) was purchased from Alfa Aesar, LDS798 was purchased from Exciton and AF455 was provided by Dr. S. Tan (US Air Force Research Lab, OH, USA)

Solvents such as tetrahydrofuran, methanol, dimethyl sulfoxide, octanol, and toluene (all HPLC grade) were purchased from Sigma Aldrich, and chloroform was purchased from Merck (99.8%). Distilled water was produced in-house.

The protonation experiments used trifluoromethanesulfonic acid (Triflic) (99%) or hydrochloric acid (HCl,  $\geq 37\%$ ). Both were purchased from Sigma Aldrich.

## 2.3 Compounds under study

The chemical structure of four coumarin 151-based fluorophores decorated with different phosphazene groups are shown in Figure 7 and were provided to us by our collaborator Prof. Ivo Leito from Tartu University. The synthesis of these compounds was described in [38], [39].

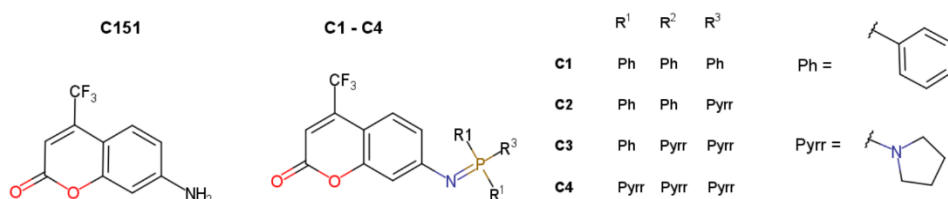


Figure 7: The chemical structures of coumarin C151 and the four phosphazene derivatives C1, C2, C3, and C4.

The compounds were received in the form of yellow powder in 15 – 20 mg quantities, as shown in Figure 8.

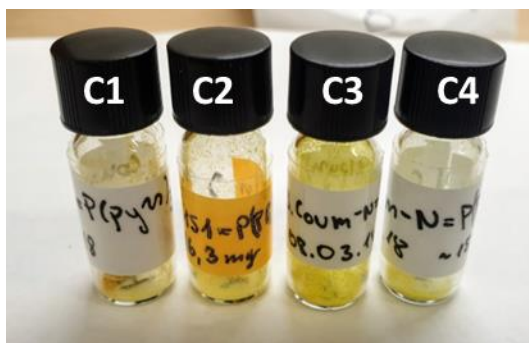


Figure 8: Vials containing C1, C2, C3, and C4 powder.

The second type of custom dyes were derivatives of pyrrolopyrroles and was prepared by the research group of Prof. Daniel T. Gryko from the Polish Academy of Sciences. Even though 2PA experiments were performed with 13 different pyrrolopyrroles, for this Thesis, we selected two representative compounds, named 1a and 3,6-bis-(2-tert-butylpyridin-4-yl)-diketopyrrolopyrrole (PDP). The corresponding structures are shown in Figure 9. The compounds were received in ~10 mg quantities as a colored powder and were used without further purification. Vials containing PDP and 1a can be seen in Figure 10. A description of the synthesis can be found in [40].

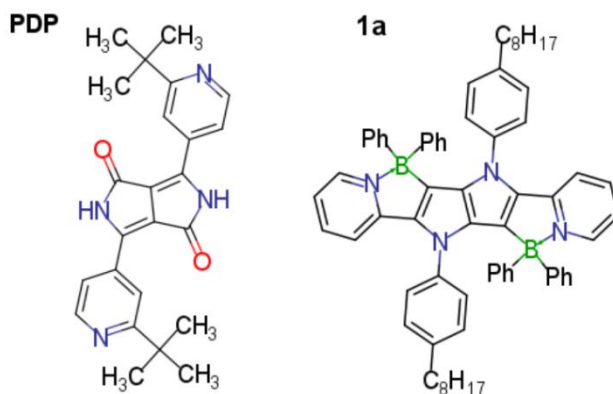


Figure 9: Chemical structures of PDP and 1a.

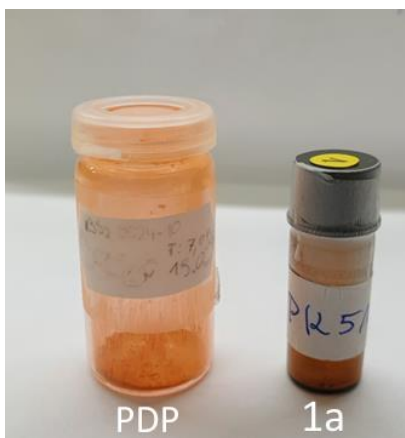


Figure 10: The vial containing PDP on the left and 1a on the right.

### 2.3.1 Measurement of linear absorbance spectra

UV-VIS spectrophotometer (UV 3600 PLUS, Shimadzu) was used to determine the linear absorbance spectra of the sample solutions. Additionally, 1PA measurements were used to characterize solution concentration, purity and photostability both, before and after each 2PA measurement. Solutions were prepared in either 1 mm or 1 cm Teflon-stoppered quartz cuvettes manufactured by Starna Scientific. The optical density of the solutions varied between 0.1 to 2.0.

### 2.3.2 Measurement of linear fluorescence emission spectra

One-photon-induced fluorescence was measured with a Perkin Elmer LS-55 spectrofluorometer. The samples were contained in Teflon-stoppered 1 cm quartz cuvettes, and the chromophore concentration was adjusted so that the maximum optical density at the excitation wavelength was below 0.1 to minimize the inner filter effect. To improve the reliability of the collected spectra, we used a custom instrument spectral correction function, which was developed in-house using a set of fluorescent reference standards (see Appendix 8 for further discussion).

### 2.3.3 Determination of molar extinction coefficient

Stock solutions  $C_{\text{Dye}} \sim 1$  mM was prepared by weighing  $\sim 0.5$  mg of the solid dye using Sartorius Lab Instruments GmbH & Co. KG MSA36P-OCE-DH analytical balance. Dye was then thoroughly stir-mixed into 1.5 ml of solvent. The stock solution was then diluted into a series of 4 to 5 samples, with concentrations in the range of 0.03 – 0.08 mM. The maximum absorbance of the diluted samples did not exceed O.D.  $\sim 1.5$  (in 1 cm cuvette).

The normalized spectra for each sample were evaluated and compared to ensure that no impurities or aggregates were present. The molar extinction coefficient (in  $\text{M}^{-1} \text{cm}^{-1}$ ) at the absorption peak was determined by fitting the measured peak absorbance vs. concentration dependence with a linear function. The process was repeated 2 to 3 times to improve fidelity, and the results were averaged.

Due to limited solubility, the stock solution of PDP was prepared in 50 ml of methanol instead of 1.5 ml, as was the case for coumarin derivatives. The extinction coefficient for compound 1a was provided by Prof. D. Gryko.

### 2.3.4 Measurement of fluorescence quantum yield

To determine the fluorescence quantum yield of coumarin samples, five solutions were prepared with different chromophore concentrations with maximum optical density ranging from 0.02 to 0.1. Fluorescence emission quantum yields were measured relative to the standards applying the method described in [41], using the equation:

$$Q_s = Q_r \left( \frac{m_s}{m_r} \right) \left( \frac{n_s}{n_r} \right)^2, \quad (31)$$

where  $Q_r$  is the reference standard fluorescence quantum yield,  $m_s$  and the  $m_r$  are respective fitted slopes for the integrated fluorescence intensity vs. absorbance for the five samples at different concentrations.  $n_s$  and  $n_r$  are the refractive indices of the reference and sample solutions. The standards used were C153 in ethanol,  $\phi_{em} = 0.53$  [42], and C151 in ACN,  $\phi_{em} = 0.57$  [43] and were chosen based on similarity to absorption and fluorescence spectral profiles of the studied samples.

### 2.3.5 Measurement of pH

Protonation (or hydronation) is adding a proton (or hydron) to an atom, molecule, or ion, and is extensively utilized in the current Thesis to alter the chromophore's properties, including its symmetry. In solution and at room temperature, protonation is usually a rapidly equilibrating process. The rate of protonation is tied to the acidity of the protonating species. In this work, trifluoromethanesulfonic acid ( $\text{CF}_3\text{SO}_3\text{H}$ ) and hydrochloric acid (HCl) are used to create an excess of hydrogen ions in the solution.

The strength of an acid is usually expressed in terms of the equilibrium dissociation constant,  $K_a$ , that characterizes the acid-base dissociation reaction and is defined as,

$$K_a = \frac{[A^-][H^+]}{[HA]}, \quad (32)$$

where  $[HA]$  is the concentration of the acid, and  $[A^-]$  and  $[H^+]$  are the concentration of the conjugate base and the hydrogen ion. A more practical quantity is the negative logarithm (acidity):

$$pK_a = -\log_{10} K_a. \quad (33)$$

and is commonly determined for aqueous solutions. For example, triflic acid is one of the strongest acids having aqueous acidity,  $-14.7$   $pK_a$  units, while the aqueous  $pK_a$  value for HCl is  $-5.9$  [44]. In this work, however, non-aqueous solvents such as methanol or THF are also used. This may affect the apparent  $pK_a$  of each acid according to the leveling effect of the solvent, although presumably both acids can be considered strong acids for each solvent investigated.

The acidity or basicity of a solution is characterized by pH, corresponding to the negative logarithm of the concentration of hydrogen ions (mol/L) also typically in water solution. A standard way of measuring pH is with a pH meter. A typical pH meter consists of pair of silver-silver chloride electrodes combined into one probe. The reference electrode is kept under constant electric potential, while the measuring electrode is immersed in a buffer solution surrounded by a glass membrane that is selective to hydrogen-ion. The pH value of a sample solution is determined by measuring the potential between the reference and the measurement electrode, linearly calibrated using two or three reference pH solutions (Aqueous solutions of pH 4, 7 & 10).

In our experiments, we used the pH meter (827 pH lab, Metrohm) and probe (Ag/AgCl electrode, Biotrode 6.0224.100, Metrohm). The probe diameter was small enough to fit inside 1x1 cm quartz cuvettes where the samples were prepared. Before each

measurement, regular two-point calibration with aqueous buffers was used. The pH probe was calibrated in methanol solution by titrating reference acids (i.e. pyridine, 1-ethylpiperidine and quinoline) in water and in the solvent of interest. The measured offset value was used to correct the pH values obtained in the solvent of interest [45], [46].

### **2.3.6 Measurement of 1PA titration spectra**

Titration measurements were conducted using a relatively dilute solution ( $C_{\text{Dye}} \sim 20 \mu\text{M}$ ) to ensure fully dissolved dye and to avoid precipitation. First, diluted triflic acid was prepared by adding one drop of concentrated acid to 5 ml of methanol. Then, the neutral methanol solution of the studied chromophore was prepared, and absorbance spectra and the pH value of the neutral solution were determined. Next, one drop of the diluted triflic acid ( $\sim 0.03 \text{ M}$ ) was added to the solution. The sample was stirred for approximately 30 s. Then the pH of the mixture was measured, followed by the measurement of the absorbance spectra.

The dropwise addition of the dilute acid was repeated until the sample showed no noticeable change in the 1PA spectrum. Finally, a drop of concentrated triflic acid was added to ensure a large excess amount of hydrogen cation in the solution. Final titration spectra were obtained by subtracting pure solvent absorbance and correcting for the concentration change due to added solvent volume. The same procedure as described above was also used for the THF but without the pH measurement.

## **2.4 Measurement of two-photon absorption spectral profiles and 2PA cross-sections**

Our experiments aimed to determine the 2PA cross-section and the 2PA spectra, i.e., the dependence of  $\sigma_{2PA}$  on the excitation wavelength, with the highest possible accuracy and fidelity. For this purpose, we measured separately the 2PA spectral shapes and the 2PA cross-section, following two related but slightly different procedures, as will be described next.

### **2.4.1 Wavelength-tunable femtosecond laser system**

To facilitate high-quality measurements, it is vital to have a broadly wavelength-tunable pulsed laser source. The laser also has to display stable output characteristics such as pulse duration, spatial mode shape, beam pointing direction, etc. The stability of the laser output was especially critical to ensure that sample and reference measurements were performed with identical excitation conditions. In our 2PA experiments, we used a wavelength-tunable femtosecond pulsed laser system manufactured by Light Conversion, Inc (Vilnius, Lithuania). The system comprises the following components: A Pharos-SP pump laser (A), Orpheus-HE optical parametric amplifier (B) (OPA), and Lyra-SH second harmonic generator (C) (SHG). The layout of the laser on our optical table is shown in Figure 11.



Figure 11: Tabletop layout of the femtosecond pulse laser system (Light Conversion). A – PHAROS-SP pump laser, B – ORPHEUS-HE optical parametric amplifier, C – LYRA second harmonic generator.

The Pharos pump laser generates  $\sim 160$  fs duration, 1 mJ energy pulses. The pump laser itself comprises a Kerr lens mode-locked femtosecond oscillator followed by a regenerative chirped pulse amplifier. The amplifier uses a directly diode-pumped Yb:KGW (ytterbium-doped potassium gadolinium tungstate) crystal gain medium, along with a femtosecond pulse optical stretcher-compressor unit. Pharos operates at the center wavelength of 1030 nm, delivers a maximum average output power of 6 W at maximum 6 kHz pulse rate and pulse duration of  $\sim 170$  fs. The pulse repetition rate may be lowered down to 100 Hz, without affecting the pulse energy or other pulse parameters, by using the built-in Pockels cell pulse-picker.

Wavelength tuning of the femtosecond pulses is achieved by using the process of optical parametric amplification with Orpheus-HE (OPA). The frequency-doubled pump laser photons at 515 nm are split into two longer-wavelengths, signal and idler photons, by three-wave mixing in type I BBO crystal. The OPA output wavelength is continuously tunable in the range  $\lambda = 630 - 1040$  nm (signal) and  $\lambda = 1022 - 2600$  nm (idler). Furthermore, by using type I SHG in BBO (Lyra-SH), additional wavelength tunability in the ranges  $\lambda = 315 - 520$  nm (SH Signal) and  $\lambda = 515 - 630$  nm (SH Idler) is achieved.

Figure 12 shows the typical average output power of the laser in the signal (SIG), idler (IDL), and the second harmonic of idler (SH-IDL), wavelength tuning ranges at 6 kHz pulse repetition rate. The average power in most signal and idler ranges is 150 – 450 mW (energy per pulse 25 – 75  $\mu$ J). The sudden power drop near 1030 nm is due to the OPA wavelength degeneracy point, i.e., when the signal and idler wavelengths coincide. The second harmonic of the idler has an average power of around 100 mW (energy per pulse 17  $\mu$ J).

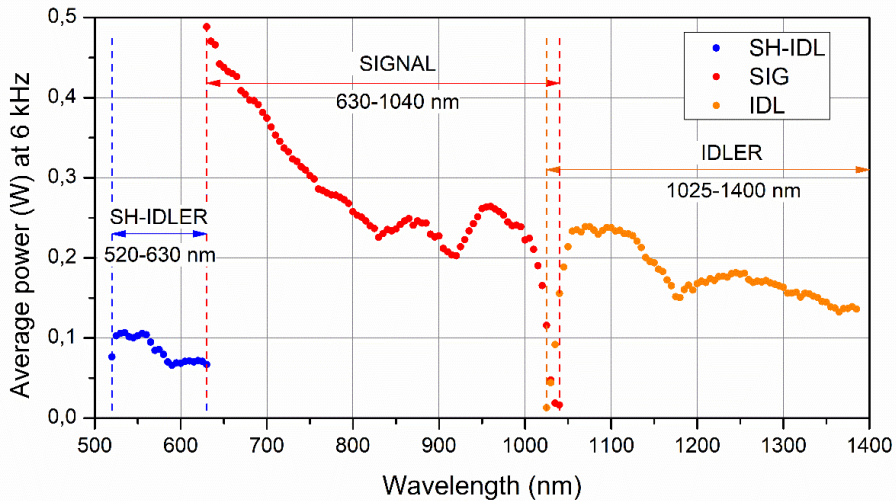


Figure 12: Typical average laser power at the signal (SIG), idler (IDL), and second harmonic of idler (SH-IDL) wavelength ranges.

The OPA output is kept vertically polarized, which is achieved by inserting a broad-band half-wave plate positioned inside the Lyra-SH, depending on whether the signal or idler.

#### 2.4.2 Two-photon-excited fluorescence spectrometer

Our 2PA measuring apparatus (Figure 13) was designated to perform two related measurements:

- Measurement of the relative two-photon excited spectral profile in a broad range of wavelengths (2PA spectral shape function).
- Comparison of the 1PA and 2PA excitation values at selected excitation wavelengths to determine absolute 2PA cross-section.

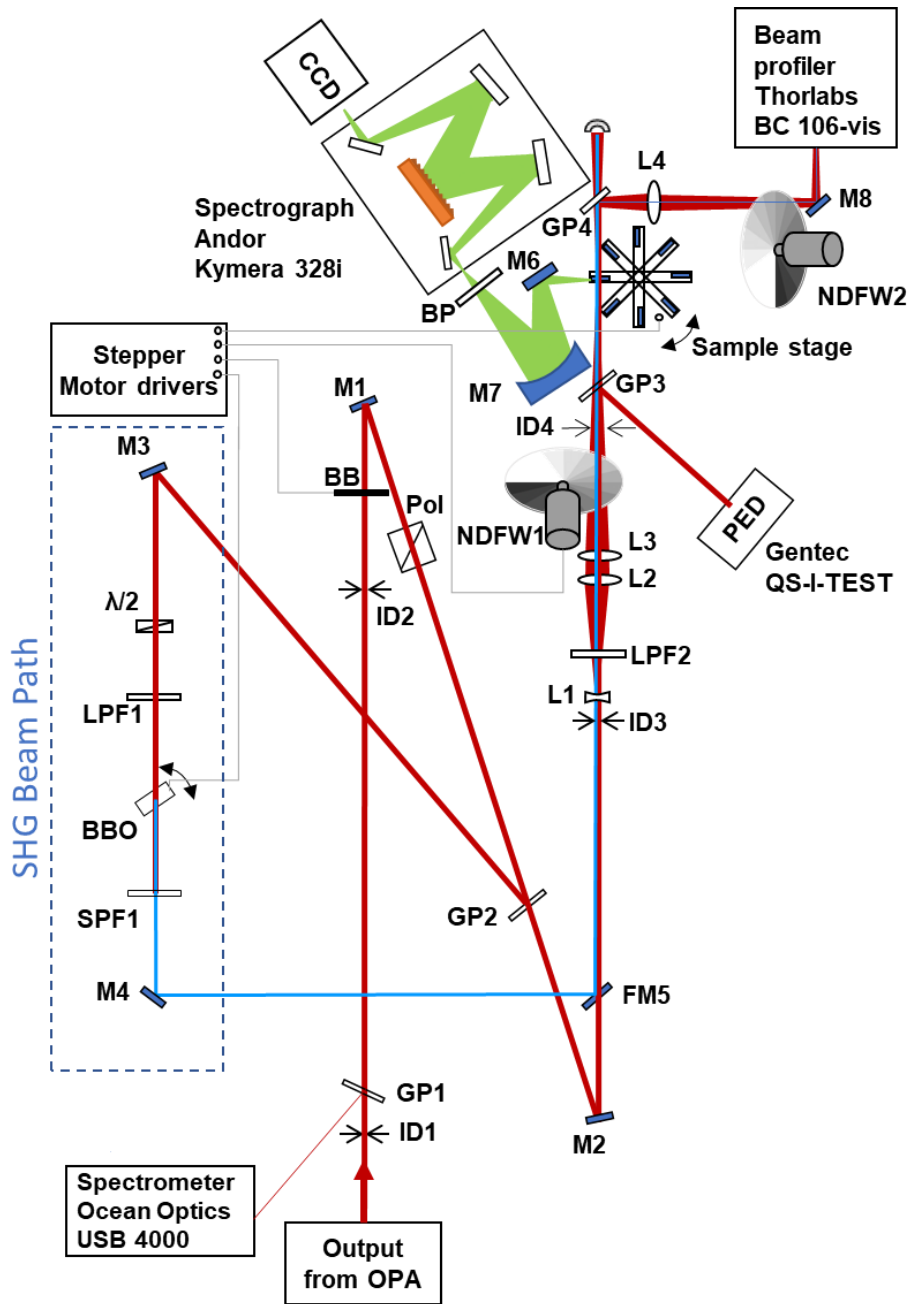


Figure 13: Schematic of the automated femtosecond 2PA spectrometer for measuring 2PA spectral profile and determining 2PA cross-section. These two measurements used slightly different beam paths (see main text for explanation). BB – motorized beam block; Pol – polarizer; GP – Glass plate; ID – iris diaphragm; L – focusing lenses; LPF – long-pass filter; BP – band-pass filter; M – Mirrors; FM – Flipper mirror;  $\lambda/2$  – half-wave plate; BBO – barium borate crystal; SPF – short-pass filter; NDFW – motorized neutral density filter wheel; PED – pyroelectric detector.



Our first task was to ensure that the OPA output contained only the desired wavelengths (signal or idler) and that any spurious wavelengths were sufficiently strongly suppressed.

Even though the manufacturer Light Conversion Ltd. supplied a set of interference filters designed for this purpose, we opted for a different approach (described below). Essentially because the commercial filters, due to their limited wavelength range, would prevent the continuous scan of the entire 2PA spectra.

In our case, the OPA output was spectrally filtered in three stages. In the first stage, the laser beam was passed through a vertically oriented Glan-Laser Calcite Polarizer (Thorlabs GL10-B). The polarizer transmitted the signal (idler) and suppressed the residual idler (signal) component. Secondly, we took advantage of the fact that the signal and idler beams propagated in slightly different directions, with the relative angle between the two beams  $\sim 2^\circ$ . This branching allowed us to further suppress undesired wavelength components with a set of iris diaphragms (ID1, ID2, ID3). Finally, a combination of color glass filters and interference filters were used to further prevent any residual undesired wavelengths from reaching the sample. The diaphragms ID1-ID4 were also used to ensure reproducible alignment of the beam path, especially when switching between signal and idler measurement regimes. The glass plate (GP1) reflected a small fraction of the OPA beam to the spectrometer (USB2000, Ocean Optics), which monitored the OPA spectral output.

To perform relative 2PA measurements, the main beam was passed through the glass plate, GP2. The beam was then expanded using a 4x Galilean telescope comprising a negative lens  $f = -75$  mm, (LC1582-ML, Thorlabs) (L1) and a positive lens,  $f = 300$  mm, (LA1484, Thorlabs) (L2). The expanded beam was focused  $\sim 50$  mm behind the sample with the lens  $f = 750$  mm, LA1978-ML, Thorlabs (L3).

Shortly after L3, the beam passed through a continuously variable neutral density filter wheel (NDFW1) (NDC-100C-2, Thorlabs). The filter was mounted on a custom motorized rotating stage, which allowed controlled attenuation of the pulse energy by a factor of 1 – 100 and which we used to determine the dependence of the fluorescence signal on the photon flux incident on the sample.

Sample solutions were contained in 1 mm path length spectroscopic quartz cuvettes positioned in a custom-made motorized rotating sample turret (Figure 14, top panel), capable of holding up to eight samples simultaneously. The automated sample turret facilitated back-to-back measurements of multiple samples without manual intervention. The turret was connected to a linear translation stage that allowed adjusting the sample position perpendicular to the excitation beam direction. The sample stage rotation was kept unidirectional to ensure repeatability of the sample positions.

The relative laser power incident on the sample was measured with a pyroelectric detector (PED) (QS-I-Test, Gentec). It monitored the energy of pulses reflected from a glass plate (GP3) positioned directly before the sample.

The position and shape of the beam on a sample were monitored by reflecting 4% of the excitation beam with a glass plate, GP4, to a CCD beam profiler camera (BC106-VIS, Thorlabs) through a lens L4 ( $f = 150$  mm, AC254-150B, Thorlabs). A manual neutral density filter wheel (NDFW2) (NDC-100C-4, Thorlabs) was placed in front of the camera and was manually rotated to avoid saturation of the CCD sensor. The diameter of the beam spot at the sample varies with the wavelength in the range of 0.3 – 1.5 mm.

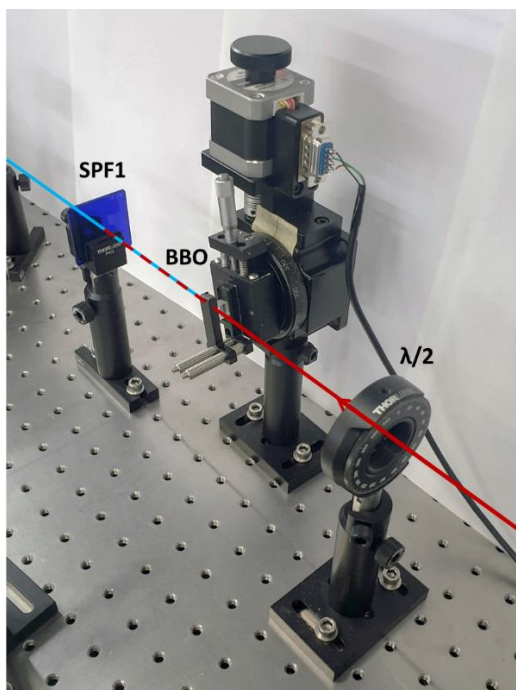
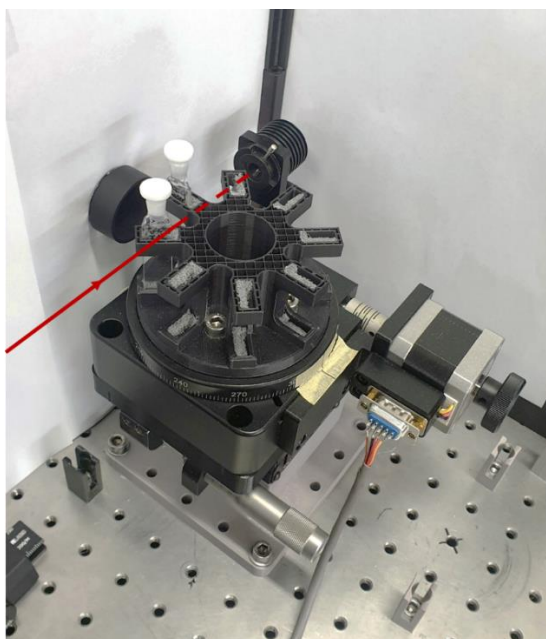


*Figure 14: Top panel: custom motorized sample turret capable of holding a maximum of 8, 1 mm cuvettes; Bottom panel: BBO crystal with automated SHG angle tuning.*

Fluorescence emitted from the sample was collected at 90 degrees with respect to the excitation beam's propagation direction. The emission was first reflected using a flat mirror M6 (2" square mirror) and then focused with a spherical mirror M7 ( $\varnothing$ 75.0 mm,

$f = 150.0$  mm, protected silver, CM750-150-P01, Thorlabs) on the entrance slit of 328 mm focal length and F/4.1 aperture spectrograph (Kymera 328i, Andor). A suitable interference band-pass (BP) filter was used before the spectrograph to cut off scattered laser light. Figure 15 shows the layout of the spectrograph and the fluorescence collection optics. The spectrograph has four interchangeable diffraction gratings with different groove counts (300 lines/mm blazed at 500 nm, 300 lines/mm blazed at 860 nm, 600 lines/mm blazed at 500 nm, 1200 lines/mm blazed at 500 nm).

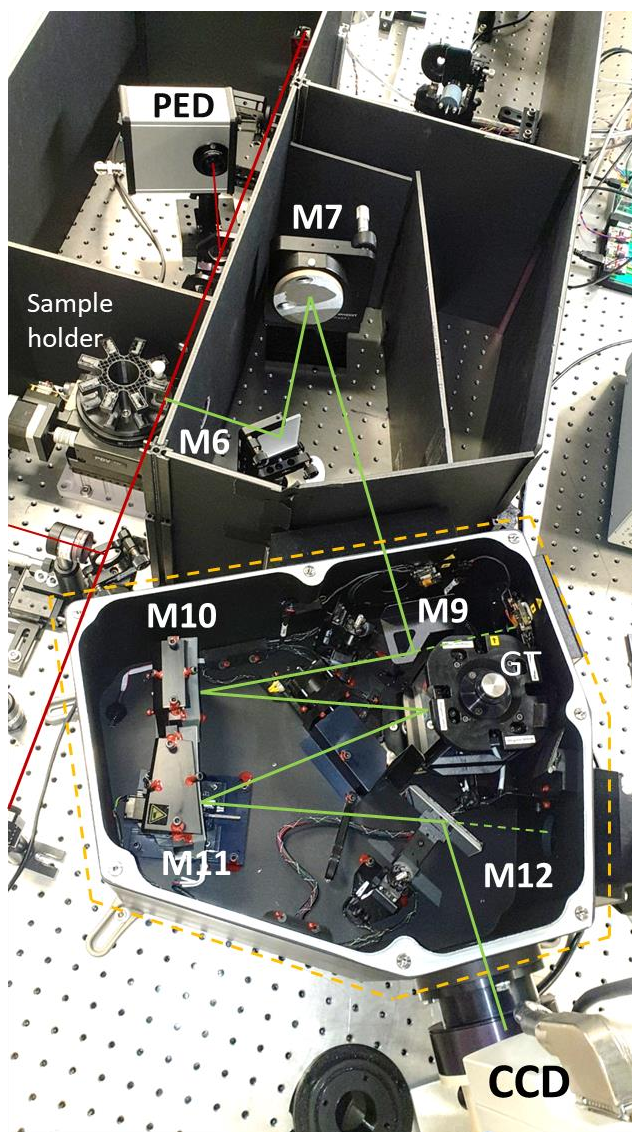


Figure 15: Andor spectrograph Kymera 328i (surrounded by a yellow dotted line). An input signal is reflected with mirror (M9) and (M10) to the Quad-grating turret (GT), allowing for selection between four gratings. Switchable mirror M12, is needed to select between two output ports of the spectrographs.

The fluorescence was detected using a liquid nitrogen cooled, 1024x256 pixels CCD (Symphony Horiba, Inc) attached to one of the two output ports of the spectrograph. The CCD readout was performed using a 20 kHz Symphony Solo controller that was synchronized with the laser pulse rate and with a mechanical shutter at the input port of the spectrograph. In our experiments, we used mainly the 300 l/mm grating, which gave a 260 – 280 nm wide spectral span over the CCD detector length. The CCD signal was binned vertically over all 256 pixels. The fluorescence spectra were recorded along with a corresponding CCD background, where the latter was obtained by blocking the excitation laser beam using a custom-built motor-driven beam block (BB).

Pulses from the reference pyroelectric detector (PED) were averaged using a 10-bit digital oscilloscope (DSOS404A, Keysight), which was synchronized with the laser and the CCD camera.

To carry out absolute 2PA cross-section measurements, we engaged ~4% reflection from the glass plate GP2, which directed a small portion of the OPA pulse energy to the frequency-doubling beam path used for one-photon excitation. A half-wave plate  $\lambda/2$  was used to rotate the polarization by 90 degrees to the horizontal direction. Long-pass near-IR glass filter was used to cut off any residual visible light emitting from the OPA. The OPA wavelength was frequency doubled in the second harmonic generation (SHG) BBO nonlinear crystal, which was angle-tuned for Type I phase matching. The crystal also changed the polarization back to vertical. For automated wavelength tuning of the SHG, the BBO crystal was mounted on a custom motorized rotation stage (Figure 14, bottom panel). The crystal angle was adjusted to achieve optimal phase matching at each laser wavelength according to the predetermined calibration curve. A linear stage was integrated into the apparatus to facilitate manual control over the crystal's vertical position. Before use, the motor position was zeroed by finding the maximum SHG power with the laser at 800 nm. The beam was routed to the sample with a flipper mirror, FM5, after which the beam traveled true the same optics as with non-frequency doubled beam. The PED reference detector was exchanged for a photodiode detector for higher sensitivity (average SHG power at the sample was  $\sim 20 \mu\text{W}$  at 6 kHz). The beam positions at the sample were monitored with the beam profiler (BC106-VIS, Thorlabs) to ensure overlap for 1PA and 2PA excitation beams.

### 2.4.3 LabView control software

A custom control program written in LabView State Machine command pattern was used for data collection from the CCD and the oscilloscope, along with control of the stepper motors and laser wavelength. The program also performed preliminary data analysis. Detailed descriptions and screenshots of the program interface are shown in Appendix 5.

## 2.5 Procedures for evaluating 2PA spectral shape

The procedure of measuring the relative 2PA spectral profile was conducted in four steps, as listed below:

- I. The fluorescence signals from the sample under study and from one or more reference solutions were collected back-to-back at each excitation wavelength,  $\lambda_{2PA}$ , under identical excitation and detection conditions.
- II. At each  $\lambda_{2PA}$  value, the laser power incident on the sample was gradually attenuated by rotating the neutral density filter wheel in  $\sim 10$  steps over an interval, O.D. 0 – 1.0.

- III. At each  $\lambda_{2PA}$  and ND filter position, the fluorescence emission spectrum integrated over a predetermined wavelength region  $\{\lambda_{\min}, \lambda_{\max}\}$  (see Figure 43 in Appendix 5) was recorded.
- IV. The power dependence was evaluated at each  $\lambda_{2PA}$  by linear fitting a log-log plot of the integrated fluorescence versus the relative laser power.

The fit function,  $M+Sx$ , served a dual purpose. First, the slope parameter,  $S$ , allowed us to determine whether the power dependence is sufficiently close to the quadratic function,  $S = 2.00 \pm 0.05$ . Secondly, the offset parameter,  $M$ , was used to evaluate the relative 2PA spectral shape of the sample using the following equation:

$$A_{2PA}^S(\lambda_{2PA}) = \frac{M_S(\lambda_{2PA})}{M_R(\lambda_{2PA})} A_{2PA}^R(\lambda_{2PA}), \quad (34)$$

where  $A_{2PA}^R(\lambda_{2PA})$  is the known 2PA spectral profile of the reference, and subscripts  $s$  and  $r$  refer to the sample and the reference, respectively.

## 2.6 Procedure for measuring 2PA cross-section

A separate measurement was conducted at select excitation wavelengths,  $\lambda_{2PA}$  to obtain the 2PA cross-section of the sample,  $\sigma_{2PA}^S(\lambda_{2PA})$ . We assume that Kasha's rule is valid, i.e., that the fluorescence spectrum and quantum yield are the same for 1PEF and 2PEF in any given sample and that the fluorescence yield is independent of the excitation wavelength. Then, by comparing the 1PEF and 2PEF signals recorded from the same sample, one can account for the fluorescence emission's efficiency and fluorescence detection's efficiency under current experimental conditions [47], [3]. The two-photon cross-section of the sample, at the wavelength  $\lambda_{2PA}$ , was evaluated using the following relation:

$$\sigma_{2PA}^S(\lambda_{2PA}) = \frac{M_S(\lambda_{2PA}) M_R(\lambda_{1PA}) C_R}{M_R(\lambda_{2PA}) M_S(\lambda_{1PA}) C_S} \sigma_{2PA}^R(\lambda_{2PA}) \frac{1-10^{-O.D.(\lambda_{1PA})_S}}{1-10^{-O.D.(\lambda_{1PA})_R}}, \quad (35)$$

where  $\sigma_{2PA}^R(\lambda_{2PA})$  is the two-photo cross-section of the reference chromophore (in GM),  $C$  is the chromophore concentration, O.D. ( $\lambda_{1PA}$ ) is the optical density of the solution in the cuvette determined at the 1-photon excitation wavelength,  $\lambda_{1PA}$ .  $M(\lambda_{1PA})$  is the 1PEF signal fitting parameter, and the sub-indices  $S$  and  $R$  refer to the sample under study and the 2PA reference standard, respectively.

The 2PA cross-sections were determined at up to six different excitation wavelengths, typically separated by  $\sim 10$  nm intervals and using at least two different reference standards. The final 2PA cross-section spectrum was obtained by scaling the spectral shape function to best fit the measured cross-section values. The latter procedure allowed to further mitigate random error.

As an example, Figure 16 shows the 2PA spectral profile of 1a scaled with respect to several  $\sigma_{2PA}^S$  measurements using four different reference standards; C153 in DMSO (square symbols), C153 in Toluene (upside-down triangles), AF455 in THF (triangles) and Rh6G in methanol (circles).

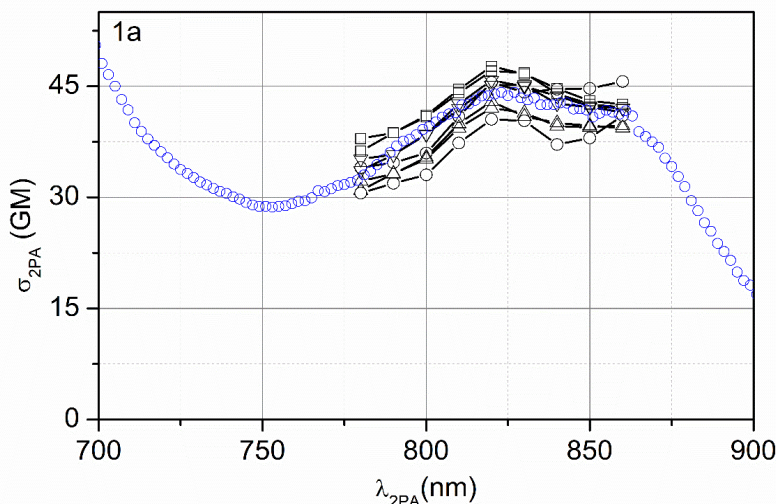


Figure 16: Example of compound 1a 2PA spectra shape (blue symbols), 2PA absolute value against reference (black symbols), C153 in DMSO (square), C153 in Tol (upside down triangle), AF455 in THF (triangle), Rh6G in MeOH (circle).

From this data, we calculate the average cross-section  $\sigma_{2PA}$  (800 nm) = 37 GM with a maximum standard deviation of 2.7 GM (~7%). It should be noted that, in general, the  $\sigma_{2PA}$  values showed a trend where measurement performed relative to AF455 in toluene consistently shows lower values than relative to C153 in toluene, which, in turn, is lower than C153 in DMSO, thus indicating that the primary source of experimental error is likely due to some systematic discrepancy in the absolute values of some of the reference standards.

## 2.7 Spectral decomposition by multivariate curve resolution-alternating least squares (MCR-ALS) method

### 2.7.1 Decomposition of linear absorption spectra

In order to proceed toward quantitative analysis of some of the titration spectra described below, it is much preferred to obtain the constituent spectral profiles in their pure form rather than a superposition of different species. For this purpose, the spectra were decomposed into constituents using a multivariate curve resolution-alternating least squares (MCR-ALS) method [48]. The method decomposes a collection of two or more linearly independent, spectrally overlapping species into their individual spectra, each of which has an exclusively positive contribution (user-defined constraint). Analysis works by iteratively optimizing some initial estimates, which in our case is made from  $K_a$  model Equation (32). In order to elucidate the current procedure, we note that, the pH-dependent absorbance spectra may be represented as a 2-dimensional ( $20_{pH} \times 600_{\lambda}$ ) matrix,  $\mathbf{A}$ . The primary assumption is that  $\mathbf{A}$  can be decomposed into three rank-one matrices, as illustrated below. Each rank-one matrix is a dyadic product of concentration and wavelength vectors of the corresponding form:

$$\mathbf{A} = \begin{matrix} \boxed{\mathbf{C} \times \lambda} \\ \end{matrix} \approx \begin{matrix} \boxed{\mathbf{C}_1} \\ \end{matrix} \times \begin{matrix} \boxed{\varepsilon_1} \\ \end{matrix} + \begin{matrix} \boxed{\mathbf{C}_2} \\ \end{matrix} \times \begin{matrix} \boxed{\varepsilon_2} \\ \end{matrix} + \begin{matrix} \boxed{\mathbf{C}_3} \\ \end{matrix} \times \begin{matrix} \boxed{\varepsilon_1} \\ \end{matrix} \quad (36)$$

which in turn is given by the product,

$$\mathbf{A} = d \cdot \mathbf{C} \cdot \boldsymbol{\varepsilon}^T. \quad (37)$$

Where  $d$  is the constant optical path length of the cuvette (1 cm),  $\mathbf{C}$  is the ( $20_{\text{pH}} \times 3$ ) concentration matrix representing the concentrations of three individual components, at each pH value, and  $\boldsymbol{\varepsilon}$  is the ( $600_{\lambda} \times 3$ ) corresponding molar extinction coefficient spectra matrix.  $\mathbf{C}$  and  $\boldsymbol{\varepsilon}$  can each be solved using the pseudoinverse of the other.

The concentration model of two reversible protonation reactions with two equilibrium constants  $k_1$  and  $k_2$ , for individual components was derived based on the Nernst equation of pH meter response and on the  $K_a$  definition (Equation (32)) further explained in Appendix 13. First, an initial guess of matrix  $\mathbf{C}$  was created using measured pH values, the Nernst equation, and guesses of  $K_a$ .  $\boldsymbol{\varepsilon}$  was determined in a linear least squares manner using the pseudoinverse of  $\mathbf{C}$  according to Equation (37),

$$\boldsymbol{\varepsilon}^T = \mathbf{C}^+ \cdot \frac{\mathbf{A}}{d} \quad (38)$$

The first estimate of the extinction spectra,  $\boldsymbol{\varepsilon}$ , was calculated taking into account the experimentally determined extinction spectra of the neutral form, DPD. The spectrum of PDP was set to a fixed value (having been determined experimentally), and the spectra of the following species were constrained to be non-negative. After correcting the molar absorption spectra, the latter was used to obtain updated concentrations using the reverse pseudoinverse,

$$\mathbf{C} = \frac{\mathbf{A}}{d} \cdot (\boldsymbol{\varepsilon}^T)^+, \quad (39)$$

where the concentration model was least-squares optimized to these new  $\mathbf{C}$  values. The procedure was iterated until the model converged. Details of this process are further discussed in [49].

## 2.7.2 Decomposition of two-photon absorption spectra

Because our initial measurement of 2PA titration did not yield absolute  $\sigma_{2PA}$  values, and because the fluorescence yield of different protonation species varied significantly, to obtain 2PEF excitation profiles of pure forms the MCR-ALS technique was applied to the excitation-emission matrix of each sample, consisting of excitation wavelengths and corresponding emission wavelengths,  $F_s(\lambda_{ex}, \lambda_{em})$ . Equation (35) to may be recast as:

$$\sigma_s(\lambda_{ex}) = \frac{F_s \cdot C_R \cdot \varphi_R(\lambda_{em})}{F_R \cdot C_S \cdot \varphi_S(\lambda_{em})} \cdot \sigma_R(\lambda_{ex}) \quad (40)$$

Where  $F$  is the observed 2PEF signal,  $C$  is the concentration,  $\varphi$  is the differential quantum efficiency over the collected emission wavelength range and  $\sigma_R(\lambda_{ex})$  is a known 2PA cross-section profile of the reference. To determine the relative spectral shape of the sample, Equation (40) can be modified by combining terms that do not depend on the excitation wavelength and substituting these collectively with the constant,  $A$  [3]. As the

emission spectra are recorded simultaneously with the two-photon excitation spectrum, **F** can be presented as a two-dimensional excitation-emission matrix (EEM), written as:

$$\mathbf{F}_S(\lambda_{ex}, \lambda_{em}) \frac{\sigma_R(\lambda_{ex})}{F_R(\lambda_{ex})} = \left( \frac{\boldsymbol{\sigma}_S(\lambda_{ex}) \cdot \mathbf{C}_S}{A_R} \right) \cdot \boldsymbol{\varphi}_S^T(\lambda_{em}) \quad (41)$$

The main objective of the reference measurements is to account for variations in the excitation pulse parameters affecting the two-photon absorption. Here the left side of the equation consists of the measured or known terms, where  $F_R$  are not recorded as a matrix but are instead integrated over the entire emission wavelength region of the reference sample to get a more stable signal for comparison. On the right side,  $\mathbf{C}_S$  is the diagonal ( $3 \times 3$ ) matrix estimated from the concentration model used in the 1PA titration measurement.  $A_R$  is the scaling factor (initially set to 1) representing the relative reference quantum yield and the CCD detector efficiency at emission wavelengths used for each sample-reference pair. The scaling factor is constant across each individually collected excitation-emission matrix, but varies for different sample-reference pairs, so after decomposition,  $A_R$  was used to match excitation profiles resulting from using different references by scaling to match overlapping excitation wavelength regions for each sample-reference pair. Submatrices  $\boldsymbol{\sigma}_S$  ( $\lambda_{ex} \times 3$ ) and  $\boldsymbol{\varphi}_S$  ( $\lambda_{em} \times 3$ ) are decomposed using the MCR-ALS technique, assuming both are larger or equal to zero. Figure 17 shows a contour plot of an example excitation-emission matrix of a PDP sample (pH 7.2) where the horizontal-axis is the laser excitation wavelength and on the vertical-axis is the recorded emission wavelength, wherein the total emission intensity is corrected for the excitation power. For comparison, the decomposed normalized emission spectra are shown on the right side, and the normalized 2PA spectra of pure forms are shown on the top.



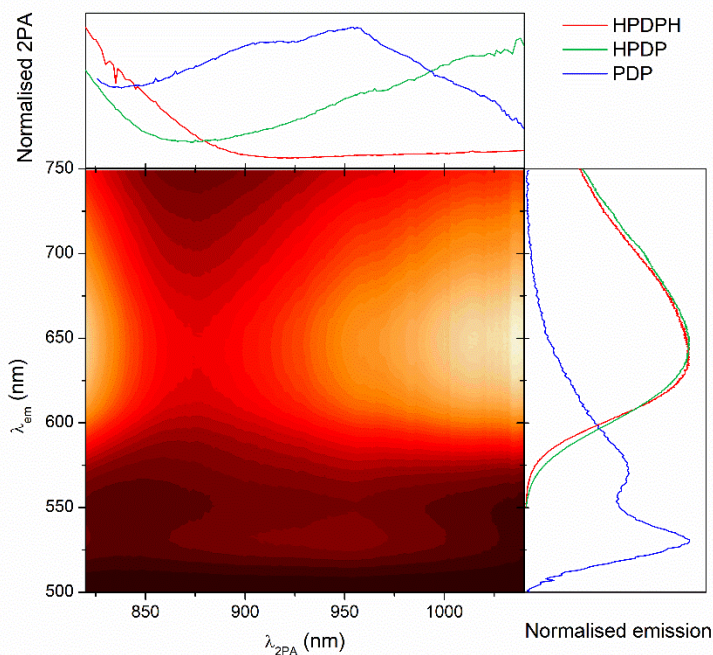


Figure 17: Excitation-emission matrix of a sample with pH 7.2,  $\lambda_{2PA}$  corresponding to laser excitation wavelengths ( $\lambda_{ex}$ ), lighter color indicating higher intensity. Decomposed normalized emission of three forms is shown on the right, and the normalized 2PA of three forms is shown on the top. The excitation-emission matrix has dimensions of  $\lambda_{ex} = 260 \times \lambda_{em} = 1024$ .

To obtain the absolute two-photon cross-section values of the components contained in a mixed sample, the 1PEF excitation-emission spectra were also collected under analogous conditions as for 2PEF and were again decomposed using MCR-ALS to obtain the pure form spectra. These decomposed 1PEF EEM signals are used to correct for the differential quantum efficiency of sample and reference, as described in chapter 3.6.

The technique mentioned above applied MCR-ALS decomposition to only a single sample-reference pair at a time, however, an alternative method was also used to validate the obtained spectra. Multiple samples with varying pH were compiled into a 3D array (sample pH  $\times$   $\lambda_{ex}$   $\times$   $\lambda_{em}$ ), using scaling index  $\mathbf{X}$  that unfolds dimensions of the sample  $S(\text{pH})$  and  $\lambda_{ex}$  into a single dimension. As a result, a larger 2D matrix can be formed ( $\mathbf{X}(\text{pH}, \lambda_{ex}) \times \lambda_{em}$ ) and decomposed with a single MCR-ALS method. In other words, essentially, multiple excitation-emission matrices were cropped and aligned to match the emission wavelengths, creating a much larger excitation-emission matrix, which was decomposed in a single optimization step. In this case,  $A_R$  was additionally solved during MCR-ALS optimization, initially set to 1, but allowed to vary for each sample-reference pair. In total, there were 57 pairs, corresponding to an additional 57  $A_R$  parameters. Finally, as this multi-sample method displayed good agreement with the single-sample method described earlier, the excitation spectral profiles obtained with both methods were averaged.

### 3 Aim of the study

One of the most widely used applications of the 2PA phenomenon is two-photon excited fluorescence microscopy (2PEFM). Multiphoton excitation offers several advantages compared to standard 1-photon excitation, such as superior sample penetration depth and improved 3D resolution [50]. Because the intrinsic fluorescence of biological tissues and cells is generally low, one typically introduces probes, such as organic fluorophores, to facilitate the imaging. Traditionally, efforts in developing new 2PEFM fluorophores have been focused on obvious attributes, such as increasing the 2PA cross-section, especially at wavelength matching the so-called tissue transparency window ( $\lambda_{2PA} = 750 - 900 \text{ nm}$ ) [51], improving the fluorescence quantum yield, higher photostability, etc.

While addressing these parameters remains important, it is becoming equally critical that new kinds of probes are developed endowed with specific sensing and quantitative reporting capabilities. The ability to quantify pH and/or concentration of different ions are of particular interest. In addition to the above, it is also desirable that the new 2-photon fluorophores would display selective affinity to particular cellular compartments, such as cell membrane, nuclei, etc.

Numerous studies have separately addressed the issues of 2PA efficiency, pH sensitivity, and lipophilicity, but only a few examples combine these properties in one functional quantitative probe [52]. Some promising fluorophores were discussed in [53], [54], [55]. In [53], designed molecules with a lipophilic fluorene core that enabled efficient cell membrane staining and showed high two-photon brightness (174 and 276 GM for basic and acidic solutions, respectively). A very similar molecule is also introduced by Werts et al. [56] with even higher reported 2PA cross-section values. However, because the comprehensive characterization of 2PA properties is often difficult, 2PA optimization has been typically limited only to a single wavelength or very narrow excitation region. Thorough photo-physical characterization is particularly important because certain spectral variations may be also resulting from local environmental changes, thus mistaken for a pH shift.

As already pointed out in the current Thesis, inversion-symmetry is a strong influencer in framing the 2PA response. Accordingly monitoring 2PA variations caused by symmetry change has been suggested for sensing pH. Pond et al. observed a significant reduction of the 2PA cross-section upon binding of Mn ions to crown-ether compounds [57]. Additionally, a blue shift of the 1PA spectra occurred. These observations were interpreted as decreasing the degree of intramolecular charge transfer in the chromophore due to the deactivation of the nitrogen lone-pair donor group at the binding site. Huang et al. reported a similar behavior with molecules obtained from 3,9-dithia-6-azaundecane, designed to detect silver ions [58]. Another related bipyridine-centered donor-acceptor-donor inversion symmetric type fluorophores were reported by Divya et al. [59] and Li et al. [60], which displayed enhancement of the 2PA cross-section upon binding of  $\text{Zn}^{2+}$ .

The work by Daniel et al. [53] reports a centro-symmetrical bolaamphiphilic (i.e., amphiphilic surfactants with two hydrophilic groups separated by a long hydrophobic chain) quadrupoles with a lipophilic fluorene core and two symmetric pH-sensitive acceptor end-groups. After adding HCl acid or NaOH to the solution, the 2PA bands red-shifted, which authors interpreted as increasing the electron-withdrawing strength of the terminal moieties. However, no distinction between single- and double-protonation

steps was reported, and neither was the vibronic structure of 2PA transitions discussed or evaluated.

Numerous preceding studies as well as experiments described in this Thesis show that, when the 2PA spectra are measured with sufficiently high quality, then deviations from the Laporte rule may be noted [5]. Such that nominally parity-forbidden transitions are still present in the 2PA spectra.

As summarized above, most previous studies of symmetry-changing 2PA systems were focused on specific applications and did not address or clarify the complex underlying photophysics. As we will show in this Thesis, in order to get a clear quantitative understanding of the protonation effect on the chromophore's symmetry, detailed characterization of vibronic transitions are of utmost importance.

Quantitative sensing of pH, of course, implies that the relation between two-photon characteristics and acidity-basicity of the environment is comprehensively known and understood. In our view, there are two different approaches toward this goal. In the first case, one takes advantage of the circumstance that attaching a proton often has the effect of changing the conjugation pattern inside the fluorophore, which in turn, may result in some changes in absorption- and emission parameters such as variation of intensity and/or shifts of peak wavelengths. This type of pH-sensitivity is rather common and is not related to the unique photophysical properties of the two-photon process. In this case, the 1PA and 2PA spectra change, if not in exact proportion to one another, then often in a very similar manner.

The second approach, studied for the first time by the author of this Thesis, takes advantage of the Laporte rule in inversion-symmetric fluorophores. Indeed, if the protonation could change the underlying molecule symmetry, e.g., by switching the inversion symmetry on or off, then that would result in profound changes in the relative spectroscopic signals of 1PA and 2PA. It is worth underlining that change of symmetry may or may not be accompanied by substantial changes in the conjugation, thus making the second approach potentially more suitable for quantitative determination of pH.

In this Thesis, we investigate both of these different approaches. First, we study how protonation changes the 1PA, 2PA, and fluorescence emission properties of a series of dipolar molecules (non-centrosymmetric). Samples are derived from Coumarin 151 by adding a single preferred protonation site. These chromophores comprise a phosphazene moiety with high lipophilicity in both neutral and protonated forms. We measure the acid titration 1PA and 2PA spectra of the neutral and (single) protonated structures and present a detailed quantitative picture of the observed behaviors.

In the second part, we perform the protonation of a nominally inversion-symmetric pyrrolopyrrole with two equivalent and symmetric protonation sites. While the neutral chromophore and its double-protonated version possess inversion symmetry, the attachment of just one proton (single protonation) causes the nominal inversion symmetry to be lowered or broken, thus altering the Laporte selection rule. However, in reality, especially in large organic fluorophores, drawing a clear distinction between the symmetric- and non-inversion symmetric two-photon spectra is often obscured due to prevalent vibronic interactions. We address this issue by performing a detailed experimental and theoretical evaluation of vibronic contribution to the 1PA and 2PA transitions. This allows us to recast the Laporte rule in a more comprehensive way, thus paving the way for the quantitative determination of pH from observed changes in the 2PA vs. 1PA ratio.

## 4 2PA study of protonation effects in novel organic chromophores

### 4.1 Spectroscopic characterization of lipophilic coumarins: Measurement of titration spectra

Figure 18 shows the linear absorption spectrum of the modified coumarin C2 (chemical structures shown in Figure 7 on page 28) in acetonitrile upon titration with HCl. The titration experiment was conducted to see protonation effects in 1PA spectra. The investigation also provided knowledge about the chromophore's reaction equilibrium and solubility. The absorption spectrum of the neutral form is marked with a blue line. The lowest-energy transition with the peak at  $\lambda_{1PA} \sim 395$  nm is identified as the  $S_0 \rightarrow S_1$  transition, most likely (see below) comprising multiple overlapping vibronic components. The second prominent feature of the neutral form spectra is a shoulder at  $\lambda_{1PA} \sim 260$  nm, and the steep increase at  $\lambda_{1PA} < 250$  nm is due to higher-energy excited singlet states. Also, it should be noted that, in the neutral form spectrum, there is no vibronic progression at  $\lambda_{1PA} \sim 270$  nm characteristic of isolated phenyls.

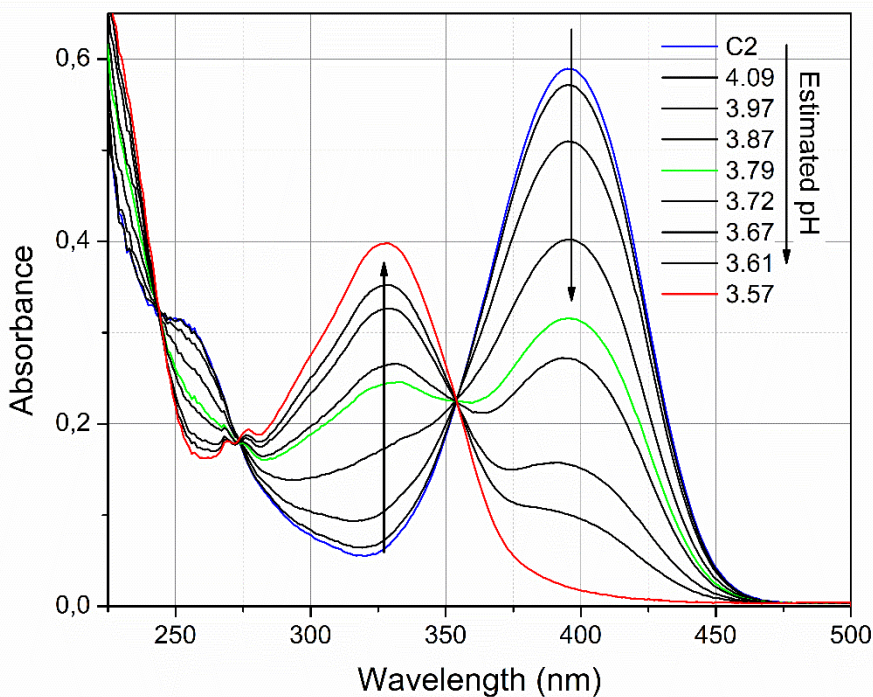


Figure 18: 1PA titration spectra of C2 with diluted HCl in acetonitrile. Neutral form (blue line) and fully protonated form (red line), and intermediate curves (black line). Black arrows indicate change upon dropwise addition of the diluted acid. The green line marks the curve where the neutral and protonated form are in equal concentrations, and the pH value corresponds to the  $pK_a$  value of 15.2 [38]. Estimated pH values derived from the amount of added acid and assuming an organic/aqueous mixture. pH values in ACN could be obtained by applying an offset of 11.4, assuming linearity.

Upon gradual addition of diluted HCl, the absorbance of the neutral form decreases while the absorbance of a new species, which we attribute to the singly protonated form, increases. The fully protonated form is marked with a red line. The intermediate titration curves are shown as solid black lines. The green curve marks the level of titration where the neutral and the protonated forms are at equal concentrations, corresponding to the  $pK_a$  value for an organic/aqueous mixture (i.e. intracellular conditions) of 3.79 [38]. The pH values shown on the right are calculated based on added acid concentration, assuming complete dissociation and an aqueous solution. Previous measurements in acetonitrile have indicated a  $pK_a$  of 15.2, indicating a solvent offset of +11.4. This large difference in estimated  $pK_a$  corresponds to the stabilization of protons in a hydrogen bonding environment compared to an aprotic solvent.

In the protonated C2, the  $S_0 \rightarrow S_1$  maximum blue-shift to  $\lambda_{1PA} \sim 330$  nm, while the peak molar extinction decreases from  $24400 \text{ M}^{-1}\text{cm}^{-1}$  in the neutral form to  $15300 \text{ M}^{-1}\text{cm}^{-1}$ . The pH of the fully protonated solution in ACN is estimated to be  $\sim 15.0$ . We also note the absence of the shoulder at,  $\lambda_{1PA} \sim 260$  nm, and the appearance of a clear phenyl-like vibronic progression around  $\lambda_{1PA} \sim 270$  nm. The existence of clear isosbestic points at 355, 275, and 235 nm indicates stoichiometric conversion between the neutral and singly protonated species.

The isosbestic points also indicate that both the protonated and neutral form are stable in acetonitrile. While this initial titration was carried out with concentrated aqueous HCl, later experiments used purified triflic acid to exclude potential artifacts caused by the presence of water molecules. The photostability of acid and base forms was assessed by conducting 1PA absorbance measurements over a prolonged time of several hours or days.

Quantum chemical calculations offer further useful insight of the 1PA spectra. The top panel of Figure 19 shows the calculated purely electronic transitions, represented with the red and blue sticks for protonated and neutral forms, respectively. The stick height represents the transition's oscillator strength. The calculations place the  $S_0 \rightarrow S_1$  absorption of the neutral form in acetonitrile solution at  $\lambda_{1PA} = 400$  nm and with the oscillator strength,  $f = 0.56$ . These results correlate very well with the experimental values of  $\lambda_{1PA} = 395$  nm and  $f = 0.47$ , fully validating the above assignment of the lowest-energy band as  $S_0 \rightarrow S_1$ . The calculations also reproduce well the higher-energy region of the neutral form spectrum, showing several closely spaced energy levels at  $\lambda_{1PA} < 230$  nm.

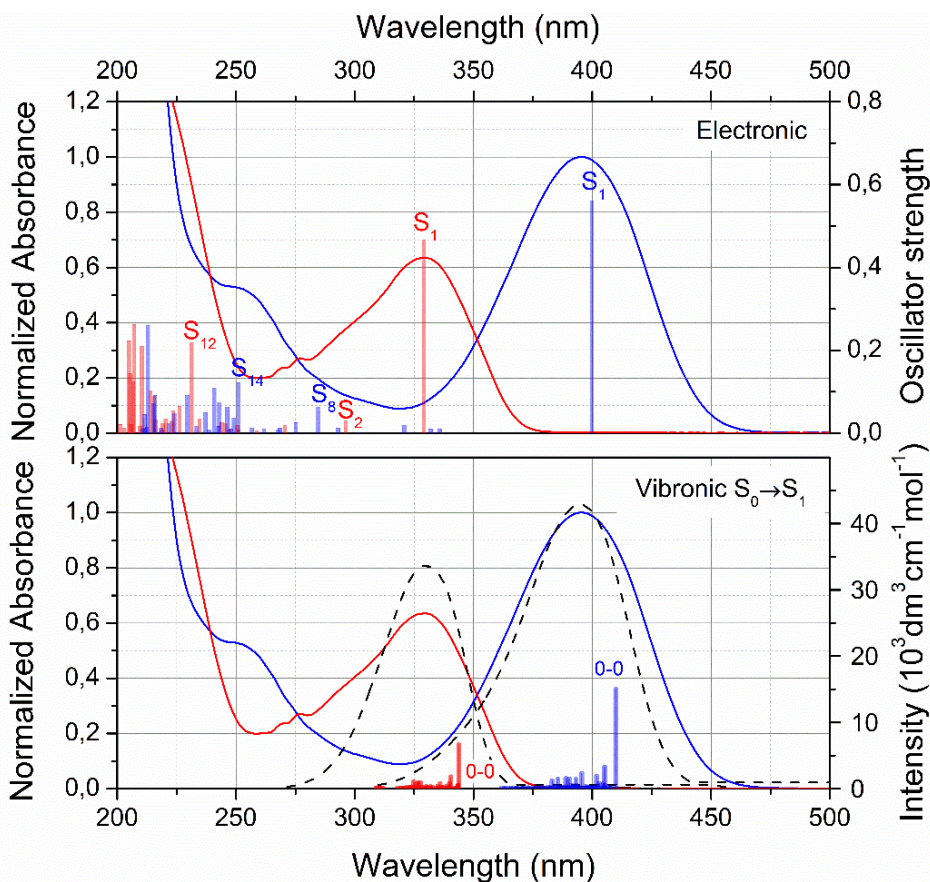


Figure 19: Comparison of the calculated and experimentally measured 1PA spectra of C2 in acetonitrile. Top panel: Neutral (blue) and protonated (red) absorbance spectra (solid lines); calculated electronic transitions are represented with vertical sticks. Bottom panel: The same absorption spectra (solid lines) compared to calculated vibronic transitions (vertical sticks) for  $S_0 \rightarrow S_1$  and vibronic transitions convolution with a Gaussian (black dashed line).

The calculated  $S_0 \rightarrow S_1$  transition wavelength of the protonated form,  $\lambda_{1PA} = 329$  nm, matches well the experimental value,  $\lambda_{1PA} = 330$  nm. The computed oscillator strength values of the protonated forms are somewhat higher compared to the experimental data,  $f = 0.47$  and  $f = 0.34$ , respectively. The onset of the strong absorption at the blue edge of the experimental 1PA spectrum of the protonated form coincides with the calculated  $S_{12}$  excited state located at  $\lambda_{1PA} \sim 230$  nm, followed by further strongly absorbing states at even shorter wavelengths.

The lower panel of Figure 19 compares the measured 1PA profiles of the neutral and protonated C2 to the calculated vibronic transitions for the lowest electronic band,  $S_0 \rightarrow S_1$ . In Franck-Condon and Herzberg-Teller (FCHT) approximation, i.e., the first two of Taylor terms expansion Equation (15). We see that in both the neutral and the protonated forms 0-0 component has a higher peak intensity than the multiple vibronic transitions. However, after convoluting the calculated stick spectrum with a Gaussian (dashed lines), the theoretical and experimental profiles become rather close, especially after allowing a small  $\sim 10$  nm redshift to better match with the experiments



inhomogeneously broadened profile. Additionally, in the case of vertical electronic transition calculation, excited state geometry is not changed compared to the ground state. In contrast, for vibronic calculations, the excited state geometry is optimized in the 0-0 transition, thus lowering the energy compared to a purely electronic transition.

Figure 20 presents the experimental 1PA and 2PA cross-section spectra of the four coumarin 151 derivatives, C1–C4, and the parent coumarin 151 (C151). The spectra were obtained in two solvents, acetonitrile (left panel) and *n*-octanol (right panel), which we selected to emulate, respectively, a polar and lipid bilayer-like environment.

The 2PA spectra (colored circles, left vertical axis) were measured in the wavelength range of  $\lambda_{2PA} = 550 - 1000$  nm. The wavelength of corresponding linear molar absorptivity spectra (solid line, right vertical axis, upper horizontal axis) is scaled as  $\lambda_{1PA} = 1/2 \cdot \lambda_{2PA}$ . Blue and red represent the neutral and fully protonated forms, respectively.

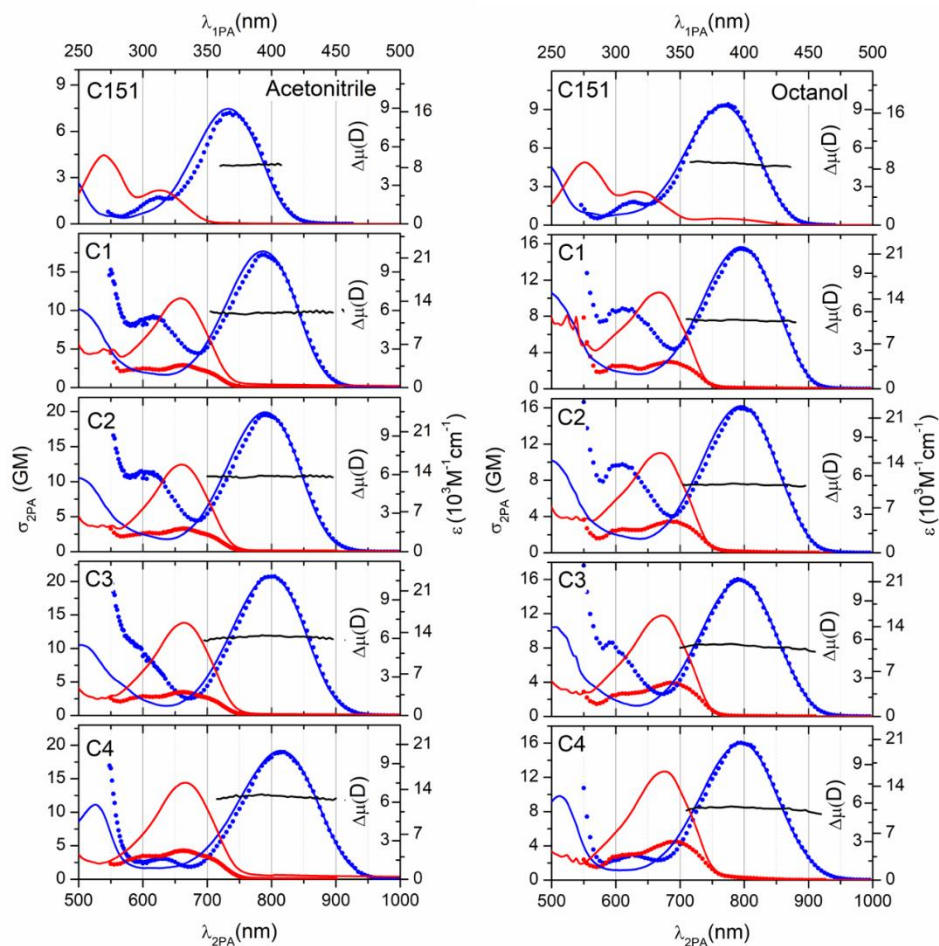


Figure 20: 1PA (blue and red lines) and 2PA (blue and red symbols) spectra of the four lipophilic derivatives, C1–C4, and the parent C151, in neutral acetonitrile (blue) and in acetonitrile with  $\sim 0.3$  M of triflic acid (red) on the left column and in neutral (neat) *n*-octanol and in *n*-octanol with the addition of  $\sim 0.3$  M triflic acid. Black lines represent the estimated change of the permanent dipole moment ( $\Delta\mu$ ) values for the neutral forms.

Table 2 collects the measured peak 1PA and 2PA wavelengths, corresponding linear peak extinction coefficients, and  $\sigma_{2PA}$  values for each coumarin sample. The calculated 1PA peak wavelengths and peak  $\sigma_{2PA}$  values are shown for comparison. Two important observations are present: First, all four neutral phosphazene-modified structures display in ACN a marked 60 – 80 nm red-shift of the  $S_0 \rightarrow S_1$  band, compared to the parent C151. The amount of this shift increases with the count of attached pyrrolidine groups. Similar changes have been observed for azaphosphane modifications in other systems, implying these groups are proficient electron donors [61]. In non-polar *n*-octanol, a slightly smaller (~40 nm) red shift is observed but without noticeable dependence on the specific phosphazene structure. The solvent polarity-dependent shifts indicate that these chromophores possess a non-vanishing permanent electric dipole moment in the ground electronic state. Overall, the redshift and slight increase of the oscillator strength suggest extended conjugation compared to C151.

In acetonitrile solution, the observed redshift correlates to increasing the number of attached pyrrolidines, while a slight enhancement of 1PA and 2PA cross-section (17 to 21 GM) is seen for the mixed-phosphazene structures. However, in neutral *n*-octanol, the peak  $\sigma_{2PA}$  values essentially coincide for all the derivatives C1–C4,  $\sigma_{2PA} = 16$  GM independent of the substituents. This difference in behavior may be attributed to different polarity of the solvents but could also indicate some reaction occurring between ACN and Ph and Pyrr groups, whereas *n*-octanol has no such effect. A second important observation that follows from the spectra presented in Figure 20 is that in all neutral forms the lowest-energy 2PA peak coincides with the  $S_0 \rightarrow S_1$  band maximum in the corresponding 1PA spectrum ( $\max \lambda_{2PA} = 2 \cdot \max \lambda_{1PA}$ ). Furthermore, the measured 2PA excitation profile closely follows the shape of the 1PA spectrum, especially on the red-wavelength side of the band. From this empirical data and the fact that the coumarins under study lack inversion symmetry, we conclude that the 2PA band observed in the 700 – 900 nm region must also be due to the  $S_0 \rightarrow S_1$  transition. In particular, the neutral forms of C2 in ACN have peak  $\sigma_{2PA} = 19 \pm 1.5$  GM at  $\lambda_{2PA} = 790$  nm, and in *n*-octanol, peak  $\sigma_{2PA} = 16 \pm 1.3$  GM at  $\lambda_{2PA} = 795$  nm, which both match the corresponding 1PA peak wavelength at 395 nm and 398 nm.

The quantitative correspondence between the  $S_0 \rightarrow S_1$  2PA and 1PA spectral profiles indicates that the 2PA spectrum is well described by the same Franck-Condon factors as in the case of 1PA, as given by the first term in Equation (23). In this case, using a two-level approximation of 2PA is well justified, and we may apply Equation (25) to estimate the value of  $\Delta\mu \approx 6$  D in ACN and slightly less,  $\Delta\mu \approx 5.5$  D in *n*-octanol. The parent C151 shows lower  $\sigma_{2PA} = 7$  GM and  $\sigma_{2PA} = 9.4$  GM in ACN and *n*-octanol, respectively. Additionally, the permanent dipole change is also lower,  $\Delta\mu \approx 5$  D. These values are shown in Figure 20 by the black line and the average value is also collected in Table 2, along with quantum chemically calculated values.

It was also noted that the neutral forms display a distinct two-photon allowed transition at 600 – 630 nm. The fact that this transition is not readily identifiable with any feature in the corresponding higher-energy portion of the 1PA spectra aligns well with previous observations reported for related coumarins [3], [37]. This band also matches well with several transition energies predicted by quantum chemical calculations, which were anticipated to have low 1PA oscillator strength.



Table 2: Summary of experimental and calculated 1PA/2PA photophysical parameters.

| Compound  | $\lambda_{1PA \text{ max}}$ , nm |          | $\epsilon_M$ , $M^{-1}cm^{-1}$ | $\sigma_{2PA \text{ max}}$ , GM ( $\lambda_{2PA}$ , nm) |                   | $\Delta\mu$ , D ( $S_0 \rightarrow S_1$ ) |          |
|-----------|----------------------------------|----------|--------------------------------|---|-------------------|---|----------|
|           | Exp                              | Calc     |                                | Exp   | Calc              | Exp                                       | Calc     |
|           | <b>acetonitrile</b>              |          |                                |   |                   |   |          |
| C151      | 366                              | 366      | 16400                          | 7 (735)   | 8 <sup>[a]</sup>  | 4.5                                       | 6.6      |
| C1        | 393                              | 396      | 22100                          | 17 (785)  | 16 <sup>[b]</sup> | 5.8                                       | 6.5      |
| C2        | 395                              | 400      | 24400                          | 19 (790)  | 15 <sup>[b]</sup> | 5.9                                       | 6.4      |
| C3        | 399                              | 400      | 23500                          | 21 (805)  | 18 <sup>[c]</sup> | 6.2                                       | 7.5      |
| C4        | 407                              | 406      | 20000                          | 19 (820)  | 23 <sup>[d]</sup> | 6.5                                       | 8.3      |
| C151-PROT | 314, 270                         | 309, 271 | 4800, 9800                     | —   | —                 | —   | 3.4, 4.9 |
| C1-PROT   | 330                              | 328      | 14500                          | 3 (664)   | 6 <sup>[e]</sup>  | 3   | 4.8      |
| C2-PROT   | 330                              | 329      | 15300                          | 3 (663)   | 6 <sup>[f]</sup>  | 3   | 4.8      |
| C3-PROT   | 332                              | 330      | 15600                          | 4 (664)   | 7 <sup>[f]</sup>  | 3   | 5.2      |
| C4-PROT   | 333                              | 331      | 15000                          | 4 (664)   | 7 <sup>[g]</sup>  | 4   | 5.6      |
|           | <b>n-octanol</b>                 |          |                                |   |                   |   |          |
| C151      | 383                              | 365      | 17044                          | 9.4 (775)   | 8 <sup>[a]</sup>  | 4.9                                       | 6.3      |
| C1        | 397                              | 397      | 22100                          | 16 (795)  | 16 <sup>[b]</sup> | 5.3                                       | 6.1      |
| C2        | 398                              | 400      | 22900                          | 16 (795)  | 15 <sup>[b]</sup> | 5.3                                       | 6        |
| C3        | 397                              | 401      | 21100                          | 16 (795)  | 20 <sup>[c]</sup> | 5.5                                       | 7.2      |
| C4        | 398                              | 406      | 20400                          | 16 (795)  | 25 <sup>[d]</sup> | 5.6                                       | 8        |
| C151-PROT | 316, 276                         | 308, 269 | 4773, 8959                     | —   | —                 | —   | 3.0, 4.3 |
| C1-PROT   | 334                              | 327      | 15000                          | 3 (685)   | 6 <sup>[e]</sup>  | 3   | 4.4      |
| C2-PROT   | 335                              | 328      | 15600                          | 4 (685)   | 6 <sup>[f]</sup>  | 3   | 4.4      |
| C3-PROT   | 336                              | 329      | 15700                          | 4 (685)   | 6 <sup>[f]</sup>  | 4   | 4.7      |
| C4-PROT   | 338                              | 329      | 16200                          | 5 (695)   | 7 <sup>[g]</sup>  | 4   | 5.2      |

Next, we consider how the 1PA and 2PA spectra are affected by adding a saturating amount of triflic acid to the solution. These spectra are shown in Figure 20 as red lines and red symbols. The protonation causes the  $S_0 \rightarrow S_1$  1PA band of C1–C4 to shift hypsochromically by as much as  $\sim 75$  nm. At the same time, the extinction coefficient decreases by 20 – 30%, whereas the spectrum of C151 splits into two bands at 325 nm and 270 nm. In the 2PA cross-section spectrum, the protonation has an equally dramatic effect. Additionally, the peak  $\sigma_{2PA}$  in C1–C4 is reduced by almost a factor of 4 to 6. For example, in C2 in ACN solution the peak cross-section is reduced from 19 GM to 3 GM.

Although the overall blue shift of the 2PA  $S_0 \rightarrow S_1$  band appears to follow that of the 1PA spectrum, we observe that the measured 2PA band profiles show a certain deviation from corresponding 1PA band profiles. Details and the potential origin of these discrepancies will be discussed in section (4.1.1) below.

2PA of C151 has been studied earlier in ethanol solution, however, the reported peak values seemed to be rather inconsistent,  $\sigma_{2PA} = 47.1$  GM (754 nm) [62],  $\sigma_{2PA} = 14.5$  (694 nm) [63], and  $\sigma_{2PA} = 88$  GM (760 nm) [64], most likely due to different measuring

techniques. Our measured values for C151 in octanol and ACN are presented in Appendix 6 and could potentially be used as future reference standards.

Another interesting feature observed in Figure 20 is that in the short wavelength region,  $\lambda_{1PA} \sim 250 - 290$  nm, the protonated forms of C1–C4 show a distinct series of peaks resembling a vibronic progression. Figure 21 expands and compares this particular section of C2 in ACN (solid line) to the absorption spectrum of phenol in hexane, dashed line [65]. Based on the close similarity of these two structures, we attribute the observed features to the vibronic spectrum of individual attached phenyls in C1–C4. However, as a similar structure is also visible in C4 in *n*-octanol, this effect could not be just due to phenyls but must also include pyrrolidines. Further investigation would be needed for a better understanding of this phenomenon.

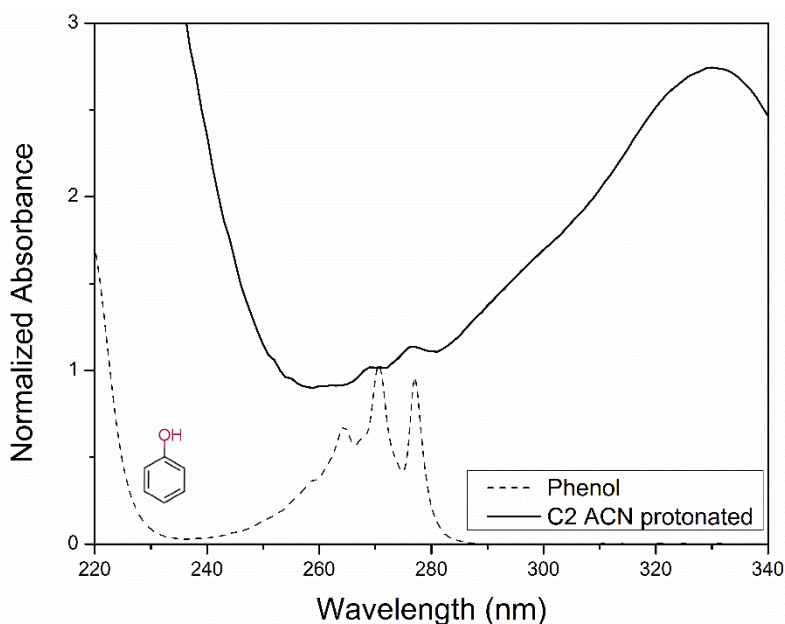


Figure 21: C2 in acidic ACN solvent (solid black line) compared to phenol dissolved in hexane (black dashed line).

#### 4.1.1 On potential causes of apparent mismatching between the spectral profiles of 1PA and 2PA of $S_0 \rightarrow S_1$ transition in protonated C1–C4

A number of strongly dipolar chromophores, including several coumarins, show a close match between the lowest electronic transition's 2PA and 1PA spectral profiles [66]. Above, we discussed that this is indeed the case for the neutral chromophores C1–C4. To further emphasize this finding, Figure 22 shows these profiles for neutral C2 in acetonitrile plotted on a logarithmic scale. We see that the profiles match very closely indeed, such that the ratio of  $\sigma_{2PA}/\epsilon_{1PA}$  (dash line) remains nearly constant over more than three orders of magnitude change of  $\sigma_{2PA}$  value in the 700 – 950 nm range.

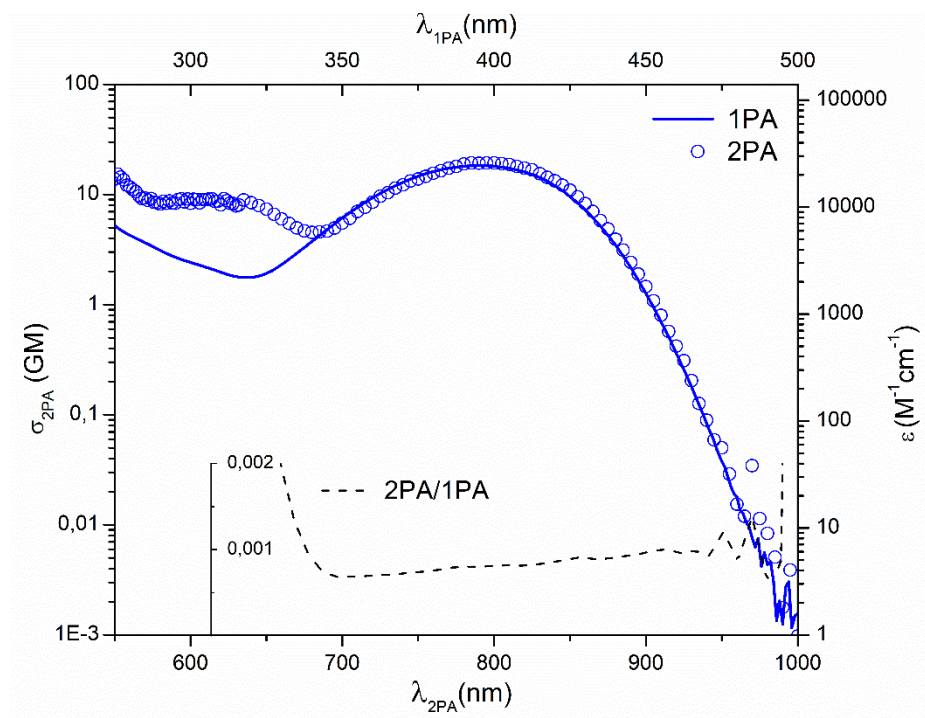


Figure 22: Comparison of 2PA and 1PA of neutral C2 in ACN, 2PA blue circles, 1PA blue line,  $\sigma_{2PA}/\epsilon_{1PA}$  ratio dash line.

However, in protonated chromophores there is notably less spectral agreement. Figure 23 presents the experimental 1PA (line) and 2PA (red symbols) spectra for C2 with 0.3 M triflic acid in acetonitrile and *n*-octanol solvents and shows a noticeable relative redshift of the 2PA profile. Magenta-colored columns represent the calculated electronic transition wavelengths and oscillator strengths ( $f$ ).

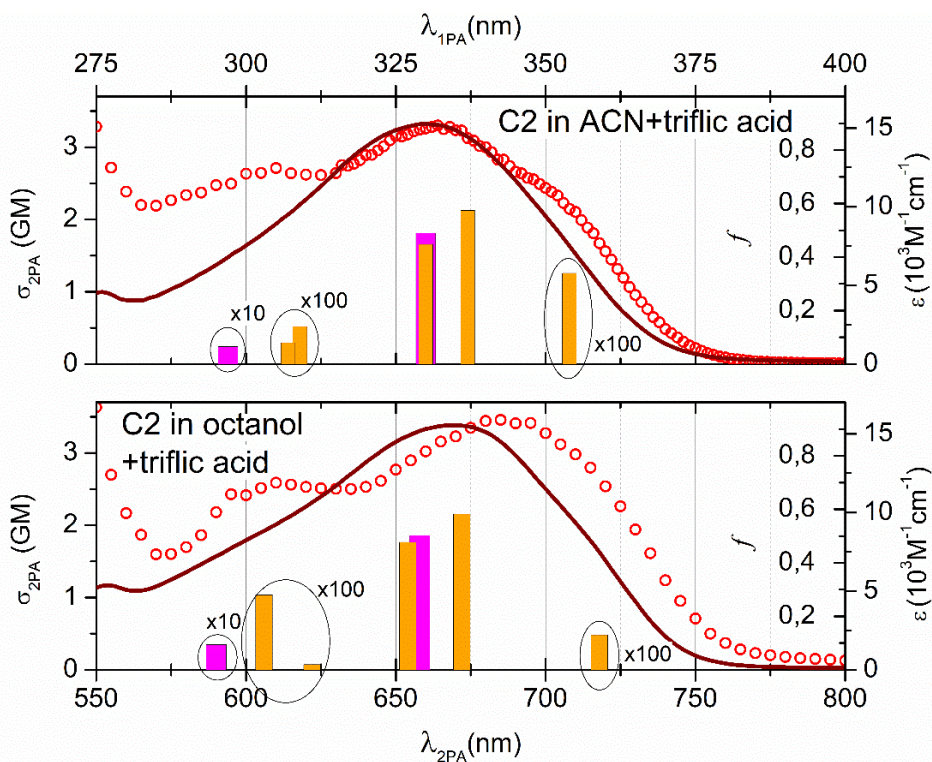


Figure 23: Expanded view of the experimental 1PA (line) and 2PA (red symbols) spectra for C2 with 0.3 M triflic acid, in acetonitrile and *n*-octanol, compared to calculated wavelengths and oscillator strengths ( $f$ ) of electronic transitions for the monomer (magenta) and dimer (orange) optimized structures. Circled transition oscillator strengths are multiplied with indicated value for visibility.

Upon close inspection of the 2PA spectra in ACN (upper panel Figure 23), we observe two overlapping bands, with the maxima at  $\lambda_{2PA} = 605$  and  $663$  nm, accompanied by a shoulder near  $\lambda_{2PA} = 705$  nm. In *n*-octanol, the middle band appears red-shifted and merged with the shoulder. Even though the 1PA spectrum in *n*-octanol also seems to display a weak low-energy shoulder at  $\lambda_{2PA} \sim 720$  nm ( $\lambda_{1PA} \sim 360$  nm), such a feature is practically absent in acetonitrile.

Even though satisfactory explanation of this behavior is currently lacking, we have investigated a few potential hypotheses as described below.

Our theoretical calculations of the 1PA electronic spectra (magenta bars in Figure 23) indicate no excited state below  $S_0 \rightarrow S_1$ , thus excluding the possibility of 2PA due to such states.

However, if one would consider formation of dimers, then such red-shifted state becomes a possibility. Orange bars in Figure 23 show the calculated wavelengths on and oscillator strength of electronic 1PA transitions in a hypothetical dimer of protonated C2 in ACN and *n*-octanol. In both cases, there is a red-shifted excited state, although the predicted 1-photon oscillator strength is much smaller than our observations would imply.

To further elucidate the possibility of dimerization we conducted concentration-dependent NMR studies of protonated C2 ACN solution. Indeed the NMR spectra confirmed the formation of dimers but only at concentrations  $\geq 3$  mM, while the 2PA

spectra were recorded at a much lower concentration,  $\sim 10 \mu\text{M}$  [67]. The negative finding also correlated with the linear absorption measurements, which did not show any evidence of dimers in the concentration range of 0,04 mM to 12 mM.

An alternative explanation for the 2PA red shift could be related to a tendency of ACN to chemically react with acids and certain other solutes [68]. In our experiments with acetonitrile triflic acid mixtures, we noticed the occurrence of some kinetic behavior over time slight rise in the absorbance at short wavelengths  $< 300 \text{ nm}$ , which could be explained by acetonitrile reacting with the triflic acid. In addition, it is acknowledged that acetonitrile may react with other acids as well, and products may contribute to secondary reactions [69]. However, such behavior has not been reported in *n*-octanol, thus rendering chemical instability an unlikely explanation for the 2PA red-shift. Nevertheless, these effects are worth considering when studying chromophores in acetonitrile acid mixtures.

#### 4.1.2 Fluorescence emission quantum yield and two-photon brightness

Figure 24 shows the fluorescence emission spectra and the fluorescence excitation profiles of the studied chromophore in acetonitrile and *n*-octanol solution. The emission spectra were recorded with the excitation tuned to the maximum 1PA wavelength, as listed in Table 3. The excitation spectra were collected at the corresponding fluorescence emission peak wavelength. Good overlap (within 10%) between the excitation profiles and the corresponding one-photon absorption spectra confirmed the validity of Kasha's rule.

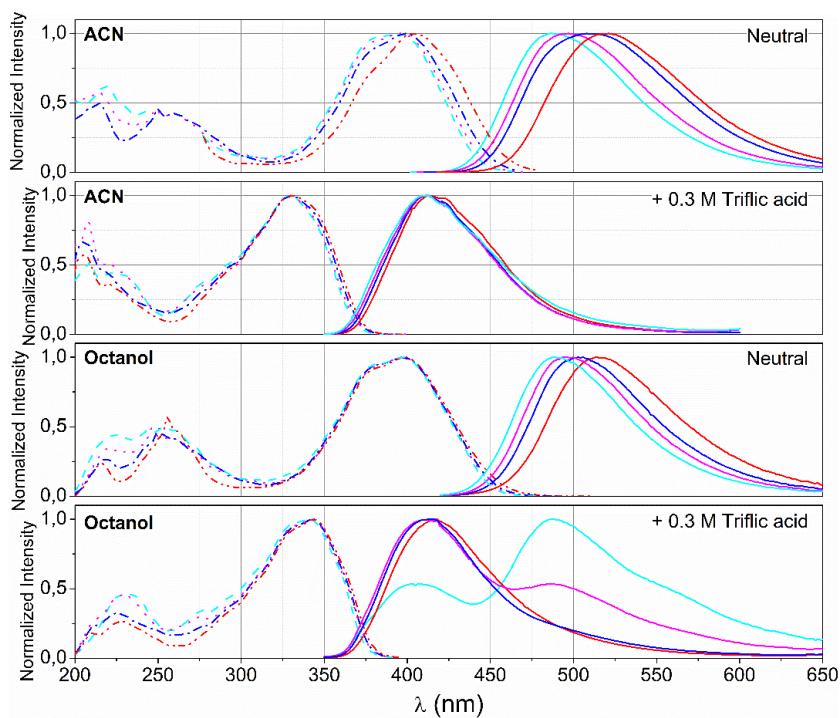


Figure 24: Normalized excitation (dashed lines) and emission spectra (solid lines) for C1 (cyan), C2 (magenta), C3 (blue) and C4 (red) in acetonitrile and *n*-octanol, in neutral (neat) solvent, and with the addition of triflic acid.

In our case, the Stokes shift constitutes as much as 80–120 nm for the neutral forms and 70 – 80 nm for the protonated versions and in both solvents, which is typical to strongly dipolar chromophores such as coumarins.

Interestingly, we see a deviation from the mirror-image law on the lowest panel in Figure 24. Where the emission spectra of compounds in acidic *n*-octanol display what appears as a peak at ~480 nm, whose relative amplitude seems to correlate with the count of attached phenyl groups. The 480 nm emission bands may indicate an additional excited state deactivation pathway involving proton transfer from the molecule to the solvent. This hypothesis is supported by the fact that we do not see a similar effect in ACN, as in the latter solvent, such charge transfer is less likely due to higher redox potential. One might assume that the 480 nm peak may be due to residual neutral form, but this is not endorsed by the measured 1PA and fluorescence excitation spectra, where there is no sign of neutral species.

In addition to the steady-state fluorescence, we performed time-correlated single-photon counting (TCSPC) measurements of nanosecond time-resolved emission kinetics, shown in Appendix 7, that support the proton transfer hypothesis. Also, a quick study on solvent dependence of C3 was conducted, summarized in Appendix 9.

It is common to characterize fluorophores for two-photon microscopy in terms of their two-photon brightness, expressed as,

$$B_{2PA} = \sigma_{2PA}^{max} \cdot \phi_{em}, \quad (42)$$

where  $\sigma_{2PA}$  is the peak 2PA cross-section (in GM) and  $\phi_{em}$  is the fluorescence quantum yield. We measured the fluorescence emission quantum yields of C1–C4 in acetonitrile and octanol solvents, following the procedure described in the experimental methods section. The results are summarized in Table 3.

*Table 3: Summary of the experimental fluorescence maximum wavelengths (nm), emission quantum yields, two-photon brightness values (GM), and Stokes shift (cm<sup>-1</sup>) of C1–C4 and parent C151 in neutral and protonated ACN and octanol solutions.*

| Compound                | Neutral        |             |           |              | Protonated     |             |           |              |
|-------------------------|----------------|-------------|-----------|--------------|----------------|-------------|-----------|--------------|
|                         | $\lambda_{em}$ | $\phi_{em}$ | $B_{2PA}$ | Stokes shift | $\lambda_{em}$ | $\phi_{em}$ | $B_{2PA}$ | Stokes shift |
| <b>acetonitrile</b>     |                |             |           |              |                |             |           |              |
| C151                    | 463            | 0.57        | 4         | 5724         | 411            | 0.02        | 0.06      | 7516         |
| C1                      | 487            | 0.65        | 11        | 4911         | 411            | 0.02        | 0.07      | 5972         |
| C2                      | 492            | 0.65        | 12        | 4991         | 411            | 0.02        | 0.06      | 5972         |
| C3                      | 508            | 0.62        | 13        | 5378         | 412            | 0.04        | 0.16      | 5849         |
| C4                      | 519            | 0.54        | 10        | 5302         | 413            | 0.06        | 0.24      | 5817         |
| <b><i>n</i>-octanol</b> |                |             |           |              |                |             |           |              |
| C1                      | 489            | 0.74        | 11.5      | 4739         | 403.5          | 0.12        | 0.39      | 5157         |
| C2                      | 495            | 0.72        | 11.6      | 4924         | 412            | 0.09        | 0.32      | 5579         |
| C3                      | 506            | 0.71        | 11.4      | 5426         | 415            | 0.1         | 0.34      | 5666         |
| C4                      | 514            | 0.64        | 10.3      | 5670         | 417            | 0.13        | 0.5       | 5605         |

As presented earlier, the protonation substantially blueshifts the peak 2PA wavelength and also reduces the peak cross-section value. The quantum yield of C1–C4 in the neutral solvents is relatively high,  $\phi_{em} = 0.54 - 0.74$ , while the corresponding two-photon brightness is also relatively high  $B_{2PA} = 10 - 13$  GM. Our two-photon brightness values are comparable to those reported earlier by Luo et al. [70] for some related phosphazene-modified coumarins, which also showed a red-shifted 1PA spectra and increased molar absorptivity.

Protonation causes a considerable drop of the quantum yield,  $\phi_{em} = 0.09 - 0.13$ , and it also reduces the  $\sigma_{2PA}$  value. As a result, the two-photon brightness of the protonated forms is reduced by a factor of 50 to 100,  $B_{2PA} = 0.3 - 0.5$  GM, for the *n*-octanol. In the case of an ACN, this decrease is even more drastic,  $\phi_{em} = 0.02 - 0.06$ , and  $B_{2PA} = 0.06 - 0.24$  GM. Furthermore, the emission of the mother compound, C151, protonated form in both solutions, was nearly completely quenched. The reason for low fluorescence emission can be related to the very flexible NH<sub>2</sub> group, which is attached to the benzopyrone moiety by a single bond. Thus, it is expected that the excited dye molecules can dissipate the excess energy very fast to the solvent bath in a non-radiative way through the flip-flop motion of the NH<sub>2</sub> group [43].

Even though higher  $B_{2PA}$  values would remain desirable, coumarins relatively low two-photon brightness is still reasonably sufficient for less demanding imaging applications, see below.

#### 4.1.3 Preliminary fluorescence microscopy studies

To fully implement chromophores in practical applications, further research is needed. At the current state, some preliminary studies are already under investigation. The first step is to look at chromophore's ability to stain cells and whether it can be done in a solvent buffer mixture that is acceptable for the living cells. For preliminary studies, C6 rat astrocytes cells were stained with five  $\mu$ g stock solution in 5 mL in a PBS puffer. The stock solution was prepared by mixing 0.446 mg of dye (C3) with 446  $\mu$ L DMSO. Rutt Taba in NICBP prepared samples. Imaging was done with one photon excitation Olympus Fluoview FV10i-LIV confocal laser-scanning microscope. Images were taken with excitation at 405 nm, and emission was collected at 455 nm. Results are shown in Figure 25, where on the left panel are control cells with no added dye, with no detectable fluorescence signal, and on the right panel, cells stained with C3 are clearly visible. The experimental setup did not allow the complete separation of fluorescence from dye in neutral or acidic environments. As preliminary results, C3 showed good staining efficacy in a solvent mixture suitable for studying living cells.



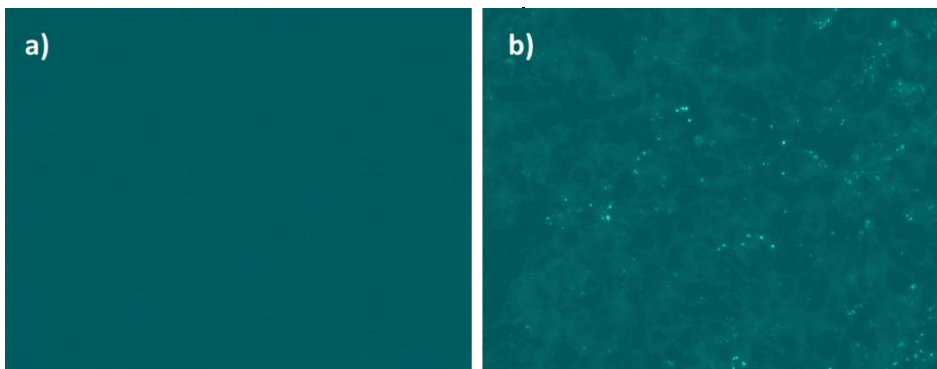


Figure 25: C6 rat astrocytes cells under fluorescence microscope a) control with no added dye, b) cells stained with C3 in DMSO and PBS buffer mixture.

## 4.2 On-off-on control of molecular inversion symmetry via multistage protonation

### 4.2.1 Photophysical properties of pyrrolopyrroles

The main objective of this Thesis is to demonstrate how protonation affects the 2PA and 2PEF characteristics of organic fluorophores depending on their intrinsic symmetry. The coumarins described in the preceding section represent inherently non-centrosymmetric fluorophores, where the presence or absence of attached protons does not affect the underlying symmetry. In the following, we focus on fluorophores with nominally inversion-symmetric structures and where the protonation formally changes the molecular symmetry. As a representative class of such fluorophores, we chose pyrrolopyrroles, one of the most electron-rich heterocycles among aromatic two-ring systems [71]. The pyrrolopyrroles have previously shown high peak 2PA cross-section values, in some cases over 1000 GM units [4]. The latter molecules also possess strong 1PA transitions in the visible wavelength region, high fluorescence yield, good stability, etc. [72], [73], [71]. As an example of characteristic 1PA and 2PA spectroscopy of these compounds, we first consider a novel pyrrolopyrrole 1a structure shown in Figure 9.

Figure 26 shows the linear absorption and fluorescence emission spectrum of 1a in toluene. Compared to the parent 1,2,4,5-Tetraarylpyrrolo[3,2-b]pyrroles (TAPPs) [40], the absorption maximum of 1a is bathochromically shifted by as much as 155 nm. At  $\lambda_{1PA} = 450 - 550$  nm, the vibronic progression of 1PA transition to the first excited state,  $S_1$ , can be seen. It is composed of a 0-0 peak at  $\lambda_{1PA} = 502$  nm with a corresponding maximum extinction coefficient value of  $42500 \text{ M}^{-1}\text{cm}^{-1}$ , followed by a second peak, 0-1, at  $\lambda_{1PA} = 474$  nm and a shoulder, 0-2, at  $\lambda_{1PA} \sim 440 - 455$  nm. Higher-energy electronic transitions  $S_0 \rightarrow S_3$  and  $S_0 \rightarrow S_4$  can be seen at  $\lambda_{1PA} = 408$  nm and  $\lambda_{1PA} = 380$  nm, with the maximum extinction coefficient values of  $20\,000 \text{ M}^{-1}\text{cm}^{-1}$  and  $26800 \text{ M}^{-1}\text{cm}^{-1}$ , respectively. The fluorescence emission spectra show a relatively small Stokes shift,  $730 \text{ cm}^{-1}$ , along with the mirror image of the  $S_0 \rightarrow S_1$  absorption with peaks,  $\lambda_{em\ 0-0} = 521$  nm,  $\lambda_{em\ 0-1} = 552$  nm and a shoulder at  $\lambda_{1PA} \sim 590 - 620$  nm.



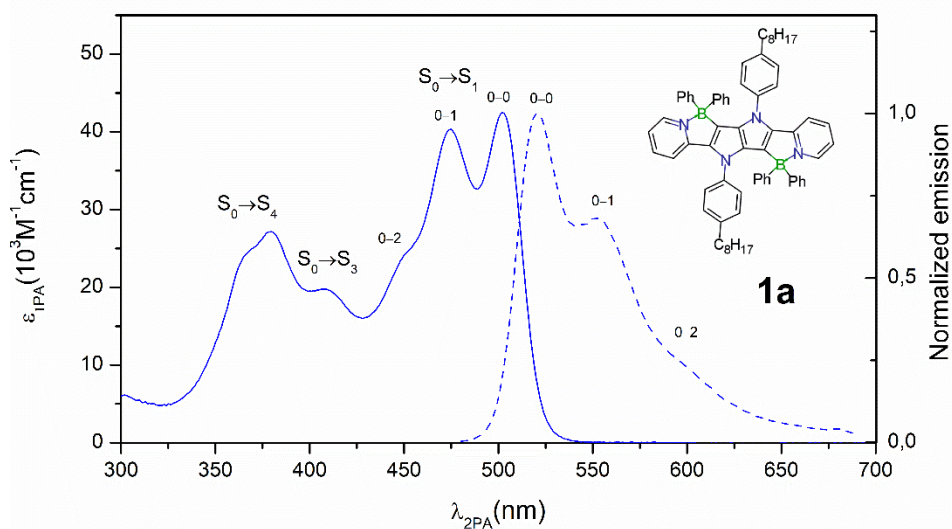


Figure 26: Pyrrolopyrrole **1a** absorbance (solid line) and normalized fluorescence emission (dash line) in toluene, along with the assigned vibronic transitions. Twelve chromophores with related structures were studied [40].

Figure 27 shows the 2PA cross-section spectra of **1a** in toluene (symbols, lower horizontal scale), superimposed for comparison with the 1PA spectral profile (upper horizontal scale) reproduced from Figure 26.

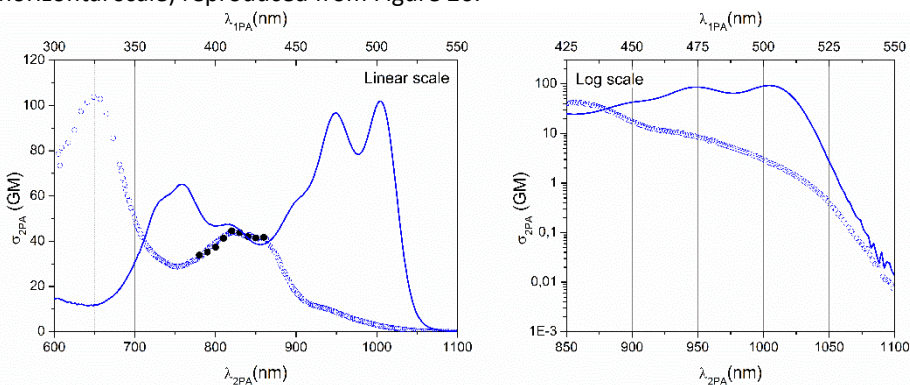


Figure 27: 2PA cross-section spectra (symbols) of **1a** in toluene presented on linear (left panel) and logarithmic (right panel) scale. Blue lines 1PA spectral shape (blue symbols) absolute 2PA cross-section values (black symbols) in toluene. Absolute  $\sigma_{2PA}$  values were determined in the  $\lambda_{2PA} = 780 - 850$  nm range (black symbols) relative to selected reference standards [37] and the results were averaged.

There are two most prominent two-photon transitions, both are at higher energies, well above the lowest-energy one-photon allowed  $S_0$  to  $S_1$  transition. A single band with the peak 2PA cross-section of 104 GM is observable at  $\lambda_{2PA} = 690$  nm, and a feature consisting of a broad double peak with a maximum 2PA cross-section of 45 GM is located at  $\lambda_{2PA} = 820$  nm. The right panel of Figure 27 presents the  $S_0 \rightarrow S_1$  vibronic 2PA

band on a logarithmic scale. According to the Laporte rule, inversion symmetry forbids purely electronic  $S_0 \rightarrow S_1$  transition. Still, there is a slight shoulder observable at,  $\lambda_{2PA} = 915 - 1070$  nm with  $\sigma_{2PA} \sim 2.5$  GM. Possible origins of this feature will be discussed in detail in the following section.

Quantum chemical calculations performed by Dr. Jacquemin [40] provide support for the above spectral assignments and are collected, along with the experimental results, in Table 4. Even though the calculated electronic  $S_0 \rightarrow S_1$ ,  $S_0 \rightarrow S_2$ ,  $S_0 \rightarrow S_3$ , and  $S_0 \rightarrow S_4$ , transitions wavelengths are blue-shifted by as much as,  $\sim 60$  nm, with the corresponding oscillator strengths relative values are still in good agreement with the experiment. The calculated fluorescence emission maximum, 493 nm, is also positioned at higher energy than the experimental findings, 521 nm. A relatively large mismatch between the computational energies compared to experimental results can be related to the particular nature of these boron-containing systems [74], [40]. The 2PA band between 800 nm and 900 nm is most likely related to the  $S_0 \rightarrow S_2$  transition that is dark in 1PA and gives the calculated peak 2PA cross-section of,  $\sigma_{2PA} = 94$  GM, which is approximately two times larger than the experimental value,  $\sigma_{2PA} = 44$  GM. Since current calculations do not account for vibrational motion of the chromophore, then due to the assumed inversion symmetry, the theoretical  $\sigma_{2PA}$  for the  $S_0 \rightarrow S_1$  transition identically vanishes.

Table 4: Comparison between experimental and quantum chemically calculated photophysical parameters of 1a.

| Transition            | $\lambda_{1PA} \text{ max, nm}$ |      | $\varepsilon, M^{-1} \text{ cm}^{-1}$ |      | $f$        |          | $\sigma_{2PA}, \text{GM} (\lambda_{2PA}, \text{nm})$ |      | $\lambda_{em}, \text{nm}$ |      |
|-----------------------|---------------------------------|------|---------------------------------------|------|------------|----------|--|------|---------------------------|------|
|                       | Exp                             | Calc | Exp                                   | Calc | Exp        | Calc     | Exp  | Calc | Exp                       | Calc |
| $S_0 \rightarrow S_1$ | 502                             | 442  | 42 500                                | 0.86 | 2.5 (1004) | 0        | 521  | 493  |                           |      |
| $S_0 \rightarrow S_2$ | —                               | 352  | —                                     | 0    | 44 (820)   | 94 (704) | —  | —    |                           |      |
| $S_0 \rightarrow S_3$ | 408                             | 351  | 20 000                                | 0.42 | 42 (816)   | 0        | —  | —    |                           |      |
| $S_0 \rightarrow S_4$ | 380                             | 322  | 26 800                                | 0.26 | 29 (760)   | 0        | —  | —    |                           |      |

### 4.3 Multi-stage protonation in a novel inversion symmetric pyrrolopyrrole

The pyrrolopyrrole described in the previous section lacks obvious binding groups or sites that could facilitate the attachment of a proton, or, for that matter, any other charged species, such as a metal ion [58], [59]. In order to gain such desired functionality, we, in collaboration with Dr. D. Gryko, designed a modified fluorophore (3,6-bis-(2-tert-butylpyridin-4-yl)-diketopyrrolopyrrole (PDP)) shown in Figure 28. The molecule features two symmetrically- placed pyridyl substitutions, such that the corresponding outermost pyridyl nitrogens could act as protonation sites.

In a neutral solvent such as methanol, the neutral form of the fluorophore would dominate as the pyridine groups are weakly basic, and not favorable for attaching or binding a proton. It is expected that addition of some acid to the solution would cause one proton to bind at one of the two sites (single protonation), while further increase of the acid concentration will eventually lead to both sites binding a proton (double protonation). This staged protonation process is shown schematically in Figure 28, where we designate the corresponding neutral form as the **PDP**, the single-protonated molecule as the **HPDP**, and the double-protonated species as the **HPDPH**.

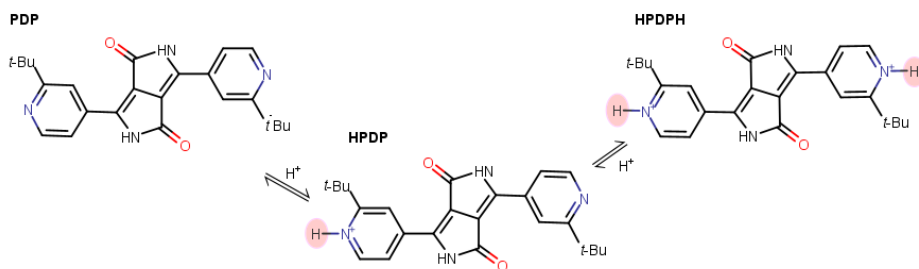


Figure 28: Two-step protonation of PDP molecule. Neutral (PDP) on the left, single-protonated (HPDP) in the middle, and double-protonated (HPDPH) on the right. The attached hydrogen ions at the nitrogen are marked with pink circles.

Figure 29 shows the 1PA and the fluorescence emission spectra of **PDP** in neutral methanol solution (is the absorption spectra in toluene, acetone, THF, DMO and Pyridine solvents are shown in Appendix 1). In an analogy to the 1a discussed above, and also supported by quantum chemical calculations discussed below, we may assign the peaks at  $\lambda_{1PA} = 508$  nm,  $\lambda_{1PA} = 476$  nm and a shoulder at  $\lambda_{1PA} \sim 430 - 455$  nm to the 0-0, 0-1, and 0-2 components of the  $S_0 \rightarrow S_1$  vibronic manifold, respectively. The Fluorescence emission spectra mirrors the 1PA with the maxima at  $\lambda_{em} = 550$  nm and at  $\lambda_{em} = 574$  nm. The Stokes shift between the 1PA and the fluorescence peaks is  $817$   $\text{cm}^{-1}$ . Compared to a1, the vibronic progression of PDP shows a slightly different intensity distribution. We note that the peak extinction coefficient for PDP,  $\epsilon = 23000$   $\text{M}^{-1}\text{cm}^{-1}$ , is only about half of that in 1a. In addition, PDP is showing only weakly pronounced higher-energy transitions futures in the  $\lambda_{1PA} \sim 300 - 450$  nm region.

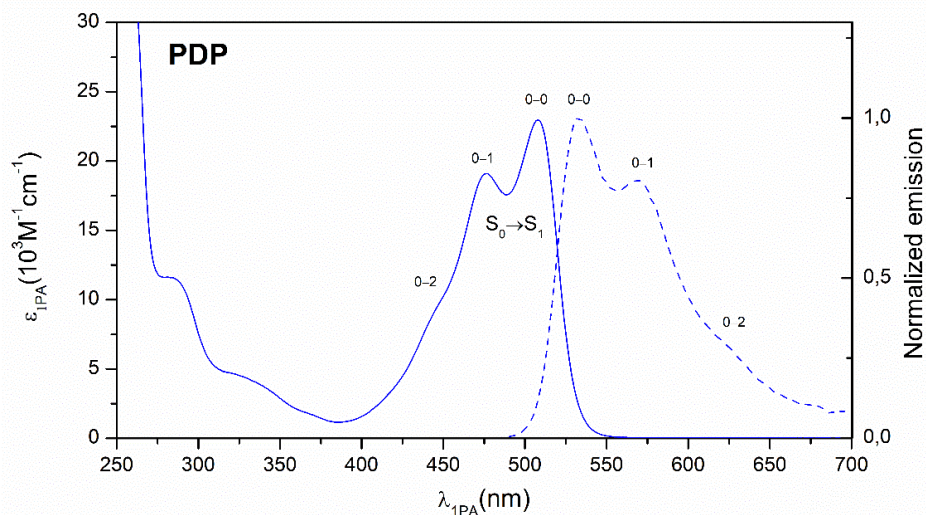


Figure 29: 1PA absorbance (solid line) and normalized fluorescence emission (dashed line) of PDP in methanol solution.

The two-photon absorption cross-section spectrum of PDP in methanol is shown in Figure 30 appears to be nearly matching (0-1) vibronic band at 476nm in the maximum at  $\lambda_{2PA} = 954$  nm, with the peak value  $\sigma_{2PA} = 0.8$  GM which is near twice the corresponding 1PA spectrum.

There is less such correspondence between the second feature at  $\lambda_{2PA} \sim 902$  nm in the 2PA spectrum and the 0-2 band in 1PA. However, in the 0-0 transition region, the 2PA spectrum shows again a weak but distinct shoulder at  $\lambda_{2PA} \sim 1020$  nm with the corresponding  $\sigma_{2PA} = 0.4$  GM. At shorter wavelengths, below  $\lambda_{2PA} < 820$  nm, the 2PA cross-section starts to rapidly increase.

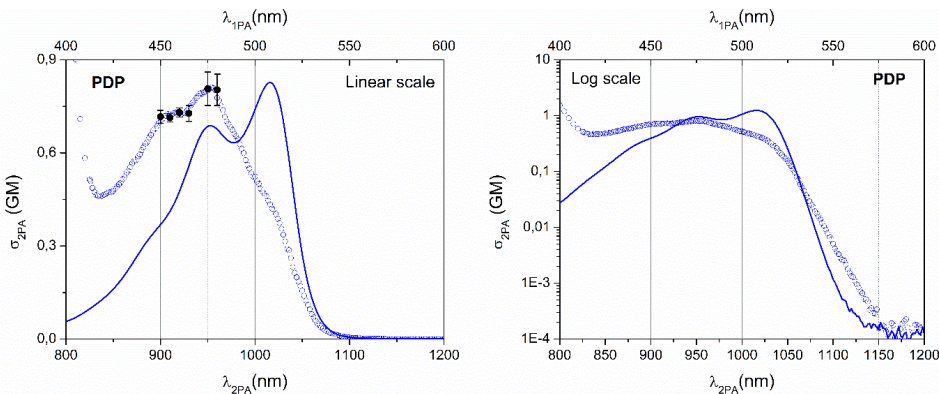


Figure 30: 2PA of the neutral PDP in methanol solution (symbols). 1PA (blue line) spectra shape is shown for comparison. The same data is presented on linear scale (left panel), and on logarithmic scale (right panel). The absolute  $\sigma_{2PA}$  values (bold circles with error bars) were determined by corresponding measurements performed in the  $\lambda_{2PA} = 780 - 850$  nm range.

Figure 31 shows how the 1PA spectrum of PDP changes upon titration of the methanol solution with triflic acid diluted in the same solvent. The insert shows the relation between the amount of acid solution added and the measured pH value of the sample solution. The spectra on the main panel are color-coded to represent corresponding pH values. At pH  $\sim 5$ , one isosbestic point can be observed at  $\lambda_{1PA} = 517$  nm. At the pH values below 2.7, two secondary isosbestic points appear at  $\lambda_{1PA} = 555$  and 434 nm. This observation can be tied to the emergence of the anticipated single-protonated and double-protonated forms, **HPDP** and **HPDPH**. These two new absorbance features show maxima at  $\lambda_{1PA} = 547$  nm and  $\lambda_{1PA} = 567$  nm, respectively.

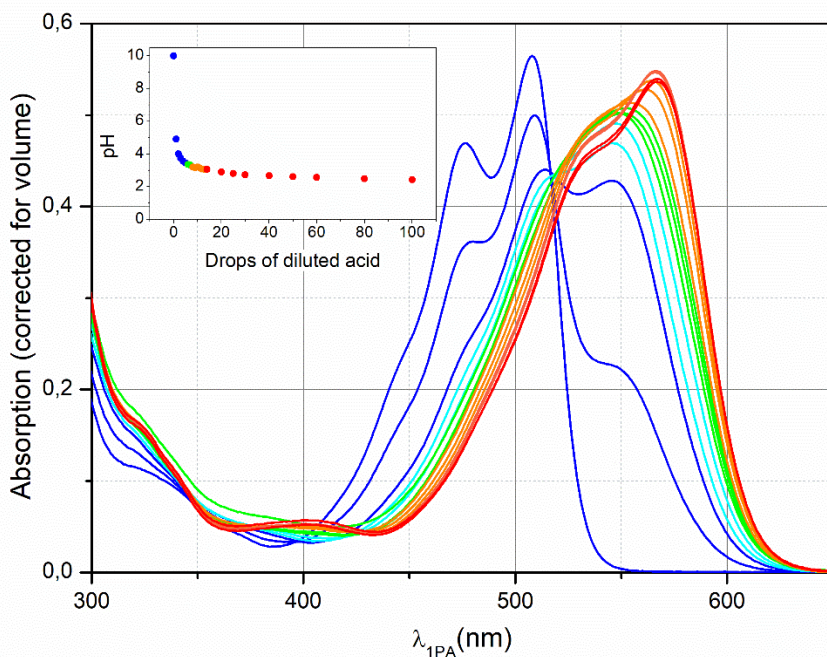


Figure 31: 1PA titration spectra of PDP in methanol solution with diluted triflic acid (one drop of concentrated triflic acid in 5 ml of methanol). The insert shows the correspondence between the measured pH and the number of added drops of the diluted acid.

To obtain pure spectral forms of HPDP and HPDPH, we used MCR-ALS decomposition of the titration spectra as described in the experimental methods section, 2.7.1. Figure 32 shows the results of the decomposition, where the green and red curves correspond to the molar extinction of the single (HPDP) and double (HPDPH) protonated forms. Two stages of protonation bring about a progressive redshift of the lowest-energy band as well as a redshift of the higher-energy portion of the spectrum. The 1PA maximum shifts from  $\lambda_{1PA} = 508$  nm to  $\lambda_{1PA} = 546$  nm and  $\lambda_{1PA} = 569$  nm for single- and double-protonated forms, respectively. Protonation also broadens the  $S_0 \rightarrow S_1$  band slightly but without significant change in the peak  $\epsilon_M$  value. These experimental parameters are collected in Table 5. Additionally, PDP and HPDPH show a similar vibronic distribution of the lowest electronic transition.

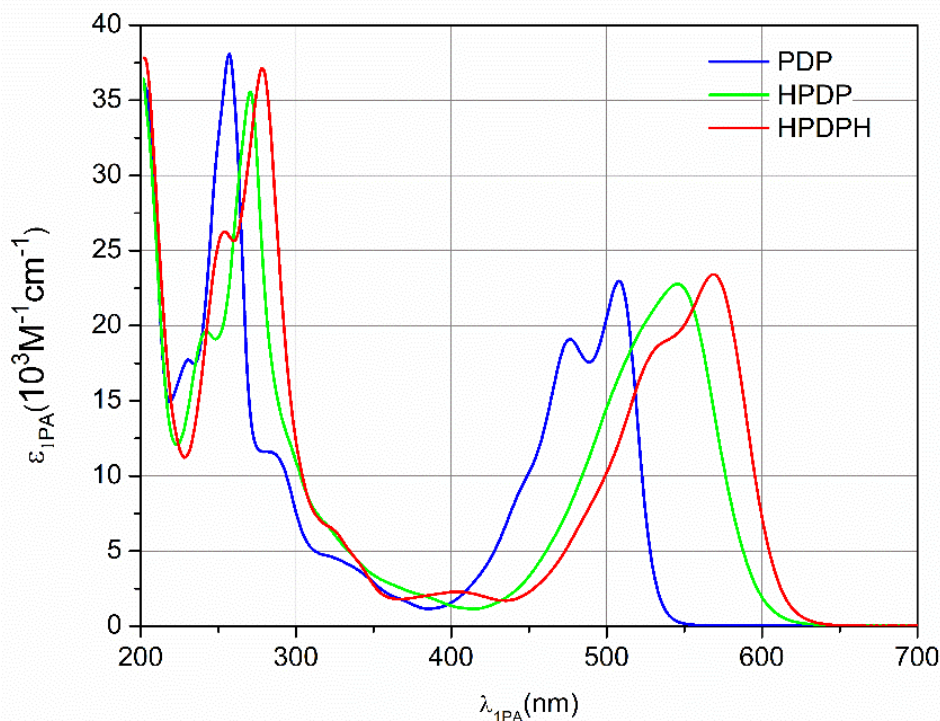


Figure 32: Molar extinction spectra PDP (blue), HPDP (green), and HPDPH (red), all in methanol solution, obtained by the MCR-ALS decomposition results. Contribution from three main species was confirmed by singular value decomposition (SVD) of the absorbance matrix **A**. The first three singular values form 99.3% of the total signal, with the remaining singular values appearing as a scree [75] indicative of random noise (not shown).

Our next objective is to obtain the two-photon absorption spectra of the protonated forms. This task was complicated by the fact that the protonation affected not only the spectral profiles, but also changed spectrum and the efficiency of the fluorescence emission. The fluorescence quantum yield of HPDP was roughly four times that of the neutral form, while the emission of the HPDPH was strongly quenched compared to both PDP and HPDP.

Figure 33 (a) shows some examples of the experimentally measured 2PEF excitation spectral profiles at different pH, for the excitation wavelength range,  $\lambda_{2PA} = 800 - 1300$  nm, covering the  $S_0 \rightarrow S_1$  transition of all the three forms. The pH values are color-coded from 2.0 to 8.2, indicated on the figure legend, together with the emission detection wavelength, which spanned,  $\lambda_{em} = 450 - 804$  nm. A slight mismatch occurred in the raw spectra at the degeneracy wavelength, 1030 nm, where the OPA switches between signal and idler output modes. This technical artifact was corrected by aligning the signal and idler sections at 1030 nm, as shown in Figure 33 (b). This allowed the general spectral changes to be compared by rescaling the excitation profiles to match at 995 nm. Showing that the PDP form is present for  $pH > 7$ , with the maximum 2PA at,  $\lambda_{2PA} = 954$  nm. Adding diluted triflic acid causes a redshift of the maxima to  $\lambda_{2PA} \sim 1100$  nm ( $pH$  around  $\sim 3.5$ ), and then a slight hypsochromic shift to  $\lambda_{2PA} \sim 1060$  nm ( $pH$  below 2.5).

Due to the lack of isosbestic points, the same straight forwarded decomposition technique used for the 1PA could not be applied here. We circumvented this issue by



using the fact that each protonation form had its unique emission spectrum. For our mixed samples, we recorded the entire emission spectrum at each excitation wavelength. This data was composed into an excitation-emission matrix (EEM) for further analysis, as described in section 2.7.2.

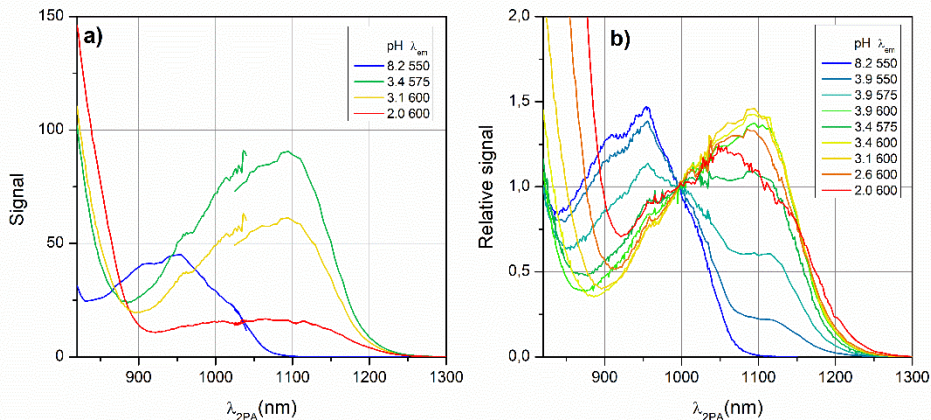


Figure 33: 2PEF excitation spectra in methanol with decreasing pH marked with different colors. a) selected unscaled 2PEF. b) All collected 2PEF spectra normalized at 995 nm.

To obtain the 2PA cross-section spectra of HPDP and HPDPH, we used two slightly different decomposition techniques. In the first, so-called ‘single-sample’ process, the MCR-ALS decomposition was applied individually to each EEM, corresponding to the measurements at each titration pH, as well as separately for the signal or idler excitation wavelength region. In the second, so-called ‘multisample’ method, all EEMs were decomposed simultaneously by combining them into one large 2D matrix.

Figure 34 shows the resulting 2PA cross-section spectra of HPDP and HPDPH in methanol. A slight difference is noted in the 2PA profiles depending on the decomposition method used. The final 2PA spectra were obtained by averaging these two results. The peak 2PA wavelengths are at  $\lambda_{2PA} = 954$  nm, 1086 nm, and 1066 nm for PDP, HPDP, and HPDPH, respectively. The corresponding peak cross-section values are  $\sigma_{2PA} = 0.81 \pm 0.05$  GM,  $7.7 \pm 0.5$  GM, and  $2.0 \pm 0.3$  GM. To obtain the absolute two-photon cross-section values of the components contained in a mixed sample, the 1PEF and 2PEF excitation-emission spectra were collected back-to-back and each decomposed using MCR-ALS, according to the “single-sample” method. Decomposed 1PEF EEM signals were used to correct for the differential quantum efficiency of sample and reference, technique is further discussed under method section (2.7).

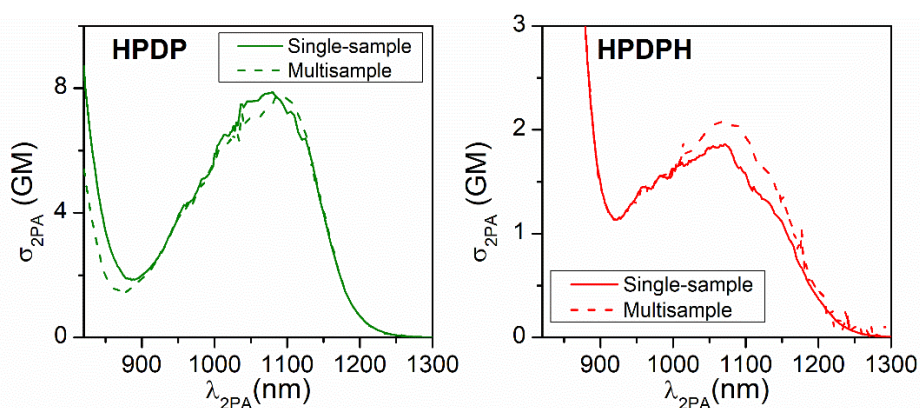


Figure 34: 2PA cross-section spectra of HPDP, and HPDPH, obtained by MCR-ALS decompositions using the single- (solid line) and multi-sample (dashed line) methods.

As a by-product of the spectral decomposition results, the fluorescence spectral profiles of HPDP and HPDPH were also obtained and are shown in along with PDP Figure 35.

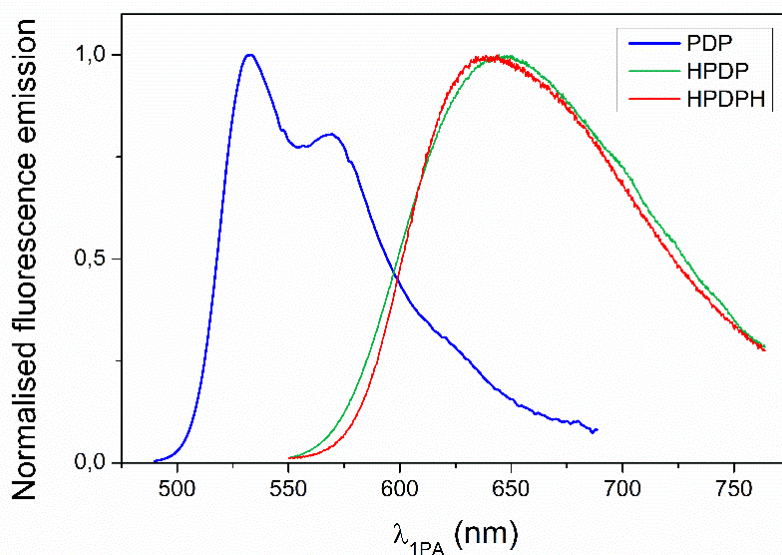


Figure 35: Normalized fluorescence emission spectra of PDP, HPDP, and HPDPH in methanol solution obtained from MCR-ARL decomposition of the titration data and EEM spectra. Spectra are uncorrected for detector sensitivity.

Interestingly, the emission spectra of the singly- and doubly protonated forms appear strikingly similar, with the peaks at  $\lambda_{em} \sim 638$  nm and  $\lambda_{em} \sim 645$  nm, respectively. Also, the structure of HPDPH is not mirroring its absorption spectra, which may be related to distortions in the relaxed  $S_1$  excited state due to intermolecular charge transfer caused by the attached proton.



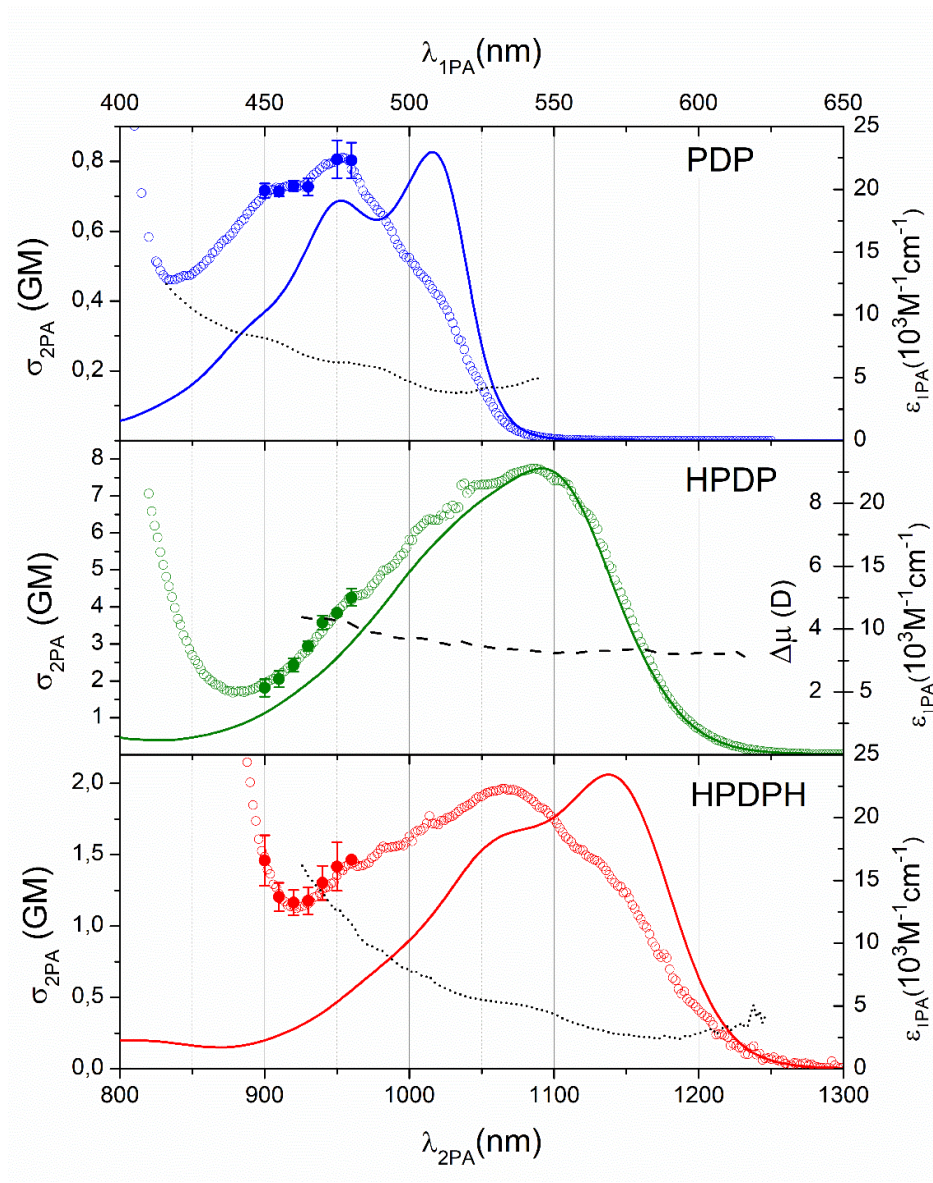


Figure 36: Summary of 1PA (solid line) and 2PA (empty symbols) spectra for PDP (blue), HPDP (green), and HPDPH (red) in methanol solution. The 2PA profiles were scaled according to the absolute cross-section values measured in the range,  $\lambda_{2PA} = 900 - 950$  nm (full symbols). Dashed black line is the change of permanent electric dipole moment in HPDP; dotted black lines are the 1PA vs. 2PA ratio in PDP and HPDPH.

Figure 36 summarizes the 2PA cross-section spectra of PDP, HPDP, and HPDPH combined with the corresponding 1PA molar extinction spectra.

The 2PA maxima of HPDP and HPDPH are both red-shifted relative to the PDP by  $\lambda_{2PA} \sim 140$  nm and  $\lambda_{2PA} \sim 110$  nm, respectively, following the same trend as in the 1PA. In the case of HPDP the 2PA spectral profile closely follows that of the 1PA, while in PDP and HPDPH they are clearly different.

While both the 1PA and 2PA profiles of HPDP are broad and feature less, the 2PA profiles of both PDP and HPDPH show a spectral maximum somewhat close to but not exactly matching the corresponding 0-1 band of the 1PA  $S_0 \rightarrow S_1$  transition. Importantly, both nominally symmetric forms also display a shoulder in the 2PA spectrum, which seems to be co-located with the 0-0 band of the 1PA  $S_0 \rightarrow S_1$  electronic transition. The fact that 1PA and 2PA profiles coincide in HPDP implies that the two-state model adequately describes the 2PA cross-section in this case. We thus use Equation (25) to estimate the permanent electric dipole moment change giving,  $\Delta\mu = 3.4$  Debye. Dashed line in Figure 36 shows the  $\Delta\mu$  value (inner right vertical scale) estimated by evaluating the ratio between 2PA and 1PA profiles. This ratio stays remarkably constant, as would be expected if  $\Delta\mu$  is independent of the vibrational contributions. On the other hand, the same ratio evaluated for PDP and HPDPH varies considerably across the vibronic band.

In order to shed light on the spectral features of the symmetric forms, we performed calculations (Table 5) indicating that the theoretical  $S_0 \rightarrow S_1$  purely electronic transition is positioned at  $\lambda_{1PA} = 485$  nm,  $\lambda_{1PA} = 546$  nm, and  $\lambda_{1PA} = 578$  nm for PDP, HPDP, and HPDPH, respectively. These values exhibit good agreement with the experimental band maxima, although computed values of  $\epsilon$  and  $\sigma_{2PA}$  are, for all forms, notably higher than the experimental counterparts. This mismatch may indicate a systematic issue that appears to be specific to diketopyrrolopyrroles [76]. However, the theoretically calculated dipole moment change,  $\Delta\mu = 4.0$  Debye, still compares favorably with the experimental finding,  $\Delta\mu = 3.4$  Debye. Table 5. also lists the calculated polarizability,  $\alpha$ , in the ground state and its change,  $\Delta\alpha$ , upon excitation. These latter two values are relatively small compared to molecular volume estimated from the  $sp^2$  carbon bond length and may originate from the molecule's axial shape. Furthermore, the calculations associate the dominant 1PA peak band in PDP and HPDPH with the corresponding 0-0 vibronic component of the  $S_0 \rightarrow S_1$  transition, while identifying no other electronic transitions in the low energy region ( $\lambda_{1PA} > 400$  nm). This suggests that the multiple absorption bands observed for PDP and HPDPH in 1PA stem from the vibronic coupling. In the case for HPDP, significant spectral broadening characteristic of dipolar systems prevents detailed assignment of accompanying features, even though vibronic nature is clear already from our above discussion of  $\Delta\mu$ .

Let us now consider in some further details what vibrations could give rise to the observed vibronic band structure. For this purpose, we performed quantum-chemical calculations of the electronic-vibrational transition strengths and wavelengths of PDP, HPDP, and HPDPH. The results are summarized in Figure 37 and Table 5. Note that because of above mentioned systematic issues with determining exact 0-0 wavelength, the spectra were shifted by 55 nm, 91 nm, and 100 nm to match best the experimental data. The black vertical lines in Figure 37 show the vibronic contributions to 1PA absorption, while the 0-0 component is shown with a red line. Selected few major vibronic modes contributing most to the 0-1 band are highlighted in yellow. The atomic displacement vectors for these selected modes are shown for each form in Appendix 16 (Figure 53, Figure 54, and Figure 55). These modes are observed to be of  $a_g$  symmetry, suggesting that the 1PA vibronic band originates mainly from Franck-Condon coupling terms. Dashed line in Figure 37 corresponds to the convolution of the calculated vibronic intensities with a Gaussian inhomogeneous profile. An excellent agreement between the experimental 1PA spectra and the convolved vibronic profile supports the vibronic quantum chemical calculation results.

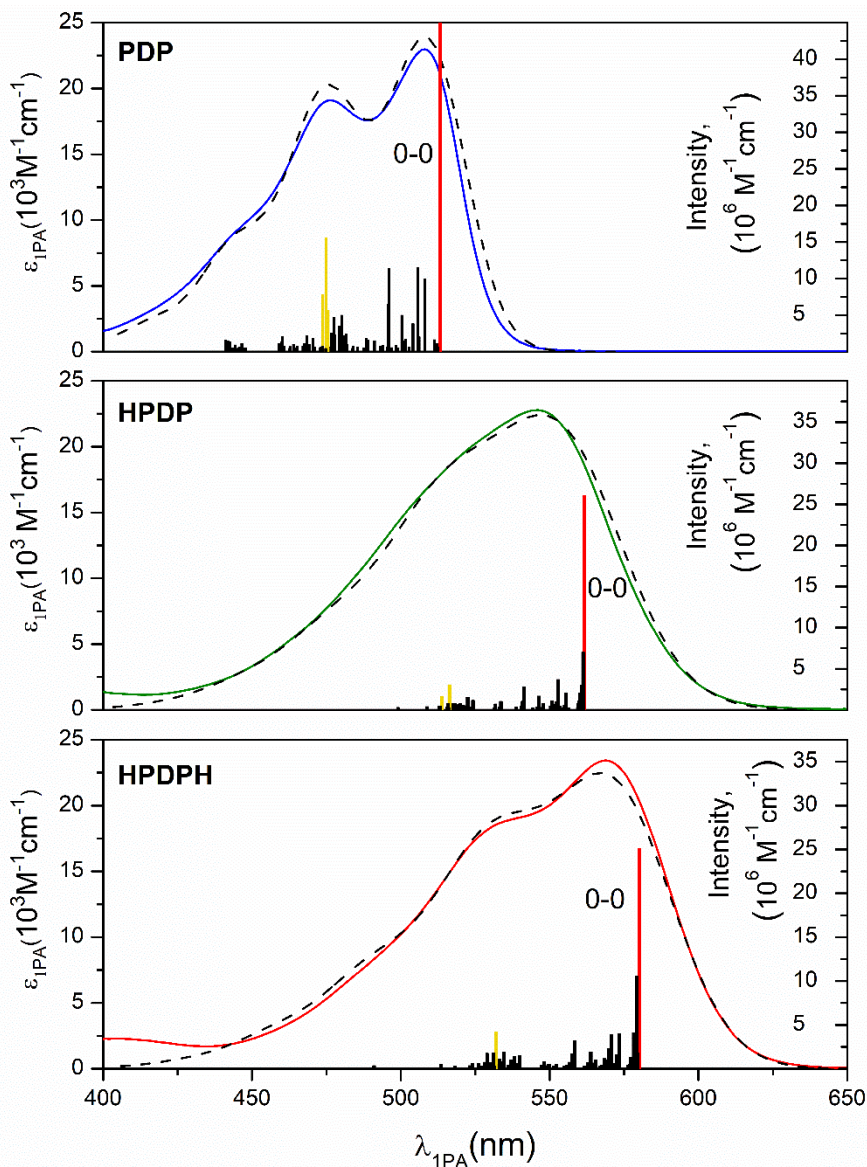


Figure 37: Calculated vibronic spectra of PDP, HPDP, and HPDPH (vertical lines). Dominant modes contributing in the 0-1 1PA range are marked with yellow, (the corresponding normalized displacement vectors are shown in Appendix 16). The experimental 1PA spectra in MeOH (solid line) and the convolution of the calculated vibronic intensities) with Gaussian distribution (HWHM = 500  $\text{cm}^{-1}$ ) to simulate line broadening (dashed lines). The calculated spectra are shifted by  $-55$  nm,  $-91$ , and  $-100$  nm for PDP, HPDP, and HPDPH, respectively.

Table 5: The experimental and calculated electronic spectral properties of the PDP series in MeOH.

| Parameter   | PDP                        |                               | HPDP           |                               | HPDPH      |                               |
|---|----------------------------|-------------------------------|----------------|-------------------------------|------------|-------------------------------|
|   | Expt                       | Calc <sup>[a]</sup>           | Expt           | Calc <sup>[a]</sup>           | Expt       | Calc <sup>[a]</sup>           |
| $\epsilon_{\max}$ , M <sup>-1</sup> cm <sup>-1</sup><br>( $\lambda_{1PA}$ , nm) | 22900 (508)<br>19000 (477) | 34600 <sup>[b]</sup><br>(485) | 23200<br>(546) | 32500 <sup>[b]</sup><br>(546) | 23400(569) | 31300 <sup>[b]</sup><br>(578) |
| $f_{01}$ (Osc. Str.)  | 0.21                       | 0.45                          | 0.32           | 0.45                          | 0.31       | 0.42                          |
| $\mu_{01}$ , D  | 4.80                       | 6.81                          | 6.10           | 7.20                          | 6.09       | 7.17                          |
| $\alpha(S_0)$ , Å <sup>3</sup>  | –                          | 70.1                          | –              | 73.4                          | –          | 72.7                          |
| $\Delta\alpha$ , Å <sup>3</sup>   | –                          | 5.9                           | –              | 7.2                           | –          | 8.0                           |
| $\mu(S_0)$ , D  | –                          | 0.01                          | –              | 23.25                         | –          | 0.41                          |
| $\mu(S_1)$ , D  | –                          | 0.01                          | –              | 18.28                         | –          | 0.35                          |
| $\Delta\mu$ , D   | NA                         | 0.0                           | 3.4            | 5.0                           | NA         | 0.1                           |
| $\delta_{2PA}$  | –                          | 0.1                           | –              | 9837                          | –          | 1.1                           |
| $\sigma_{2PA}$ , GM<br>( $\lambda_{2PA}$ )                                      | 0.81 (954)                 | 0 <sup>[c]</sup> (969)        | 7.7 (1086)     | 16 <sup>[c]</sup> (1112)      | 3.1 (878)  | 0 <sup>[c]</sup> (1157)       |
| $\sigma_{02}$ , GM ( $\lambda_{2PA}$ )  | 3 (785)                    | 0 (748)                       | >7 (<820)      | 5 (834)                       | 6 (860)    | 3 (866)                       |
| $\sigma_{03}$ , GM ( $\lambda_{2PA}$ )  | –                          | 34 (690)                      | –              | 1357 (796)                    | –          | 5522 (832)                    |
| $\lambda_{em}$ , nm   | 533                        | –                             | 649            | –                             | 639        | –                             |

[a] For symmetric PDP the transition energies and oscillator strengths from PCM/mCAM-B3LYP ( $\alpha = 0.08$ ,  $\beta = 0.92$ ,  $\mu = 0.15$ ), for HPDP and for HPDPH from PCM/mCAM-B3LYP ( $\alpha = 0.08$ ,  $\beta = 0.92$ ,  $\mu = 0.135$ ) calculations at 6-311G(d,p) level. [b] 1PA FWHM 0.35, 0.37 and 0.36 eV for PDP, HPDP and HPDPH, respectively (Gaussian line shape) [c] 2PA FWHM 0.25, 0.22 and 0.27 eV for PDP, HPDP and HPDPH, respectively.

Next, let us turn our attention to HPDP, which displays coinciding 1PA and 2PA profiles for the  $S_0 \rightarrow S_1$  transition. Since the 1PA shape is most likely due to Frank-Condon factors, then we may conclude that the 2PA shape originates from similar factors in the two-photon transition probability. Indeed, According to Equation (21) and Equation (24) in the first approximation, the vibronic intensity distribution in both 1PA and 2PA are determined mainly by the same Condon integral.

On the other hand, for the inversion symmetric PDP and HPDPH, vibronic transition allowed in the 1PA, should be strictly 2PA forbidden. However, the 2PA spectra displays a notable shoulder at,  $\lambda_{2PA} \sim 1025$  nm in PDP and at  $\lambda_{2PA} \sim 1150$  nm in HPDPH, i.e., at a wavelength that is approximately twice the corresponding 1PA 0-0 band, thus potentially implying a mechanism that circumvents the parity.

One obvious possible mechanism is via symmetry-breaking molecular conformations, [77], [78], [79] and in particular the rotation around the single-bond linking the peripheral pyridine groups appears a likely candidate. In this regard, theoretical calculations were performed to determine the potential effect of inversion symmetry-breaking conformations. Figure 38 shows three representative conformers with different rotations of the pyridyl moieties, of which (A) was determined to be the lowest-energy ground state configuration for all three forms.

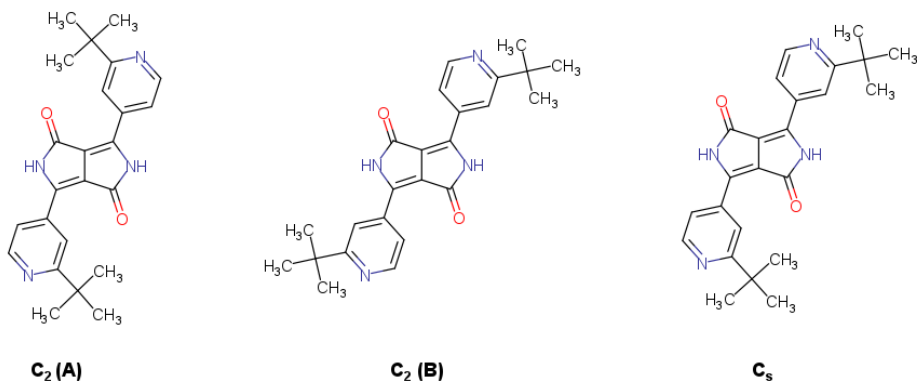


Figure 38: Symmetry assignments for the different conformers of PDP. Conformer A represents the lowest-energy configurations for all three protonation states.

The computational results are summarized in Table 9 (Appendix 15). Although the rotation of pyridyl moieties along the linking single-bond can lead to slightly higher energy non-inversion symmetric conformers, our calculations showed that in all cases, the 0-0 2PA cross-section remains negligible for both PDP and HPDPH. This makes some physical sense as well, as *tert*-butyl groups would not be expected to contribute to conjugation, so these conformers would have the same  $\pi$ -conjugated structure. We thus conclude that conformational changes are most likely not involved in the non-vanishing 2PA.

Our second hypothesis is that the 2PA spectra of PDP and HPDPH are due to Herzberg-Teller coupling with vibrational modes as described by the equation:

$$\sigma_{2PA}(\omega) \cong \gamma \left| \langle k|i \rangle \mu_{fg} \Delta\mu + \langle k|Q_{(i)}|i \rangle \left( \mu_{fg} \frac{\partial(\Delta\mu)}{\partial Q} + \frac{\partial\mu_{fg}}{\partial Q} (\Delta\mu) \right) \right|^2, \quad (43)$$

where

$$\gamma = \frac{\pi}{15 n^2 c^2 \epsilon_0^2 \hbar^2} (2 \cos^2(\beta) + 1). \quad (44)$$

Since in inversion-symmetric molecules,  $\Delta\mu = 0$ , the first (Franck-Condon) term as well as the last term in the Herzberg-Teller expansion are zero. Thus, in the two-level approximation, the 2PA cross-section may be only due to the derivative term of the permanent dipole moment change with respect to a displacement,  $Q$ . Additionally, the magnitude of this change is scaled by the square of the overlap integral of the displaced ground- and the excited-state vibrational wave functions,  $\langle k|Q_{(i)}|i \rangle$ . Unfortunately, the derivative terms cannot be analytically computed for 2PA at present, so full quantitative treatment remains outside the scope of this analysis. However, Equation (43) does offer some approximate investigations.

To this effect, nuclear distortions along select ground-state vibrational mode eigenvectors were prepared computationally for the neutral PDP molecule, for which 1PA, 2PA and molecular dipole moments were calculated in a similar manner as the initial lowest-energy structure, summarized in Table 6. This method has been previously, applied to dipolar molecules [80]. The magnitude of the displacement was selected relative to the mass-weighted normalized mode vector, depicted in Figure 39, which for different modes corresponds to a different total distance of atomic coordinates. For each

mode, the displacement was selected to be relatively small, but large enough to observe a change in either dipole moment terms. In general, larger displacements were required for vibrations which encompass motions for many atoms in a shallow potential well, while smaller displacements demonstrated effects in more localized and higher energy vibrational modes.

*Table 6: The calculated electronic spectral properties of PDP in MeOH and its analogs when distorted along selected vibrational modes with various scaling factors applied to respective displacement vectors. For  $\Delta\mu$  and  $\sigma$ , the first value is directly computed by TD-DFT, while the value within parentheses calculated by applying the two-level model (Equation 25) to the quantum chemical estimates of  $\sigma$  or  $\Delta\mu$ , respectively. The 1PA-active vibrational modes are highlighted in gray.*

| Parameter                            | PDP          | Mode 12 ( $b_u$ , 171 $\text{cm}^{-1}$ ) |                 | Mode 21 ( $b_u$ , 267 $\text{cm}^{-1}$ ) |                 | Mode 14 ( $a_g$ , 198 $\text{cm}^{-1}$ ) | Mode 24 ( $a_g$ , 293 $\text{cm}^{-1}$ ) |
|--------------------------------------|--------------|--|-----------------|--|-----------------|--|--|
|                                      |              | $\pm 0.8^{[a]}$                          | $\pm 1.2^{[a]}$ | $\pm 0.8^{[a]}$                          | $\pm 1.2^{[a]}$ | $\pm 0.8^{[a]}$                          | $\pm 0.8^{[a]}$                          |
| $S_0 \rightarrow S_1$ transition, nm | 485          | 485                                      | 484             | 486                                      | 487             | 478                                      | 470                                      |
| $f$ (oscillator strength)            | 0.45         | 0.45                                     | 0.45            | 0.45                                     | 0.44            | 0.47                                     | 0.48                                     |
| $\Delta\mu$ , D                      | 0.0<br>(0.0) | 0.4<br>(0.2)                             | 0.7<br>(0.4)    | 0.6<br>(0.4)                             | 0.9<br>(0.5)    | 0.0 (0.0)                                | 0.0 (0.0)                                |
| $\sigma_{2PA}$ , GM                  | 0.0<br>(0.0) | 0.06<br>(0.18)                           | 0.13<br>(0.41)  | 0.13<br>(0.35)                           | 0.28<br>(0.75)  | 0.00<br>(0.00)                           | 0.00<br>(0.00)                           |

| Parameter                            | Mode 36 ( $b_u$ , 432 $\text{cm}^{-1}$ ) |                 | Mode 132 ( $b_u$ , 1624 $\text{cm}^{-1}$ ) |                 |                 | Mode 134 ( $b_u$ , 1637 $\text{cm}^{-1}$ ) |                 |
|--------------------------------------|--|-----------------|--|-----------------|-----------------|--|-----------------|
|                                      | $\pm 0.4^{[a]}$                          | $\pm 0.8^{[a]}$ | $\pm 0.1^{[a]}$                            | $\pm 0.2^{[a]}$ | $\pm 0.4^{[a]}$ | $\pm 0.1^{[a]}$                            | $\pm 0.2^{[a]}$ |
| $S_0 \rightarrow S_1$ transition, nm | 488                                      | 495             | 486  | 488             | 497             | 492  | 509             |
| $f$ (oscillator strength)            | 0.44                                     | 0.40            | 0.45                                       | 0.44            | 0.43            | 0.44                                       | 0.43            |
| $\Delta\mu$ , D                      | 0.7 (0.2)                                | 1.3 (0.3)       | 0.4 (0.2)                                  | 0.7 (0.4)       | 1.4 (0.8)       | 1.6 (0.9)                                  | 2.6 (1.6)       |
| $\sigma_{2PA}$ , GM                  | 0.02<br>(0.42)                           | 0.07<br>(1.45)  | 0.04<br>(0.12)                             | 0.15<br>(0.48)  | 0.62<br>(1.81)  | 0.85<br>(2.45)                             | 2.39<br>(6.67)  |

[a] Scaling factor for displacement vectors

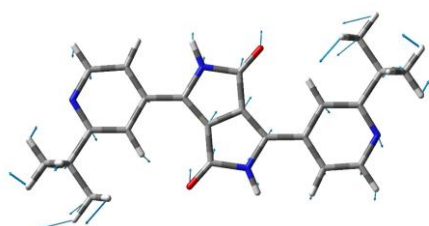
The magnitude of the displacement vectors was determined by arbitrary scaling factors as explained above. Even though our current model lacks desired quantitative accuracy, it does qualitatively reproduce our key experimental observations, including the apparent violation of the Laporte Rule.

According to the  $C_{2h}$  symmetry of PDP, vibrational modes can occur as irreducible representations  $a_g$ ,  $b_g$ ,  $a_u$ , and  $b_u$ . Due to the significant computational cost of a full analysis, we selected only a few representative  $b_u$  modes, which introduce an in-plane asymmetric distortion, as well as  $a_g$  modes, which are Franck-Condon active in 1PA.

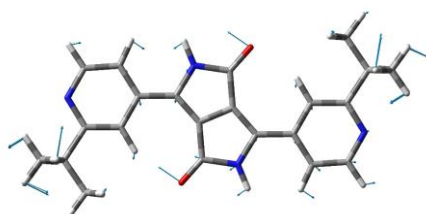


Modes with  $a_u$  symmetry were excluded as these occur perpendicular to the plane of the molecule, and so would have a negligible effect on molecule's in-plane transitions, while  $b_g$  modes would behave analogous to  $a_g$  and not break the inversion symmetry of the molecule. While  $a_g$  modes contribute to low-energy 1PA vibronic transitions by affecting the transition dipole, they show a negligible effect on 2PA, as seen in Table 6. In contrast, specific 1PA inactive  $b_u$  modes, demonstrated in Figure 39 (the average direction and magnitude of displacements of the atoms are indicated with arrows), significantly boost the  $\Delta\mu$  value of the  $S_0 \rightarrow S_1$  transition, up to  $\Delta\mu = 2.6$  D. Given that the calculated oscillator strengths for different normal modes stay relatively constant,  $f = 0.40 - 0.48$ , this is indicating possibility (at least in principle) of non-vanishing 2PA due to this type of H-T coupling.

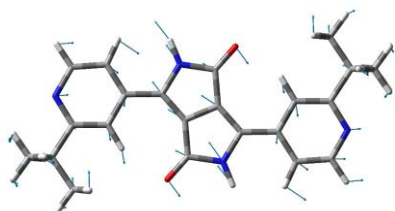
Mode 12 (171  $\text{cm}^{-1}$ ):



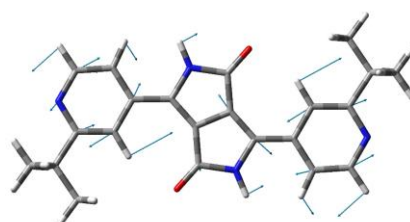
Mode 21 (267  $\text{cm}^{-1}$ ):



Mode 36 (432  $\text{cm}^{-1}$ ):



Mode 132 (1624  $\text{cm}^{-1}$ ):



Mode 134 (1637  $\text{cm}^{-1}$ ):

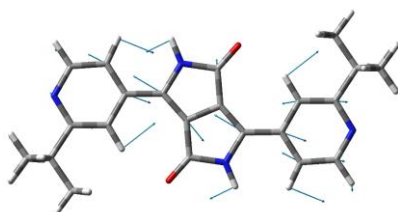


Figure 39: Average direction and magnitude of displacements for the selected ground-state normal modes of  $b_u$  symmetry for PDP, which may contribute to the observed 2PA in 0-0 region.

Figure 40 (a) shows how the calculated change of the permanent dipole upon  $S_0 \rightarrow S_1$  transition,  $\Delta\mu$ , depends on the displacement,  $\Delta Q$ , for some selected low- and high-frequency vibrational modes. The  $b_u$  modes are shown in black, while  $a_g$  modes are in red, with labels corresponding to the mode-numbers in Table 6. For all  $b_u$  modes,  $\Delta\mu$  terms show a linear dependence. In contrast, for  $a_g$  modes,  $\Delta\mu$  remains exactly zero, independent of the displacement  $\Delta Q$ .

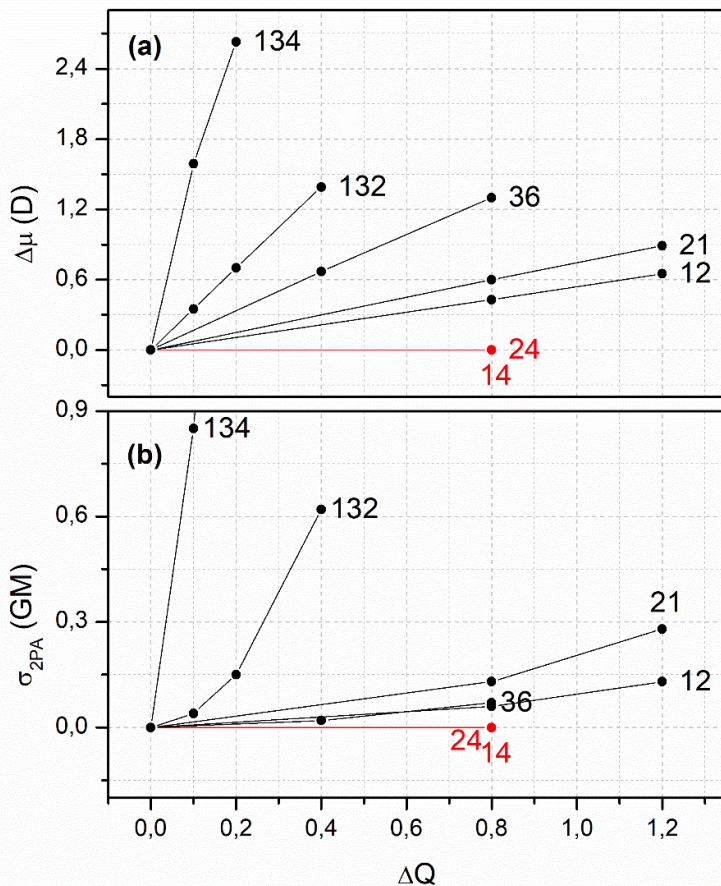


Figure 40: Dependence of the dipole moment change (a) and 2PA cross-section (b) on the ground state displacement along vibrational modes,  $Q$ . Different modes are indicated with numbers, colors denote the  $a_g$  (red) or  $b_u$  (black) vibrational symmetry.

Similar trends observed for  $\sigma_{2PA}$  (Figure 40 (b)) were calculated according to standard tensor formalisms in Dalton, which is not currently able to incorporate full vibronic 2PA effects, because numerical evaluation of the derivatives of second-order moments over vibrational coordinate space which is required for calculating H-T expansion terms, remains prohibitive for the structures with over 150 vibrational degrees of freedom like PDP. In that respect, more advanced techniques for treating derivative terms are currently under development [81]. Essentially,  $\partial\mu$ ,  $\partial\Delta\mu$ , and vibrational overlap terms,  $\langle k|Q_{(i)}|i\rangle$ , as they are in Equation (43), are not able to be separated from Dalton's composite result for vibrationally distorted structures. However, the calculated change in  $\Delta\mu$  can be used as an approximation for the H-T  $\partial\Delta\mu$  term. From the linear dependence in  $\Delta\mu$ , one would anticipate a quadratic increase in the cross-section when distorting along any  $Q$ -coordinate, which is observed in Figure 40 (b) for  $b_u$  modes. Likewise, the  $a_g$  modes, which do not change the  $\Delta\mu$ , have vanishing calculated cross-sections. Together, these trends suggest that it is primarily the  $\partial\Delta\mu/\partial Q$  term that dominates the vibronic enhancement of 2PA through H-T coupling.



#### 4.3.1 Quantitative relation between 2PA spectra and pH

The results presented above indicate that pH induced symmetry breaking affects 2PA to a much greater extent than the corresponding 1PA. A strong correlation between the measured 2PA spectra and pH values creates opportunities to use this effect for quantitatively optical monitoring of the pH. However, for this purpose, it is important to determine corresponding  $pK_a$  as reliably as possible. Our measured 1PA titration spectra of PDP lead to  $pK_a$  values for the first- and second protonation step,  $\sim 4.6$  and  $\sim 3.2$  respectively. At the same time, our quantum chemical COSMO-RS calculations [82], [83] indicate corresponding  $pK_a$  values, 5.9 and 4.2. We point out that the calculations include regression adjustment due to other pyridines. Which were obtained by calculating the Gibbs free energy differences ( $\Delta G_s$ ) between the protonated and dissociated forms. The latter was inserted into Eq. (27) to establish a correlation between the computed  $\Delta G_s$  and  $pK_a$  values [84], [85] of 11 differently substituted pyridines (further discussed in theoretical section 1.1.7).

While the calculated values are slightly higher than the experimental, both display a  $\sim 1.5$  pH interval between the two protonation stages, supporting the experimental  $pK_a$  results.

With the known  $pK_a$  values, quantitative estimation of pH could be made e.g., by monitoring the ratio of fluorescence signals of two excitation wavelengths corresponding predominantly to the neutral and doubly protonated form of PDP. Phenomenologically, the symmetry breaking effects are not limited to only pH sensing, but could be applied to detect some other local environmental factors, such as concentration of metal ions, protein conformational changes etc.

## 5 Conclusions and outlook

In this thesis, two sets of novel organic fluorophores were studied, possessing two different mechanisms that change two-photon absorbance depending on the pH of the environment. For detailed quantification of these phenomena, a custom-built automated femtosecond spectrometer for measuring the 2PA spectral profile and determining the 2PA cross-section was created, achieving efficient and repeatable acquisitions over a wide range of visible and NIR two-photon excitation wavelengths. This advanced experimental technique led to unmatched accuracy in determining the spectral properties and absolute cross-sections, even in complex mixed samples, revealing information about their interaction mechanisms with their surroundings and demonstrating potential use as two-photon pH sensitive probes.

In the first part, four coumarin 151 derivatives [38] were investigated as candidates for pH-sensitive lipophilic two-photon active probes. These probes display a large (60 nm) shift in 1PA and 2PA absorption upon changes in pH, stemming from a disruption of molecular conjugation upon protonation. The measured two-photon brightness was on the order of 10 and 0.20 GM for the neutral and protonated forms, respectively, making them potentially useful for microscopy measurements. By comparison, the precursor compound, C151, was found to have a brightness of 4.0 GM at 735 nm in acetonitrile, which is significantly lower than the previously reported value of 27 GM (754 nm) in ethanol [62]. In an acidic environment, the new derivatives show a lower brightness, but the values remain viable for practical microscopy, while the emission of C151 is completely quenched. Furthermore, when placed in polar and non-polar solvents, these new coumarin derivatives displayed unchanging absorption and emission characteristics making them robust sensors of pH or in mixed-polarity environments, such as near or in cell membranes. These findings have been confirmed in a preliminary fluorescence microscopy result conducted using 1PA, although applying these probes in two-photon microscopy is left for future studies.

The second part of the Thesis focuses on pyrrolopyrrole fluorophores which have a nominally inversion-symmetric structure. We performed a comprehensive study of 1PA and 2PA properties of novel pyrrolopyrrole which was decorated on opposite ends with an affective protonation site. It was shown that such system presents potentially an even more efficient sensor of pH because protonation of only one site breaks the inversion symmetry, while attachment of the second proton restores the symmetry, leading to large qualitative changes in the 2PA according to Laporte rule.

We performed detailed 1PA and 2PA titration experiments using diluted triflic acid in methanol solution and showed that while the peak 1PA extinction changes very little in low pH environment, the corresponding 2PA spectra show marked changes, wherein the basic form has a peak 2PA cross-section of 0.8 GM (954 nm), which is greatly enhanced to 7.7 GM (1086 nm), upon single protonation. The second protonation step reduces 2PA absorbance to 2 GM (1066 nm). These 1PA and 2PA observations match with the on-off-on switching of molecular inversion symmetry, which establishes, for the first time, a quantitative relationship between symmetry-switching and 2PA cross-section. It is important to note that even for a fairly large molecular system, a single proton at one end can result in a nearly 10x enhancement of the 2PA signal.

Along with changes in 2PA cross-section, protonation also appears to dictate changes in two-photon spectral shapes. For the single-protonated form, 2PA and 1PA profiles match, adhering to the explanation that neither spectrum experiences differing selection

rules, and both are likely dominated by Franck-Condon vibrational components. These electronic and vibrational terms are forbidden in the case of neutral- and double-protonated forms, according to the Laporte rule. However, perhaps surprisingly, both formally forbidden cases retain small but non-vanishing cross-sections in the lowest-energy 0-0 region. Quantum computational modelling indicates that these nonvanishing 2PA components stem not from conformational changes that break the symmetry, but likely from low energy Herzberg-Teller vibronic coupling, which vibrationally distorts the ground state. Importantly, these asymmetric vibrational terms appear to extend to very near the 0-0 transition, which should indeed remain Laporte Rule forbidden. We emphasize that our the high-precision measurement techniques were instrumental in revealing these very important details in the 2PA spectrum. Our results may be regarded as a textbook example of application of the Laporte rule while shedding further light on the origin of vibronic 2PA transitions. Furthermore, a strong correlation between the measured 2PA spectra and the pH values creates opportunities to use optical measurements to quantitatively monitor the environment's pH.

The common tool used throughout this work was protonation and demonstrating its ability to manipulate molecular behavior and provoke changes in the 2PA domain, for which it has proven to be a powerful operant. In addition, the use of 2PA to quantitatively monitor pH or establish  $pK_a$  values is concurrently demonstrated. The experimental synergy of these two themes provides an extraordinarily efficient and valuable means of characterizing molecular systems, particularly for those with symmetric qualities. This method could be further deployed for investigating other 2PA dyes, such as octopolar molecular pH-sensors that possess high symmetry and generally strong 2PA. Another future prospect would be to replace protons with other metal ions, for example, silver, attached to the PDP compound. This could lead to somewhat different vibronic behavior. These investigations would lead to innovative highly-specific molecular probes, whilst also revealing further important details concerning aspects of 2PA phenomena.

## List of figures

|   |    |
|---|----|
| Figure 1: Jablonski diagram of optically induced transitions by absorption of one photon or two photons..   | 13 |
| Figure 2: Different transition dipole moments contributions to the molecule's transition from the initial state $E_g$ to the final state $E_f$ .  | 16 |
| Figure 3: Schematic representation of inversion of coordinates.   | 16 |
| Figure 4: Few essential state models of 2PA.  | 18 |
| Figure 5: One-photon transitions between a set of vibrational levels in the ground and an excited electronic state.   | 19 |
| Figure 6: One- and two-photon-induced electronic-vibrational transitions.   | 20 |
| Figure 7: The chemical structures of coumarin C151 and the four phosphazene derivatives C1, C2, C3, and C4.   | 28 |
| Figure 8: Vials containing C1, C2, C3, and C4 powder.   | 29 |
| Figure 9: Chemical structures of PDP and 1a.  | 29 |
| Figure 10: The vial containing PDP on the left and 1a on the right.   | 30 |
| Figure 11: Tabletop layout of the femtosecond pulse laser system (Light Conversion).  | 33 |
| Figure 12: Typical average laser power at the signal (SIG), idler (IDL), and second harmonic of idler (SH-IDL) wavelength ranges.   | 34 |
| Figure 13: Schematic of the automated femtosecond 2PA spectrometer.   | 35 |
| Figure 14: Custom motorized sample turret capable and BBO crystal with automated SHG angle tuning.  | 37 |
| Figure 15: Andor spectrograph Kymera 328i.  | 38 |
| Figure 16: Example of compound 1a 2PA spectra against reference: C153-DMSO, C153-Tol, AF455 THF, Rh6G-MeOH.   | 41 |
| Figure 17: Excitation-Emission Matrix.  | 44 |
| Figure 18: 1PA titration spectra of C2 with diluted HCl in acetonitrile.  | 47 |
| Figure 19: Comparison of the calculated and experimentally measured 1PA spectra of C2 in acetonitrile.  | 49 |
| Figure 20: 1PA and 2PA spectra of the four lipophilic coumarin derivatives, C1-C4, and the parent C151, in neutral acetonitrile and in acetonitrile with $\sim 0.3$ M of triflic acid and in neutral n-octanol and in n-octanol with the addition of $\sim 0.3$ M triflic acid. | 50 |
| Figure 21: C2 in acidic ACN solvent compared to phenol dissolved in hexane.   | 53 |
| Figure 22: Comparison of 2PA and 1PA of neutral C2 in ACN.  | 54 |
| Figure 23: Expanded view of the experimental 1PA and 2PA spectra for C2 with 0.3 M triflic acid, in acetonitrile and n-octanol, compared to calculated wavelengths and oscillator strengths of electronic transitions for the monomer and dimer optimized structures.           | 55 |
| Figure 24: Normalized excitation and emission spectra for C1, C2, C3 and C4 in acetonitrile and n-octanol.  | 56 |
| Figure 25: C6 rat astrocytes cells under fluorescence microscope stained with C3.   | 59 |
| Figure 26: Pyrrolo pyrrole 1a absorbance and normalized fluorescence emission.  | 60 |
| Figure 27: 2PA cross-section spectra of 1a in toluene on a linear and logarithmic scale.  | 60 |
| Figure 28: Two-step protonation of PDP molecule.  | 62 |

|  |     |
|--|-----|
| Figure 29: 1PA absorbance and normalized fluorescence emission of PDP in methanol solution.....  | 62  |
| Figure 30: 2PA of neutral PDP in methanol solution.....  | 63  |
| Figure 31: 1PA titration spectra of PDP in methanol solution with triflic acid. The insert shows the correspondence between pH and the number of added drops of diluted triflic acid (one drop of concentrated triflic acid in 5 ml of methanol). 64 | 64  |
| Figure 32: Molar extinction spectra PDP (blue), HPDP (green), and HPDPH (red), all in methanol solution, obtained by the MCR-ALS decomposition results.....  | 65  |
| Figure 33: 2PEF excitation spectra in methanol with increasing triflic acid.....   | 66  |
| Figure 34: 2PA cross-section spectra of HPDP and HPDPH in methanol solution.....   | 67  |
| Figure 35: Normalized fluorescence emission spectra of PDP, HPDP, and HPDPH in methanol solution.....  | 67  |
| Figure 36: Summary of 1PA and 2PA spectra for PDP, HPDP, and HPDPH in methanol solution.....   | 68  |
| Figure 37: Comparison between the experimental 1PA spectra of PDP, HPDP, and HPDPH in MeOH and convolution of vibronic intensities from FCHT calculations in MeOH.....   | 70  |
| Figure 38: Symmetry assignments for the different conformers of PDP.....   | 72  |
| Figure 39: Average direction and magnitude of displacements for the selected ground-state normal modes.....  | 74  |
| Figure 40: Dependence of dipole moment and 2PA cross-section on the ground state displacement along vibrational modes, Q.....  | 75  |
| Figure 41: LabView control program measurement configuration window.....   | 132 |
| Figure 42: LabView Symphony CCD control window.....  | 133 |
| Figure 43: LabView Kymera spectrograph control window.....   | 133 |
| Figure 44: Oscilloscope display screenshot of PED detector signal waveform.....  | 134 |
| Figure 45: AF455 in toluene.....   | 135 |
| Figure 46: C151 2PA spectra in n-octanol and acetonitrile.....   | 136 |
| Figure 47: Time-resolved log-emission of neutral C2 in acetonitrile.....   | 139 |
| Figure 48: Spectrofluorometer instrumental correction function.....  | 140 |
| Figure 49: 1PA and fluorescence emission of neutral and protonated C3 in variable solvents.....  | 141 |
| Figure 50: Schematic of the automated femtosecond 2PA/3PA spectrometer.....  | 143 |
| Figure 51: Simplified schematics of the optical parametric amplifier.....  | 145 |
| Figure 52: LYRA-SH housing polarization rotator and frequency mixing stage with nonlinear crystal.....   | 145 |
| Figure 53: Average direction and magnitude of displacements for the selected 1PA-active ground-state normal modes for PDP.....   | 153 |
| Figure 54: Average direction and magnitude of displacements for the selected 1PA-active ground-state normal modes for HPDP.....  | 154 |
| Figure 55: Average direction and magnitude of displacements for the selected 1PA-active ground-state normal mode for HPDPH.....  | 154 |
| Figure 56: PDP Solvent dependence, one-photon absorption, and fluorescence emission profiles in variety of solvents.....   | 155 |

## List of tables

|  |     |
|--|-----|
| Table 1: Comparison of direct and indirect methods for measuring 2PA spectra and cross-sections. ....  | 27  |
| Table 2: Experimental and calculated 1PA/2PA photophysical parameters of C1, C2, C3 and C4. ....   | 51  |
| Table 3: Summary of the experimental fluorescence emission wavelengths, emission quantum yields, two-photon brightness values, and Stokes shift of C1-C4 and C151. ....  | 57  |
| Table 4: Comparison between experimental and quantum chemically calculated photophysical parameters of 1a. ....  | 61  |
| Table 5: The experimental and calculated electronic spectral properties of the PDP series in MeOH. ....  | 71  |
| Table 6: The calculated electronic spectral properties of PDP structure in MeOH. ....  | 73  |
| Table 7: C151 2PA values in the 550 – 925 nm in octanol and acetonitrile solution. ....  | 137 |
| Table 8: Fluorescence decay measurement results. ....  | 138 |
| Table 9: The experimental and calculated electronic spectral properties of the C <sub>2</sub> and C <sub>s</sub> point group representations of PDP series in MeOH. .... | 152 |

## References

- [1] M. Göppert-Mayer, "Elementary processes with two quantum transitions," *Ann. Phys.*, vol. 18, no. 7–8, pp. 466–479, Aug. 2009, doi: 10.1002/andp.200910358.
- [2] W. Kaiser and C. G. B. Garrett, "Two-Photon Excitation in Ca F 2 : Eu 2 +," *Phys. Rev. Lett.*, vol. 7, no. 6, pp. 229–231, Sep. 1961, doi: 10.1103/PhysRevLett.7.229.
- [3] N. S. Makarov, M. Drobizhev, and A. Rebane, "Two-photon absorption standards in the 550–1600 nm excitation wavelength range," *Opt. Express*, vol. 16, no. 6, pp. 4029–4047, Mar. 2008, doi: 10.1364/OE.16.004029.
- [4] Ł. G. Łukasiewicz *et al.*, "Ground- and Excited-State Symmetry Breaking and Solvatofluorochromism in Centrosymmetric Pyrrolo[3,2-b]pyrroles Possessing two Nitro Groups," *ChemPhotoChem*, vol. 4, no. 7, pp. 508–519, 2020, doi: 10.1002/cptc.202000013.
- [5] A. Karotki *et al.*, "Enhancement of two-photon absorption in tetrapyrrolic compounds," *JOSA B*, vol. 20, no. 2, pp. 321–332, Feb. 2003, doi: 10.1364/JOSAB.20.000321.
- [6] N. S. Makarov, M. Drobizhev, G. Wicks, E. A. Makarova, E. A. Lukyanets, and A. Rebane, "Alternative selection rules for one- and two-photon transitions in tribenzotetraazachlorin: Quasi-centrosymmetrical  $\pi$ -conjugation pathway of formally non-centrosymmetrical molecule," *J. Chem. Phys.*, vol. 138, no. 21, p. 214314, Jun. 2013, doi: 10.1063/1.4807594.
- [7] Ł. G. Łukasiewicz *et al.*, "Ground- and Excited-State Symmetry Breaking and Solvatofluorochromism in Centrosymmetric Pyrrolo[3,2-b]pyrroles Possessing two Nitro Groups," *ChemPhotoChem*, vol. 4, no. 7, pp. 508–519, 2020, doi: 10.1002/cptc.202000013.
- [8] R. S. Price, G. Dubinina, G. Wicks, M. Drobizhev, A. Rebane, and K. S. Schanze, "Polymer Monoliths Containing Two-Photon Absorbing Phenylenevinylene Platinum(II) Acetylide Chromophores for Optical Power Limiting," *ACS Appl. Mater. Interfaces*, vol. 7, no. 20, pp. 10795–10805, May 2015, doi: 10.1021/acsami.5b01456.
- [9] N. S. Makarov, A. Rebane, M. Drobizhev, H. Wolleb, and H. Spahn, "Optimizing two-photon absorption for volumetric optical data storage," *JOSA B*, vol. 24, no. 8, pp. 1874–1885, Aug. 2007, doi: 10.1364/JOSAB.24.001874.
- [10] M. K. Kuimova *et al.*, "Photophysical properties and intracellular imaging of water-soluble porphyrin dimers for two-photon excited photodynamic therapy," *Org. Biomol. Chem.*, vol. 7, no. 5, pp. 889–896, 2009, doi: 10.1039/B814791D.
- [11] J. Fischer, J. B. Mueller, A. S. Quick, J. Kaschke, C. Barner-Kowollik, and M. Wegener, "Exploring the Mechanisms in STED-Enhanced Direct Laser Writing," *Adv. Opt. Mater.*, vol. 3, no. 2, pp. 221–232, 2015, doi: 10.1002/adom.201400413.
- [12] I. Coto Hernández *et al.*, "Two-Photon Excitation STED Microscopy with Time-Gated Detection," *Sci. Rep.*, vol. 6, no. 1, Art. no. 1, Jan. 2016, doi: 10.1038/srep19419.
- [13] R. C. Hilborn, "Einstein coefficients, cross sections, f values, dipole moments, and all that," *Am. J. Phys.*, vol. 50, no. 11, pp. 982–986, Nov. 1982, doi: 10.1119/1.12937.
- [14] S. de Reguardati di Castelfranco, "High-Accuracy Reference Standards for Quantitative Two-Photon Absorption Spectroscopy," 2017. Accessed: Mar. 17, 2023. [Online]. Available: <https://digikogu.taltech.ee/et/item/25608687-730f-4f51-804a-97bfc5c25923>

- [15] J. M. Hales *et al.*, “Resonant enhancement of two-photon absorption in substituted fluorene molecules,” *J. Chem. Phys.*, vol. 121, no. 7, pp. 3152–3160, Aug. 2004, doi: 10.1063/1.1770726.
- [16] A. Rebane, G. Wicks, M. Drobizhev, T. Cooper, A. Trummal, and M. Uudsemaa, “Two-Photon Voltmeter for Measuring a Molecular Electric Field,” *Angew. Chem. Int. Ed Engl.*, vol. 54, no. 26, pp. 7582–7586, Jun. 2015, doi: 10.1002/anie.201502157.
- [17] A. Rebane, M. Drobizhev, N. S. Makarov, E. Beuerman, S. Tillo, and T. Hughes, “New all-optical method for measuring molecular permanent dipole moment difference using two-photon absorption spectroscopy,” *J. Lumin.*, vol. 130, no. 9, pp. 1619–1623, Sep. 2010, doi: 10.1016/j.jlumin.2009.12.005.
- [18] F. Terenziani, A. Painelli, C. Katan, M. Charlot, and M. Blanchard-Desce, “Charge Instability in Quadrupolar Chromophores: Symmetry Breaking and Solvatochromism,” *J. Am. Chem. Soc.*, vol. 128, no. 49, pp. 15742–15755, Dec. 2006, doi: 10.1021/ja064521j.
- [19] *Modern Optical Spectroscopy*. 2007. Accessed: Jun. 03, 2022. [Online]. Available: <https://link.springer.com/book/10.1007/978-3-540-37542-5>
- [20] W. L. Smith, “The Franck–Condon principle, two-photon spectroscopy and the system of benzene,” *J. Mol. Spectrosc.*, vol. 219, no. 2, pp. 227–237, Jun. 2003, doi: 10.1016/S0022-2852(03)00051-1.
- [21] S. S. Andrews, “Using Rotational Averaging To Calculate the Bulk Response of Isotropic and Anisotropic Samples from Molecular Parameters,” *Sci. Educ.*, p. 9, Jun. 2004.
- [22] M. J. Frisch, *et al.*, “Gaussian 09.” Gaussian Inc, Wallingford CT, 2009.
- [23] M. J. Frisch, *et al.*, “Gaussian 16.” Gaussian Inc, Wallingford CT, 2009.
- [24] “Dalton/LSDalton program - Home.” <https://daltonprogram.org/> (accessed May 25, 2022).
- [25] C. Lee, W. Yang, and R. G. Parr, “Development of the Colle-Salvetti correlation-energy formula into a functional of the electron density,” *Phys. Rev. B*, vol. 37, no. 2, pp. 785–789, Jan. 1988, doi: 10.1103/PhysRevB.37.785.
- [26] A. D. Becke, “Density-functional thermochemistry. III. The role of exact exchange,” *J. Chem. Phys.*, vol. 98, no. 7, pp. 5648–5652, Apr. 1993, doi: 10.1063/1.464913.
- [27] M. J. Frisch, J. A. Pople, and J. S. Binkley, “Self-consistent molecular orbital methods 25. Supplementary functions for Gaussian basis sets,” *J. Chem. Phys.*, vol. 80, no. 7, pp. 3265–3269, Apr. 1984, doi: 10.1063/1.447079.
- [28] E. Cancès, B. Mennucci, and J. Tomasi, “A new integral equation formalism for the polarizable continuum model: Theoretical background and applications to isotropic and anisotropic dielectrics,” *J. Chem. Phys.*, vol. 107, no. 8, pp. 3032–3041, Aug. 1997, doi: 10.1063/1.474659.
- [29] B. Mennucci, E. Cancès, and J. Tomasi, “Evaluation of Solvent Effects in Isotropic and Anisotropic Dielectrics and in Ionic Solutions with a Unified Integral Equation Method: Theoretical Bases, Computational Implementation, and Numerical Applications,” *J. Phys. Chem. B*, vol. 101, no. 49, pp. 10506–10517, Dec. 1997, doi: 10.1021/jp971959k.
- [30] E. Runge and E. K. U. Gross, “Density-Functional Theory for Time-Dependent Systems,” *Phys. Rev. Lett.*, vol. 52, no. 12, pp. 997–1000, Mar. 1984, doi: 10.1103/PhysRevLett.52.997.



- [31] T. Yanai, D. P. Tew, and N. C. Handy, "A new hybrid exchange–correlation functional using the Coulomb-attenuating method (CAM-B3LYP)," *Chem. Phys. Lett.*, vol. 393, no. 1–3, pp. 51–57, Jul. 2004, doi: 10.1016/j.cplett.2004.06.011.
- [32] R. L. Martin, "Natural transition orbitals," *J. Chem. Phys.*, vol. 118, no. 11, pp. 4775–4777, Mar. 2003, doi: 10.1063/1.1558471.
- [33] K. Aidas *et al.*, "The Dalton quantum chemistry program system," *WIREs Comput. Mol. Sci.*, vol. 4, no. 3, pp. 269–284, 2014, doi: 10.1002/wcms.1172.
- [34] Y. Wang, Y. Wang, G. Wang, and D. Liu, "Two-photon absorption cross-section results of three tri-branched derivatives: A comparison between open-aperture Z-scan and two-photon excited fluorescence method," *Optik*, vol. 172, pp. 186–190, Nov. 2018, doi: 10.1016/j.ijleo.2018.07.020.
- [35] A. Rebane *et al.*, "Symmetry Breaking in Platinum Acetylide Chromophores Studied by Femtosecond Two-Photon Absorption Spectroscopy," *J Phys Chem A*, p. 11, 2014.
- [36] M. Rumi and J. W. Perry, "Two-photon absorption: an overview of measurements and principles," *Adv. Opt. Photonics*, vol. 2, no. 4, pp. 451–518, Dec. 2010, doi: 10.1364/AOP.2.000451.
- [37] S. de Reguardati, J. Pahapill, A. Mikhailov, Y. Stepanenko, and A. Rebane, "High-accuracy reference standards for two-photon absorption in the 680–1050 nm wavelength range," *Opt. Express*, vol. 24, no. 8, pp. 9053–9066, Apr. 2016, doi: 10.1364/OE.24.009053.
- [38] S. Selberg *et al.*, "Synthesis and photophysics of a series of lipophilic phosphazene-based fluorescent indicators," *J. Phys. Org. Chem.*, vol. 32, no. 7, p. e3950, 2019, doi: <https://doi.org/10.1002/poc.3950>.
- [39] S. Selberg, "Synthesis and properties of lipophilic phosphazene-based indicator molecules," Thesis, 2019. Accessed: May 25, 2022. [Online]. Available: <https://dspace.ut.ee/handle/10062/64821>
- [40] M. Tasiar *et al.*, "Going beyond the borders: pyrrolo[3,2-b]pyrroles with deep red emission," *Chem. Sci.*, vol. 12, no. 48, pp. 15935–15946, Dec. 2021, doi: 10.1039/D1SC05007A.
- [41] Kathryn Lawson-Wood, Steve Upstone, and Kathryn Lawson-Wood, "Determination of Relative Fluorescence Quantum Yields using the FL6500 Fluorescence Spectrometer." PerkinElmer, Inc. Seer Green, UK, 2018.
- [42] C. Würth, M. Grabolle, J. Pauli, M. Spieles, and U. Resch-Genger, "Comparison of Methods and Achievable Uncertainties for the Relative and Absolute Measurement of Photoluminescence Quantum Yields," *Anal. Chem.*, vol. 83, no. 9, pp. 3431–3439, May 2011, doi: 10.1021/ac2000303.
- [43] S. Nad and H. Pal, "Unusual Photophysical Properties of Coumarin-151," *J. Phys. Chem. A*, vol. 105, no. 7, pp. 1097–1106, Feb. 2001, doi: 10.1021/jp003157m.
- [44] A. Trummal, L. Lipping, I. Kaljurand, I. A. Koppel, and I. Leito, "Acidity of Strong Acids in Water and Dimethyl Sulfoxide," *J. Phys. Chem. A*, vol. 120, no. 20, pp. 3663–3669, May 2016, doi: 10.1021/acs.jpca.6b02253.
- [45] M. Rosés, "Determination of the pH of binary mobile phases for reversed-phase liquid chromatography," *J. Chromatogr. A*, vol. 1037, no. 1–2, pp. 283–298, May 2004, doi: 10.1016/j.chroma.2003.12.063.
- [46] F. Rived, M. Rosés, and E. Bosch, "Dissociation constants of neutral and charged acids in methyl alcohol. The acid strength resolution," *Anal. Chim. Acta*, vol. 374, no. 2–3, pp. 309–324, Nov. 1998, doi: 10.1016/S0003-2670(98)00418-8.

- [47] C. Xu and W. W. Webb, "Measurement of two-photon excitation cross sections of molecular fluorophores with data from 690 to 1050 nm," *J. Opt. Soc. Am. B*, vol. 13, no. 3, p. 481, Mar. 1996, doi: 10.1364/JOSAB.13.000481.
- [48] A. de Juan, J. Jaumot, and R. Tauler, "Multivariate Curve Resolution (MCR). Solving the mixture analysis problem," *Anal. Methods*, vol. 6, no. 14, pp. 4964–4976, Jun. 2014, doi: 10.1039/C4AY00571F.
- [49] C. W. Stark *et al.*, "On-off-on Control of Molecular Inversion Symmetry via Multi-stage Protonation: Elucidating Vibronic Laporte Rule," *Angew. Chem. Int. Ed.*, vol. 61, no. 51, Oct. 2022, doi: 10.1002/anie.202212581.
- [50] R. K. P. Benninger and D. W. Piston, "Two-Photon Excitation Microscopy for the Study of Living Cells and Tissues," *Curr. Protoc. Cell Biol. Editor. Board Juan Bonifacio Al*, vol. 0 4, p. Unit-4.1124, Jun. 2013, doi: 10.1002/0471143030.cb0411s59.
- [51] S. L. Jacques, "Optical properties of biological tissues: a review," *Phys. Med. Biol.*, vol. 58, no. 11, p. R37, May 2013, doi: 10.1088/0031-9155/58/11/R37.
- [52] H. Jin, M. Yang, Z. Sun, and R. Gui, "Ratiometric two-photon fluorescence probes for sensing, imaging and biomedicine applications at living cell and small animal levels," *Coord. Chem. Rev.*, vol. 446, p. 214114, Nov. 2021, doi: 10.1016/j.ccr.2021.214114.
- [53] J. Daniel *et al.*, "pK<sub>a</sub> tuning in quadrupolar-type two-photon ratiometric fluorescent membrane probes," *Chem. Commun.*, vol. 51, no. 83, pp. 15245–15248, 2015, doi: 10.1039/C5CC04573H.
- [54] M. H. V. Werts, S. Gmouh, O. Mongin, T. Pons, and M. Blanchard-Desce, "Strong modulation of two-photon excited fluorescence of quadripolar dyes by (de)protonation," p. 13.
- [55] L. Antonov, K. Kamada, D. Nedeltcheva, K. Ohta, and F. S. Kamounah, "Gradual change of one- and two-photon absorption properties in solution—Protonation of 4-N,N-dimethylamino-4'-aminoazobenzene," *J. Photochem. Photobiol. Chem.*, vol. 181, no. 2–3, pp. 274–282, Jul. 2006, doi: 10.1016/j.jphotochem.2005.07.025.
- [56] M. H. V. Werts, S. Gmouh, O. Mongin, T. Pons, and M. Blanchard-Desce, "Strong Modulation of Two-Photon Excited Fluorescence of Quadripolar Dyes by (De)Protonation," *J. Am. Chem. Soc.*, vol. 126, no. 50, pp. 16294–16295, Dec. 2004, doi: 10.1021/ja0446606.
- [57] S. J. K. Pond *et al.*, "Metal-Ion Sensing Fluorophores with Large Two-Photon Absorption Cross Sections: Aza-Crown Ether Substituted Donor–Acceptor–Donor Distyrylbenzenes," *J. Am. Chem. Soc.*, vol. 126, no. 30, pp. 9291–9306, Aug. 2004, doi: 10.1021/ja049013t.
- [58] C. Huang, X. Peng, Z. Lin, J. Fan, A. Ren, and D. Sun, "A highly selective and sensitive two-photon chemosensor for silver ion derived from 3,9-dithia-6-azaundecane," *Sens. Actuators B Chem.*, vol. 133, no. 1, pp. 113–117, Jul. 2008, doi: 10.1016/j.snb.2008.02.010.
- [59] K. P. Divya *et al.*, "A ratiometric fluorescent molecular probe with enhanced two-photon response upon Zn<sup>2+</sup> binding for in vitro and in vivo bioimaging," *Chem Sci*, vol. 5, no. 9, pp. 3469–3474, 2014, doi: 10.1039/C4SC00736K.
- [60] W. Li, B. Fang, M. Jin, and Y. Tian, "Two-Photon Ratiometric Fluorescence Probe with Enhanced Absorption Cross Section for Imaging and Biosensing of Zinc Ions in Hippocampal Tissue and Zebrafish," *Anal. Chem.*, vol. 89, no. 4, pp. 2553–2560, Feb. 2017, doi: 10.1021/acs.analchem.6b04781.

- [61] K. V. Katti *et al.*, “First Examples of Azaphosphanes as Efficient Electron Donors in the Chemical Architecture of Thermally Stable New Nonlinear Optical Materials,” *Chem. Mater.*, vol. 14, no. 6, pp. 2436–2438, Jun. 2002, doi: 10.1021/cm025564b.
- [62] A. Fischer, C. Cremer, and E. H. K. Stelzer, “Fluorescence of coumarins and xanthenes after two-photon absorption with a pulsed titanium–sapphire laser,” *Appl. Opt.*, vol. 34, no. 12, p. 1989, Apr. 1995, doi: 10.1364/AO.34.001989.
- [63] J. P. Hermann and J. Ducuing, “Absolute Measurement of Two-Photon Cross Sections,” *Phys. Rev. A*, vol. 5, no. 6, pp. 2557–2568, Jun. 1972, doi: 10.1103/PhysRevA.5.2557.
- [64] A. C. B. Rodrigues *et al.*, “Bioinspired water-soluble two-photon fluorophores,” *Dyes Pigments*, vol. 150, pp. 105–111, Mar. 2018, doi: 10.1016/j.dyepig.2017.11.020.
- [65] “Phenol.” <https://omlc.org/spectra/PhotochemCAD/html/072.html> (accessed Jan. 02, 2023).
- [66] A. Rebane *et al.*, “Quantitative Prediction of Two-Photon Absorption Cross Section Based on Linear Spectroscopic Properties,” *J. Phys. Chem. C*, vol. 112, no. 21, pp. 7997–8004, May 2008, doi: 10.1021/jp800104q.
- [67] M. Rammo *et al.*, “Novel pH-responsive highly fluorescent lipophilic coumarins as efficient two-photon sensors of acidic and basic environments,” in *Multiphoton Microscopy in the Biomedical Sciences XXI*, A. Periasamy, P. T. So, and K. König, Eds., Online Only, United States: SPIE, Mar. 2021, p. 48. doi: 10.1117/12.2584084.
- [68] G. E. Salnikov, A. M. Genaev, V. G. Vasiliev, and V. G. Shubin, “Interaction of acetonitrile with trifluoromethanesulfonic acid: unexpected formation of a wide variety of structures,” *Org. Biomol. Chem.*, vol. 10, no. 11, p. 2282, 2012, doi: 10.1039/c2ob06841a.
- [69] K. Palmi, “An Investigation of the Self-Association Behaviour of Novel Lipophilic Fluorophores in Acidic Conditions with NMR Spectroscopy,” Tallinn University of Technology, 2022.
- [70] L.-Y. Hsia *et al.*, “ $\pi$ -Extended Coumarins Derived with Nonhydrolyzable Iminophosphoranes as Two-Photon-Excited Fluorophores,” *J. Org. Chem.*, vol. 85, no. 14, pp. 9361–9366, Jul. 2020, doi: 10.1021/acs.joc.0c00901.
- [71] D. H. Friese *et al.*, “Pyrrolo[3,2-*b*]pyrroles-From Unprecedented Solvatofluorochromism to Two-Photon Absorption,” *Chem. - Eur. J.*, vol. 21, no. 50, pp. 18364–18374, Dec. 2015, doi: 10.1002/chem.201502762.
- [72] M. Krzeszewski, D. Gryko, and D. T. Gryko, “The Tetraarylpyrrolo[3,2-*b*]pyrroles—From Serendipitous Discovery to Promising Heterocyclic Optoelectronic Materials,” *Acc. Chem. Res.*, vol. 50, no. 9, pp. 2334–2345, Sep. 2017, doi: 10.1021/acs.accounts.7b00275.
- [73] Y. Zhou *et al.*, “Pyrrolopyrrole aza boron dipyrromethene based two-photon fluorescent probes for subcellular imaging,” *J. Mater. Chem. B*, vol. 6, no. 35, pp. 5570–5581, Sep. 2018, doi: 10.1039/C8TB01832D.
- [74] B. Le Guennic and D. Jacquemin, “Taking Up the Cyanine Challenge with Quantum Tools,” *Acc. Chem. Res.*, vol. 48, no. 3, pp. 530–537, Mar. 2015, doi: 10.1021/ar500447q.
- [75] R. B. Cattell, “The Scree Test For The Number Of Factors,” *Multivar. Behav. Res.*, vol. 1, no. 2, pp. 245–276, Apr. 1966, doi: 10.1207/s15327906mbr0102\_10.

- [76] S. Luňák Jr. *et al.*, "The geometry and absorption of diketo-pyrrolo-pyrroles substituted with various aryls," *Dyes Pigments*, vol. 85, no. 1–2, pp. 27–36, Apr. 2010, doi: 10.1016/j.dyepig.2009.09.014.
- [77] A. Rebane *et al.*, "Symmetry Breaking in Platinum Acetylide Chromophores Studied by Femtosecond Two-Photon Absorption Spectroscopy," *J. Phys. Chem. A*, vol. 118, no. 21, pp. 3749–3759, May 2014, doi: 10.1021/jp5009658.
- [78] T. M. Cooper *et al.*, "Two-Photon Spectroscopy of a Series of Platinum Acetylides: Conformation-Induced Ground-State Symmetry Breaking," *J. Phys. Chem. A*, vol. 121, no. 29, pp. 5442–5449, Jul. 2017, doi: 10.1021/acs.jpca.7b04784.
- [79] A. Mikhaylov *et al.*, "Spontaneous Symmetry Breaking Facilitates Metal-to-Ligand Charge Transfer: A Quantitative Two-Photon Absorption Study of Ferrocene-phenyleneethynylene Oligomers," *J. Phys. Chem. Lett.*, vol. 9, no. 8, pp. 1893–1899, Apr. 2018, doi: 10.1021/acs.jpcllett.8b00525.
- [80] E. Kamarchik and A. I. Krylov, "Non-Condon Effects in the One- and Two-Photon Absorption Spectra of the Green Fluorescent Protein," *J. Phys. Chem. Lett.*, vol. 2, no. 5, pp. 488–492, Mar. 2011, doi: 10.1021/jz101616g.
- [81] J. Bednarska, R. Zalesny, G. Tian, N. A. Murugan, H. Ågren, and W. Bartkowiak, "Nonempirical Simulations of Inhomogeneous Broadening of Electronic Transitions in Solution: Predicting Band Shapes in One- and Two-Photon Absorption Spectra of Chalcones," *Molecules*, vol. 22, no. 10, Art. no. 10, Oct. 2017, doi: 10.3390/molecules22101643.
- [82] A. Klamt, V. Jonas, T. Bürger, and J. C. W. Lohrenz, "Refinement and Parametrization of COSMO-RS," *J. Phys. Chem. A*, vol. 102, no. 26, pp. 5074–5085, Jun. 1998, doi: 10.1021/jp980017s.
- [83] A. Klamt, "Conductor-like Screening Model for Real Solvents: A New Approach to the Quantitative Calculation of Solvation Phenomena," *J. Phys. Chem.*, vol. 99, no. 7, pp. 2224–2235, Feb. 1995, doi: 10.1021/j100007a062.
- [84] D. Augustin-Nowacka, M. Makowski, and L. Chmurzynski, "Acid–base equilibria in systems involving substituted pyridines in polar aprotic protophobic media and in the amphiprotic methanol," *Anal. Chim. Acta*, vol. 418, no. 2, pp. 233–240, Aug. 2000, doi: 10.1016/S0003-2670(00)00967-3.
- [85] J. J. Christensen, L. D. Hansen, and R. M. Izatt, *Handbook of Proton Ionization Heats and Related Thermodynamic Quantities*. Wiley, 1976.
- [86] R. W. Boyd, *Nonlinear Optics*. Elsevier, 2003, pp 553-555.
- [87] A. Aubret, M. Orrit, and F. Kulzer, "Understanding Local-Field Correction Factors in the Framework of the Onsager–Böttcher Model," *ChemPhysChem*, vol. 20, no. 3, pp. 345–355, 2019, doi: 10.1002/cphc.201800923.
- [88] D. J. Skowron, Y. Zhang, A. A. Beckstead, J. M. Remington, M. Strawn, and B. Kohler, "Subnanosecond Emission Dynamics of AT DNA Oligonucleotides," *ChemPhysChem*, vol. 17, no. 21, pp. 3558–3569, 2016, doi: 10.1002/cphc.201600566.
- [89] J. R. Lakowicz, Ed., *Principles of Fluorescence Spectroscopy*. Boston, MA: Springer US, 2006. doi: 10.1007/978-0-387-46312-4.
- [90] J. A. Gardecki and M. Maroncelli, "Set of Secondary Emission Standards for Calibration of the Spectral Responsivity in Emission Spectroscopy," *Appl. Spectrosc.*, vol. 52, no. 9, pp. 1179–1189, Sep. 1998, doi: 10.1366/0003702981945192.
- [91] K. Petritšenko, "Two-photon absorption spectroscopy study of centrosymmetric metalloporphyrins: Shedding light on the elusive one-photon parity-forbidden transitions," Tallinn University of Technology, 2021.

- [92] A.-W. Naumann, E. R., G. J., and S. P., "Traceability of pH measurements by glass electrode cells: performance characteristic of pH electrodes by multi-point calibration," *Anal. Bioanal. Chem.*, vol. 374, no. 5, pp. 778–786, Nov. 2002, doi: 10.1007/s00216-002-1506-5.
- [93] C. Yang *et al.*, "N-Monoalkylated 1,4-diketo-3,6-diphenylpyrrolo[3,4-c]pyrroles as effective one- and two-photon fluorescence chemosensors for fluoride anions," *J. Mater. Chem. A*, vol. 1, no. 16, p. 5172, 2013, doi: 10.1039/c3ta00160a.

## **Acknowledgements**

I would like to express my heartfelt gratitude to our entire research group. I am much thankful to my supervisors Prof. Aleksander Rebane, for his support and the opportunity to work and learn in his group. I am very grateful to my co-supervisor, Dr. Charles William Stark, who has helped me a lot on this journey and by whom I have the opportunity to learn so much by working next to him. Many thanks also to Dr. Meelis-Mait Sildoja, who has also been a great help, without whom it would probably have been difficult to keep our measurement system running. I would also like to thank Jüri Pahapill, who was very helpful with his common sense and long-term experience. And last but certainly not least, I would like to thank Dr. Merle Uudsemaa and Dr. Aleksander Trummal, who performed our quantum chemical calculations.

## Abstract

### Two-photon spectroscopy as a new quantitative protonation probe

Two photon spectroscopy is the study of the interaction of matter with two simultaneous photons, as a function of photon wavelengths. Since the invention of the laser, research interest in this nonlinear optics subfield has grown exponentially, with its uses progressing from detecting traditionally forbidden optical transitions to modern improved microscopy, photodynamic therapy, and commercial 3D printing. These current applications, as well as others that are still in the future, rely on fundamental research in the field of 2PA, both in the design of molecular probes tailored to produce specific 2PA effects, as well as the design of 2PA spectrometers to measure these effects efficiently. This dissertation uses a custom-built femtosecond 2PA spectrometer, with two-photon-induced fluorescence-based technique, combined with established high accuracy 2PA reference standards to investigate novel purpose-synthesized molecules.

The first set consists of four novel fluorophores, based on a coumarin core structure, made lipophilic with a covalently attached phosphazene moiety. They could be potentially used as membrane-specific ratiometric probes, combining the high brightness of two-photon excited fluorescence with pH sensitivity. Changing the environmental acidity using trifluoromethanesulfonic (triflic) acid leads to profound changes in the linear fluorescence and 2PEF characteristics due to chromophores' switching between neutral- and protonated forms. Coumarin derivatives are characterized by measuring the two-photon absorption (2PA) spectra over the region  $\lambda_{2PA} = 550 - 1000$  nm, observing 2PA cross-sections of  $\sigma_{2PA} = 10 - 20$  GM, with associated 2PEF brightness of  $10 - 13$  GM, in neutral solutions of both acetonitrile and *n*-octanol. Corresponding acidic forms each show a decrease in 2PA cross-section and brightness. An interesting mismatch between 1PA and 2PA spectra of protonated forms is observed and several hypotheses are investigated but a definite explanation of the origin is not reached. In addition, 2PA high-quality spectra of the coumarin 151 in acetonitrile and *n*-octanol solvents are provided.

The second set studies novel symmetric pyrrolopyrroles. Multistage protonation is used in one system, a bis-pyridinyldiketopyrrolopyrrole (PDP), to switch inversion symmetry off and on. The corresponding changes in selection rules result in a nearly tenfold change in absorption cross-section for 2PA. In addition to this symmetry switching, the vibronic contributions to the allowed- or forbidden-transition demonstrate clear trends. Combined with quantum chemical calculations, the small 2PA signals observed for symmetric forms are shown to originate primarily from Herzberg-Teller coupled vibrational modes which break the molecular symmetry. Understanding these mechanisms allows for the rational design of new symmetry-switching probes, while at the same time, the strong correlation between 2PA and solution pH creates opportunities to use optical measurements to quantitatively monitor pH using the PDP molecule.

## Lühikokkuvõte

### Kahefotoonne neeldumisspektroskoopia kui uus kvantitatiivne protoneerimise sond

Kahefotoonses neeldumisspektroskoopias on toimunud pidev areng, hõlmates nii mõõtmistehnikaid, aparatuuri kui ka tulemuste tõlgendamise ja mõistmise võimekust. Nüüdseks on jõutud tasemele, kus selles, kiiresti arenevas valdkonnas ei tehta ainult fundamentaalset teadustööd -kahefotoonsel neeldumisel põhinevaid praktilisi rakendusi kasutatakse igapäevaselt näiteks elusrakkude mikroskoopias, meditsiinilistes rakendustes, nagu fototeraapia, ning isegi kaubanduslikes 3D-printerites.

Käesolevas väitekirjas kasutatakse mõõtmisteks kauaaegse arendustöö tulemusena KBFI mittelineaarse optika laboris valminud femtosekund laseril põhinevat kahefotoonse neeldumise (2PA) spektromeetrit, mis registreerib kahefotoonse neeldumise poolt indutseeritud fluorestsentsi. Mõõtmistulemuste kalibreerimisel lähtutakse laboris eelnevalt suure täpsusega mõõdetud 2PA referentsstandarditest. Väitekirjas käsitletakse kahte hiljuti sünteesitud molekulide rühma. Seejuures on uurimistöo fookuses protoneerumisest põhjustatud muutused kahefotoonsetes neeldumisspektrites.

Esimene ainerühm koosneb neljast uudsest molekulist, mis on sünteesitud kumariin-151 baasil. Saadud ained on kovalentselt seotud fosfaaseni fragmenti tõttu lipofiilsed ja seetõttu võib neid potentsiaalselt kasutada raku membraanispetsiifiliste sondidena, mille omadused väljenduvad nii kahefotoonselt ergastatud fluorestsentsi (2PEF) kõrge heleduse kui ka tundlikkusena keskkonna happelisuse suhtes. Uuritava värvaine lahusele trifluorometaansulfoonhappe lisamine põhjustab märkimisväärsed muutusi ühefotoonselt ergastatud fluorestsentsi ja 2PEF-i omadustes kromofoori protoneerumise tõttu. Kumariini derivaatide kahefotoonsed neeldumisspektrid mõõdeti  $\lambda_{2PA} = 550 - 1000$  nm vahemikus, ning neutraalse vormi puhul saadud maksimaalsed 2PA ristlõiked olid  $\sigma_{2PA} = 10 - 20$  GM, nendele vastav 2PEF heledus oli 10 – 13 GM. Mõõtmised teostati nii atsetonitrili kui ka n-oktanolis keskkonnas. Happeliste vormide puhul täheldati nii 2PA ristlõikete kui ka heleduse olulist vähenemist. Märkimisväärne oli ka protoneeritud vormide 1PA ja 2PA spektrikujude omavaheline erinevus. Lisaks mõõdeti ja esitati sünteesi lähteaineks olnud kumariin-151 2PA ristlõike kõrgekvaliteetsed spektrid atsetonitrilis ja n-oktanolis.

Töö teises osas uuritakse modifitseeritud sümmeetrilisi pürrolopürroole. Spetsiifilisemalt keskendutakse ühele diketopürrolopürroolile ning uuritakse mitmeastmelist protoneerimist. Ühekordsel protoneerimisel kaotab molekul oma esialgse sümmeetria, mille tulemusena suureneb varem Laporte valikureeglga keelatud madalaima energiaga elektroonse ülemineku 2PA ristlõige kümme korda ning eelnevalt erinevad 2PA ja 1PA spektraalsed kujud kattuvad. Teistkordsel protoneerimisel sümmeetria taastub, ning mõõdetud 2PA spektrid on väga sarnased neutraalsele vormile. Mõlema sümmeetrilise vormi puhul on märgata nõrka kahefotoonset neeldumist keelatud ülemineku piirkonnas. Koos mõõtmistulemusi toetavate kvantkeemiliste arvutustega näidatakse, et väikesed 2PA signaalid pärinevad peamiselt Herzberg-Telleri seostuse kaudu vibratsioonimoodidest, mis rikuvad molekulaarset sümmeetriat. Lisaks loob avastatud tugev korrelatsioon tiitrimisspektri dekompositsiooni teel saadud astmelist protoneerimist iseloomustavate pH väärtuste ja mõõdetud 2PA spektrite vahel võimaluse kasutada optilisi mõõtmisi keskkonna pH kvantitatiivse määramise rakendustes.





## Appendix 1

### Publication I

Rammo, M.; Trummal, A.; Uudsemaa, M.; Pahapill, J.; Petritsenko, K.; Sildoja, M.-M.; Stark, C. W.; Selberg, S.; Leito, I.; Palmi, K.; Adamson, J.; Rebane, A., "Novel Lipophilic Fluorophores with Highly Acidity-Dependent Two-Photon Response," *Chem. – Eur. J.*, vol. 28, no. 8, p. e202103707, 2022.



# Novel Lipophilic Fluorophores with Highly Acidity-Dependent Two-Photon Response

Matt Rammo,<sup>[a]</sup> Aleksander Trummal,<sup>[a]</sup> Merle Uudsemaa,<sup>[a]</sup> Juri Pahapill,<sup>[a]</sup> Katrin Petritsenko,<sup>[a]</sup> Meelis-Mait Sildoja,<sup>[a]</sup> Charles W. Stark,<sup>[a]</sup> Sigrid Selberg,<sup>[b]</sup> Ivo Leito,<sup>\*,[b]</sup> Kirsti Palmi,<sup>[a]</sup> Jasper Adamson,<sup>[a]</sup> and Aleksander Rebane<sup>\*,[a, c]</sup>

**Abstract:** Lipophilic fluorophores are widely implemented in nonlinear microscopy; however, few existing membrane-specific probes combine the high brightness of two-photon excited fluorescence (2PEF) with pH sensitivity. Herein we describe four novel two-photon excited fluorophores, based on a coumarin 151 core structure, where lipophilicity is induced by a covalently attached phosphazene moiety. Changing the environmental acidity using trifluoromethanesulfonic (triflic) acid leads to profound changes in the linear fluorescence and 2PEF characteristics, due to chromophores' switching between neutral- and protonated forms. We

characterize this dependence by measuring the two-photon absorption (2PA) spectra over the region  $\lambda_{2PA} = 550\text{--}1000$  nm, observing 2PA cross sections of  $\sigma_{2PA} = 10\text{--}20$  GM, with an associated 2PEF brightness of 10–13 GM, in neutral solutions of both acetonitrile and *n*-octanol. Although quantum chemical modelling and NMR measurements show that, at high chromophore concentrations, protonation may be accompanied by a dimerization process, these dimers likely do not form at the lower concentrations used in optical spectroscopy.

## Introduction

Advances in non-linear fluorescence excitation microscopy are increasingly dependent on developing specialized fluorophores to perform specific reporting, such as quantifying pH values or monitoring other ionic species inside- or in the vicinity of cell membranes, combined with an exemplary multiphoton brightness and photostability. While a number of pH-sensing lipophilic probes have been established for linear photoexcitation,<sup>[1,2]</sup> there are only a limited number of examples that display high 2PEF-brightness.<sup>[3]</sup>

While 2PEF techniques offer benefits compared to linear microscopy techniques in terms of tissue penetration depth and three-dimensional resolution,<sup>[4]</sup> one reason for the relative scarcity of probes is that nonlinear photophysical properties are


difficult to quantify. In pH-sensing lipophilic dyes, this pronounced lack of photophysical characterization can lead to instances where changing local environments may be misinterpreted as changes in pH.<sup>[5]</sup> In order to have a probe that is robust to such environmental effects such as solvent polarity, hydrogen bonding, or aggregation behavior, fundamental research of a probes 2PA cross section, absorption wavelength, and quantum yield should be accurately determined, as well as how these photophysical parameters are affected by local conditions. Ideally, observed spectral changes should be conspicuously large in accordance with pH, but minimal for all other measured factors.

We have recently reported on the synthesis of a series of novel fluorophores, where the high lipophilicity is achieved by conjugating various phosphazene moieties to a coumarin 151 core, and where the solvent acidity-dependent linear absorption- and fluorescence spectral characteristics change in a ratiometric manner upon switching between the fluorophore's neutral- and protonated forms.<sup>[6,7]</sup> Based on one-photon photometric titration measurements,<sup>[6]</sup> it was estimated (from  $pK_a$  values in ACN as described in Ref. [8]) that the aqueous  $pK_a$  values of these compounds are 6.8–9.3 units while biphasic (*n*-octanol/water)  $pK_a$  values (see Ref. [9]) are lower, at 1.8–5.9 units. However, one should note that biphasic  $pK_a$  values strongly depend on the used counterion as discussed in Ref. [9] and respective values are expected to be somewhat higher in case of  $Cl^-$  replacement with  $SO_4^{2-}$ . The fact that the high lipophilicity of these systems both in protonated/deprotonated forms is characterized by favorable partition coefficient values in *n*-octanol/water and in toluene/water systems, in the range of 5.9–6.6 and 4.0–7.3 log*P* units, respectively, renders these C151-based structures suitable as membrane-specific acidity

[a] M. Rammo, Dr. A. Trummal, Dr. M. Uudsemaa, J. Pahapill, K. Petritsenko, Dr. M.-M. Sildoja, Dr. C. W. Stark, K. Palmi, Dr. J. Adamson, Prof. A. Rebane  
Laboratory of Chemical Physics  
National Institute of Chemical Physics and Biophysics  
23, Akadeemia tee, 12618 Tallinn (Estonia)  
E-mail: arebane@montana.edu

[b] Dr. S. Selberg, Prof. I. Leito  
Institute of Chemistry  
University of Tartu  
14a Ravila st, 50411 Tartu (Estonia)  
E-mail: ivo.leito@ut.ee

[c] Prof. A. Rebane  
Department of Physics  
Montana State University  
Bozeman, MT 59717 (USA)  
E-mail: arebane@montana.edu

 Supporting information for this article is available on the WWW under <https://doi.org/10.1002/chem.202103707>

probes for linear fluorescence excitation microscopy.<sup>[10–13]</sup> In addition, the pH transition range of these compounds is easily tunable by modifying the structure of the phosphazene moiety.

Here, we extend spectroscopic investigations of the above chromophoric series into the nonlinear-optical regime of 2PA. For this, we use broadly wavelength-tunable femtosecond laser pulses in the range,  $\lambda_{2PA} = 550\text{--}1000\text{ nm}$ , to quantify the 2PA cross sections and 2PA spectra, associated 2PEF brightness as well as emission quantum yield in acetonitrile and *n*-octanol solutions of varying acidity, controlled by addition of trifluoromethanesulfonic (triflic) acid. We perform comprehensive quantum chemical calculations using a time-dependent density functional theory (TD-DFT) approach to evaluate both the linear- and nonlinear spectroscopic parameters, such as the 1PA and 2PA transition wavelengths, along with transition cross sections of fluorophores in solvents represented by a polarized continuum. By comparing the calculations with the experimental results, we are able to reveal how key photophysical characteristics depend on different solvent/acid environments as well as different lipophilic moieties, thus establishing, for the first time, a quantitative structure-property relationship between the chromophores' structure, its two-photon activity and its potential to serve as a membrane-specific acidity probe. Moreover, we use the fact that, in the neutral form, the 2PEF transition energy spectral profile of the lowest-energy singlet electronic-vibrational band follows closely that of the corresponding 1PA spectral profile, which we use to determine the change of the permanent dipole moment upon the transition from the ground state ( $\Delta\mu$ ).<sup>[14]</sup> While the protonation enacts similar hypsochromic shifts, both in the 1PA and 2PA spectra, along with lowering of the permanent dipole moment change, this also leads to a slight mismatch between the spectral profiles. The latter observation is interpreted as a possible indication of presence of protonated fluorophore's dimers, and is evaluated by measuring the NMR spectra and by quantum chemical calculations.

## Results and Discussion

Chemical structures of coumarin 151 (C151) and its 7-phosphazene derivatives (C1, C2, C3 and C4) are shown in Figure 1. Each compound was studied in acetonitrile (ACN) and *n*-octanol solutions, under neutral (neat solvent) or acidic conditions, where the acidity was controlled by addition of triflic acid. The named pair of solvents are chosen to emulate both polar as well as biphasic or lipid bilayer environments.<sup>[9,15,16]</sup>

Figure 2 presents the 2PA cross section spectra (left vertical axis, in units of Goepfert-Mayer,  $1\text{ GM} = 10^{-50}\text{ cm}^4\text{ s photon}^{-1}$ ) of the four C151-derivatives, C1–C4, along with the parent chromophore, measured in the wavelength range,  $\lambda_{2PA} = 550\text{--}1000\text{ nm}$ . Using the fluorescence excitation method,<sup>[7]</sup> 2PA was measured at each excitation wavelength, with an evaluated quadratic dependence of the fluorescence on incident photon flux of  $2.0 \pm 0.05$ . The samples were dissolved in neat acetonitrile (blue symbols) and in acetonitrile with  $\sim 0.3\text{ M}$  triflic

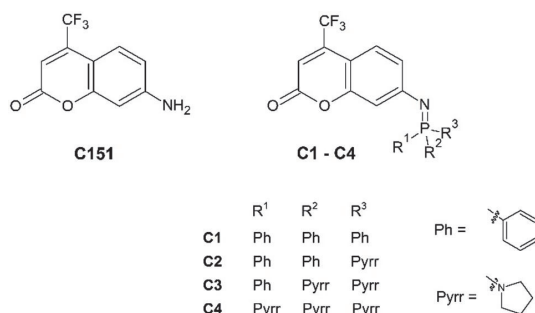


**Figure 1.** Chemical structures of parent coumarin C151 and its four phosphazene derivatives, C1, C2, C3 and C4, studied in this work.

acid (red symbols). The corresponding linear molar absorptivity (right outer vertical axis) in the neutral (blue line) and acidic (red line) acetonitrile are shown for comparison, such that the 1PA wavelength (upper horizontal axis) has calibration,  $\lambda_{1PA} = \frac{1}{2}\lambda_{2PA}$ . In the neutral acetonitrile spectra, the main absorption band is due to the  $S_0 \rightarrow S_1$  dipole-allowed transition, and is located for 2PA and 1PA at 740–800 nm and 370–400 nm, respectively.

Compared to the parent C151, the phosphazene-modified structures display a marked 60–80 nm red-shift of the 2PA peak (30–40 nm in 1PA). Similar shifts have been observed for phosphazene modifications in other systems.<sup>[17]</sup> Most importantly, the red shift is accompanied by an increase of the peak 2PA cross section by a factor of 2–3. These observations, along with the facts that derivatization increases the peak molar extinction coefficient by  $\sim 20\text{--}50\%$ , and that larger absorption red shifts are observed with increasing the number of attached pyrrolidines, indicate that, in the neutral form, the modified structures have an extended conjugation compared to C151.

This conclusion is corroborated by our quantum-chemically calculated transition wavelengths, oscillator strengths and 2PA peak cross sections, which match quantitatively with the experimental values, as shown in Table 1. We refer to Ref. [7] for computational details, and the calibration of the CAM-B3LYP density functional in Ref. [18]. The spectra in Figure 2 show that, in addition to the  $S_0 \rightarrow S_1$  transition, which appears, with closely matching shapes, both in 2PA and 1PA, there exists a distinct two-photon allowed transition at 600–630 nm. The fact that this transition is not readily identifiable with any feature in the corresponding higher-energy portion of the 1PA spectra, aligns well with previous observations reported for related coumarins.<sup>[19]</sup>

Addition of triflic acid causes the main 1PA band to shift hypsochromically by as much as  $\sim 75\text{ nm}$ , while, at the same time, its peak extinction coefficient decreases by  $\sim 20\text{--}30\%$ . Note that, as will be discussed in more detail below, exact determination of photophysical parameters for the protonated form was complicated by an unusual mismatch of 1PA and 2PA spectra at long wavelengths. Consequently, only estimated values are given in Table 1. We also note that the fluorescence

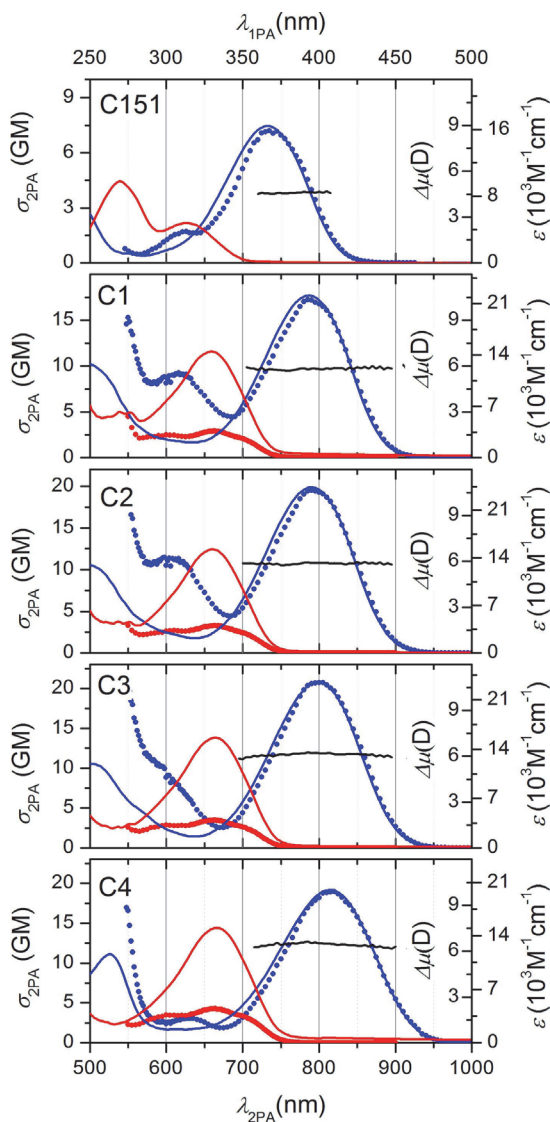


**Figure 2.** Dependence of 2PA cross section (symbols) and 1PA molar extinction (lines) on the wavelength of the parent C151 and C1–C4, in neutral (neat) acetonitrile (blue) and in acetonitrile with ~0.3 M of triflic acid (red). Black lines represent the molecular permanent electric dipole moment estimated for the neutral form.

emission was considerably reduced by the protonation, and in case of C151 the emission was nearly completely quenched, thus complicating, in the latter case, the determination of 2PA. Further details regarding the fluorescence behavior will be described below. The maximum 2PA wavelength for protonated C1–C4 also shifts by respective amount, ~150 nm, while the peak  $\sigma_{2\text{PA}}$  value decreases, from 17–19 GM in the neutral solvent, to ~3–4 GM in the acidic environment. Together, these

trends indicate that, upon protonation, some of the conjugation pathways are reduced. This conclusion is again confirmed by our model calculations, which yield the protonated peak transition wavelengths, oscillator strengths and 2PA cross sections, in agreement with the estimated experimental values, as collected in Table 1.

Figure 3 shows the corresponding 2PA and 1PA spectra of C151 and C1–C4 measured in neutral and acidic *n*-octanol, which is often used as a suitably approximate representation

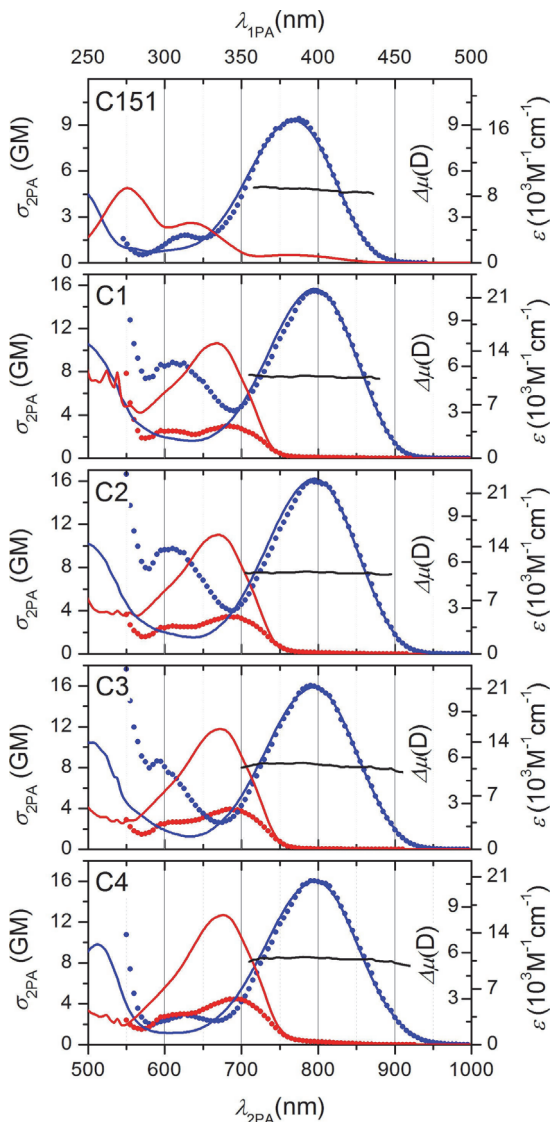


**Figure 3.** 1PA (blue and red lines) and 2PA (blue and red symbols) spectra of the four lipophilic derivatives, C1–C4, in neutral (neat) *n*-octanol (blue) and in *n*-octanol with the addition of triflic acid (red). Black lines are the molecular permanent electric dipole moment estimated for the neutral form.

**Table 1.** Summary of the experimental and calculated 1PA and 2PA parameters for the studied compounds in neutral- and acidic acetonitrile and *n*-octanol.

| Compound          | $\lambda_{1PA}$ , nm |          | $\epsilon_{M}$ , M <sup>-1</sup> cm <sup>-1</sup> | $\sigma_{2PA}$ , GM |                   | $\delta_{2PA}$ | $\Delta\mu$ , D |          |
|-------------------|----------------------|----------|---|---------------------|-------------------|----------------|-----------------|----------|
|                   | Expt.                | Calc.    |   | Expt.               | Calc.             |                | Expt.           | Calc.    |
| acetonitrile      |                      |          |   |                     |                   |                |                 |          |
| C151              | 366                  | 366      | 16400   | 7 (735)             | 8 <sup>[a]</sup>  | 2632           | 4.5             | 6.6      |
| C1                | 393                  | 396      | 22100   | 17 (785)            | 16 <sup>[b]</sup> | 5459           | 5.8             | 6.5      |
| C2                | 395                  | 400      | 24400   | 19 (790)            | 15 <sup>[b]</sup> | 5296           | 5.9             | 6.4      |
| C3                | 399                  | 400      | 23500   | 21 (805)            | 18 <sup>[c]</sup> | 6508           | 6.2             | 7.5      |
| C4                | 407                  | 406      | 20000   | 19 (820)            | 23 <sup>[d]</sup> | 8403           | 6.5             | 8.3      |
| C151-PROT         | 314, 270             | 309, 271 | 4800, 9800  | –                   | –                 | 92, 131        | –               | 3.4, 4.9 |
| C1-PROT           | 330                  | 328      | 14500   | 3 (664)             | 6 <sup>[e]</sup>  | 2085           | 3               | 4.8      |
| C2-PROT           | 330                  | 329      | 15300   | 3 (663)             | 6 <sup>[f]</sup>  | 1901           | 3               | 4.8      |
| C3-PROT           | 332                  | 330      | 15600   | 4 (664)             | 7 <sup>[f]</sup>  | 2023           | 3               | 5.2      |
| C4-PROT           | 333                  | 331      | 15000   | 4 (664)             | 7 <sup>[g]</sup>  | 2416           | 4               | 5.6      |
| <i>n</i> -octanol |                      |          |   |                     |                   |                |                 |          |
| C151              | 383                  | 365      | 17044   | 9.4 (775)           | 8 <sup>[a]</sup>  | 2878           | 4.9             | 6.3      |
| C1                | 397                  | 397      | 22100   | 16 (795)            | 16 <sup>[b]</sup> | 5557           | 5.3             | 6.1      |
| C2                | 398                  | 400      | 22900   | 16 (795)            | 15 <sup>[b]</sup> | 5474           | 5.3             | 6.0      |
| C3                | 397                  | 401      | 21100   | 16 (795)            | 20 <sup>[c]</sup> | 6959           | 5.5             | 7.2      |
| C4                | 398                  | 406      | 20400   | 16 (795)            | 25 <sup>[d]</sup> | 9007           | 5.6             | 8.0      |
| C151-PROT         | 316, 276             | 308, 269 | 4773, 8959  | –                   | –                 | 84, 123        | –               | 3.0, 4.3 |
| C1-PROT           | 334                  | 327      | 15000   | 3 (685)             | 6 <sup>[e]</sup>  | 1858           | 3               | 4.4      |
| C2-PROT           | 335                  | 328      | 15600   | 4 (685)             | 6 <sup>[f]</sup>  | 1765           | 3               | 4.4      |
| C3-PROT           | 336                  | 329      | 15700   | 4 (685)             | 6 <sup>[f]</sup>  | 1914           | 4               | 4.7      |
| C4-PROT           | 338                  | 329      | 16200   | 5 (695)             | 7 <sup>[g]</sup>  | 2269           | 4               | 5.2      |

2PA FWHM [a] 0.282 eV; [b] 0.248 eV; [c] 0.249 eV; [d] 0.250 eV; [e] 0.336 eV; [f] 0.317 eV; and [g] 0.332 eV.

of lipid environments. Upon protonation, the 2PA maximum blue-shifts by ~110 nm, accompanied by a decrease in the 2PA cross section, similar to that in acidic acetonitrile. Closer comparison of the spectra in Figures 3 and 2 reveals several additional interesting trends. Firstly, while solvation in *n*-octanol red shifts the peak 2PA wavelength of C151 by ~60 nm compared to acetonitrile, the modified compounds show much smaller environmental variation, each displaying shifts in peak positions <25 nm. Secondly, the peak 2PA wavelength,  $\lambda_{2PA}=795$  nm (397 nm for 1PA) in neutral *n*-octanol essentially coincides for C1–C4, and no longer depends on the substituents, as was the case in acetonitrile. Thirdly, the 1PA spectrum of the protonated C1–C4 shows, in both solvents, in the short wavelength region,  $\lambda_{1PA}=260$ –280 nm, features that closely resemble the vibronic progression of the lowest-energy dipole-allowed transition of independently-dissolved phenyl rings,<sup>[20]</sup> indicating that, under certain conditions, the phenyl rings may behave as if they are excluded from the overall conjugation pattern. While in acetonitrile these features decrease in amplitude with decreasing count of the phenyl rings attached to the phosphorus atom, in *n*-octanol such dependence is not observed.

Finally, the peak 2PA cross sections of C1–C4 obtained in neutral *n*-octanol have constant value,  $\sigma_{2PA}=16$  GM, whereas in acetonitrile a distinct dependence on the varying substituents is observed. From this we surmise that, as already evidenced by the  $pK_a$ , solvent interaction with the phosphazene moieties appears to have a marked effect on the lipophilic fluorophore's linear- and two-photon properties. In addition to the main absorption band, each modified compound displays a higher energy 2PA peak, ~600 nm, which also becomes more pronounced due to reduced

spectral broadening in *n*-octanol compared to acetonitrile and can be observed clearly for C3.

Figure 4 displays the one-photon excitation spectra and one-photon excited fluorescence spectra, measured in acetonitrile and *n*-octanol, for both neutral and protonated forms. Emission spectra were excited at maximum 1PA wavelengths listed in Table 1, while excitation spectra were collected at corresponding fluorescence emission peak wavelengths listed in Table 2. Figure 4 highlights that protonation-induced hypsochromic shift in the absorption and emission maxima is more pronounced in *n*-octanol. It is interesting to

**Table 2.** Summary of the experimental fluorescence emission wavelengths, emission quantum yields and two-photon brightness values.

| Compound          | $\lambda_{em}$ , nm | $\phi_{em}$ | $\sigma_{2PA}\phi_{em}$ <sup>[a]</sup> |
|-------------------|---------------------|-------------|--|
| acetonitrile      |                     |             |  |
| C151              | 463                 | 0.57        | 4.0                                    |
| C1                | 487                 | 0.65        | 11                                     |
| C2                | 492                 | 0.65        | 12                                     |
| C3                | 508                 | 0.62        | 13                                     |
| C4                | 519                 | 0.54        | 10                                     |
| C151-PROT         | 411                 | 0.02        | 0.06                                   |
| C1-PROT           | 411                 | 0.02        | 0.07                                   |
| C2-PROT           | 411                 | 0.02        | 0.06                                   |
| C3-PROT           | 412                 | 0.04        | 0.16                                   |
| C4-PROT           | 413                 | 0.06        | 0.24                                   |
| <i>n</i> -octanol |                     |             |  |
| C1                | 489                 | 0.74        | 11.5                                   |
| C2                | 495                 | 0.72        | 11.6                                   |
| C3                | 506                 | 0.71        | 11.4                                   |
| C4                | 514                 | 0.64        | 10.3                                   |
| C1-PROT           | 403.5               | 0.12        | 0.39                                   |
| C2-PROT           | 412                 | 0.09        | 0.32                                   |
| C3-PROT           | 415                 | 0.10        | 0.34                                   |
| C4-PROT           | 417                 | 0.13        | 0.50                                   |

[a] Two-photon brightness.



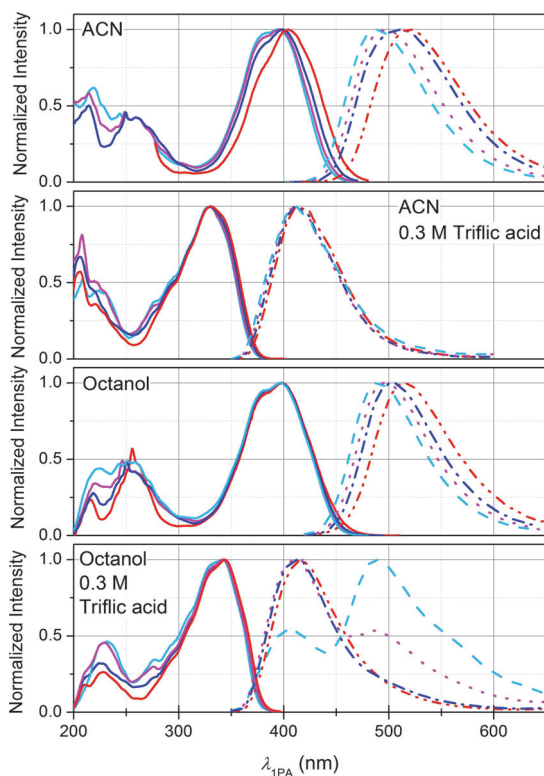


**Figure 4.** Normalized excitation (solid lines) and emission spectra (dashed lines) for C1 (cyan), C2 (magenta), C3 (blue) and C4 (red) in acetonitrile and *n*-octanol. For each respective solvent, upper plots are observed for compounds in neutral (neat) solvent, while lower plots include an addition of triflic acid.

note that the emission spectra of compounds in acidic *n*-octanol display what appears as a vibronic second peak at  $\sim 480$  nm, whose relative amplitude appears to correlate with the count of attached phenyl groups. The 480 nm emission bands may also indicate an additional excited state deactivation pathway involving a proton transfer mechanism, as previous studies also observed complex photophysical kinetics for protonated C2 after excitation in acetonitrile.<sup>[7]</sup> However, if such behavior is present in acetonitrile, it is much less obvious.

Protonation, as well as the solvent, have a profound effect not only on the wavelength, but also on efficiency of the fluorescence emission. The fluorescence quantum yield, measured against emission standards of C153 in ethanol,  $\phi_{em} = 0.53$ ,<sup>[21]</sup> and C151,  $\phi_{em} = 0.57$ ,<sup>[22]</sup> along with corresponding 2PEF brightness values, are collected in Table 2. The values of quantum yield and 2PEF brightness for C1–C4 in the neutral solvents are relatively high,  $\phi_{em} = 0.6–0.7$ , and,  $\sigma_{2PA} \cdot \phi_{em} = 10–13$  GM, making them comparable to yields observed by Luo et al.<sup>[23]</sup> for similar phosphazene-modified coumarin compounds, although this emission drops upon

protonation. In acetonitrile, the drop is considerable, down to,  $\phi_{em} = 0.02–0.06$ , and,  $\sigma_{2PA} \cdot \phi_{em} = 0.06–0.24$  GM, while in *n*-octanol the values still remain relatively high,  $\phi_{em} = 0.09–0.13$ , and,  $\sigma_{2PA} \cdot \phi_{em} = 0.3–0.5$  GM. Again, the effect of solvent on the fluorescence efficiency, displayed most evidently for C1, appears to trend along with the number of phenyl groups attached to the phosphazene.

In the neutral environments, all systems studied show a very close match between the 2PA and 1PA spectral profiles, which is characteristic of strongly dipolar chromophores.<sup>[24]</sup> However, in acidic solutions, this correspondence becomes more involved. As an example, Figure 5 displays the side-by-side comparison of 1PA and 2PA spectra for C2 in acidic solutions, along with computed 1PA electronic transition wavelengths and oscillator strengths. In acetonitrile (upper plot), two overlapping 2PA bands are observed, with the maxima at 605 and 663 nm, accompanied by a shoulder near 705 nm. In the case of *n*-octanol (lower plot), the two distinct bands are even more separated, while the shoulder is likely already merging with the longer-wavelength component. Even though the 1PA spectrum in *n*-octanol also appears to display a low-energy shoulder, in acetonitrile such feature is practically absent, meaning that close correspondence between the 2PA and 1PA spectral profiles does not apply here. According to our calculations, with corresponding 1PA electronic transitions shown as magenta bars in Figure 5, these low-energy spectral differences cannot be assigned to a (0,0) component of the vibronic progression of  $S_0 \rightarrow S_1$ , because the entire vibronic envelope must be placed at notably shorter wavelengths than the red component of the experimental spectrum.<sup>[7]</sup> Because of that, we evaluate an alternative explanation using NMR spectroscopy along with some further theoretical modelling, as described below.

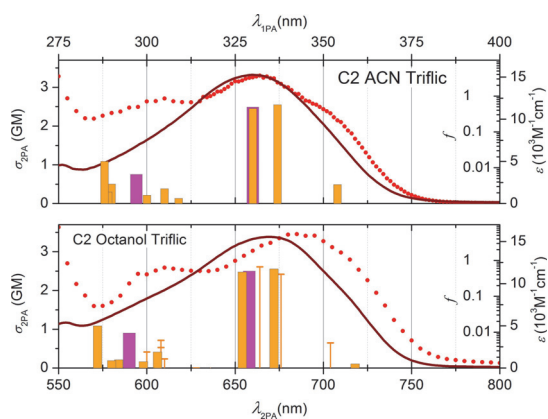


**Figure 5.** Expanded view of the experimental 1PA (line) and 2PA (red symbols) spectra for C2 with 0.3 M triflic acid, in acetonitrile and *n*-octanol, compared to calculated wavelengths and oscillator strengths ( $f$ ) of electronic transitions for the monomer (magenta) and dimer (orange) optimized structures. Vertical bars indicate models using a polarized-continuum, while orange lines also include an explicit hydrogen bonded *n*-octanol.



Figure 6a presents the  $^1\text{H}$  NMR spectra for C1 in acetonitrile without and with addition of triflic acid. Protonation causes a substantial downfield chemical shift in the coumarin aromatic core's hydrogen atoms, thus directly confirming our above empirical observations, as well as previous theoretical analysis,<sup>[7]</sup> that the large hypsochromic shift in the  $S_0 \rightarrow S_1$  transition is a result of the loss of conjugation due to protonation of the nitrogen in the phosphazene group. The fact that electron density is significantly reduced in the ring system also suggests that the nitrogen atom in the structure has become protonated and, as a result, no longer acts as a strong electron donating group.

A second, albeit smaller, shift was observed upon gradual lowering of the concentration of the protonated C1, while keeping the acidity of the solution at a constant high level. No similar behavior was detected in neutral solutions upon dilution (Figure 6b).

The facts that the  $H_6$  and  $H_8$  positions shift upfield at higher concentrations, while the  $H_3$  position is slightly shifted downfield, points at formation of protonated C1 dimer aggregates.<sup>[25,26]</sup> Upon dilution, the dimers increasingly dissociate, which results in a change in the chemical shifts, as the equilibrium is increasingly shifting towards the monomeric forms. In contrast, changing the concentration had no effect on the NMR spectra in the low acidity range, where C1 stays in the neutral form, excluding possibility of aggregate structures. This behavior correlates with some previous self-associating examples, where similar chemical shift dynamics were detected in dilution NMR experiments.<sup>[27,28]</sup>

One way to rationalize the dimer formation is to assume that, due to partially-charged nature of the protonated compound, the nitrogen site, near  $H_6$  and  $H_8$ , experiences

increased electron density donated from an adjacent negative site near  $H_3$ . This may lead to hydrogen bonding (HB) between two adjacent fluorophores, for which the structural features of C1-C4 already serve as an enabling factor. To test this hypothesis, a series of dimeric structures including single-charged as well as double-charged C2 species with either one or two HB contacts were analyzed theoretically, using full geometry optimizations in both acetonitrile and *n*-octanol, followed by normal mode analysis. These calculations revealed several dimeric minima, appreciably stabilized in respect to attached monomers. The TDDFT calculations for these so obtained dimeric structures were carried out at PCM/B3LYP/6-311(d,p) level of theory and representative results indicate that spectral profiles of double-charged single HB dimers (shown for C1 in Figure 6c, and detailed in Table S1 in the Supporting Information) are consistent with the measured 1PA and 2PA spectra of protonated C2.

Vertical orange bars in Figure 5 represent few calculated lowest-energy electronic transitions of the double-charged dimer. Both the wavelength and relative intensity of the second and the third electronic transitions of the dimeric structure, in acetonitrile at 337 nm and 330 nm, respectively, would match well with the lower-energy part of the experimental 1PA and 2PA spectra, which, while slightly redshifted in respect to protonated monomer, maintains high degree of similarity with corresponding monomeric profile. However, the distinct  $S_0 \rightarrow S_1$  excitation of the dimer at 354 nm, unseen in 1PA due to the low oscillator strength ( $f=0.003$ ) could be a proper match for the previously unresolved contribution for the red shoulder observed in acetonitrile at 705 nm in 2PA. This low energy transition appears much more evident in the 2PA spectrum compared to the 1PA case, and also seems to be enhanced in *n*-octanol. It is also evident

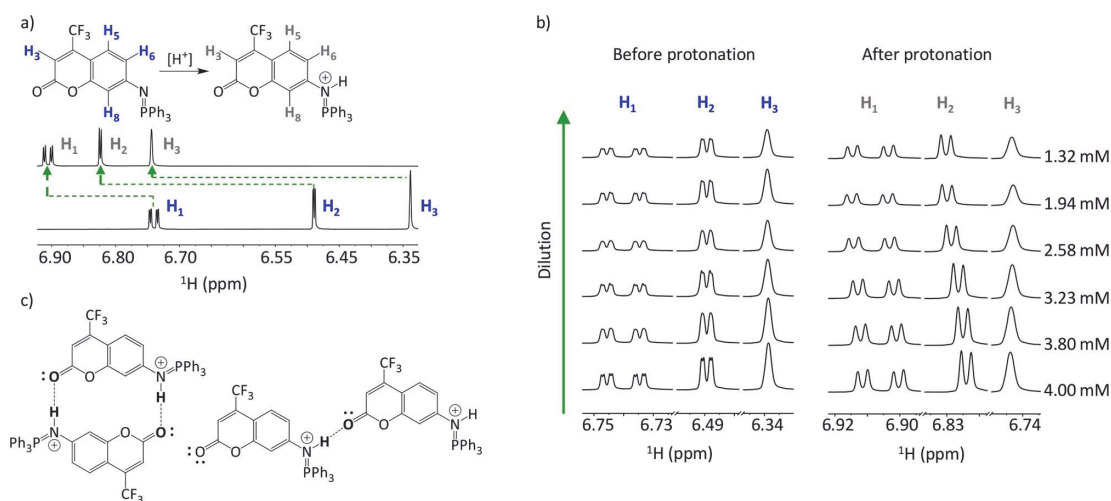


**Figure 6.** Summary of NMR results for C1; (a)  $^1\text{H}$  NMR spectra of a 4 mM solution of C1 in acetonitrile before and after the addition of triflic acid; (b) stacked  $^1\text{H}$  NMR spectra of decreasing concentration for C1 before and after the addition of triflic acid, with minor chemical shifts suggesting dimerization for the protonated molecule; (c) Example of potential structural arrangement of hydrogen-bonded dimers.

that for the latter case, a discrete-continuum representation of solvent environment, which includes an explicit *n*-octanol molecule, substantially increases the lowest-energy oscillator strength and provides notably better match for observed spectral features than pure continuum model (Figure 5, lower panel), consistent with effects of solvent-specific HB patterns on spectral line shapes.<sup>[29]</sup> The solvent dependence is consistent with an ion-pairing dimer description, as formation would be enhanced in nonpolar solvents, while polar solvents could stabilize individual charged species. The enhanced appearance of the dimer in 2PA relative to 1PA is difficult to describe, as 2PA spectral intensities can be affected by complex vibronic contributions. Our observations appear similar to spectral shifts and 2PA cross-section increases resulting from aggregation for other systems.<sup>[30]</sup> In such cases, dependencies have been treated with phenomenological<sup>[31]</sup> and computational<sup>[32–34]</sup> models, although in general calculating 2PA vibronic progressions remains a challenge.

Although the tentative assignment of the red-shifted absorption to dimer formation appears appealing at first glance, such dimers are expected to be minor components for the much lower concentrations used in our spectroscopic measurements, compared to those used to obtain the NMR spectra. As a consequence, any effects of dimers on the 1PA and 2PA absorbance profiles would be expected to be negligible, and which would then imply that some other phenomena are likely responsible for the discrepancies we observe. The origin of these observed spectral features remains under investigation.

As already noted, in the neutral form, the  $S_0 \rightarrow S_1$  transition profiles of 1PA and 2PA nearly coincide, which we utilize to estimate the absolute value of permanent electric dipole moment change,  $\Delta\mu$ , upon the transition, following the relation:<sup>[14]</sup>

$$|\Delta\mu| = \sqrt{\frac{5}{4(1+2\cos^2\beta)} \frac{hc^2 N_A}{\pi 10^3 \ln 10} \frac{n \sigma_{2PA} (2 \cdot \lambda_{1PA})}{f^2 \lambda_{1PA} \cdot \varepsilon (\lambda_{1PA})}}$$

Where  $\varepsilon$  is the measured molar extinction coefficient,  $\sigma_{2PA}$  is the peak 2PA cross section,  $h$  is the Planck constant,  $c$  is the speed of light in vacuum,  $N_A$  is the Avogadro constant,  $n$  is the solvent index of refraction, and  $f$  is the optical field correction factor,  $f = (n^2 + 2)/3$ . The parameter  $\beta$  represents the angle between the transition dipole moment vector ( $\mu$ ) and  $\Delta\mu$ , which for dipolar molecules can be approximated as  $0^\circ$ . This resulting dipole moment change across the band is plotted as black lines in Figures 2 and 3 (right inner vertical axis), and amount to  $\sim 6$  Debye (D) in acetonitrile and  $\sim 5$  D in *n*-octanol. Table 1 lists the over-the-band averages, along with similar estimates obtained for the protonate forms of the fluorophores. In the latter case, it was assumed that even though, due to potential dimer formation, we are unable to spectrally separate monomers from the dimers, because we are calculating the ratio between the 2PA and 1PA spectra, the result should be  $\Delta\mu$  value that is representative of average over all species present in the solution.

## Conclusion

Two-photon excited fluorescence microscopy probes can be used to measure of pH of biological systems with nanoscale resolution.<sup>[3]</sup> However, many probe molecules used in this technique lack rigorous nonlinear optical characterization, which can lead to misinterpretation of their excitation behavior in varied environments. Here, we report on four novel lipophilic two-photon active probes that are sensitive to pH. We characterize their 2PA spectra, cross section and associated brightness, and show that absorption and emission behavior for protonated and neutral states remain distinct in diverse environments. These features make them potentially suitable for imaging and quantifying cytosolic pH changes near cell membranes, as well as in membranous regions of subcellular compartments such as mitochondria, lysosomes, endoplasmic reticulum or other complex membrane systems. Imaging applications will be addressed in an upcoming study. To further accommodate potential applications, these molecular probes may be tailored via modifications of the phosphazene substituent groups or coumarin motif, which have been shown to affect the  $pK_a$ <sup>[6]</sup> or 2PEF brightness,<sup>[22]</sup> respectively.

## Experimental Section

Synthesis of coumarin derivatives were reported previously by Selberg et al.,<sup>[6]</sup> while spectroscopic sample preparation and techniques are detailed in Rammo et al.<sup>[7]</sup> Briefly, for optical measurements, samples were dissolved in solutions of acetonitrile ( $\geq 99.9\%$ , HPLC grade, Rathburn chemicals) or *n*-octanol ( $\geq 99.9\%$ , HPLC grade, Honeywell) were prepared by dissolving a small amount of C1–C4, such that the absorption through a  $1 \times 1$  cm cuvette was 0.1 OD for 1PA and fluorescence measurements or a 1 mm cuvette was 0.1 OD for 2PA measurements, using instrumentation described in Ref. [7].

**Experimental methods for NMR measurements:** All the spectra were collected in acetonitrile- $d_3$  (CD<sub>3</sub>CN) at 293.15 K, using a QCI CryoProbe on a Bruker AVANCE III 800 MHz spectrometer. The samples were thoroughly shaken before the measurements using a Vortex mixer. Measurements were comprised of 8 to 64 duplicate scans, such that the signal to noise ratio was greater than 250 for the recorded spectra. A relaxation delay of 5 s was used. The acquisition time was set to 2.4 s. The spectra were processed in MestreNova and zero filled to 128k points to follow the chemical shift changes for the diluted samples.

**Computational details:** The one-photon absorption (1PA) vertical excited state energies, oscillator strengths, and the change of the permanent electric dipole moment ( $\Delta\mu$ ) upon electronic excitation for all monomers in acetonitrile and *n*-octanol were obtained from Gaussian09<sup>[35]</sup> and Gaussian16<sup>[36]</sup> TDDFT calculations using modified Coulomb Attenuated Method B3LYP (CAM-B3LYP)<sup>[37]</sup> functional. Dalton2018 software suite<sup>[38,39]</sup> was used for all quadratic response two-photon absorption (2PA) calculations in both solvents. The solvent effects were treated in the framework of polarized continuum approximation. As a prerequisite, all structures were optimized in respective solvents using PCM/B3LYP<sup>[40,41]</sup>/6-311G(d,p)<sup>[41]</sup> method and the lack of imaginary frequencies in harmonic vibrational spectra was confirmed in each case. The resulting lowest energy conformers were selected for the calcu-

lation of optical properties. For dimeric structures of C2, the 1PA spectral properties were obtained at TD/B3LYP level of theory and the spectra for respective monomers were also recalculated using the same theoretical method to maintain consistency for comparisons. For these calculations, the discrete-continuum approach involving one explicit molecule of *n*-octanol was implemented as well to account for the specific solvation contribution of this HBD-capable solvent. Additional computational details are reported in Ref. [7].

## Acknowledgements

This work was supported by the Ministry of Education and Research, Republic of Estonia (grants PRG661, PRG690, PSG317, PSG400, and MOBTP128) and European Regional Development Fund (projects TK134 “EQUITANT” and TK141 “Advanced materials and high-technology devices for energy recuperation systems”). Quantum chemical calculations were in part carried out at the High-Performance Computing Centre of the University of Tartu. The authors are grateful to Dr. Tuuli Käambre and Dr. Igor Shevchuk for fruitful discussions.

## Conflict of Interest

The authors declare no conflict of interest.

## Data Availability Statement

The data that support the findings of this study are available from the corresponding author upon reasonable request.

**Keywords:** fluorescent pH indicator · lipophilic probe · two-photon absorption · two-photon cross section · two-photon excitation fluorescence

- [1] A. Steinegger, O. S. Wolfbeis, S. M. Borisov, *Chem. Rev.* **2020**, *120*, 12357–12489.
- [2] X. Huang, J. Song, B. C. Yung, X. Huang, Y. Xiong, X. Chen, *Chem. Soc. Rev.* **2018**, *47*, 2873–2920.
- [3] H. Jin, M. Yang, Z. Sun, R. Gui, *Coord. Chem. Rev.* **2021**, *446*, 214114.
- [4] A. Diaspro, G. Chirico, M. Collini, *Q. Rev. Biophys.* **2005**, *38*, 97–166.
- [5] H. Zhang, M. Tian, R. Yang, X. He, X. Yu, *Spectrochim. Acta Part A* **2021**, *246*, 119035.
- [6] S. Selberg, T. Pagano, S. Tshepelevitsh, T. Haljasorg, S. Vahur, J. Luik, J. Saame, I. Leito, *J. Phys. Org. Chem.* **2019**, *32*, e3950.
- [7] M. Rammo, A. Trummal, M. Uudsemaa, J. Pahapill, K. Petritsenko, M.-M. Sildoja, C. Stark, S. Selberg, I. Leito, A. Rebane, in *Multiphoton Microscopy in the Biomedical Sciences XXI* (Eds.: A. Periasamy, P. T. So, K. König), SPIE, Online Only, United States, **2021**, p. 48.
- [8] A. Kütt, S. Selberg, I. Kaljurand, S. Tshepelevitsh, A. Heering, A. Darnell, K. Kaupmees, M. Piirsalu, I. Leito, *Tetrahedron Lett.* **2018**, *59*, 3738–3748.
- [9] S. Selberg, S. Tshepelevitsh, I. Leito, *Croat. Chem. Acta* **2018**, *91*, 599–602.
- [10] S. Charier, O. Ruel, J.-B. Baudin, D. Alcor, J.-F. Allemand, A. Meglio, L. Jullien, B. Valeur, *Chem. Eur. J.* **2006**, *12*, 1097–1113.
- [11] X. Xie, J. Zhai, Z. Jarolimová, E. Bakker, *Anal. Chem.* **2016**, *88*, 3015–3018.
- [12] G. C. Kemmer, S. A. Bogh, M. Urban, M. G. Palmgren, T. Vosch, J. Schiller, T. Günther-Pomorski, *Analyst* **2015**, *140*, 6313–6320.
- [13] S. Bassnett, L. Reinisch, D. C. Beebe, *Am. J. Physiol. Cell Physiol.* **1990**, *258*, C171–C178.
- [14] A. Rebane, M. Drobizhev, N. S. Makarov, E. Beuerman, S. Tillo, T. Hughes, *J. Lumin.* **2010**, *130*, 1619–1623.
- [15] H. R. Guy, *Biophys. J.* **1985**, *47*, 61–70.
- [16] J. Sangster, *J. Phys. Chem. Ref. Data* **1989**, *18*, 1111–1229.
- [17] K. V. Katti, K. Raghuraman, N. Pillarsetty, S. R. Karra, R. J. Gulotty, M. A. Chartier, C. A. Langhoff, *Chem. Mater.* **2002**, *14*, 2436–2438.
- [18] M. Uudsemaa, A. Trummal, S. de Reguardati, P. Callis, A. Rebane, *Phys. Chem. Chem. Phys.* **2017**, *19*, 28824–28833.
- [19] S. de Reguardati, J. Pahapill, A. Mikhailov, Y. Stepanenko, A. Rebane, *Opt. Express* **2016**, *24*, 9053–9066.
- [20] J. Guan, J. J. R. Arias, K. Tomobe, R. Ansari, M. de F. V. Marques, A. Rebane, S. Mahbub, J. C. Furgal, N. Yodsin, S. Jungsuttiwong, D. Hashemi, J. Kieffer, R. M. Laine, *ACS Appl. Polym. Mater.* **2020**, *2*, 3894–3907.
- [21] C. Würth, M. Grabolle, J. Pauli, M. Spieles, U. Resch-Genger, *Anal. Chem.* **2011**, *83*, 3431–3439.
- [22] S. Nad, H. Pal, *J. Phys. Chem. A* **2001**, *105*, 1097–1106.
- [23] L.-Y. Hsia, H.-N. Chen, C.-H. Chiang, M.-Y. Hung, H.-K. Wei, C.-W. Luo, M.-Y. Kuo, S.-Y. Luo, C.-C. Chu, *J. Org. Chem.* **2020**, *85*, 9361–9366.
- [24] A. Rebane, N. S. Makarov, M. Drobizhev, B. Spangler, E. S. Tarter, B. D. Reeves, C. W. Spangler, F. Meng, Z. Suo, *J. Phys. Chem. C* **2008**, *112*, 7997–8004.
- [25] C. Shao, M. Grüne, M. Stolte, F. Würthner, *Chem. Eur. J.* **2012**, *18*, 13665–13677.
- [26] H. Sun, Y. Zhao, Z. Huang, Y. Wang, F. Li, *J. Phys. Chem. A* **2008**, *112*, 11382–11390.
- [27] R. B. Martin, *Chem. Rev.* **1996**, *96*, 3043–3064.
- [28] P. Thordarson, in *Supramolecular Chemistry: From Molecules to Nanomaterials* (Eds.: P. A. Gale, J. W. Steed), John Wiley & Sons, Ltd, Chichester, UK, **2012**, pp. 239–274.
- [29] C. W. Stark, A. Trummal, M. Uudsemaa, J. Pahapill, M. Rammo, K. Petritsenko, M.-M. Sildoja, A. Rebane, *Commun. Chem.* **2019**, *2*, 108.
- [30] Y. Zhang, J. Li, B. Z. Tang, K. S. Wong, *J. Phys. Chem. C* **2014**, *118*, 26981–26986.
- [31] M. Drobizhev, N. S. Makarov, S. E. Tillo, T. E. Hughes, A. Rebane, *J. Phys. Chem. B* **2012**, *116*, 1736–1744.
- [32] H. Ma, Y. Zhao, W. Liang, *J. Chem. Phys.* **2014**, *140*, 094107.
- [33] R. Zalešny, N. A. Murugan, G. Tian, M. Medved', H. Ågren, *J. Phys. Chem. B* **2016**, *120*, 2323–2332.
- [34] E. Kamarchik, A. I. Krylov, *J. Phys. Chem. Lett.* **2011**, *2*, 488–492.
- [35] M. Frisch, G. Trucks, H. Schlegel, G. Scuseria, M. Robb, J. Cheeseman, G. Scalmani, V. Barone, B. Mennucci, G. Petersson, H. Nakatsuji, M. Caricato, X. Li, H. Hratchian, A. Izmaylov, J. Bloino, G. Zheng, J. Sonnenberg, M. Hada, M. Ehara, K. Toyota, R. Fukuda, J. Hasegawa, M. Ishida, T. Nakajima, Y. Honda, O. Kitao, H. Nakai, T. Vreven, J. Montgomery, J. Peralta, F. Ogliaro, M. Bearpark, J. Heyd, E. Brothers, K. Kudin, V. Staroverov, R. Kobayashi, J. Normand, K. Raghavachari, A. Rendell, J. Burant, S. Iyengar, J. Tomasi, M. Cossi, N. Rega, J. Millam, M. Klene, J. Knox, J. Cross, V. Bakken, C. Adamo, J. Jaramillo, R. Gomperts, R. Stratmann, O. Yazyev, A. Austin, R. Cammi, C. Pomelli, J. Ochterski, R. Martin, K. Morokuma, V. Zakrzewski, G. Voth, P. Salvador, J. Dannenberg, S. Dapprich, A. Daniels, Ö. Farkas, J. Foresman, J. Ortiz, J. Cioslowski, D. Fox, *Gaussian, Inc.: Wallingford, CT* **2009**.
- [36] M. Frisch, G. Trucks, H. Schlegel, G. Scuseria, M. Robb, J. Cheeseman, G. Scalmani, V. Barone, G. Petersson, H. Nakatsuji, X. Li, M. Caricato, A. Marenich, J. Bloino, B. Janesko, R. Gomperts, B. Mennucci, H. Hratchian, J. Ortiz, A. Izmaylov, J. Sonnenberg, D. Williams-Young, F. Ding, F. Lipparini, F. Egidi, J. Goings, B. Peng, A. Petrone, T. Henderson, D. Ranasinghe, V. Zakrzewski, J. Gao, N. Rega, G. Zheng, W. Liang, M. Hada, M. Ehara, K. Toyota, R. Fukuda, J. Hasegawa, M. Ishida, T. Nakajima, Y. Honda, O. Kitao, H. Nakai, T. Vreven, K. Throssell, J. Montgomery, J. Peralta, F. Ogliaro, M. Bearpark, J. Heyd, E. Brothers, K. Kudin, V. Staroverov, T. Keith, R. Kobayashi, J. Normand, K. Raghavachari, A. Rendell, J. Burant, S. Iyengar, J. Tomasi, M. Cossi, J. Millam, M. Klene, C. Adamo, R. Cammi, J. Ochterski, R. Martin, K. Morokuma, O. Farkas, J. Foresman, D. Fox, *Gaussian, Inc.: Wallingford, CT* **2016**.
- [37] T. Yanai, D. P. Tew, N. C. Handy, *Chem. Phys. Lett.* **2004**, *393*, 51–57.
- [38] K. Aidas, C. Angeli, K. L. Bak, V. Bakken, R. Bast, L. Boman, O. Christiansen, R. Cimraglia, S. Coriani, P. Dahle, E. K. Dalskov, U. Ekström, T. Enevoldsen, J. J. Eriksen, P. Ettenhuber, B. Fernández, L. Ferrighi, H. Flieg, L. Frediani, K. Hald, A. Halkier, C. Hättig, H. Heiberg, T. Helgaker, A. C. Hennum, H. Hettema, E. Hjertenaes, S. Høst, I.-M. Høyvik, M. F. Iozzi, B. Jansik, H. J. A. Jensen, D. Jonsson, P. Jørgensen, J. Kauczor, S. Kirpekar, T. Kjaergaard, W. Klopper, S. Knecht, R. Kobayashi, H. Koch, J. Kongsted, A. Krapp, K. Kristensen, A. Ligabue, O. B. Lutnaes, J. I. Melo, K. V.

- Mikkelsen, R. H. Myhre, C. Neiss, C. B. Nielsen, P. Norman, J. Olsen, J. M. H. Olsen, A. Osted, M. J. Packer, F. Pawłowski, T. B. Pedersen, P. F. Provasi, S. Reine, Z. Rinkevicius, T. A. Ruden, K. Ruud, V. V. Rybkin, P. Sałek, C. C. M. Samson, A. S. de Merás, T. Saue, S. P. A. Sauer, B. Schimmelpfennig, K. Sneskov, A. H. Steindal, K. O. Sylvester-Hvid, P. R. Taylor, A. M. Teale, E. I. Tellgren, D. P. Tew, A. J. Thorvaldsen, L. Thøgersen, O. Vahtras, M. A. Watson, D. J. D. Wilson, M. Ziolkowski, H. Ågren, *Wiley Interdiscip. Rev.: Comput. Mol. Sci.* **2014**, *4*, 269–284.
- [39] *Dalton, a molecular electronic structure program, Release v2018.2 (2019)*, see <http://daltonprogram.org>.
- [40] A. D. Becke, *J. Chem. Phys.* **1993**, *98*, 5648–5652.
- [41] C. Lee, W. Yang, R. G. Parr, *Phys. Rev. B* **1988**, *37*, 785–789.
- [42] M. J. Frisch, J. A. Pople, J. S. Binkley, *J. Chem. Phys.* **1984**, *80*, 3265–3269.

---

Manuscript received: October 25, 2021

Accepted manuscript online: December 29, 2021

Version of record online: January 25, 2022



## Appendix 2

### Publication II

Stark, C. W.; Rammo, M.; Trummal, A.; Uudsemaa, M.; Pahapill, J.; Sildoja, M.-M.; Tshepelevitsh, S.; Leito, I.; Young, D. C.; Szymański, B.; Vakuliuk, O.; Gryko, D. T.; Rebane, A., "On-off-on Control of Molecular Inversion Symmetry via Multi-stage Protonation: Elucidating Vibronic Laporte Rule," *Angew. Chem. Int. Ed.*, vol. 61, no. 51, Oct. 2022.



# On-off-on Control of Molecular Inversion Symmetry via Multi-stage Protonation: Elucidating Vibronic Laporte Rule

Charles W. Stark, Matt Rammo, Aleksander Trummal, Merle Uudsemaa, Juri Pahapill, Meelis-Mait Sildoja, Sofja Tshepelevitsh, Ivo Leito, David C. Young, Bartosz Szymański, Olena Vakuliuk, Daniel T. Gryko,\* and Aleksander Rebane\*

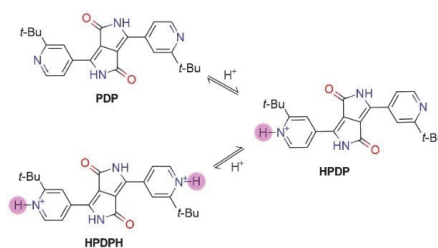
**Abstract:** The Laporte rule dictates that one- and two-photon absorption spectra of inversion-symmetric molecules should display alternatively forbidden electronic transitions; however, for organic fluorophores, drawing clear distinction between the symmetric- and non-inversion symmetric two-photon spectra is often obscured due to prevalent vibronic interactions. We take advantage of consecutive single- and double-protonation to break and then reconstitute inversion symmetry in a nominally symmetric diketopyrrolopyrrole, causing large changes in two-photon absorption. By performing detailed one- and two-photon titration experiments, with supporting quantum-chemical model calculations, we explain how certain low-frequency vibrational modes may lead to apparent deviations from the strict Laporte rule. As a result, the system may be indeed considered as an on-off-on inversion symmetry switch, opening new avenues for two-photon sensing applications.

Inversion-symmetric organic chromophores commonly feature, in the singlet manifold, alternating-parity electronic states, where a *gerade* (*g*) or *ungerade* (*u*) parity  $S_0$  ground-state connects via one-photon allowed but two-photon forbidden electric dipole transition to opposite-parity (*u* or *g*) lowest-energy  $S_1$  excited state.<sup>[1]</sup> Bonding of a proton may disrupt ground-state inversion symmetry, such that the

above exclusion, commonly called Laporte rule, no longer applies, and two-photon absorption (2PA) efficiency of the  $S_0 \rightarrow S_1$  transition may drastically increase.

Monitoring 2PA variations has been suggested for studying pH,<sup>[2,3]</sup> ion sensing,<sup>[4–8]</sup> redox reactions,<sup>[9]</sup> and solvent polarity.<sup>[10]</sup> However, unambiguous spectroscopic evidence for Laporte rule controlling the 2PA remains scarce. This is, in part, because presence of spectrally-overlapping species, e.g. different protonation forms, makes acquiring reliable 2PA cross section spectra an arduous task; and even if such spectra are obtained, for room temperature and condensed phases, both linear (1PA) and 2PA transitions are often of electronic-vibrational (vibronic) origin, making interpretation of this data debatable. To make matters worse, while quantum-chemical calculations deliver reliable vibronic features of 1PA spectra, predicting analogous vibronic spectra for 2PA, especially for complex chromophores, remains extremely challenging.<sup>[11]</sup> It is therefore of significant fundamental- and practical interest to elucidate how attaching a proton changes vibronic 2PA of a nominally inversion-symmetric chromophore. Moreover, if a second proton binds at a symmetric site, then that should revive the Laporte rule, thus shedding further light on the origin of vibronic 2PA transitions.

Here, we synthesize a novel inversion-symmetric 3,6-bis-(2-*tert*-butylpyridin-4-yl)-diketopyrrolopyrrole (PDP), which combines a diketopyrrolopyrrole (DPP) core with two flanking pyridyl moieties, as shown in Scheme 1. The pyridyl substituents offer the opportunity for reversible single- and double-protonation, while their small,  $\leq 7^\circ$ , dihedral angle with the DPP core suggests a single  $\pi$ -conjugated system, whereas *tert*-butyl groups secure suitable solubility.<sup>[12]</sup> The



**Scheme 1.** Structure of neutral (PDP), single-protonated (HPDP) and double-protonated (HPDPH) chromophore.

[\*] Dr. C. W. Stark, M. Rammo, Dr. A. Trummal, Dr. M. Uudsemaa, J. Pahapill, Dr. M.-M. Sildoja, Prof. A. Rebane  
 Laboratory of Chemical Physics,  
 Keemilise ja Bioloogilise Füüsika Instituut  
 Akadeemia tee 23, 12618 Tallinn (Estonia)  
 E-mail: arebane@montana.edu  
 Dr. S. Tshepelevitsh, Prof. I. Leito  
 Institute of Chemistry,  
 Tartu Ülikool  
 14a Ravila Str, 50411 Tartu (Estonia)  
 Dr. D. C. Young, B. Szymański, Dr. O. Vakuliuk, Prof. D. T. Gryko  
 Instytut Chemii Organicznej,  
 Polska Akademia Nauk Kasprzaka 44/52, 01-224 Warsaw (Poland)  
 E-mail: dtgryko@icho.edu.pl  
 Prof. A. Rebane  
 Department of Physics,  
 Montana State University  
 264 EPS, Bozeman, MT 59717 (USA)



inherent rigidity of the dyes' backbone limits symmetry-lowering conformations and promotes photostability in organic solvents, while also leading to pronounced  $S_0 \rightarrow S_1$  vibronic transitions along with efficient one- and two-photon excited fluorescence (2PEF).<sup>[13]</sup>

Figure 1 (upper panel) shows changes in the 1PA spectrum of PDP in methanol (dark blue curve) upon titration with triflic acid. Initially, at  $\text{pH} > 4$ , one observes an isosbestic point at  $\lambda_{1\text{PA}} = 517 \text{ nm}$ , whereas at  $\text{pH} < 2.7$ , there appear two secondary isosbestic points at  $\lambda_{1\text{PA}} = 555$  and  $434 \text{ nm}$ . This behavior indicates presence, in addition to the neutral form, of single-protonated (HPDP) and double-protonated (HPDPH) forms of PDP. To isolate these overlapping 1PA spectra, we use a multivariate curve resolution-alternating least squares (MCR-ALS) decomposition method,<sup>[14]</sup> detailed in the Supporting Information. The resulting individual 1PA spectra are shown with solid lines in Figure 2 (1PA wavelength—upper horizontal scale). Single-protonation red-shifts the 1PA maximum, from the neutral PDP value at  $\lambda_{1\text{PA}} = 508 \text{ nm}$ , to  $546 \text{ nm}$ , while double-protonation shifts the maximum even further to the red, to  $569 \text{ nm}$ . Based on our quantum-chemical calculations (see below), and similarity to other pyrrolopyrroles,<sup>[15]</sup> we attribute the highest-intensity 1PA band in PDP and HPDPH to the 0-0 vibronic component of the  $S_0 \rightarrow S_1$  transition. For HPDP, the calculations show that 1PA maximum is also due to  $S_0 \rightarrow S_1$  transition, however, significant spectral broadening characteristic to dipolar systems

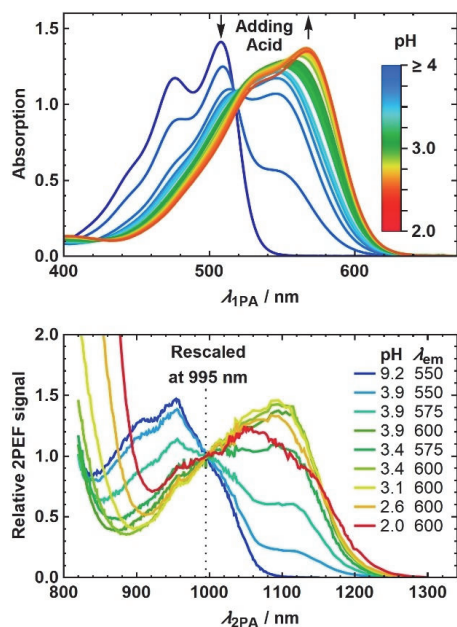


**Figure 1.** pH-dependence of 1PA (top) and 2PEF excitation (bottom) spectra for PDP in methanol upon addition of triflic acid. The two-photon profiles are rescaled for convenience at  $995 \text{ nm}$  (dotted line), as raw maximum signals varied by a factor of  $\approx 40$ .

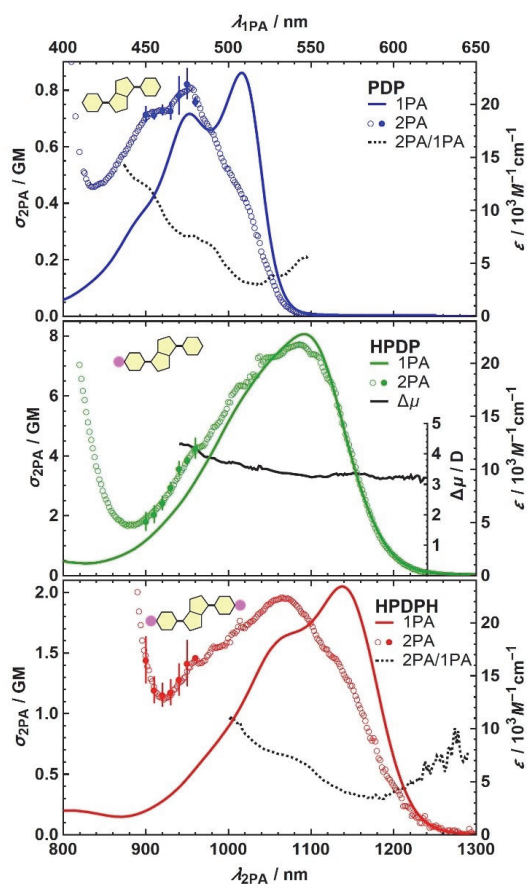


**Figure 2.** Decomposed 1PA and 2PA spectra for all PDP forms in methanol. 2PA cross section (circles) are shown as a function of the excitation wavelength (lower horizontal axis), while corresponding one-photon molar absorption (colored lines) are shown according to the 1PA wavelength (upper axis). Inset dashed black lines depict the ratio of 2PA to 1PA spectra, while the solid black line is the change in permanent dipole moment calculated from Equation (1).

complicates more detailed assignment of accompanying vibronic features.

The MCR-ALS model of 1PA titration data also results in experimental  $\text{p}K_{\text{aH}}$  (the  $\text{p}K_{\text{a}}$  of the protonated base) for the first- and second-protonation steps of 4.6 and 3.2, respectively. Comparative calculations by linear regression of energies obtained with COSMO-RS method and  $\text{p}K_{\text{aH}}$  values of other pyridines<sup>[16]</sup> give  $\text{p}K_{\text{aH}}$  values of 5.9 and 4.2, respectively. The  $\approx 1 \text{ pH}$  unit mismatch between the experimental and theoretical values is within typical uncertainties of computational and experimental calibrations,<sup>[17]</sup> while both methods support a  $\approx 1.5 \text{ pH}$  interval between the two protonation stages.

Lower panel of Figure 1 shows results from two-photon pH experiments, normalized to unit value at  $995 \text{ nm}$ . The

2PEF excitation profiles were measured in the range,  $\lambda_{2PA} = 820\text{--}1300\text{ nm}$ , thus encompassing the whole  $S_0 \rightarrow S_1$  transition of all three forms, using  $\approx 150\text{ fs}$  duration pulses from a 6 kHz pulse rate, wavelength-tuned optical parametric amplifier. Each spectrum was shape corrected, and absolute 2PA cross section determined, by comparison to suitable reference standards,<sup>[18–20]</sup> discussed in the Supporting Information. In neutral methanol solution, PDP shows 2PA maximum at,  $\lambda_{2PA} = 954\text{ nm}$ . Upon addition of small amounts of triflic acid ( $\text{pH} \approx 3.5$ ), the maximum red-shifts to  $\approx 1100\text{ nm}$ , whereas at lower  $\text{pH} < 2.5$ , the peak undergoes a slight hypsochromic shift to,  $\approx 1060\text{ nm}$ .

In contrast to the 1PA titration, the raw 2PEF data shows no clear isosbestic points, likely a result of largely varying fluorescence quantum yields and 2PA cross sections of the simultaneously excited different forms. Nevertheless, by applying the MCR-ALS technique to the measured excitation-emission matrix (the latter was obtained by recording, at each excitation wavelength, the emission spectrum spanning,  $\lambda_{em} = 450\text{--}804\text{ nm}$ , using a CCD-spectrometer, see Supporting Information for details), the relevant 2PA spectra and 2PA cross sections were reliably evaluated, as shown by symbols (2PA wavelength—lower horizontal scale) in the Figure 2. The 2PA peaks of PDP, HPDP and HPDPH are respectively at,  $\lambda_{2PA} = 954, 1086$  and  $1066\text{ nm}$ , with corresponding peak cross section values,  $\sigma_{2PA} = 0.81, 7.7$  and  $2.0\text{ GM}$  ( $1\text{ GM} = 10^{-50}\text{ cm}^2\text{ s}^{-1}\text{ photon}^{-1}$ ). To highlight where 2PA transitions match or deviate from the corresponding 1PA transitions, we plotted in Figure 2 the 2PA vs 1PA profile ratios for all three species (black lines in Figure 2).

In case of HPDP (middle panel), we observe that the 2PA profile follows very closely that of the 1PA, which results in nearly constant ratio over the entire  $S_0 \rightarrow S_1$  transition wavelength range (black line). The fact that the ground- and excited vibronic levels appear to be contributing, on average, in the same manner to the 2PA as they do for the 1PA, suggests that the 2PA cross section should be adequately described by the two essential states model, meaning that any third-level (intermediate-level) contributions may be neglected. To estimate the value of permanent electric dipole moment change ( $\Delta\mu$ ) in the  $S_0 \rightarrow S_1$  transition, we use the relation,<sup>[21]</sup>

$$|\Delta\vec{\mu}| = \sqrt{\frac{hc^2 N_A}{\pi 10^3 \ln 10} \frac{5}{4(1 + 2\cos^2\beta)} \frac{n}{f^2} \frac{\sigma_{2PA}}{\lambda_{1PA} \epsilon}} \quad (1)$$

where  $\sigma_{2PA}$  is the 2PA cross section ( $\text{cm}^4\text{ s photon}^{-1}$ ),  $\epsilon$  is the molar extinction coefficient ( $\text{M}^{-1}\text{ cm}^{-1}$ ),  $\lambda_{1PA}$  is the 1PA transition wavelength (cm),  $c$  is the speed of light in vacuum ( $\text{cm s}^{-1}$ ),  $h$  is the Planck constant (erg s),  $f = (n^2 + 2)/3$  is the optical field correction factor,  $n$  is the solvent index of refraction and  $\beta$  is the angle between the  $\Delta\mu$ -vector and direction of the transition dipole moment  $\mu$ -vector. Equation (1) gives the value,  $\Delta\mu = 3.4$  Debye, which compares well with our theoretically calculated value,  $\Delta\mu = 4.0$  Debye, obtained via linear and quadratic response TD-DFT using tuned CAM-B3LYP<sup>[22,23]</sup> density functional and a polarized continuum approximation of the methanol environment. Experimental and theoretical values for 1PA and 2PA parameters of PDP, HPDP and HPDPH are collected in Table 1.

For PDP and HPDPH, one may be tempted to interpret the low  $\sigma_{2PA}$  compared to HPDP, as well as the hypsochromically shifted maximum compared to respective 1PA, as confirmation of Laporte rule. However, as noted already, such approach may need to be revised, especially as it does not fully account for the vibronic nature of the underlying transitions. Indeed, the 2PA maxima of PDP and HPDPH approximately match the 478 nm and 535 nm features in the corresponding 1PA spectra, and since our calculations indicate  $S_1$  is the only electronic state in the  $\lambda_{2PA} = 900\text{--}1300\text{ nm}$  range, we tentatively assign these peak 2PA bands to vibronic components of the  $S_0 \rightarrow S_1$  transition. According to formal  $C_{2h}$  molecular symmetry, this  $B_u$  electronic transition is 2PA forbidden, but can be allowed via Herzberg-Teller (HT) coupling with  $b_u$  or  $a_u$  vibrational modes, which match experimental frequency shifts,  $\nu = 1200\text{--}1500\text{ cm}^{-1}$ .<sup>[24]</sup> However, these potential vibronic couplings should be less effective in the 0-0 region, where experimental 2PA should vanish, especially in the red part of the spectrum. In contrast, the experimental 2PA versus 1PA ratio (dotted black curves in Figure 2) remain finite for both PDP and HPDPH in the 0-0 region, accompanied by a modest increase towards longer wavelengths, which could be perceived as a relaxed Laporte rule.

**Table 1:** Spectroscopic results of PDP forms in methanol.

|   | PDP        | HPDP                     | HPDPH      |
|---|------------|--------------------------|------------|
|   |            | Experiment               |            |
| $\epsilon, 10^3\text{ M}^{-1}\text{ cm}^{-1}$ ( $\lambda_{1PA}, \text{ nm}$ ) | 22.9 (508) | 22.8 (546)               | 23.4 (569) |
| $\sigma_{2PA}, \text{ GM}$ ( $\lambda_{2PA}, \text{ nm}$ )                    | 0.81 (954) | 7.7 (1086)               | 2.0 (1066) |
| $\Delta\mu, \text{ D}$  | N.A.       | 3.4                      | N.A.       |
|   |            | Calculation              |            |
| $\epsilon, 10^3\text{ M}^{-1}\text{ cm}^{-1}$ ( $\lambda_{1PA}, \text{ nm}$ ) | 34.6 (485) | 32.5 (546)               | 31.3 (578) |
| $\sigma_{2PA}, \text{ GM}$ ( $\lambda_{2PA}, \text{ nm}$ )                    | 0 (969)    | 16 (1112)                | 0 (1157)   |
| $\Delta\mu, \text{ D}$  | 0.0        | 4.0 (5.0) <sup>[a]</sup> | 0.06       |

[a] Permanent electric dipole moment change obtained from calculated linear electronic properties.

In order to eliminate the possibility that these features may result from inversion symmetry-breaking conformations,<sup>[25–27]</sup> we have performed theoretical calculations showing that although rotation of pyridyl moieties along the linking single-bond can lead to slightly higher energy asymmetric conformers, the 2PA 0-0 band from such conformations remains negligible for both PDP and HPDPH. As an alternative mechanism, one might consider symmetry breaking as a result of excited state bistability,<sup>[28,29]</sup> however, PDP doesn't show the associated solvent-dependent Stokes-shift (see Supporting Information for a detailed discussion of the bistability model).

While seeking an explanation of why 2PA for PDP and HPDPH is far from entirely suppressed in the 0-0 region, we turn our attention to potential coupling between electronic levels and low-energy vibrational modes,  $<500\text{ cm}^{-1}$ . Unfortunately, evaluation of HT terms involve calculating derivatives of the second-order moments over vibrational coordinate space, for which computational methods are still under development.<sup>[30–34]</sup> One approach applied previously to dipolar molecules models molecular distortion along select ground-state vibrational mode eigenvectors and then calculates corresponding effective 2PA cross section.<sup>[11]</sup> We extend this non-Condon 2PA calculation to select high- and low-frequency modes for symmetric PDP, encompassing several  $b_u$  modes, which introduce an in-plane asymmetric distortion, as well as for  $a_g$  modes, which are also Franck-Condon active in 1PA. We omitted  $a_u$  modes as they would not lead to nonvanishing in-plane dipoles due to their out-of-plane displacement vectors. While  $a_g$  modes contribute to low-energy 1PA vibronic transitions, they show negligible 2PA effect. In contrast, certain 1PA inactive  $b_u$  modes significantly boost the  $\Delta\mu$  value, leading to the 2PA cross sections in the range (Table S2),  $\sigma_{2PA} = 0.06\text{--}0.75\text{ GM}$ . Even though our current model lacks desired quantitative accuracy, it does qualitatively reproduce our key experimental observations, including the apparent violation of Laporte Rule.

In conclusion, we have shown, for the first time, that multi-stage protonation in a nominally inversion-symmetric dye not only facilitates large changes in 2PA, but also provides direct experimental proof of on-off-on control of the molecular inversion symmetry. While the marked 2PA effects may be used for molecular sensing, careful analysis of the experimental 1PA and 2PA titration spectra, reveals that neutral- and double-protonated forms both retain nonvanishing 2PA in the 0-0 region, even though such transitions should be strictly forbidden. Theoretical model calculations clarify that this is due to non-Condon coupling of the electronic transition to matching-symmetry low-energy molecular vibrations, thus restoring the Laporte rule's canonical status. Our results also suggest that symmetry switching of 2PA could be used in novel analytical applications including quantitative monitoring of pH as well as establishing reliable  $pK_a$  values, or extended to elucidate similar binding effects in more complex molecular symmetries, including star-shaped (octupolar) and dendritic structures.

## Acknowledgements

This work was supported by the Ministry of Education and Research, Republic of Estonia (grants PRG661, PRG690, PSG317), European Regional Development Fund (projects TK134 "EQUiTANT" and TK141 "Advanced materials and high-technology devices for energy recuperation systems") as well as the National Science Center, Poland (HARMONIA 2018/30/M/ST5/00460). A.R. acknowledges support from NSF Award 2103628. Quantum chemical calculations were in part carried out at the High-Performance Computing Centre of the University of Tartu.

## Conflict of Interest

The authors declare no conflict of interest.

## Data Availability Statement

The data that support the findings of this study are available from the corresponding author upon reasonable request.

**Keywords:** Laporte Rule · Molecular Symmetry · Nonlinear Optics · Protonation · Two-Photon Absorption

- [1] M. J. Wirth, A. Koskelo, M. J. Sanders, *Appl. Spectrosc.* **1981**, 35, 14–21.
- [2] J. Daniel, C. Mastrodonato, A. Sourdon, G. Clermont, J.-M. Vabre, B. Goudeau, H. Voltaire, S. Arbault, O. Mongin, M. Blanchard-Desce, *Chem. Commun.* **2015**, 51, 15245–15248.
- [3] M. H. V. Werts, S. Gmouh, O. Mongin, T. Pons, M. Blanchard-Desce, *J. Am. Chem. Soc.* **2004**, 126, 16294–16295.
- [4] S. J. K. Pond, O. Tsutsumi, M. Rumi, O. Kwon, E. Zojer, J.-L. Brédas, S. R. Marder, J. W. Perry, *J. Am. Chem. Soc.* **2004**, 126, 9291–9306.
- [5] C. Huang, X. Peng, Z. Lin, J. Fan, A. Ren, D. Sun, *Sens. Actuators B* **2008**, 133, 113–117.
- [6] K. P. Divya, S. Sreejith, P. Ashokkumar, K. Yuzhan, Q. Peng, S. K. Maji, Y. Tong, H. Yu, Y. Zhao, P. Ramamurthy, A. Ajayaghosh, *Chem. Sci.* **2014**, 5, 3469–3474.
- [7] W. Li, B. Fang, M. Jin, Y. Tian, *Anal. Chem.* **2017**, 89, 2553–2560.
- [8] C. Yang, M. Zheng, Y. Li, B. Zhang, J. Li, L. Bu, W. Liu, M. Sun, H. Zhang, Y. Tao, S. Xue, W. Yang, *J. Mater. Chem. A* **2013**, 1, 5172–5178.
- [9] K. Kamada, S. Fukui-en, S. Minamide, K. Ohta, R. Kishi, M. Nakano, H. Matsuzaki, H. Okamoto, H. Higashikawa, K. Inoue, S. Kojima, Y. Yamamoto, *J. Am. Chem. Soc.* **2013**, 135, 232–241.
- [10] H. Y. Woo, D. Korystov, A. Mikhailovsky, T.-O. Nguyen, G. C. Bazan, *J. Am. Chem. Soc.* **2005**, 127, 13794–13795.
- [11] E. Kamarchik, A. I. Krylov, *J. Phys. Chem. Lett.* **2011**, 2, 488–492.
- [12] M. Grzybowski, D. T. Gryko, *Adv. Opt. Mater.* **2015**, 3, 280–320.
- [13] M. Grzybowski, V. Hugues, M. Blanchard-Desce, D. T. Gryko, *Chem. Eur. J.* **2014**, 20, 12493–12501.
- [14] A. de Juan, J. Jaumot, R. Tauler, *Anal. Methods* **2014**, 6, 4964–4976.

- [15] Ł. G. Łukasiewicz, M. Rammo, C. W. Stark, M. Krzeszewski, D. Jacquemin, A. Rebane, D. T. Gryko, *ChemPhotoChem* **2020**, *4*, 508–519.
- [16] D. Augustin-Nowacka, M. Makowski, L. Chmurzynski, *Anal. Chim. Acta* **2000**, *418*, 233–240.
- [17] R. Carabias-Martínez, E. Rodríguez-Gonzalo, J. Domínguez-Álvarez, E. Miranda-Cruz, *Anal. Chim. Acta* **2007**, *584*, 410–418.
- [18] S. de Reguardati, J. Pahapill, A. Mikhailov, Y. Stepanenko, A. Rebane, *Opt. Express* **2016**, *24*, 9053–9066.
- [19] N. S. Makarov, J. Campo, J. M. Hales, J. W. Perry, *Opt. Mater. Express* **2011**, *1*, 551–563.
- [20] N. S. Makarov, M. Drobizhev, A. Rebane, *Opt. Express* **2008**, *16*, 4029–4047.
- [21] A. Rebane, M. Drobizhev, N. S. Makarov, E. Beuerman, S. Tillo, T. Hughes, *J. Lumin.* **2010**, *130*, 1619–1623.
- [22] T. Yanai, D. P. Tew, N. C. Handy, *Chem. Phys. Lett.* **2004**, *393*, 51–57.
- [23] M. Uudsemaa, A. Trummal, S. de Reguardati, P. Callis, A. Rebane, *Phys. Chem. Chem. Phys.* **2017**, *19*, 28824–28833.
- [24] S. Ohira, I. Rudra, K. Schmidt, S. Barlow, S.-J. Chung, Q. Zhang, J. Matichak, S. R. Marder, J.-L. Brédas, *Chem. Eur. J.* **2008**, *14*, 11082–11091.
- [25] A. Mikhaylov, M. Uudsemaa, A. Trummal, E. Arias, I. Moggio, R. Ziolo, T. M. Cooper, A. Rebane, *J. Phys. Chem. Lett.* **2018**, *9*, 1893–1899.
- [26] T. M. Cooper, J. E. Haley, D. M. Krein, A. R. Burke, J. E. Slagle, A. Mikhailov, A. Rebane, *J. Phys. Chem. A* **2017**, *121*, 5442–5449.
- [27] A. Rebane, M. Drobizhev, N. S. Makarov, G. Wicks, P. Wnuk, Y. Stepanenko, J. E. Haley, D. M. Krein, J. L. Fore, A. R. Burke, J. E. Slagle, D. G. McLean, T. M. Cooper, *J. Phys. Chem. A* **2014**, *118*, 3749–3759.
- [28] B. Dereka, A. Rosspeintner, Z. Li, R. Liska, E. Vauthey, *J. Am. Chem. Soc.* **2016**, *138*, 4643–4649.
- [29] F. Terenziani, A. Painelli, C. Katan, M. Charlot, M. Blanchard-Desce, *J. Am. Chem. Soc.* **2006**, *128*, 15742–15755.
- [30] H. Ma, Y. Zhao, W. Liang, *J. Chem. Phys.* **2014**, *140*, 094107.
- [31] R. Zaleśny, N. A. Murugan, G. Tian, M. Medved', H. Ågren, *J. Phys. Chem. B* **2016**, *120*, 2323–2332.
- [32] J. Bednarska, R. Zaleśny, G. Tian, N. A. Murugan, H. Ågren, W. Bartkowiak, *Molecules* **2017**, *22*, 1643.
- [33] W. Liang, H. Ma, H. Zang, C. Ye, *Int. J. Quantum Chem.* **2015**, *115*, 550–563.
- [34] D. W. Silverstein, L. Jensen, *J. Chem. Phys.* **2012**, *136*, 064111.

Manuscript received: August 25, 2022

Accepted manuscript online: October 26, 2022

Version of record online: November 22, 2022



## Appendix 3

### Publication III

Tasior, M.; Kowalczyk, P.; Przybył, M.; Czichy, M.; Janasik, P.; Bousquet, M. H. E.; Łapkowski, M.; **Rammo, M.**; Rebane, A.; Jacquemin, D.; Gryko, D. T., "Going beyond the borders: pyrrolo[3,2-b]pyrroles with deep red emission," *Chem. Sci.*, vol. 12, no. 48, pp. 15935–15946, Dec. 2021.



Cite this: *Chem. Sci.*, 2021, 12, 15935

All publication charges for this article have been paid for by the Royal Society of Chemistry

## Going beyond the borders: pyrrolo[3,2-*b*]pyrroles with deep red emission†

Mariusz Tasiar,<sup>a</sup> Paweł Kowalczyk,<sup>a</sup> Marta Przybył,<sup>a</sup> Małgorzata Czichy,<sup>b</sup> Patryk Janasik,<sup>b</sup> Manon H. E. Bousquet,<sup>c</sup> Mieczysław Łapkowski,<sup>\*bd</sup> Matt Rammo,<sup>e</sup> Aleksander Rebane,<sup>\*ef</sup> Denis Jacquemin<sup>id</sup> <sup>\*c</sup> and Daniel T. Gryko<sup>id</sup> <sup>\*a</sup>

A two-step route to strongly absorbing and efficiently orange to deep red fluorescent, doubly B/N-doped, ladder-type pyrrolo[3,2-*b*]pyrroles has been developed. We synthesize and study a series of derivatives of these four-coordinate boron-containing, nominally quadrupolar materials, which mostly exhibit one-photon absorption in the 500–600 nm range with the peak molar extinction coefficients reaching 150 000, and emission in the 520–670 nm range with the fluorescence quantum yields reaching 0.90. Within the family of these ultrastable dyes even small structural changes lead to significant variations of the photophysical properties, in some cases attributed to reversal of energy ordering of alternate-parity excited electronic states. Effective preservation of ground-state inversion symmetry was evidenced by very weak two-photon absorption (2PA) at excitation wavelengths corresponding to the lowest-energy, strongly one-photon allowed purely electronic transition.  $\pi$ -Expanded derivatives and those possessing electron-donating groups showed the most red-shifted absorption- and emission spectra, while displaying remarkably high peak 2PA cross-section ( $\sigma_{2PA}$ ) values reaching  $\sim 2400$  GM at around 760 nm, corresponding to a two-photon allowed higher-energy excited state. At the same time, derivatives lacking  $\pi$ -expansion were found to have a relatively weak 2PA peak centered at ca. 800–900 nm with the maximum  $\sigma_{2PA} \sim 50$ –250 GM. Our findings are augmented by theoretical calculations performed using TD-DFT method, which reproduce the main experimental trends, including the 2PA, in a nearly quantitative manner. Electrochemical studies revealed that the HOMO of the new dyes is located at ca.  $-5.35$  eV making them relatively electron rich in spite of the presence of two  $B^-N^+$  dative bonds. These dyes undergo a fully reversible first oxidation, located on the diphenylpyrrolo[3,2-*b*]pyrrole core, directly to the diradical cation) stage.

Received 9th September 2021  
Accepted 19th November 2021

DOI: 10.1039/d1sc05007a

rsc.li/chemical-science

## Introduction

In recent years, boron has found new distinct roles in materials science, being incorporated in various polycyclic aromatic hydrocarbons (PAHs).<sup>1–7</sup> It has been discovered that doping with three-coordinate,  $sp^2$ -hybridized boron has the most

pronounced effect on aromatic systems among main group elements, due to its low Pauling electronegativity and enhanced  $\pi$ -conjugation resulting from its vacant  $p_z$  orbital. As a consequence, in such systems boron atoms can act simultaneously as  $\pi$ -electron acceptors and  $\sigma$ -electron donors. The fascinating properties of the materials obtained in such a way (so-called B-PAHs), such as strong fluorescence<sup>8–11</sup> and enhanced charge-transport characteristics,<sup>12,13</sup> has resulted in a wide range of applications in optoelectronics, including materials for organic light-emitting diodes (OLEDs)<sup>14–16</sup> circularly polarized luminescence,<sup>17</sup> organic photovoltaics (OPVs)<sup>18</sup> and organic field-effect transistors (OFETs)<sup>19–21</sup> as well as materials for electrodes in lithium batteries.<sup>22</sup> Much attention has also been paid to the B-N/O isosteres of PAHs, *i.e.* compounds in which two adjacent carbons in a  $\pi$ -conjugated core have been replaced by one boron and one N/O atom.<sup>23–28</sup> Of particular importance are  $\pi$ -conjugated systems containing a B-N covalent bond, B $\leftarrow$ N coordination bond<sup>29</sup> and N-B $\leftarrow$ N motif, as evidenced by growing number of reports dealing with BN-embedded heteroarenes<sup>29–32</sup> and BODIPY analogues,<sup>33–37</sup> mostly due to their

<sup>a</sup>Institute of Organic Chemistry, Polish Academy of Sciences, Kasprzaka 44–52, 01-224 Warsaw, Poland. E-mail: dtgryko@icho.edu.pl

<sup>b</sup>Faculty of Chemistry, Silesian University of Technology, Strzody 9, 44-100 Gliwice, Poland. E-mail: mieczyslaw.lapkowski@polsl.pl

<sup>c</sup>CEISAM Lab—UMR 6230, CNRS, University of Nantes, Nantes, France. E-mail: Denis.Jacquemin@univ-nantes.fr

<sup>d</sup>Centre of Polymer and Carbon Materials, Polish Academy of Sciences, Curie-Skłodowskiej 34, 41-819 Zabrze, Poland

<sup>e</sup>National Institute of Chemical Physics and Biophysics, Tallinn, Estonia

<sup>f</sup>Department of Physics, Montana State University, Bozeman, MT, 59717, USA. E-mail: arebane@montana.edu

† Electronic supplementary information (ESI) available: Details of the synthesis and spectroscopic characterization of new compounds. CCDC 2101152. For ESI and crystallographic data in CIF or other electronic format see DOI: 10.1039/d1sc05007a



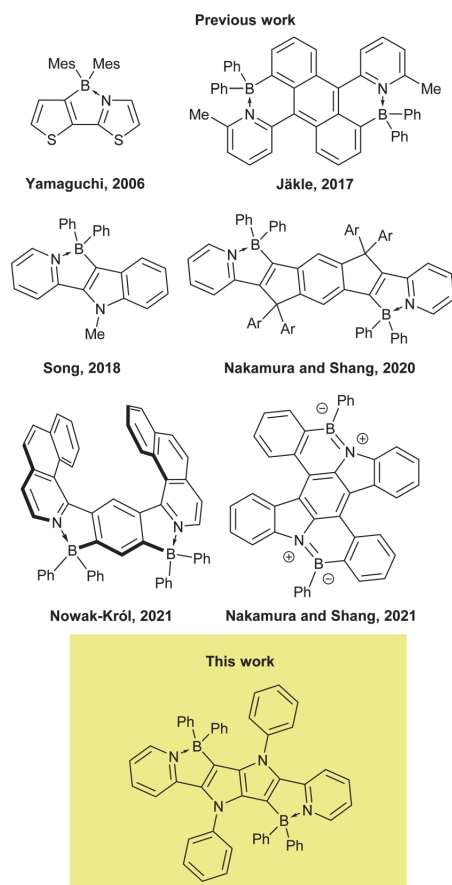


Fig. 1 Chemical structures of the representative dyes possessing a B←N coordination motif.

excellent performance in OLEDs<sup>38a</sup> and OPVs.<sup>38b,c</sup> They were also computed to possess inverted singlet-triplet gap.<sup>39</sup> In such systems, the N–B–N motif not only constrains the  $\pi$ -conjugated skeleton in a coplanar fashion, but also considerably lowers the LUMO level, making the core of the dye a strong acceptor.

1,2,4,5-Tetraarylpyrrolo[3,2-*b*]pyrroles (TAPPs)<sup>40</sup> are aza-analogues of well-known thieno[3,2-*b*]thiophenes.<sup>41</sup> Recent synthetic breakthroughs,<sup>42</sup> prompted their application in research related to studying symmetry breaking in the excited state,<sup>43</sup> solvatochromism,<sup>43b,c</sup> direct solvent probing *via* H-bonding interactions<sup>44</sup> photochromic analysis of halocarbons<sup>45</sup> organic light emitting diodes<sup>46</sup> resistive memory devices,<sup>47</sup> bulk heterojunction organic solar cells,<sup>48</sup> dye-sensitized solar cells,<sup>49</sup> aggregation-induced emission<sup>50</sup> and MOFs.<sup>51</sup> Furthermore, the very high reactivity at positions 3 and 6 of the pyrrolo[3,2-*b*]pyrrole core makes them very convenient starting materials for the construction of ladder type heterocycles. Taking advantage of this feature, many reports have been published on the synthesis and properties of TAPP-based PAHs,<sup>52</sup> however, there

has only been one successful synthesis of BN-embedded TAPPs (Fig. 1).<sup>53</sup> The resulting dyes, containing boron atoms incorporated into six-membered cycles, exhibited very high absorption coefficients and strong fluorescence, both in solution and the solid state, with very small Stokes shifts.

Although the combination of suitable photophysical properties have made TAPPs and fused TAPP analogues popular chromophores for a range of applications, shifting their emission to the red region of the visible spectrum has proved difficult. We have sought to address this issue in this work. Here, we have considered the reaction of pyrrolo[3,2-*b*]pyrroles bearing 2-pyridyl substituents in positions 2 and 5 (C=N bonds in N-heteroaromatic rings are effective in coordinating with boron moieties) with an appropriate boron source (Scheme 1). The resultant B←N=C five membered chelate ring fuses the pyrrolopyrrole and pyridine substituents together and effectively fixes the  $\pi$ -conjugated framework in a coplanar fashion resulting in the formation of a unique chromophore, which perfectly fits into the current intense research on BN-embedded heteroarenes.

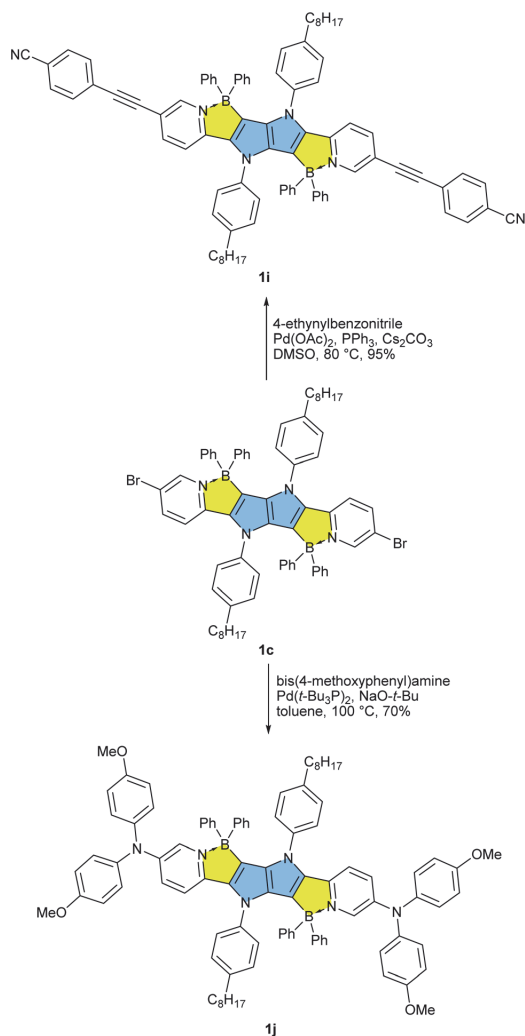
## Results and discussion

### Design and synthesis

Our approach towards new BN-embedded heterocycles capitalizes on pyrrolo[3,2-*b*]pyrroles' intrinsically high reactivity at positions 3 and 6, and on the straightforward access to derivatives bearing pyridyl substituents at positions 2 and 5 (Scheme 1). The necessary TAPPs **2a–2e** were obtained in good yields from appropriate formylpyridines and 4-octylaniline using our optimized multicomponent condensation (see ESI† for details).<sup>42a</sup> TAPPs **2f–2h** were formed in lower, but sufficient yields from appropriate quinoline- and isoquinoline-derived aldehydes. We anticipated that the planar structure of BN-embedded heterocycles would result in extensive  $\pi$ -stacking, therefore long alkyl chains were installed on the N-linked aryl substituents in order to secure good solubility of the final products. In the next step, we planned to apply a well-known strategy consisting of treatment of the parent pyrrolopyrrole with  $\text{BBr}_3$  in the presence of base, however, this led to complete decomposition of the starting material. An alternative route was to use diarylchloroboranes, but this seemed difficult due to the limited availability of such reagents. Fortunately, Song and co-workers recently developed a straightforward cascade B–Cl/C–B cross-metathesis and C–H bond borylation procedure,<sup>54</sup> which we successfully used in the synthesis of the desired four-coordinated boron-containing pyrrolo[3,2-*b*]pyrroles **1a–1h** (BN-TAPPs) (Scheme 1). According to Song's findings, in this procedure aryltrifluoroborate reacts with  $\text{SiCl}_4$  to form aryl-dichloroborane in highly selective manner, which then reacts with another molecule of aryltrifluoroborate to give diphenylchloroborane. Subsequent pyridine directed electrophilic aromatic borylation leads to four-coordinate triarylborane. The yields in the last step are greatly improved when sterically hindered organic base is applied. Importantly, this simple procedure can be conveniently applied to starting materials containing both pyridyl and quinolinyl substituents, and it

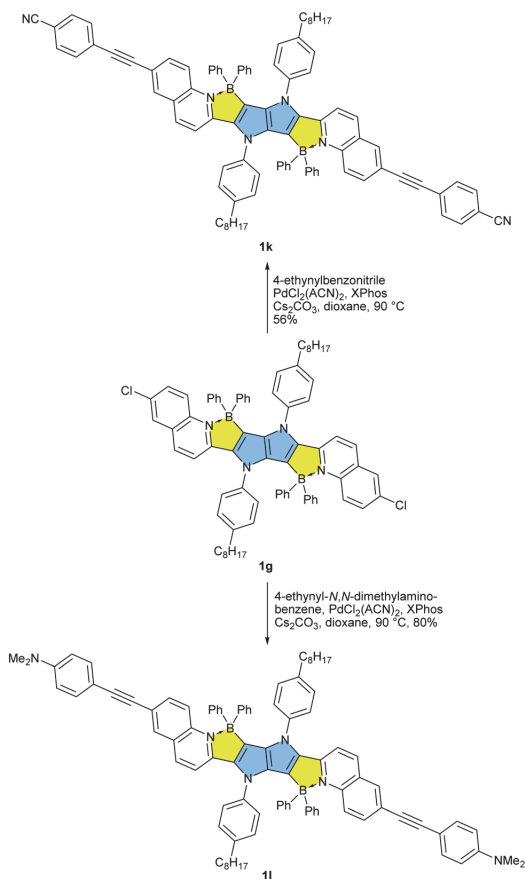






Scheme 2 Post functionalization of BN-TAPP **1c** leading towards dyes **1i** and **1j**.

band between 600 and 700 nm (see ESI†). Theoretical calculations indicate that the latter is most likely not connected to the isolated **1h** structure (see below), whereas preliminary measurements did not detect formation of aggregates or other related structures. Similarly, the emission maxima were red-shifted by over 100 nm, with very small Stokes shifts of less than  $1000\text{ cm}^{-1}$  and large fluorescence quantum yields for most of the dyes. These results clearly indicate a rigidifying effect of the boron component thanks to the character of boron atoms. Noticeably, in the case of compounds **1k** and **1l**, in which the  $\pi$ -systems were further expanded, the barrier of 600 nm for both absorption and emission maxima was broken, which means that these are the first examples of pyrrolo[3,2-*b*]pyrrole derivatives absorbing and



Scheme 3 Post functionalization of BN-TAPP **1g** leading towards dyes **1k** and **1l**.

emitting in the deep-red region. For dyes **1i**, **1k** and **1l**, exceptionally high extinction coefficients were observed, exceeding  $100\,000\text{ M}^{-1}\text{ cm}^{-1}$ , together with large  $\Phi_{\text{fl}}$ . This combination of properties is particularly rare for deep red-emitting dyes due to additional deactivation pathways by vibrational relaxation (*energy gap law*). A very weak emission was detected at 670 nm for dye **1h**. The excitation spectrum however, is not consistent with the absorption profile, which points at potential more complex underlying photophysics to be addressed in subsequent investigations. When compared to recently published, structurally related B/N-doped *p*-arylenevinylene chromophores,<sup>35</sup> BN-TAPPs absorb and emit at much longer wavelengths, with the difference being most noticeable for the derivatives bearing similar, unsubstituted quinoline moieties (63 nm and 80 nm bathochromic shift in the absorption and emission maxima, respectively). *p*-Arylenevinylene analogues of BN-TAPPs exhibit higher fluorescence quantum yields which are close to being quantitative, although the latter compounds are characterized by much higher molar extinction coefficients, which overall results in



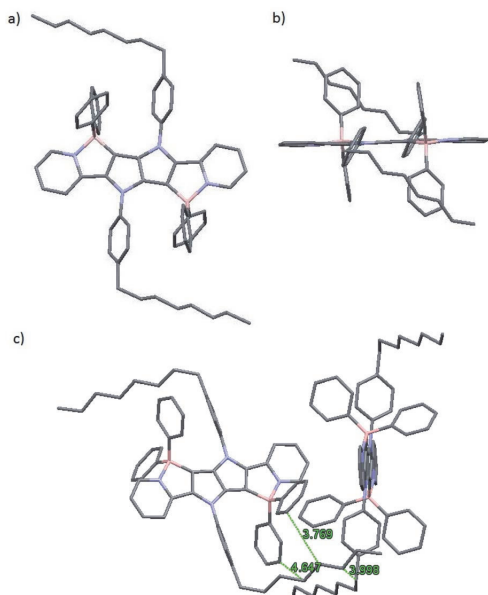


Fig. 2 (a) Top view, (b) side view and (c) crystal packing of **1a** as determined from X-ray crystallography (CCDC). Hydrogen atoms were omitted for clarity. Distances are given in angstroms.

a similar emissive brightness for these two classes of organic chromophores.

### Photostability

Photostability tests were carried out for compounds **1a** and **2a** as representative examples (Fig. 4). TAPPs, which generally exhibit very poor stability under irradiation, acquire remarkable photostability upon incorporation of boron, as demonstrated by comparing the properties of **1a** with common dyes, such as **BODIPY** and **diketopyrrolopyrroles**. Even prolonged exposure to a strong light source did not cause any noticeable changes in the absorption spectrum of **1a**.

### Two-photon absorption

Two-photon absorption studies were performed using a two-photon excited fluorescence (2PEF) method (Table 1 and Fig. 5). Similarly to previously studied symmetric TAPPs,<sup>40,43b,c</sup> the most prominent two-photon transitions are observed at higher energies, well above the lowest-energy one-photon allowed  $S_0 \rightarrow S_1$  transition. The latter is only very weakly present in the two-photon spectra, thus following the Laporte rule for low-energy bands. At energies above the  $S_0 \rightarrow S_1$  transition, the 2PA profiles of **1a–e** show similar features comprising a double-band or vibronic progression at 800–950 nm and a distinct peak at ca. 650–670 nm. At <600 nm there is a steep increase of the cross section due to the near-resonance enhancement effect, followed by onset of linear absorption at even shorter wavelengths (not shown). When pyridine is

replaced with quinoline (**1f**, **1g**) and further with the addition of diarylamino groups, these spectral features undergo a gradual bathochromic shift. Two-photon absorption was not investigated in the case of dye **1h** for two main reasons: (1) the fluorescence intensity is too weak for 2PEF method to be used; (2) the perplexing photophysics of this BN-TAPP has to be delineated before intrinsically more complex non-linear phenomena will be studied. The substantial change, however, comes only after adding strong electron-withdrawing groups at the periphery (dyes **1j** and **1k**).

In such case the peak  $\sigma_2$  becomes remarkably large, exceeding  $10^3$  GM. In the case of the dyes **1k** and **1l**, the peak values at 760–870 nm reach  $\sigma_2 = 2500$  GM and 1800 GM, respectively, whereas strongly resonance-enhanced values at higher energy become even larger. These values are significantly higher than for simpler A–D–A type TAPPs.<sup>43b,c</sup> An important feature to note is that the values are higher for the case with the peripheral diaryl-amino groups which would suggest that the new heterocyclic core is somewhat electron-withdrawing.

### First-principle studies

Time-Dependent Density Functional Theory (TD-DFT) has been used to explore the nature of the excited-states involved in the BN-TAPPs **1a–1k**. The technical details are given in the ESI.† Table 2 summarizes the main results obtained by the calculations.

Let us start our analysis by the one-photon absorption. In the full series (except for **1h**), the  $S_0 \rightarrow S_1$  transition is well separated from the next one, and is strongly dipole allowed with oscillator strengths ranging from 0.71 to 2.33. The  $S_0 \rightarrow S_1$  transition undoubtedly corresponds to the observed most red-shifted absorption band. Experimentally, this absorption band is typically composed of two peaks and a shoulder, resulting from vibronic couplings. To ascertain this statement, we have performed vibrationally resolved calculations within the FC-AH approach<sup>57</sup> for a simplified version of dye **1f** (see Fig. S4†). As can be seen, the overall topology of both the absorption and emission bands is reproduced confirming the vibronic nature of these two peaks. For **1h**, the three lowest excited-states are very close according to theory (Table 1), with differences below the TD-DFT accuracy, so that it is not possible to have a definitive information regarding their ordering.

While one cannot compare directly computed vertical absorption wavelengths to experimental  $\lambda_{\text{abs}}^{\text{max}}$ , it is also obvious that the trends in the series are reproduced by calculations. Indeed, taking **1a** as reference, one notices that the strongest red-shift is obtained for **1c** (theory: +17 nm, experiment: +26 nm) in the **1a–1e** series. For the six dyes showing the most red-shifted absorption, the experimental order is **1j** ~ **1i** < **1f** < **1g** < **1l** ~ **1k**, whereas theory yields: **1j** < **1f** < **1i** ~ **1g** < **1l** ~ **1k**.

For all investigated dyes but **1j**, the second and third excited states are very close on the energy scale, but possess vastly different oscillator strengths, which is a consequence of the nearly centro-symmetric nature of the investigated dyes. This second (or third) state corresponds to the second weaker absorption band found in the 380–420 nm region



Table 1 Spectroscopic properties of dyes 1a-1l in toluene

| Compound  | $\lambda_{\text{abs}}^{\text{max}}$ [nm] | $\epsilon_{\text{max}}$ [M <sup>-1</sup> cm <sup>-1</sup> ] | $\lambda_{\text{em}}^{\text{max}}$ [nm] | Stokes shift [cm <sup>-1</sup> ] | $\Phi_{\text{fl}}$ | $2\lambda_{\text{abs}}^{\text{max}}$ [nm] | $\lambda_{2\text{PA}}^{\text{max}}$ [nm] | $\sigma_{2\text{PA}}^{\text{max}}$ [GM] | $\sigma_{2\text{PA}}^{\text{max}} \Phi_{\text{fl}}$ [GM] |
|-----------|--|---|---|----------------------------------|--------------------|---|--|---|--|
|           |  |   |   |                                  |                    |   |  |   |  |
| <b>1a</b> | 502                                      | 42 500  | 521                                     | 730                              | 0.78 <sup>a</sup>  | 1004                                      | 650                                      | 104                                     | 80   |
|           | 474                                      | 40 100  |   |                                  |                    | 948                                       |  |   |  |
|           | 380                                      | 26 800  |   |                                  |                    | 760                                       |  |   |  |
| <b>1b</b> | 504                                      | 52 500  | 520                                     | 610                              | 0.77 <sup>a</sup>  | 1008                                      | 660                                      | 102                                     | 80   |
|           | 476                                      | 44 100  |   |                                  |                    | 952                                       |  |   |  |
|           | 406                                      | 18 200  |   |                                  |                    | 812                                       |  |   |  |
| <b>1c</b> | 528                                      | 42 800  | 553                                     | 860                              | 0.28 <sup>a</sup>  | 1056                                      | 670                                      | 188                                     | 50   |
|           | 499                                      | 42 700  |   |                                  |                    | 998                                       |  |   |  |
|           | 397                                      | 34 000  |   |                                  |                    | 794                                       |  |   |  |
| <b>1d</b> | 513                                      | 48 700  | 533                                     | 730                              | 0.42 <sup>a</sup>  | 1026                                      | 660                                      | 176                                     | 70   |
|           | 484                                      | 44 600  |   |                                  |                    | 968                                       |  |   |  |
|           | 392                                      | 29 200  |   |                                  |                    | 784                                       |  |   |  |
| <b>1e</b> | 520                                      | 20 900  | 557                                     | 1280                             | 0.28 <sup>a</sup>  | 1040                                      | 640                                      | 93                                      | 25   |
|           | 494                                      | 25 500  |   |                                  |                    | 988                                       |  |   |  |
|           | 391                                      | 34 500  |   |                                  |                    | 782                                       |  |   |  |
| <b>1f</b> | 583                                      | 80 000  | 601                                     | 510                              | 0.78 <sup>b</sup>  | 1166                                      | 940                                      | 200                                     | 160  |
|           | 542                                      | 57 600  |   |                                  |                    | 1084                                      |  |   |  |
|           | 379                                      | 27 600  |   |                                  |                    | 758                                       |  |   |  |
| <b>1g</b> | 598                                      | 80 900  | 616                                     | 490                              | 0.75 <sup>b</sup>  | 1196                                      | 920                                      | 270                                     | 200  |
|           | 555                                      | 57 900  |   |                                  |                    | 1110                                      |  |   |  |
|           | 388                                      | 29 800  |   |                                  |                    | 776                                       |  |   |  |
| <b>1h</b> | 469                                      | 84 100  | — <sup>c</sup>                          | — <sup>c</sup>                   | — <sup>c</sup>     | —   | — <sup>c</sup>                           | —                                       | —  |
| <b>1i</b> | 566                                      | 134 000   | 589                                     | 690                              | 0.92 <sup>b</sup>  | 1132                                      | 800                                      | 1400                                    | 1300   |
|           | 431                                      | 90 700  |   |                                  |                    | 862                                       |  |   |  |
|           | 420                                      | 28 200  |   |                                  |                    | 840                                       |  |   |  |
| <b>1j</b> | 563                                      | 62 900  | 590                                     | 810                              | 0.75 <sup>b</sup>  | 1124                                      | 790                                      | 590                                     | 440  |
|           | 533                                      | 51 600  |   |                                  |                    | 1066                                      |  |   |  |
|           | 424                                      | 50 500  |   |                                  |                    | 848                                       |  |   |  |
| <b>1k</b> | 620                                      | 150 000   | 639                                     | 480                              | 0.78 <sup>b</sup>  | 1240                                      | 760                                      | 2500                                    | 2000   |
|           | 574                                      | 93 800  |   |                                  |                    | 1148                                      |  |   |  |
|           | 536                                      | 37 500  |   |                                  |                    | 1072                                      |  |   |  |
| <b>1l</b> | 618                                      | 135 000   | 639                                     | 530                              | 0.88 <sup>b</sup>  | 1236                                      | 870                                      | 1800                                    | 1600   |
|           | 573                                      | 81 300  |   |                                  |                    | 1146                                      |  |   |  |
|           | 534                                      | 29 600  |   |                                  |                    | 1068                                      |  |   |  |

<sup>a</sup> Determined with fluorescein in NaOH (0.01 M) as a standard. <sup>b</sup> Determined with cresyl violet perchlorate in MeOH as a standard. <sup>c</sup> Fluorescence of dye **1h** was not investigated in 2PA due to the inconsistency of the one-photon fluorescence excitation results.

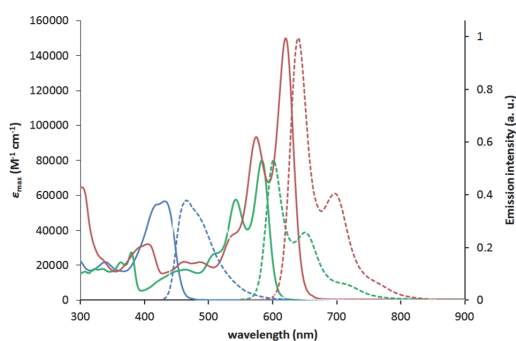


Fig. 3 Absorption (solid lines) and normalized emission (dashed lines) of compounds **2f** (blue), **1f** (green) and **1k** (red) measured in toluene.

experimentally (Tables 1 and 2). For dye **1a**, we show density difference plots in Fig. 6. For all three states the central pyrrolopyrrole unit acts as a donor group and the side pyridine rings

are accepting moieties. The quadrupolar CT character is, however, not strongly marked for the lowest transition and becomes significantly stronger in the two higher ones. As can be seen, the nature of the state is conserved when going to **1f** (derived from quinoline), the contribution of the additional benzene rings being trifling for the first state and remaining limited in the two higher states. In dye **1i**, the lowest excited state is partially delocalized on the ethynyl bridges, whereas in **1j**, the electron-donating amino groups play their expected role (Fig. 7) explaining the observed redshifts.

As far as fluorescence is concerned, for only one dye of the series, namely, **1h**, the optimization of the excited-state geometry led to a nearly dark state ( $f = 0.009$ ), suggesting a very slow radiative decay rate. This is consistent with the trifling emission quantum yield measured experimentally (see Table 1). Indeed the computational studies revealed that the lowest energy allowed transition is markedly blue-shifted placing is energetically close to the dark state. The fact that this pair of opposite-parity electronic states may become almost isoenergetic corroborates the anomalous photophysical behavior of dye **1h**





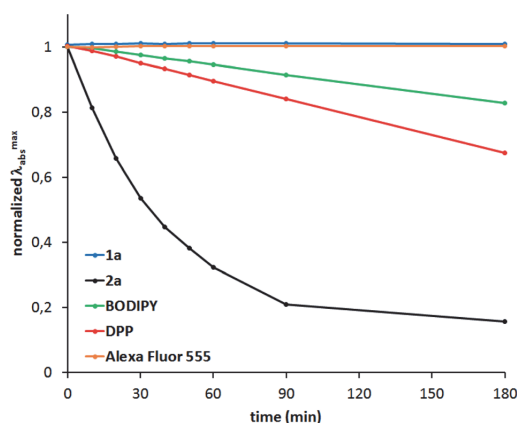


Fig. 4 Photostability of **1a** and **2a** compared to a BODIPY (BODIPY 493/503), DPP (2,5-dioctyl-3,6-bis(3,4,5-trimethoxyphenyl)pyrrolo [3,4-c]pyrrole-1,4(2H,5H)-dione) and Alexa Fluor 555 measured using a collimated light source from a 300 W Xe lamp.

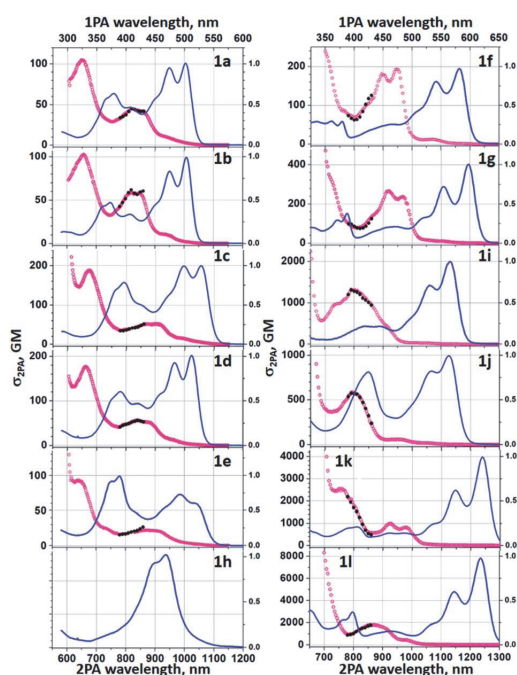


Fig. 5 2PA cross section spectra of **1a**–**1l** in toluene (red symbols, lower horizontal and left vertical axis); Normalized to the peak linear absorption spectra (blue line, upper horizontal and right vertical axis) is shown for comparison. Absolute  $\sigma_{2PA}$  values were measured in the range  $\lambda_{2PA} = 780$ – $850$  nm (black symbols).

(*vide infra*). Apart from this specific case, one globally finds similar substituent effects as for absorption. In Table 2, we also report the 0–0 wavelengths that offer more physically well-

Table 2 Computed vertical absorption wavelengths (in nm) for the lowest singlet states of all compounds with the corresponding oscillator strengths and 2PA cross-sections (in GM). For the lowest state, we also report the vertical emission wavelength and the computed 0–0 wavelength. See the experimental section for details

| Compound  | Vert. $\lambda_{\text{abs}}$ | $f$   | $\sigma_{2PA}$ | Vert. $\lambda_{\text{em}}$ | $\lambda_{0-0}$ |
|-----------|------------------------------|-------|----------------|-----------------------------|-----------------|
| <b>1a</b> | 422                          | 0.86  | 0              | 493                         | 463             |
|           | 352                          | 0.00  | 94             |                             |                 |
|           | 351                          | 0.42  | 0              |                             |                 |
|           | 322                          | 0.26  | 0              |                             |                 |
| <b>1b</b> | 424                          | 0.88  | 0              | 496                         | 465             |
|           | 348                          | 0.00  | 119            |                             |                 |
|           | 314                          | 0.23  | 0              |                             |                 |
| <b>1c</b> | 439                          | 1.03  | 0              | 514                         | 472             |
|           | 367                          | 0.00  | 122            |                             |                 |
|           | 362                          | 0.43  | 0              |                             |                 |
| <b>1d</b> | 336                          | 0.34  | 0              |                             |                 |
|           | 430                          | 0.86  | 0              | 502                         | 460             |
|           | 362                          | 0.42  | 0              |                             |                 |
|           | 358                          | 0.00  | 118            |                             |                 |
| <b>1e</b> | 330                          | 0.30  | 0              |                             |                 |
|           | 427                          | 0.71  | 0              | 500                         | 472             |
|           | 372                          | 0.00  | 74             |                             |                 |
| <b>1f</b> | 351                          | 0.41  | 0              |                             |                 |
|           | 335                          | 0.41  | 0              |                             |                 |
|           | 479                          | 1.14  | 0              | 560                         | n.d.            |
|           | 384                          | 0.00  | 418            |                             |                 |
| <b>1g</b> | 379                          | 0.39  | 0              |                             |                 |
|           | 317                          | 0.29  | 3              |                             |                 |
|           | 494                          | 1.17  | 0              | 572                         | 534             |
| <b>1h</b> | 395                          | 0.00  | 428            |                             |                 |
|           | 394                          | 0.43  | 0              |                             |                 |
|           | 326                          | 0.32  | 4              |                             |                 |
|           | 424                          | 1.04  | 0              | 541 <sup>a</sup>            | 484             |
| <b>1i</b> | 418                          | 0.00  | 6              |                             |                 |
|           | 417                          | 0.77  | 0              |                             |                 |
|           | 489                          | 2.33  | 0              | 572                         | 524             |
| <b>1j</b> | 386                          | 0.52  | 0              |                             |                 |
|           | 373                          | 0.01  | 1790           |                             |                 |
|           | 343                          | 0.353 | 1              |                             |                 |
|           | 469                          | 1.43  | 0              | 552                         | 505             |
| <b>1k</b> | 410                          | 0.00  | 82             |                             |                 |
|           | 378                          | 0.57  | 0              |                             |                 |
|           | 346                          | 0.50  | 0              |                             |                 |
|           | 334                          | 0.00  | 1760           |                             |                 |
| <b>1l</b> | 518                          | 2.11  | 0              | 599                         | 558             |
|           | 405                          | 0.57  | 0              |                             |                 |
|           | 400                          | 0.00  | 1600           |                             |                 |
|           | 340                          | 0.92  | 5              |                             |                 |
| <b>1l</b> | 516                          | 2.26  | 0              | 597                         | 560             |
|           | 406                          | 0.01  | 381            |                             |                 |
|           | 395                          | 0.61  | 1              |                             |                 |
|           | 358                          | 0.00  | 10 900         |                             |                 |

<sup>a</sup> Nearly dark state after optimization.

grounded comparisons with experiment,<sup>57b</sup> and more precisely, with the crossing point between absorption and emission. Illustratively, for **1a**, **1j** and **1l**, we compute  $\lambda_{0-0}$  of 463, 505, and 560 nm, respectively. These values are blue-shifted by +0.26, 0.31, and 0.24 eV as compared to the measured values of 512, 577, and 629 nm. These errors are on the upper side of the



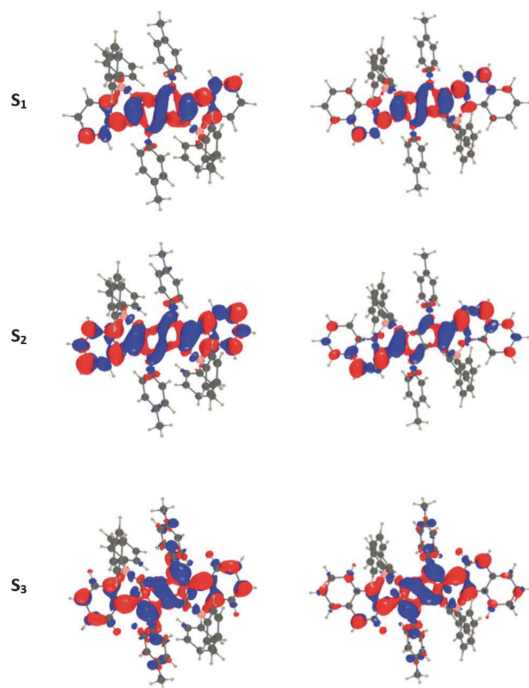


Fig. 6 Density difference plots for the three lowest transitions of **1a** (left) and **1f** (right). From top to bottom excitation to  $S_1$ ,  $S_2$ , and  $S_3$ . The crimson and blueberry lobes indicate an increase and decrease of density upon excitation, respectively. Contour threshold: 0.001 au.

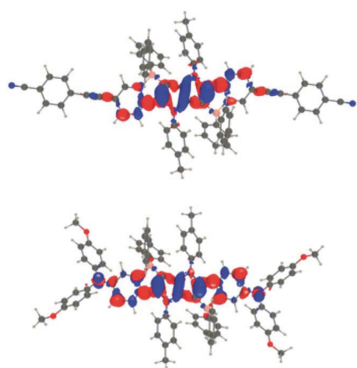


Fig. 7 Density difference plots for the lowest transitions of **1i** (top) and **1j** (bottom). See caption of Fig. 6 for more details.

typical TD-DFT errors, which can be explained by the very specific nature of these boron-containing systems: TD-DFT is known to overshoot the transition energies of such states.<sup>58</sup>

We have also computed two-photon absorption cross sections. In **1a**, the experimental rather broad response around 800–900 nm is due to the  $S_0 \rightarrow S_2$  transition that is dark in one-

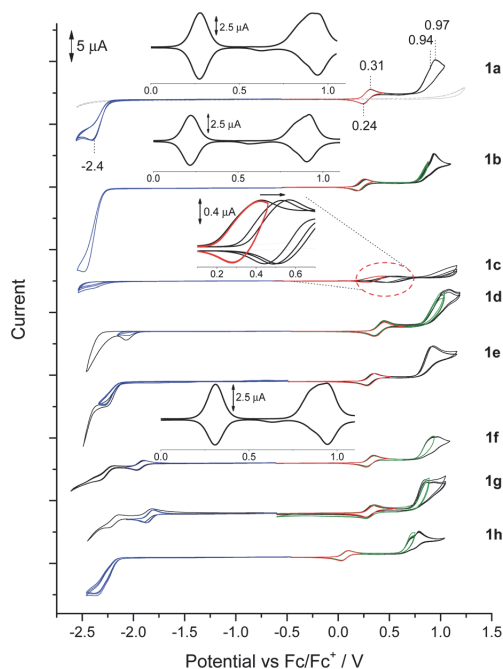


Fig. 8 Cyclic voltammograms in the solution of BN-TAPP-series compounds (1 mM) in 0.1 M  $\text{Bu}_4\text{NBF}_4/\text{DCM}$ . Oxidation (red, black CVs), reduction (blue, black CVs), second oxidation (green, black CVs).

photon, a typical outcome in quadrupolar dyes. Theory provides a peak  $\sigma_{2\text{PA}}$  of 94 GM, of the same order of magnitude as the experimental response (45 GM). This response remains of the same order of magnitude but is slightly increased in **1b**, **1c**, and **1d**, but slightly decreased in **1e**, which holds both in the experiment and in the simulations. In **1f**, the  $\sigma_{2\text{PA}}$  attains the respectable value of ca. 220 GM experimentally, and it is clear that it is again the second state that is responsible for this response (418 GM theoretically). The situation is totally similar in **1g**. In the more extended **1i**, the calculations indicate that the 2PA response comes from the  $S_0 \rightarrow S_3$  transition, which is consistent with the experimental spectra. Again, theory gives value that closely matches the experiment (1500 GM *versus* 1400 GM). In **1i**, the experimental 2PA spectrum shows two bands, one moderately active due to the second transition, and one much more intense due to the fifth state. In **1k**, the second and third states appear at almost the same energy but have different (pseudo) symmetry, one being active in one-photon, the other in two-photon absorption, potentially explaining the shape of the experimental spectra resembling a superposition between the two phenomena. The computed response is 1600 GM for the 2PA-active transition, again with the same order of magnitude as the experimental measurement. Eventually, the analysis is more difficult in **1l**, but it appears that the second excited state should be responsible for the shoulder in the 2PA experimental spectrum at ca. 475 nm, whereas the fourth transition likely yields the much more intense peaks at ca. 440 nm.



**Table 3** Potential of cathodic peak (cp) and anodic peak (ap) of oxidation (ox) and reduction (red) processes of BN-TAPPs (1 mM) in 0.1 M Bu<sub>4</sub>NBF<sub>4</sub>/DCM; values in volts vs. Fc/Fc<sup>+</sup> couple; potential sweep rate 0.05 V s<sup>-1</sup>

| Compound  | $E_{ox}^1$ |            | $E_{ox}^{2a}$ | $E_{ox}^{2b}$ | $E_{red}^1$ |            | $E_{red}^2$ |            | HOMO (eV) | LUMO (eV) |
|-----------|------------|------------|---------------|---------------|-------------|------------|-------------|------------|-----------|-----------|
|           | $E_{ap}^1$ | $E_{cp}^1$ | $E_{ap}^{2a}$ | $E_{ap}^{2b}$ | $E_{cp}^1$  | $E_{ap}^1$ | $E_{cp}^2$  | $E_{ap}^2$ |           |           |
| <b>1a</b> | 0.31       | 0.24       | 0.94          | 0.97          | -2.40       | —          | —           | —          | -5.30     | -2.84     |
| <b>1b</b> | 0.25       | 0.19       | 0.87          | 0.93          | -2.48       | —          | —           | —          | -5.26     | -2.81     |
| <b>1c</b> | 0.42       | 0.28       | —             | —             | -2.38       | —          | —           | —          | -5.31     | -2.81     |
| <b>1d</b> | 0.45       | 0.36       | 1.02          | 1.08          | -2.04       | —          | —           | —          | -5.43     | -3.13     |
| <b>1e</b> | 0.34       | 0.26       | 0.90          | —             | -2.30       | —          | —           | —          | -5.34     | -2.98     |
| <b>1f</b> | 0.35       | 0.28       | 0.93          | 0.97          | -1.97       | -1.90      | -2.32       | —          | -5.35     | -3.24     |
| <b>1g</b> | 0.41       | 0.34       | 0.92          | 1.01          | -1.78       | -0.68      | -1.11       | —          | -5.35     | -3.32     |
| <b>1h</b> | 0.11       | 0.05       | 0.74          | 0.81          | -2.46       | —          | —           | —          | -5.12     | -2.96     |

### Electrochemical properties

BN-TAPPs **1a–1l** are characterized by the presence of a reversible redox pair of the first oxidation process (Fig. 8, red CVs, Table 3) which according to its potential value can be tentatively attributed to the oxidation of the *N,N'*-diphenylpyrrolo[3,2-*b*]pyrrole core. An exception is **1c** where partial reversibility was found, the cause of which was further investigated during spectroelectrochemical measurements (*vide infra*). The lowest value of the first oxidation potential in the entire BN-TAPP series (0.11 V) was recorded for the derivative **1h** with isoquinoline scaffolds. For the remaining dyes the first oxidation occurs between 0.25 and 0.45 V which corresponds to HOMO values in the range (-5.26 eV)–(-5.43 eV) (Table 3). Compared to structurally analogous dyes possessing two thiophene rings BN-TAPPs are slightly less electron-rich but they are more electron-rich than dyes  $\pi$ -expanded TAPPs possessing two thiophene-*S,S*-dioxide moieties.<sup>52b</sup>

The second oxidation curve is partially irreversible in all cases (Fig. 8, green and black CVs) and shows a dual nature more visible in differential pulse voltammetry (DPV) experiments (Fig. 8, e.g. **1a** and **1b** – inserts). The double peak of the second oxidation state may indicate a slight difference in oxidation potential between both peripheral units, which was also registered in separate processes as green and black CV curves with the peak potential marked as  $E_{ox}^{2a}$  and  $E_{ox}^{2b}$ , respectively. Dyes **1h** and **1d** possess, respectively, the lowest (0.74 V) and highest (1.02 V) potential of  $E_{ox}^{2a}$ . Irreversibility of the second oxidation does not impact on the potential and reversibility of the first redox couple in subsequent CV cycles after polarity reversal.

DPV measurements also show that the peak areas of the first and second oxidation peaks are comparable, which indicates the full oxidation of the *N,N'*-diphenylpyrrolo[3,2-*b*]pyrrole scaffold under the potential of the first oxidation peak to

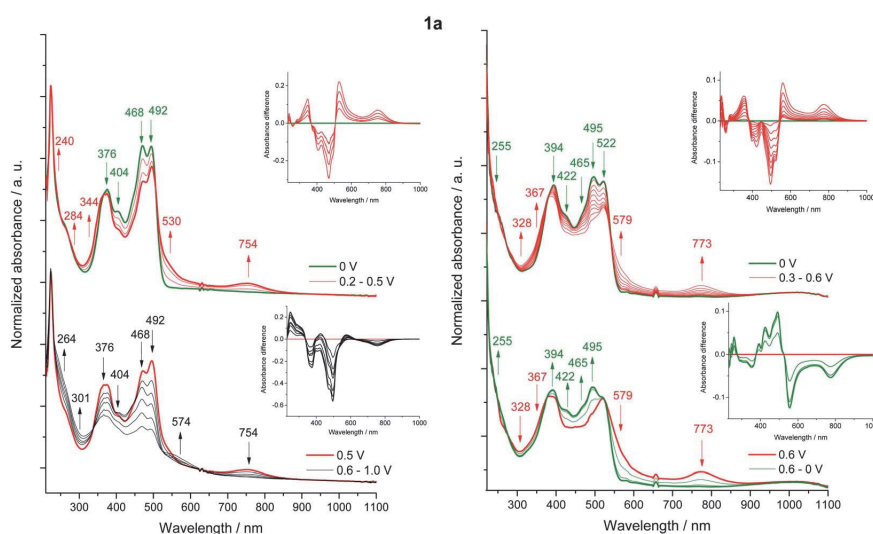


**Fig. 9** *In situ* UV-Vis-NIR spectra of **1a** (left) and **1c** (right); differential UV-Vis-NIR absorbance (insets) in 1 mM sample solution in 0.1 M Bu<sub>4</sub>NBF<sub>4</sub>/DCM within the potential of the first (red) (**1a**, **1c**) and second (black) oxidation peaks (**1a**); at 0 V or the returning to 0 V (green).





dication or di(radical cation), while the second oxidation peak is associated with the oxidation of both the peripheral moieties.

One irreversible reduction process was registered for BN-TAPPs **1a–1e** bearing two pyridine moieties at (−2.40)–(−2.04 V). In the case of dye **1f** (bearing two quinoline moieties), we observed two reduction processes, and the first was fully reversible. The values of reduction were shifted towards positive potentials, compared with the pyridine series.

### Spectroelectrochemistry

Changes in the UV-Vis-NIR absorption spectra during polarization within the first oxidation peak revealed a decrease in the intensity of the bands at 468, 492 nm (**1a**) and 495 and 522 nm (**1c**)<sup>59</sup> (Fig. 9), while the shift of the absorption in the infrared direction of the output bands of **1c** indicates a decrease in the energy of the  $\pi$ – $\pi^*$  transition due to a partial localization of the HOMO orbital also on the pyridine rings. Polarization within the first oxidation peak causes an increase in the bands at 530, 734 nm (**1a**) and 579, 773 nm (**1c**), characteristic for a di(radical cationic) state, as was observed in a previous spectroelectrochemical study of dyes based on the pyrrolo[3,2-*b*]pyrrole scaffold.<sup>52b</sup> The gradual formation of a radical cation and its transition to di(radical cation) was not observed.

ESR spectroelectrochemical measurements were performed for representative dyes **1a** and **1c**, where the reversible first redox process is associated with the formation of a di(radical cation) in both cases. Unpaired electrons of the di(radical cation) of **1a** are located on the *N,N'*-diphenylpyrrolo[3,2-*b*]pyrrole core and are characterized by a low value of the *g*-factor ( $g = 2.0023$ ). In turn, the ESR signal recorded under polarization of the first oxidation state of **1c** gives the *g*-factor equal 2.0050, which may indicate the coupling of one of the electrons of the di(radical cation) with nitrogen and/or boron atoms, as proposed in Scheme S1.† Although the ESR signals are quite broad in both cases, which may indicate the cleavage of the energy levels of the unpaired electron by the nuclei coupled to it, the hyperfine structure was not recorded.

### Conclusions

In summary, we have designed, synthesized and fully characterized a new family of BN-embedded heteroacenes. This was achieved through incorporation of dual cyclopenta[*c*][1,2]azaborole moieties with a pyrrolo[3,2-*b*]pyrrole core in a straightforward two-step synthetic procedure. The  $B^-N^+$  dative bond reduces the HOMO–LUMO gap of the parent dye, which results in a marked red-shift of absorption and emission and almost quantitative fluorescence quantum yield. Their excellent properties, such as superb photostability, strong absorption and intense emission in the orange to deep red region, together with large two-photon absorption cross sections and rich electrochemistry, opens the door for future applications in optoelectronics. Given the recent renaissance of interest in boron-doped PAHs and their related B–N/O isosteres, this work should inspire the future design and synthesis of pyrrolopyrrole and related frameworks with distinctive  $\pi$ -expanded architectures.

### Data availability

Data associated with this article, including experimental procedures, compound characterization, steady-state absorption and emission along with the two-photon absorption details, electrochemical details and computational analysis details are available in the ESI.†

### Author contributions

M. T. conceived the idea and wrote the manuscript. M. T., P. K. and M. P. performed all synthetic experiments including condition optimizations and exploring the scope. M. C. and P. J. performed electrochemical and spectroelectrochemical measurements. M. B. performed several TD-DFT calculations, and vibronic analysis. M. R. performed 2PA measurements. M. L. wrote formal electrochemical analysis and reviewed the manuscript. A. R. performed 2PA measurements, wrote formal analysis of this part of the manuscript and reviewed the manuscript. D. J. performed DFT and TD-DFT calculations, analyzed data, wrote and reviewed the manuscript. D. G. supervised the project, performed formal analysis, wrote and reviewed the manuscript. All the authors discussed the results and commented on the manuscript.

### Conflicts of interest

There are no conflicts to declare.

### Acknowledgements

The work was financially supported by the Polish National Science Centre, Poland (HARMONIA 2018/30/M/ST5/00460), the Foundation for Polish Science (TEAM POIR.04.04.00-00-3CF4/16-00) and EC (MSC ITN CHAIR). A.R. and M.R. acknowledge support by the Ministry of Education and Research, Republic of Estonia grant PRG661 and A.R. by National Science Foundation award CHE 2103628. The authors also thank Dr David C. Young for proofreading the manuscript. M.H.E. and D.J. thank the CCIPL computational center installed in Nantes for generous allocation of computational time.

### Notes and references

- M. Yang, I. S. Park and T. Yasuda, *J. Am. Chem. Soc.*, 2020, **142**, 19468–19472.
- (a) J. A. Knçller, G. Meng, X. Wang, D. Hall, A. Pershin, D. Beljonne, Y. Olivier, S. Laschat, E. Zysman-Colman and S. Wang, *Angew. Chem., Int. Ed.*, 2020, **59**, 3156–3160; (b) Y. Chen, W. Chen, Y. Qiao, X. Lu and G. Zhou, *Angew. Chem., Int. Ed.*, 2020, **59**, 7122–7130.
- R. E. Messersmith, S. Yadav, M. A. Siegler, H. Ottosson and J. D. Tovar, *J. Org. Chem.*, 2017, **82**, 13440–13448.
- F. Qiu, F. Zhang, R. Tang, Y. Fu, X. Wang, S. Han, X. Zhuang and X. Feng, *Org. Lett.*, 2016, **18**, 1398–1401.



- 5 M. Numano, N. Nagami, S. Nakatsuka, T. Katayama, K. Nakajima, S. Tatsumi, N. Yasuda and T. Hatakeyama, *Chem.-Eur. J.*, 2016, **22**, 11574–11577.
- 6 G. Meng, T. Peng, Y. Shi, H. Li, X. Wang, X. Yin, D.-T. Yang, S. Wang and N. Wang, *J. Mater. Chem. C*, 2020, **8**, 7749.
- 7 (a) V. M. Hertz, M. Bolte, H.-W. Lerner and M. Wagner, *Angew. Chem., Int. Ed.*, 2015, **54**, 8800–8804; (b) M. Fingerle, J. Dingerkus, H. Schubert, K. M. Wurst, M. Scheele and H. F. Bettinger, *Angew. Chem., Int. Ed.*, 2021, **60**, 15798–15802; (c) M. Fingerle, C. Maichle-Mössmer, S. Schundelmeier, B. Speiser and H. F. Bettinger, *Org. Lett.*, 2017, **19**, 4428–4431.
- 8 (a) C. J. Saint-Louis, L. L. Magill, J. A. Wilson, A. R. Schroeder, S. E. Harrell, N. S. Jackson, J. A. Trindell, S. Kim, A. R. Fisch, L. Munro, V. J. Catalano, C. E. Webster, P. P. Vaughan, K. S. Molek, A. K. Schrock and M. T. Huggins, *J. Org. Chem.*, 2016, **81**, 10955–10963; (b) A. Caruso Jr, M. A. Siegler and J. D. Tovar, *Angew. Chem., Int. Ed.*, 2010, **49**, 4213–4217.
- 9 (a) A. Abengózar, D. Sucunza, P. García-García, D. Sampedro, A. Pérez-Redondo and J. J. Vaquero, *J. Org. Chem.*, 2019, **84**, 7113–7122; (b) A. Wakamiya, K. Mori and S. Yamaguchi, *Angew. Chem., Int. Ed.*, 2007, **46**, 4273–4276.
- 10 K. Kamada, T. Namikawa, S. Senatore, C. Matthews, P.-F. Lenne, O. Maury, C. Andraud, M. Ponce-Vargas, B. LeGuennic, D. Jacquemin, P. Agbo, D. D. An, S. S. Gauny, X. Liu, R. J. Abergel, F. Fages and A. D'Aléo, *Chem.-Eur. J.*, 2016, **22**, 5219–5232.
- 11 (a) C. Reus, S. Weidlich, M. Bolte, H.-W. Lerner and M. Wagner, *J. Am. Chem. Soc.*, 2013, **135**, 12892–12907; (b) N. Ando, T. Yamada, H. Narita, N. N. Oehlmann, M. Wagner and S. Yamaguchi, *J. Am. Chem. Soc.*, 2021, **143**, 9944–9951; (c) K. Schickedanz, J. Radtke, M. Bolte, H.-W. Lerner and M. Wagner, *J. Am. Chem. Soc.*, 2017, **139**, 2842–2851; (d) P.-F. Zhang, J.-C. Zeng, F.-D. Zhuang, K.-X. Zhao, Z.-H. Sun, Z.-F. Yao, Y. Lu, X.-Y. Wang, J.-Y. Wang and J. Pei, *Angew. Chem., Int. Ed.*, 2021, **60**, 23313–23319; (e) C. Li, Y. Shi, P. Li, N. Zhang, N. Wang, X. Yin and P. Chen, *Org. Lett.*, 2021, **23**, 7123–7128.
- 12 B. Adelizzi, P. Chidchob, N. Tanaka, B. A. G. Lamers, S. C. J. Meskers, S. Ogi, A. R. A. Palmans, S. Yamaguchi and E. W. Meijer, *J. Am. Chem. Soc.*, 2020, **142**, 16681–16689.
- 13 Y.-Q. Yan, Y.-B. Li, J.-W. Wang and C.-H. Zhao, *Chem.-Asian J.*, 2013, **8**, 3164–3176.
- 14 G. Li, Y. Zhao, J. Li, J. Cao, J. Zhu, X.-W. Sun and Q. Zhang, *J. Org. Chem.*, 2015, **80**, 196–203.
- 15 T. Hatakeyama, K. Shiren, K. Nakajima, S. Nomura, S. Nakatsuka, K. Kinoshita, J. Ni, Y. Ono and T. Ikuta, *Adv. Mater.*, 2016, **28**, 2777–2781.
- 16 Y. Xia, M. Zhang, S. Ren, J. Song, J. Ye, M. G. Humphrey, C. Zheng, K. Wang and X. Zhang, *Org. Lett.*, 2020, **22**, 7942–7946.
- 17 J. Full, S. P. Panchal, J. Götz, A.-M. Krause and A. Nowak-Król, *Angew. Chem., Int. Ed.*, 2021, **60**, 4350–4357.
- 18 M. Pinheiro Jr, F. B. C. Machado, F. Plasser, A. J. A. Aquino and H. Lischka, *J. Mater. Chem. C*, 2020, **8**, 7793–7804.
- 19 For review articles, see: (a) A. Wakamiya and S. Yamaguchi, *Bull. Chem. Soc. Jpn.*, 2015, **88**, 1357–1377; (b) S. K. Mellerup and S. Wang, *Trends Chem.*, 2019, **1**, 77–89; (c) S. Agnoli and M. Favaro, *J. Mater. Chem. A*, 2016, **4**, 5002–5025; (d) J. Huang and Y. Li, *Front. Chem.*, 2018, **6**, 341; (e) J. Huang, X. Wang, Y. Xiang, L. Guo and G. Chen, *Advanced Energy and Sustainability Research*, 2021, **2**, 2100016; (f) S. Mukherjee and P. Thilagar, *J. Mater. Chem. C*, 2016, **4**, 2647–2662.
- 20 X.-Y. Wang, F.-D. Zhuang, R.-B. Wang, X.-C. Wang, X.-Y. Cao, J.-Y. Wang and J. Pei, *J. Am. Chem. Soc.*, 2014, **136**, 3764–3767.
- 21 F. Miyamoto, S. Nakatsuka, K. Yamada, K. Nakayama and T. Hatakeyama, *Org. Lett.*, 2015, **17**, 6158–6161.
- 22 S. Osumi, S. Saito, C. Dou, K. Matsuo, K. Kume, H. Yoshikawa, K. Awaga and S. Yamaguchi, *Chem. Sci.*, 2016, **7**, 219–227.
- 23 H. L. van de Wouw, J. Y. Lee, M. A. Siegler and R. S. Klausen, *Org. Biomol. Chem.*, 2016, **14**, 3256–3263.
- 24 H. Helten, *Chem*, 2016, **22**, 12972–12982.
- 25 Y. Zhang, C. Zhang, Y. Guo, J. Ye, B. Zhen, Y. Chen and X. Liu, *J. Org. Chem.*, 2021, **86**, 6322–6330.
- 26 J. Zhou, R. Tang, X. Wang, W. Zhang, X. Zhuang and F. Zhang, *J. Mater. Chem. C*, 2016, **4**, 1159.
- 27 S. Nakatsuka, N. Yasuda and T. Hatakeyama, *J. Am. Chem. Soc.*, 2018, **140**, 13562–13565.
- 28 H. Xin, J. Li, X. Yang and X. Gao, *J. Org. Chem.*, 2020, **85**, 70–78.
- 29 (a) A. Wakamiya, T. Taniguchi and S. Yamaguchi, *Angew. Chem., Int. Ed.*, 2006, **45**, 3170–3173; (b) Y. Min, C. Dou, H. Tian, J. Liu and L. Wang, *Chem.-Eur. J.*, 2021, **27**, 4364–4372; (c) S. A. Iqbal, K. Yuan, J. Cid, J. Pahl and M. J. Ingleson, *Org. Biomol. Chem.*, 2021, **13**, 2949–2958; (d) K. Liu, R. A. Lalancette and F. Jäkle, *J. Am. Chem. Soc.*, 2017, **139**, 18170–18173; (e) T. Sakamaki, T. Nakamuro, K. Yamashita, K. Hirata, R. Shang and E. Nakamura, *Chem. Mater.*, 2021, **33**, 5337–5344.
- 30 (a) F.-D. Zhuang, Z.-H. Sun, Z.-F. Yao, Q.-R. Chen, Z. Huang, J.-H. Yang, J.-Y. Wang and J. Pei, *Angew. Chem., Int. Ed.*, 2019, **58**, 10708–10712; (b) A. Abengózar, I. Valencia, G. G. Otárola, D. Sucunza, P. García-García, A. Pérez-Redondo, F. Mendicuti and J. J. Vaquero, *Chem. Commun.*, 2020, **56**, 3669–3672; (c) X.-Y. Wang, D.-C. Yang, F.-D. Zhuang, J.-J. Liu, J.-Y. Wang and J. Pei, *Chem.-Eur. J.*, 2015, **21**, 8867–8873; (d) A. Abengózar, P. García-García, D. Sucunza, A. Pérez-Redondo and J. J. Vaquero, *Chem. Commun.*, 2018, **54**, 2467–2470; (e) G. Li, W.-W. Xiong, P.-Y. Gu, J. Cao, J. Zhu, R. Ganguly, Y. Li, A. C. Grimsdale and Q. Zhang, *Org. Lett.*, 2015, **17**, 560–563; (f) Y. Chen, W. Chen, Y. Qiao and G. Zhou, *Chem.-Eur. J.*, 2019, **25**, 9326–9338; (g) D.-T. Yang, Y. Shi, T. Peng and S. Wang, *Organometallics*, 2017, **36**, 2654–2660; (h) H. Huang, Y. Zhou, Y. Wang, X. Cao, C. Han, G. Liu, Z. Xu, C. Zhan, H. Hu, Y. Peng, P. Yana and D. Cao, *J. Mater. Chem. A*, 2020, **8**, 22023–22031.
- 31 P. B. Pati, E. Jin, Y. Kim, Y. Kim, J. Mun, S. J. Kim, S. J. Kang, W. Choe, G. Lee, H.-J. Shin and Y. S. Park, *Angew. Chem., Int. Ed.*, 2020, **59**, 14891–14895.



- 32 M. Ando, M. Sakai, N. Ando, M. Hirai and S. Yamaguchi, *Org. Biomol. Chem.*, 2019, **17**, 5500.
- 33 (a) D. C. Young, M. Tasior, A. D. Laurent, L. Dobrzycki, M. K. Cyrański, N. Tkachenko, D. Jacquemin and D. T. Gryko, *J. Mater. Chem. C*, 2020, **8**, 7708–7717; (b) S. Shimizu, T. Iino, A. Saeki, S. Seki and N. Kobayashi, *Chem.–Eur. J.*, 2015, **21**, 2893–2904; (c) Y. Kage, S. Mori, M. Ide, A. Saeki, H. Furuta and S. Shimizu, *Mater. Chem. Front.*, 2018, **2**, 112–120; (d) S. Shimizu, T. Iino, Y. Araki and N. Kobayashi, *Chem. Commun.*, 2013, **49**, 1621–1623; (e) T. Marks, E. Daltrozzi and A. Zumbusch, *Chem.–Eur. J.*, 2014, **20**, 6494–6504; (f) T. Nakano, A. Sumida and K. Naka, *J. Org. Chem.*, 2021, **86**, 5690–5701.
- 34 K. Yang, G. Zhang and Q. Song, *Chem. Sci.*, 2018, **9**, 7666.
- 35 H. Lu, T. Nakamuro, K. Yamashita, H. Yanagisawa, O. Nureki, M. Kikkawa, H. Gao, J. Tian, R. Shang and E. Nakamura, *J. Am. Chem. Soc.*, 2020, **142**, 18990–18996.
- 36 H. Shimogawa, Y. Murata and A. Wakamiya, *Org. Lett.*, 2018, **20**, 5135–5138.
- 37 C. Yu, Z. Huang, X. Wang, W. Miao, Q. Wu, W.-Y. Wong, E. Hao, Y. Xiao and L. Jiao, *Org. Lett.*, 2018, **20**, 4462–4466.
- 38 (a) D. Li, H. Zhang and Y. Wang, *Chem. Soc. Rev.*, 2013, **42**, 8416–8433; (b) R. Zhao, J. Liu and L. Wang, *Acc. Chem. Res.*, 2020, **53**, 1557–1567; (c) J. Huang and Y. Li, *Front. Chem.*, 2018, **6**, 341.
- 39 S. Pios, X. Huang, A. S. Sobolewski and W. Domcke, *Phys. Chem. Chem. Phys.*, 2021, **23**, 12968–12975.
- 40 M. Krzeszewski, D. Gryko and D. T. Gryko, *Acc. Chem. Res.*, 2017, **50**, 2334–2345.
- 41 M. E. Cinar and T. Ozturk, *Chem. Rev.*, 2015, **115**, 3036–3140.
- 42 (a) M. Tasior, B. Koszarna, D. C. Young, B. Bernard, D. Jacquemin, D. Gryko and D. T. Gryko, *Org. Chem. Front.*, 2019, **6**, 2939–2948; (b) A. Janiga, E. Glodkowska-Mrowka, T. Stoklosa and D. T. Gryko, *Asian J. Org. Chem.*, 2013, **2**, 411–415.
- 43 (a) A. I. Ivanov, B. Dereka and E. Vauthey, *J. Chem. Phys.*, 2017, **146**, 164306; (b) D. H. Friese, A. Mikhaylov, M. Krzeszewski, Y. M. Poronik, A. Rebane, K. Ruud and D. T. Gryko, *Chem.–Eur. J.*, 2015, **21**, 18364–18374; (c) E. G. Lukaszewicz, H. G. Ryu, A. Mikhaylov, C. Azarias, M. Banasiewicz, B. Kozankiewicz, K. H. Ahn, D. Jacquemin, A. Rebane and D. T. Gryko, *Chem.–Asian J.*, 2017, **12**, 1736–1748; (d) B. Bardi, M. Krzeszewski, D. T. Gryko, A. Painelli and F. Terenziani, *Chem.–Eur. J.*, 2019, **25**, 13930–13938.
- 44 B. Dereka and E. Vauthey, *Chem. Sci.*, 2017, **8**, 5057–5066.
- 45 J.-Y. Wu, C.-H. Yu, J.-J. Wen, C.-L. Chang and M.-k. Leung, *Anal. Chem.*, 2016, **88**, 1195–1201.
- 46 Y. Zhou, M. Zhang, J. Ye, H. Liu, K. Wang, Y. Yuan, Y.-Q. Du, C. Zhang, C.-J. Zheng and X.-H. Zhang, *Org. Electron.*, 2019, **65**, 110–115.
- 47 R. K. Canjeevaram Balasubramanyam, R. Kumar, S. J. Ippolito, S. K. Bhargava, S. R. Periasamy, R. Narayan and P. Basak, *J. Phys. Chem. C*, 2016, **120**, 11313–11323.
- 48 R. Domínguez, N. F. Montcada, P. de la Cruz, E. Palomares and F. Langa, *ChemPlusChem*, 2017, **82**, 1096–1104.
- 49 J. Wang, Z. Chai, S. Liu, M. Fang, K. Chang, M. Han, L. Hong, H. Han, Q. Li and Z. Li, *Chem.–Eur. J.*, 2018, **24**, 18032–18042.
- 50 (a) B. Sadowski, K. Hassanein, B. Ventura and D. T. Gryko, *Org. Lett.*, 2018, **20**, 3183–3186; (b) Y. Ji, Z. Peng, B. Tong, J. Shi, J. Zhi and Y. Dong, *Dyes Pigm.*, 2017, **139**, 664–671; (c) K. Li, Y. Liu, Y. Li, Q. Feng, H. Hou and B. Z. Tang, *Chem. Sci.*, 2017, **8**, 7258–7267; (d) Y. Ma, Y. Zhang, L. Kong and J. Yang, *Molecules*, 2018, **23**, 3255.
- 51 C. S. Hawes, G. M. ÓMáille, K. Byrne, W. Schmitt and T. Gunnlaugsson, *Dalton Trans.*, 2018, **47**, 10080–10092.
- 52 (a) S. Mishra, M. Krzeszewski, C. A. Pignedoli, P. Ruffieux, R. Fasel and D. T. Gryko, *Nat. Commun.*, 2018, **9**, 1714; (b) M. Tasior, M. Czichy, M. Łapkowski and D. T. Gryko, *Chem.–Asian J.*, 2018, **13**, 449–456; (c) D. Wu, J. Zheng, C. Xu, D. Kang, W. Hong, Z. Duan and F. Mathey, *Dalton Trans.*, 2019, **48**, 6347–6352.
- 53 (a) M. Tasior and D. T. Gryko, *J. Org. Chem.*, 2016, **81**, 6580–6586; (b) M. Krzeszewski, L. Dobrzycki, A. L. Sobolewski, M. K. Cyrański and D. T. Gryko, *Angew. Chem., Int. Ed.*, 2021, **60**, 14998–15005.
- 54 K. Yang, G. Zhang and Q. Song, *Chem. Sci.*, 2018, **9**, 7666–7672.
- 55 D. Kunchala, S. Sa, P. Nayak, S. J. Ponniah and K. Venkatasubbaiah, *Organometallics*, 2019, **38**, 870.
- 56 M. Más-Montoya, M. F. Montenegro, A. E. Ferao, A. Tárraga, J. N. Rodríguez-López and D. Curiel, *Org. Lett.*, 2020, **22**, 3356.
- 57 (a) F. Santoro, R. Improta, A. Lami, J. Bloino and V. Barone, *J. Chem. Phys.*, 2007, **126**, 084509; (b) F. Santoro and D. Jacquemin, *Wiley Interdiscip. Rev.: Comput. Mol. Sci.*, 2016, **6**, 460–486; (c) J. Cerezo and F. Santoro, *FCclasses 3.0*, <http://www.pi.iccom.cnr.it/fcclasses>.
- 58 B. Le Guennic and D. Jacquemin, *Acc. Chem. Res.*, 2015, **48**, 530–537.
- 59 M. Tasior, O. Vakuliuk, D. Koga, B. Koszarna, K. Górski, M. Grzybowski, Ł. Kielesiński, M. Krzeszewski and D. T. Gryko, *J. Org. Chem.*, 2020, **85**, 13529–13543.



## Appendix 4

### One-photon absorption

A combination of quantum and classical mechanics can be used to describe media interaction with light. This semi-classical approach uses quantum mechanics to describe media composed of atoms or molecules, and classical Maxwell theory is used to describe light fields interacting with molecules.

The Schrodinger equation for an unperturbed molecule can be written as:

$$\hat{H}_0 \varphi_n = E_n \varphi_n. \quad (44)$$

Where  $\hat{H}_0$  is the Hamiltonian of the unperturbed molecule,  $\varphi_n$  is the wavefunction of the  $n$  energy state and the  $E_n$  is the energy of that state.

When the atom interacts with an electromagnetic field, Hamiltonian can be written as:

$$\hat{H} = \hat{H}_0 + \hat{V}(t). \quad (45)$$

The interaction energy  $\hat{V}(t)$  is small compared to  $\hat{H}_0$  and can be expressed as:

$$\hat{V}(t) = -\vec{\partial} \vec{\mu} \vec{E}(t). \quad (46)$$

Where  $\vec{\mu}$  is the molecule's electric transition dipole moment,  $\vec{e}$  is the unit polarization vector and  $\vec{E}(t)$  is the oscillating electric field:

$$\vec{E}(t) = \frac{E}{2} (e^{-i\omega t} + e^{i\omega t}) = E \cos \omega t. \quad (47)$$

Based on the time-dependence perturbation theory, a molecule interacting with an electromagnetic field can be described by a linear combination of the unperturbed molecule eigenfunctions:

$$\Psi(\vec{r}, t) = \sum_n c_n(t) \varphi_n e^{-i\omega_n t}, \quad (48)$$

where  $|c_n(t)|^2$  is the probability that the electron is in state  $n$  at the time  $t$ .

The time-dependent Schrödinger equation can now be written as:

$$\frac{1}{\hbar} \frac{\partial}{\partial t} \Psi(\vec{r}, t) = [\hat{H}_0 + \hat{V}(t)] \Psi(\vec{r}, t). \quad (49)$$

Combining Equation (48) and Equation (49), we obtain:

$$\frac{1}{\hbar} \sum_n \frac{\partial}{\partial t} c_n(t) \varphi_n(\vec{r}) e^{-i\omega_n t} = \sum_n [\hat{H}_0 + \hat{V}(t)] c_n(t) \varphi_n(\vec{r}) e^{-i\omega_n t}. \quad (50)$$

The time derivative of the first part is taken:

$$\frac{1}{\hbar} \sum_n \frac{\partial}{\partial t} c_n(t) \varphi_n(\vec{r}) e^{-i\omega_n t} = \sum_n \hat{V}(t) c_n(t) \varphi_n(\vec{r}) e^{-i\omega_n t}. \quad (51)$$

Latter can be simplified by multiplying with the complex conjugate of the wavefunction of the  $n$  energy  $\varphi_n(\vec{r})^*$  and integrates over space:

$$i\hbar \frac{dc_k(t)}{dt} e^{-i\omega_k t} = \sum_n V_{kn}(t) c_n(t) \varphi_n(\vec{r}) e^{-i\omega_{nk} t}, \quad (52)$$

where:

$$\omega_{nk} = \omega_n - \omega_k = \frac{E_n - E_k}{\hbar}. \quad (53)$$

The coefficients  $c_n(t)$  can be represented as the following expansion series in powers of the interaction according to the time-dependent perturbation theory:

$$c_n(t) = c_n^0 + c_n^1(t) + c_n^2(t) \dots, \quad (54)$$

where  $c_n^0$  is the probability amplitude of an unperturbed system, e.g., ground state  $g$  and  $c_n^1(t)$  the probability amplitude of 1st-order perturbation, i.e., one-photon absorption.  $c_n^2(t)$  the probability amplitude of 2nd-order perturbation, and so on.

The second term in the series of Equation (54) corresponds to the probability amplitude that, some later time  $t$ , after absorbing a photon whose energy is  $\hbar\omega$ , the molecule reaches the state  $f$ :

$$\frac{da_f^1(t)}{dt} = \frac{1}{i\hbar} \sum_n c_n^0 V_{fn} e^{i(\omega_n - \omega)t}, \quad (55)$$

$$\frac{da_f^1(t)}{dt} = \frac{1}{i\hbar} V_{mg} e^{i(\omega_n - \omega)t}. \quad (56)$$

The solution of this differential equation with the initial condition  $c_f^1(-\infty) = 0$  (no perturbation at the time 0) for  $m \neq g$  and considering Equation (46) and Equation (47) leads to:

$$\frac{dc_m^1(t)}{dt} = \frac{1}{i\hbar} \hat{V}_{mg} e^{-i\omega_{mg}t} = \frac{1}{i\hbar} \vec{\mu}_{mg} e \vec{E} e^{-i\omega_{mg}t}, \quad (57)$$

$$c_m^1(t) = \int \frac{1}{i\hbar} \vec{\mu}_{mg} \vec{e} \frac{E}{2} (e^{-i\omega t} + e^{i\omega t}) e^{-i\omega_{mg}t} dt, \quad (58)$$

$$c_m^1(t) = \frac{E}{2i\hbar} \vec{\mu}_{mg} \vec{e} \int (e^{-i\omega t} + e^{i\omega t}) e^{-i\omega_{mg}t} dt, \quad (59)$$

$$c_m^1(t) = \frac{E}{2\hbar} \vec{\mu}_{mg} \vec{e} \left( \frac{e^{i(\omega_{mg} - \omega)t}}{(\omega_{mg} - \omega)} - \frac{e^{i(\omega_{gm} - \omega)t}}{(\omega_{gm} - \omega)} \right). \quad (60)$$

In the brackets, the first term corresponds to absorption and the second term to emission; here, we are interested in the first, and the second term can be disregarded.

The probability of the transition from ground state  $g$  to excited state  $f$  by absorbing one photon with energy  $\hbar\omega$  after a time  $t$  is therefore given by:

$$P_{g \rightarrow f}(t) = |c_f^1(t)|^2 = \frac{E^2}{4\hbar^2} \left| \vec{\mu}_{fg} \vec{e} \right|^2 \left[ \left| \frac{\sin \frac{\omega_{fg} - \omega}{2} t}{\frac{\omega - \omega_{fg}}{2}} \right|^2 \right]. \quad (61)$$

When  $t \rightarrow -\infty$  function in brackets is a narrow Dirac delta function. To obtain a better representative of the solution absorption bands normalized line shape function  $g_M(\omega)$  can be used where:

$$\int g(\omega) d\omega = 1. \quad (62)$$

Equation (61) takes form [86]:

$$P_{g \rightarrow f}(t) = \frac{\pi E^2 t}{2\hbar^2} \left| \vec{\mu}_{fg} \vec{e} \right|^2 g_M(\omega). \quad (63)$$

The corresponding transition rate of one-photon absorption is:

$$R_{g \rightarrow f}(t) = \frac{d}{dt} P_{g \rightarrow f}(t) = \frac{\pi E^2}{2\hbar^2} \left| \vec{\mu}_{fg} \vec{e} \right|^2 g_M(\omega). \quad (64)$$

To obtain the one-photon absorbance, transition rate, and the first term in Equation (61) can be combined, resulting in:

$$\sigma_{1PA}(\omega) = \frac{\pi\omega}{nc\epsilon_0\hbar} \left| \vec{\mu}_{fg} \vec{e} \right|^2 g_M(\omega). \quad (65)$$

As we look at molecules in a solution, the positions of particles are not fixed, and molecules are randomly and isotropically oriented. Using a body-fixed coordinate system following averaging can be used:

$$\langle |(\Delta \vec{\mu}_{fg} \cdot \vec{e})|^2 \rangle = \frac{1}{8\pi^2} \int_0^\pi \int_0^{2\pi} \int_0^{2\pi} |\vec{\mu}_{fg} \cdot \vec{e}|^2 \sin \theta d\theta d\varphi d\chi, \quad (66)$$

$$\langle |(\Delta \vec{\mu}_{fg} \cdot \vec{e})|^2 \rangle = \frac{1}{3} |\vec{\mu}_{fg}|^2, \quad (67)$$

and the 1PA cross-section in a solution can be expressed as:

$$\sigma_{1PA}(\omega) = \frac{\pi\omega}{3nc\varepsilon_0\hbar} \left| \vec{\mu}_{fg} \right|^2 g_M(\omega). \quad (68)$$

### Probability for 2PA

Once the expression for  $c_n^1(t)$  has been obtained above, we can use the same derivation to calculate the third term corresponding to the second approximation and related to the probability that the molecule reaches the final state  $f$  after absorbing two identical photons i.e.,  $\vec{e}$  are identical, with energy of  $\hbar\omega$ . That is to say, the molecule absorbs one photon that raises it to the virtual level  $m$  - with probability  $|c_m^1(t)|^2$  - and then absorbs a second photon within time  $\tau_v \rightarrow 0$  to reach the final state  $f$ ,

$$\frac{dc_f^2(t)}{dt} = \frac{1}{i\hbar} \sum_m c_m^1(t) V_{fm} e^{i(\omega_{fm}-\omega)t}, \quad (69)$$

$$\frac{dc_f^2(t)}{dt} = \frac{iE^2}{4\hbar^2} \sum_m \frac{(\vec{\mu}_{mg} \cdot \vec{e})(\vec{\mu}_{fm} \cdot \vec{e})}{(\omega_{mg} - \omega)} \left[ e^{i(\omega_{fm}-\omega)t} + e^{i(\omega_{fm}+\omega)t} - e^{i(\omega_{fg}-2\omega)t} - e^{i\omega_{fg}t} \right]. \quad (70)$$

The physical meaning of the subscripts  $f$ ,  $m$ , and  $g$  is excited (final) level, intermediate level, and ground level. In this case, two photons are absorbed. As was the case in 1PA, we are only interested in 2PA, and discard terms related to stimulated emission

$$\frac{dc_f^2(t)}{dt} = \frac{iE^2}{4\hbar^2} \sum_m \frac{(\vec{\mu}_{mg} \cdot \vec{e})(\vec{\mu}_{fm} \cdot \vec{e})}{(\omega_{mg} - \omega)} e^{i(\omega_{fg}-2\omega)t}. \quad (71)$$

Integrating over time:

$$c_f^2(t) = \frac{E^2}{4\hbar^2} \sum_m \frac{(\vec{\mu}_{mg} \cdot \vec{e})(\vec{\mu}_{fm} \cdot \vec{e})}{(\omega_{mg} - \omega)} \left[ \frac{e^{i(\omega_{fg}-2\omega)t} - 1}{\omega_{fg} - 2\omega} \right]. \quad (72)$$

Square of Equation (72) gives the probability,  $P_f^{(2)}(t)$ , of finding the molecule at the final level  $f$  is:

$$P_f^{(2)}(t) = |c_f^2(t)|^2 = \frac{E^4}{16\hbar^4} \left| \sum_m \frac{(\vec{\mu}_{mg} \cdot \vec{e})(\vec{\mu}_{fm} \cdot \vec{e})}{(\omega_{mg} - \omega)} \right|^2 \left[ \left| \frac{\sin \frac{\omega_{mg} - \omega}{2} t}{\frac{\omega_{mg} - \omega}{2}} \right|^2 \right]. \quad (73)$$

Again, to account for the broad line shape of the absorption band, we switch over to using the normalized line shape function  $g_M(2\omega)$  and take the time derivative to obtain the corresponding two-photon transition rate:

$$R_{g \rightarrow f}^{(2)}(t) = \frac{\pi E^4}{8\hbar^4} \left| \sum_m \frac{(\vec{\mu}_{mg} \cdot \vec{e})(\vec{\mu}_{fm} \cdot \vec{e})}{(\omega_{mg} - \omega)} \right|^2 g_M(2\omega). \quad (74)$$

From Equation (3):

$$\Delta\Phi = \sigma_{2PA} N_g \Phi_0^2 \Delta z. \quad (75)$$

As there are two photons needed to excite one molecule

$$\frac{\Delta\Phi}{2} = N_g \Delta z R_{g \rightarrow f}^{(2)}(t). \quad (76)$$

Using the latter, two-photon absorbance can be expressed as follows:

$$\sigma_{2PA} = \frac{\pi \omega^2}{\varepsilon_0^2 c^2 \hbar^2 n^2} \left| \sum_m \frac{(\vec{\mu}_{mg} \cdot \vec{e}) \times (\vec{\mu}_{fm} \cdot \vec{e})}{(\omega_{mg} - \omega)} \right|^2 g_M(2\omega). \quad (77)$$

### Simplifications of 2PA models

When looking at centrosymmetric molecules, in most cases, the ground and final state can be considered as gerade, and to allow 2PA transition intermediate state must be ungerade. Using the three-level model for the centrosymmetric molecule, Equation (77) can be simplified for the lowest energy transition, where  $\omega \cong 1/2\omega_{fg}$ , as:

$$\sigma_{2PA}(\omega) \cong \frac{\pi \omega^2 L^4}{n^2 c^2 \epsilon_0^2 \hbar^2} \left\langle \left| \frac{(\vec{\mu}_{fg} \cdot \vec{e})(\Delta\vec{\mu}_{fg} \cdot \vec{e})}{\omega} + \frac{(\vec{\mu}_{ig} \cdot \vec{e})(\vec{\mu}_{fi} \cdot \vec{e})}{(\omega_{ig} - \omega)} \right|^2 \right\rangle g_M(2\omega), \quad (78)$$

where  $L$  is the optical local field correction factor, this correction is used to correct solvent effects on the external field as often the electric field acting on the molecule may be different from the one applied. For correction, Lorentz field factor  $L = (n^2 + 2)/3$  is often used [87].

The molecules that possess permanent dipole moment changes upon excitation, i.e., are non-centrosymmetric intermediate level, is unnecessary. A two-level model can be used to describe the lowest energy transition:

$$\sigma_{2PA}(\omega) = \frac{\pi \omega^2 L^4}{n^2 c^2 \epsilon_0^2 \hbar^2} \left\langle \left| \frac{(\vec{\mu}_{fg} \cdot \vec{e})(\Delta\vec{\mu}_{fg} \cdot \vec{e})}{\omega} \right|^2 \right\rangle g_M(2\omega). \quad (79)$$

As molecules are randomly and isotropically oriented in the solvent, using a body-fixed coordinate system following averaging can be used [21]:

$$\langle |(\vec{\mu}_{fg} \cdot \vec{e})(\Delta\vec{\mu}_{fg} \cdot \vec{e})|^2 \rangle = \frac{1}{8\pi^2} \int_0^\pi \int_0^{2\pi} \int_0^{2\pi} |\vec{\mu}_{fg} \cdot \vec{e}|^2 |\Delta\vec{\mu}_{fg} \cdot \vec{e}|^2 \sin \theta d\theta d\varphi d\chi, \quad (80)$$

$$\langle |(\vec{\mu}_{fg} \cdot \vec{e})(\Delta\vec{\mu}_{fg} \cdot \vec{e})|^2 \rangle = \frac{2 \cos^2(\beta) + 1}{15} |\vec{\mu}_{fg}|^2 |\Delta\vec{\mu}_{fg}|^2, \quad (81)$$

where the parameter  $\beta$  represents the angle between the transition dipole moment vector  $\vec{\mu}_{fg}$  and  $\Delta\vec{\mu}_{fg}$ . Therefore, the two-level model can be written as:

$$\sigma_{2PA}(\omega) = \frac{\pi L^4}{15 n^2 c^2 \epsilon_0^2 \hbar^2} (2 \cos^2(\beta) + 1) |\vec{\mu}_{fg}|^2 |\Delta\vec{\mu}_{fg}|^2 g_M(2\omega). \quad (82)$$

## Appendix 5

### LabView program and data collection

LabView is used to control hardware directly, like the Horiba CCD, or by sending predetermined commands to two Arduino microcontrollers (Nano and Pro Micro). The microcontrollers in turn run corresponding signal sequences to drivers connected to stepper motors moving sample stage, neutral density filter wheel, and BBO crystal. A motorized shutter/beam block (BB) is connected to the solenoid, and for operation, the voltage is turned on or off again by the corresponding driver connected to the Arduino microcontroller. Wavelength change in OPA is performed through communication via TOPAS 4 server.

Prior to measurements, the user inputs desired parameters for excitation wavelengths and sample control, as indicated in Figure 41 :

- a) determine the number of samples ( $\leq 8$ ) and sample names;
- b) wavelength region and step size in nm;
- c) amount of power attenuation points per wavelength (number of NDFW1 positions, usually 6 – 10);
- d) a number of scans per power (1 – 6).

The CCD control window is seen in Figure 42, where the user can set the following:

- e) CCD integration wavelength region (indicated with red and yellow vertical lines);
- f) CCD gain value.

Florescence collection range is controlled by editing Kymera spectrograph parameters, seen in Figure 43, where three main variables are:

- g) center emission wavelength;
- h) selected grating;
- i) spectrometer input and output slit and slit widths.



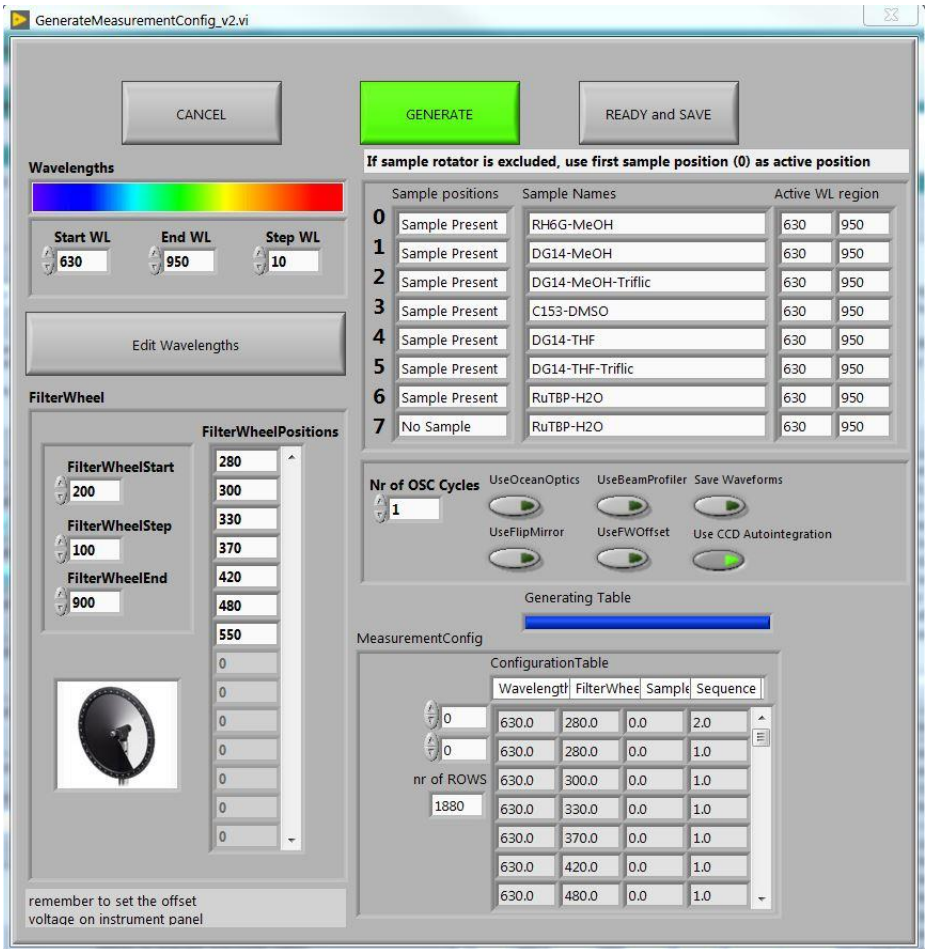


Figure 41: LabView control program measurement configuration window. The user can specify the wavelength range and step to be scanned, enter the names of the samples, and specify the filter wheel steps (power points at one wavelength).



Figure 42: LabView Symphony CCD control window, integrated fluorescence is collected between red,  $\lambda_{min}$ , and yellow,  $\lambda_{max}$ , vertical markers at the bottom graph. The user can also set the integration time (1120 ms at the current acquisition) and amplification factor (1.0).

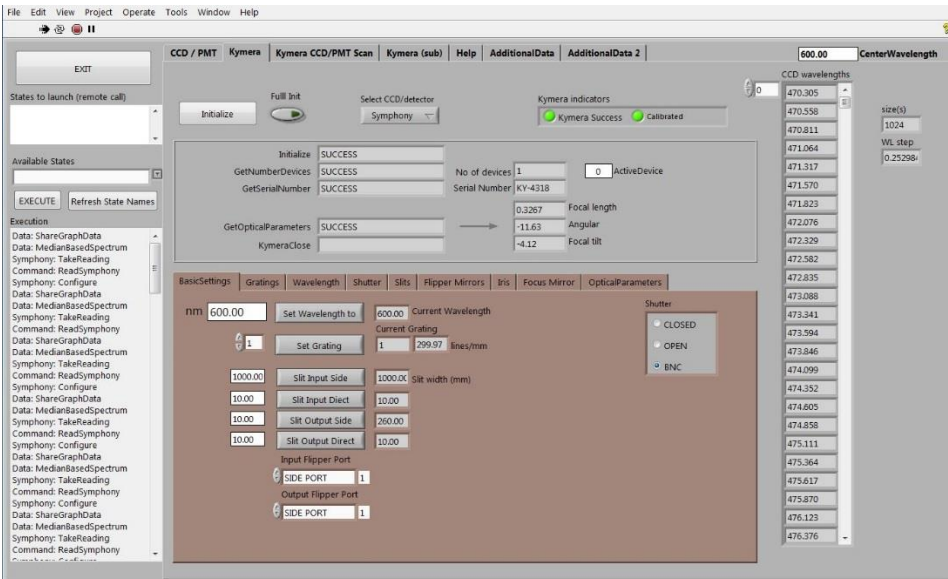


Figure 43: LabView Kymera spectrograph control window. The user defines the grating to be used, the central wavelength and the width of the input slit.

As all the samples have somewhat different fluorescence signals in terms of intensity and wavelength, to increase dynamic range, the highest possible (below saturation level) CCD integration time is automatically chosen at the lowest NDFW value for a given wavelength and sample. According to integration time, a corresponding number of

reference detector pulses are calculated and collected via an oscilloscope. Pulse duration is chosen so that the first 50  $\mu\text{s}$  of the reference detector waveform (Figure 44) are dark signal and the next 50  $\mu\text{s}$  is the PED response. The oscilloscope is used in segmented mode to have the fastest possible acquisition time. This means that a predetermined number of pulses/segments of a certain length are read into oscilloscope memory and analyzed later. The saved waveform's first ( $-50 \mu\text{s}$  to 0 s) and the second part (0 s to 50  $\mu\text{s}$ ) are integrated separately. Afterward dark signal (first part) is subtracted from the signal (second part).

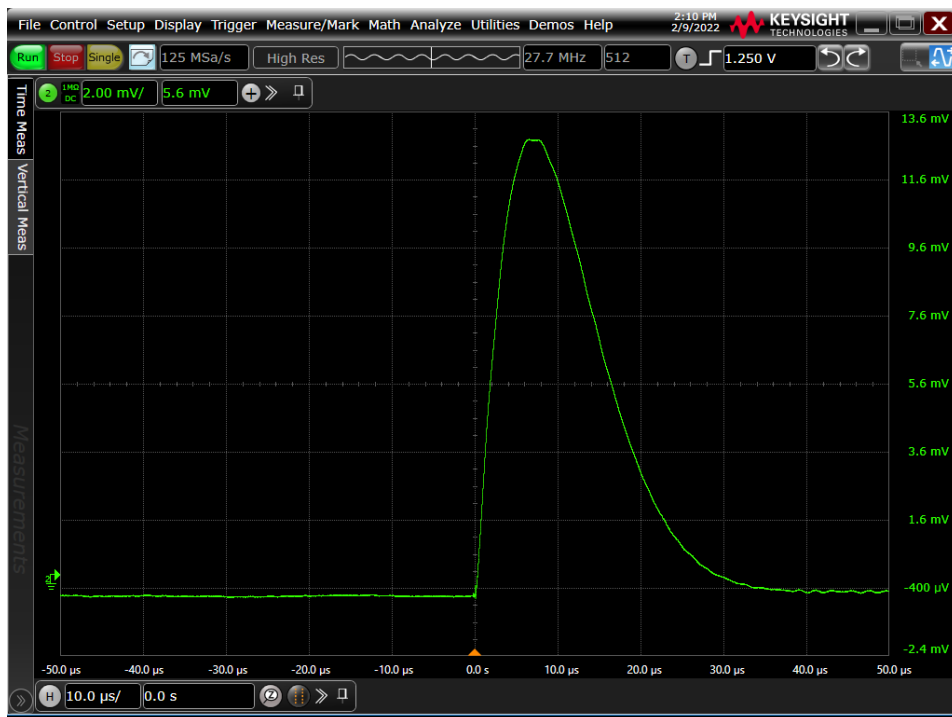


Figure 44: Oscilloscope display screenshot of PED detector signal waveform. The waveform is collected from  $-50 \mu\text{s}$  to  $50 \mu\text{s}$  from the laser trigger signal.

CCD signal is being collected cumulatively, i.e., not by selecting individual pulses. The signal is integrated over a user-defined wavelength region (the following is chosen to have the best overlap between references and sample fluorescence spectra), and the dark signal is subtracted. In a later analysis, the results are corrected for the variable integration time used.

2PA has a quadratic dependence on incident photons. The reference detector signal with different power attenuations (filter wheel positions) is plotted against fluorescence intensity on a double-log scale. The slope of the linear fit gives the power law coefficient, as is shown in Figure 45a. The following is monitored turning a scan as an indicator of measurement quality. The signal was signed to be origin only from the 2PA process when the slope was not deviating from 2.00 more than 5 percent.

Multiple processes may contribute to the deviation from the square dependence. The main problem at shorter wavelengths is 2PA spectra overlap with the red edge of

the 1PA band. As the probability of 1PA is much higher, even a small absorption will significantly distort the measurement results. Some solvents have strong absorption around 1-micrometer wavelengths, which may also cause some artifacts.

In some cases, the fitted slope rises well above two, as seen in Figure 45b, at wavelengths above 900 nm. This deviation could indicate the three-photon absorption process. Other nonlinear processes may affect the results as well. For example, a too tightly focused laser beam can cause white light to be generated in a sample cuvette or nearby optical elements. Another source of error might come from the long detector response curve. The reference detector (PED or photodiode) background is collected and subtracted right before the signal. If the previous pulse has not fully relaxed, this may lead to an underestimation of the corrected fluorescence emission signal and effectively gives a slope value over two. Scattered laser light might also affect results if it reaches the fluorescence detector. The latter is more problematic in a system that uses PMT detector, as there is no direct indication of what wavelengths contribute to the fluorescence signal intensity.

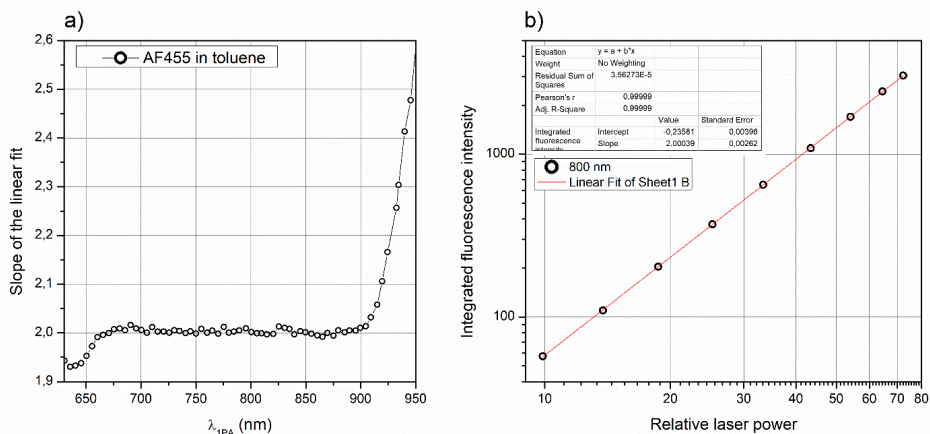


Figure 45: AF455 in toluene, a) slope of the linear fit over the excitation wavelength region, rise above  $\lambda_{2PA} > 900$  nm is caused by three-photon absorption b) example of excitation laser power-fluorescence intensity dependence on a log-log scale linear fit at 800 nm.

## Appendix 6

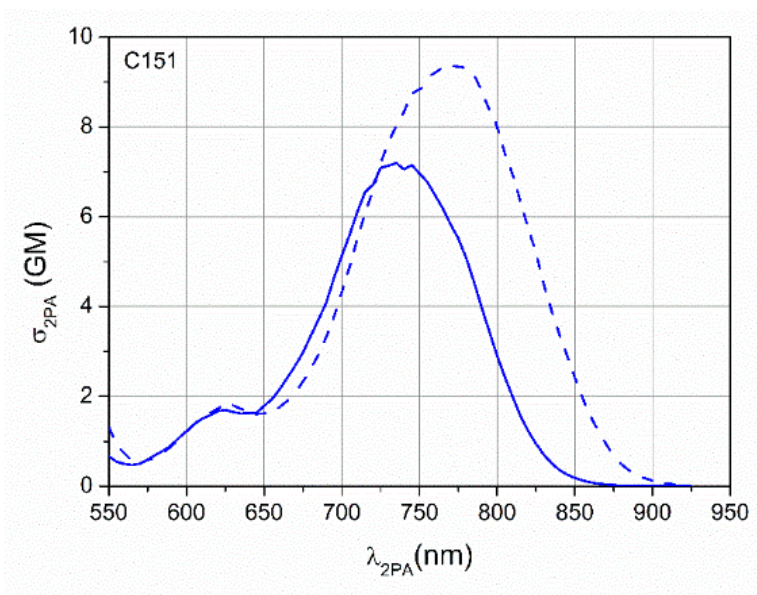


Figure 46: C151 2PA spectra in n-octanol (dash line) and acetonitrile (solid line).

Table 7: C151 2PA values in the 550 – 925 nm in *n*-octanol and acetonitrile solution.

|                | Acetonitrile        | <i>n</i> -octanol   |                | Acetonitrile        | <i>n</i> -octanol   |
|----------------|---------------------|---------------------|----------------|---------------------|---------------------|
| Wavelength, nm | $\sigma_{2PA}$ , GM | $\sigma_{2PA}$ , GM | Wavelength, nm | $\sigma_{2PA}$ , GM | $\sigma_{2PA}$ , GM |
| 550            | 0.67                | 1.32                | 740            | 7.05                | 8.32                |
| 555            | 0.55                | 0.95                | 745            | 7.15                | 8.75                |
| 560            | 0.50                | 0.71                | 750            | 6.96                | 8.79                |
| 565            | 0.47                | 0.58                | 755            | 6.77                | 9.05                |
| 570            | 0.50                | 0.53                | 760            | 6.48                | 9.25                |
| 575            | 0.59                | 0.57                | 765            | 6.19                | 9.30                |
| 580            | 0.70                | 0.66                | 770            | 5.83                | 9.32                |
| 585            | 0.79                | 0.75                | 775            | 5.52                | 9.41                |
| 590            | 0.91                | 0.87                | 780            | 5.08                | 9.27                |
| 595            | 1.07                | 1.04                | 785            | 4.55                | 9.16                |
| 600            | 1.23                | 1.21                | 790            | 3.98                | 8.80                |
| 605            | 1.38                | 1.38                | 795            | 3.44                | 8.38                |
| 610            | 1.50                | 1.55                | 800            | 2.90                | 8.02                |
| 615            | 1.57                | 1.63                | 805            | 2.42                | 7.39                |
| 620            | 1.67                | 1.73                | 810            | 1.98                | 6.94                |
| 625            | 1.70                | 1.81                | 815            | 1.57                | 6.34                |
| 630            | 1.65                | 1.80                | 820            | 1.23                | 5.73                |
| 635            | 1.62                | 1.72                | 825            | 0.94                | 5.20                |
| 640            | 1.63                | 1.66                | 830            | 0.70                | 4.49                |
| 645            | 1.64                | 1.61                | 835            | 0.51                | 3.90                |
| 650            | 1.79                | 1.62                | 840            | 0.36                | 3.39                |
| 655            | 1.94                | 1.66                | 845            | 0.26                | 2.91                |
| 660            | 2.16                | 1.76                | 850            | 0.18                | 2.42                |
| 665            | 2.42                | 1.90                | 855            | 0.13                | 1.95                |
| 670            | 2.68                | 2.10                | 860            | 0.09                | 1.56                |
| 675            | 2.98                | 2.32                | 865            | 0.06                | 1.24                |
| 680            | 3.35                | 2.62                | 870            | 0.04                | 0.94                |
| 685            | 3.72                | 2.93                | 875            | 0.03                | 0.68                |
| 690            | 4.09                | 3.32                | 880            | 0.02                | 0.48                |
| 695            | 4.64                | 3.77                | 885            | 0.01                | 0.35                |
| 700            | 5.13                | 4.32                | 890            | 0.01                | 0.25                |
| 705            | 5.60                | 4.89                | 895            | 0.01                | 0.18                |
| 710            | 6.11                | 5.52                | 900            | 0.01                | 0.12                |
| 715            | 6.55                | 6.08                | 905            | 0.00                | 0.09                |
| 720            | 6.71                | 6.59                | 910            | 0.00                | 0.06                |
| 725            | 7.09                | 7.20                | 915            | 0.00                | 0.04                |
| 730            | 7.14                | 7.66                | 920            | 0.00                | 0.02                |
| 735            | 7.20                | 8.02                | 925            | 0.00                | 0.02                |

## Appendix 7

### Fluorescence decay measurements

To further gain insight into the fluorescence behavior of coumarin derivative neutral and protonated forms, TCSPC measurements were performed of nanosecond time-resolved emission kinetics. Neutral forms of C1-C4 showed single-exponential decay with the fitted lifetime value,  $\tau = 4.8 - 5.0$  ns, seen in Table 8.

Table 8: Fluorescence lifetime measurement results.

| Compound          | $\lambda_{em}$ , nm | $\tau$ , ns <sup>a</sup>                  |
|-------------------|---------------------|---|
| C151              | 463                 | $5.4 \pm 0.1$                             |
| C1                | 487                 | $4.8 \pm 0.1$                             |
| C2                | 492                 | $4.8 \pm 0.1$                             |
| C3                | 508                 | $5.0 \pm 0.1$                             |
| C4                | 519                 | $5.0 \pm 0.1$                             |
| C2-PROT (triflic) | 411                 | $0.25 \pm 0.02^b$                         |
| C2-PROT (HCl)     | 411                 | $0.34 \pm 0.02$ (98)<br>$3.7 \pm 0.3$ (2) |

a, % total emission. b, Maximum of Lorentzian distribution.

The decay time for the parent compound C151 in ACN,  $\tau = 5.4 \pm 0.1$ , is comparable to the previously reported value of 5.13 ns by Nad et al. [43]. In the acidic form, measurements only for C2 in acetonitrile were carried out, seen side-by-side with the neutral form in Figure 47. As might be expected, the quantum yield's decrease upon protonation also correlates to substantially faster emission decay. Compared to the neutral form, protonated species shows non-exponential decay comprising multiple decay constants. To achieve a satisfactory fitting of the data, continuous Lorentzian distribution of the lifetimes, with a maximum of 0.25 ns and an FWHM duration of 0.069 ns, was used. Compared to triflic, early-time kinetics are slower with HCl, while the latter components are shorter-lived. Decay could be modeled by using two components provided in Table 8.

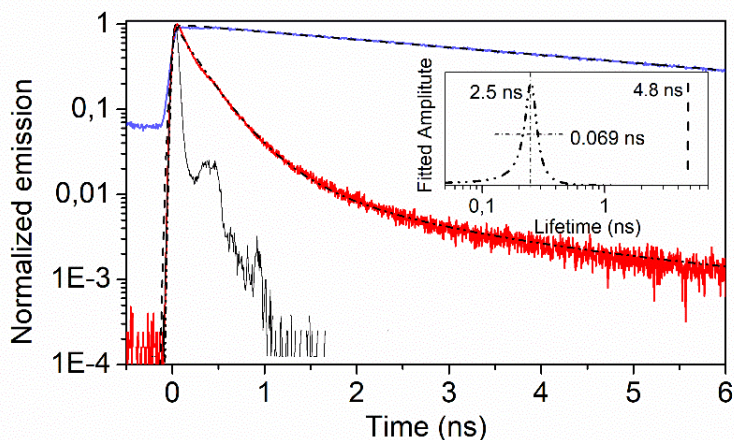


Figure 47: Time-resolved log-emission of neutral C2 (blue line,  $\lambda_{ex} - 260$  nm,  $\lambda_{em} - 495$  nm) in acetonitrile, fit with a black dashed line, compared to the same sample protonated with triflic acid (red line,  $\lambda_{ex} - 270$  nm,  $\lambda_{em} - 425$  nm) fit with dot-dash-dot components, described by a Lorentzian distribution for the protonated form and single decay component in the case of the neutral form.

In the Fluorescence decay kinetics measurements, samples were excited with 140 fs pulses generated by an 80 MHz pulse repetition rate mode-locked femtosecond Ti:sapphire laser (Chameleon Ultra II, Coherent) equipped with a second- and third-harmonic generator (HarmoniXX THG, Angewandte Physik & Elektronik GmbH), followed by an electro-optic modulator (M350- 80, Conoptics) used to lower the pulse rate down to 2 MHz. The fluorescence decay was quantified using a commercial time-correlated single-photon counting (TCSPC) system (FluoTime200, PicoQuant) and the associated data analysis software package FluoFit. Fluorescence was detected with a microchannel plate photomultiplier (R3809U-50, Hamamatsu) combined with a monochromator. The instrument response function (IRF) was obtained using a silicon scattering solution in place of the sample. The used setup is further described in work done by Skowron et al. [88].



## Appendix 8

### Fluorometer correction function

Renewed instrumental correction function was obtained using a set of well-trusted fluorescent reference samples: C153 in methanol, alfaNPO-MeOH, DCM-MeOH, Perylene Cyclohexane, TPB-Cyclohexane, and Tryptophan H<sub>2</sub>O [89] and [90]. Samples were measured and compared to the literature value to obtain the correction function and stitched together while scaled according to the old correction function.

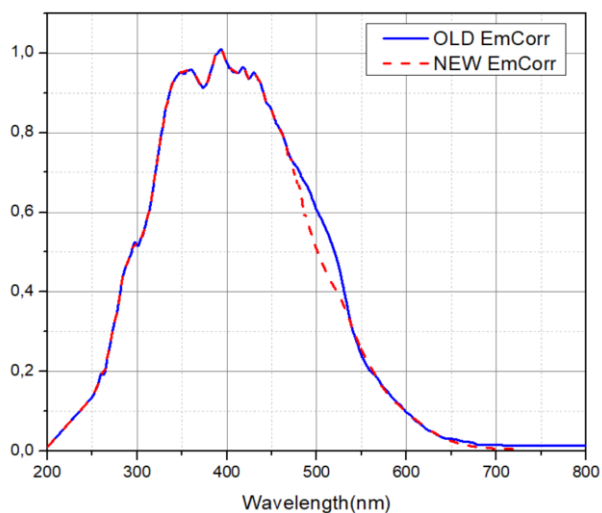


Figure 48: Comparison of spectrofluorometer instrumental correction function old(blue) and new (dash red).

Figure 48 shows a comparison between old and new correction functions. As seen, the most significant discrepancy occurs in the range of 450 – 550 nm. This also coincides with the maximum fluorescence spectra of coumarins studied in this work.

## Appendix 9

### Solvent dependence of C3

In Figure 49, C3 is shown in different solvents; blue lines show the absorption spectrum in neutral forms. Corresponding triflic-protonated absorbance is shown with red lines, dash lines indicate fluorescence with the same color scheme. The absorbance and fluorescence are normalized to the maximum.

In neutral cyclohexane, the least polar solvent, the 1PA spectrum shows emerging features resembling those observed in the 2PA spectrum of the acidic form. Unfortunately, adding a small amount of acid did not result in a stable protonated solution but rather led to the formation of insoluble aggregates that precipitated out, in a matter of hours. Cyclohexane displays the smallest Stokes shift, while octanol, acetonitrile, and DMSO are reasonably similar, while methanol neutral form shows the largest stoke shift  $\sim 130$  nm.

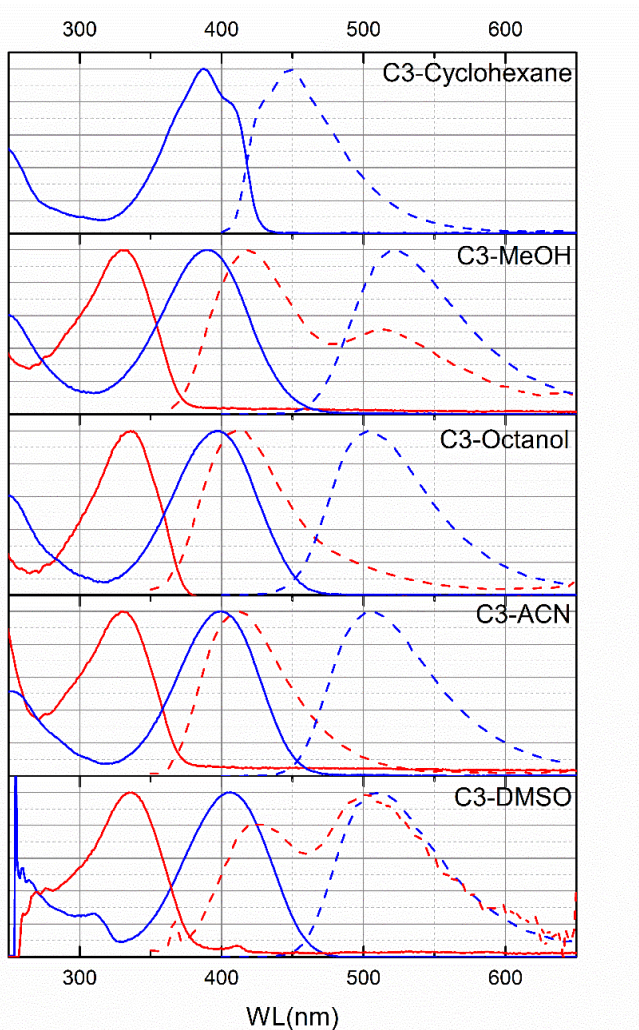


Figure 49: 1PA (solid lines) and fluorescence emission (dashed lines) of neutral (blue) and protonated (red) C3 in variable solvents.

DMSO protonated form indicates the presence of some neutral C3 visible in both absorbance and fluorescence spectra. Methanol and octanol fluorescence may also show not fully protonated samples, but this cannot be confirmed by looking absorption spectrum. As the QY of the neutral form is much higher, even a very small amount of the neutral form may be contributed significantly to fluorescence spectra. Another hypothesis, as presented earlier, may be excited state proton transfer.

## Appendix 10

The experimental setup used to measure coumarin samples. The principle and the structure of the measuring apparatus (Figure 50) closely resemble the updated measurement scheme shown in chapter 3. Exception being the fluorescence collection part. Instead of a spectrograph and CCD camera, a photomultiplier tube (PMT) is used. A set of lenses is used to collect as much fluorescence signal as possible. A short pass filter is used to cut off the scattered laser light. Setup is further discussed in the Master thesis of Katrin Petritšenko [91].

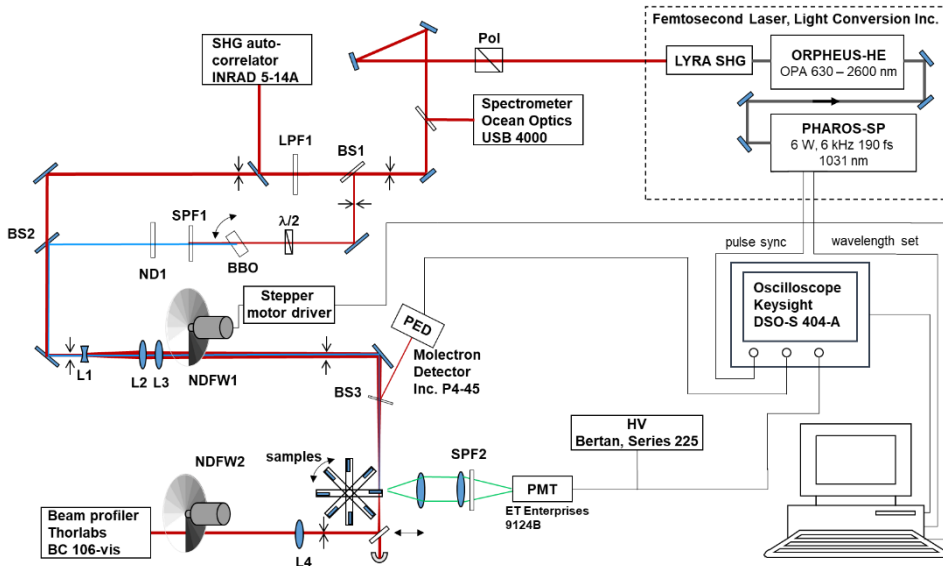


Figure 50: Schematic of the automated femtosecond 2PA/3PA spectrometer; Pol - polarizer; BS – Beam splitter; L - lens; LPF - long-pass filter; SPF - short-pass filter; M-Mirror;  $\lambda/2$  - half-wave plate.

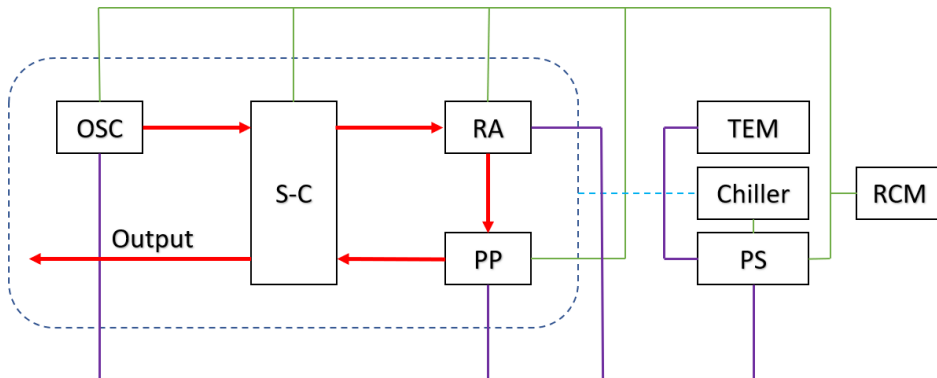
## Appendix 11

### Laser system

A description of the pump laser can be followed with the help of scheme 1. Chiller provides water cooling to the oscillator, regenerative amplifier RA, stretcher-compressor S-C, and Pockels cell driver modules.

The oscillator generates the femtosecond pulses with a duration of 70 – 90 fs, an average power of 0.6 - 2 W, and a pulse repetition rate of 76 MHz. These generated seed pulses are directed through the pulse stretcher. It uses dispersion of diffraction gratings to increase the pulse length and decrease their peak intensity to facilitate amplification in the regenerative amplifier. One or two continuous wave laser diode modules pump the regenerative amplifier. RA has two Pockels cells, first used to inject the seed pulses into the regenerative amplifier at the rate of 1 - 6 kHz. The second Pockels cell is used as a pulse picker (PP), selecting the output pulses and enabling the laser repetition rate in the range of 100 Hz to 6 kHz.

System operation is automatically controlled by the timing electronics module (TEM). The Pharos system can be operated via Pharos control software on a PC, which is connected to the power supply through USB.



*Scheme 1: Pharos laser, oscillator (OSC), stretcher-compressor(S-C), regenerative amplifier (RA), Pulse picker (PP), Timing electronics module (TEM) Chiller, Power supply (PS), and Remote-control module (RCM). A dashed line surrounds water-cooled components. The green and violet lines mark power supply and timing electronics module connections, respectively.*

The output from the Pharos system is directed to the OPA input using a periscope and three external mirrors. The optical layout of the OPA can be followed in Figure 51. After passing through the input port (A), the beam is split into three components by two beam splitters, BS1 and BS2. From BS2 transmitted part is used for white-light continuum (WLC) generation, and the reflections from BS1 and BS2 are passed through Beta Barium Borate (BBO) crystals (SH1 and SH2), where the second harmonic wavelength of the laser (515 nm) is created.

One of the second harmonics beams is used to pump the non-collinear parametric pre-amplifier (first amplification stage) in the BBO Type I nonlinear crystal NC1 "Crystal 1". The temporal dispersion medium (TD) element disperses the white light in time to allow selective amplification of a specific wavelength by tuning the computer-controlled delay translation stage (M1 and M2) "Delay 1". The pre-amplified wavelength is routed



## Appendix 12

Here is presented a reproduction of Herzberg-Teller description for two-photon absorption spectra published by W.L. Smith [20].

In the harmonic approximation, the vibrational wavefunction  $\chi_i$  for multi-atom molecules can be represented as a product of one-dimensional functions. Neglecting the Duschinsky effect, we can write the Condon integral as a product of one-dimensional harmonic oscillator overlap integrals:

$$\langle k|i\rangle = \prod_l \langle k(l)|i(l)\rangle, \quad (84)$$

$k(l)$  and  $i(l)$  are presenting a single quantum number in normal mode  $l$  at the states  $k$  and  $i$ .

For two-photon transitions, we define the following energy values with respective quantum numbers:

$$\begin{aligned} E(f, k) &= E_f + E_k \text{ (final state),} \\ E(m, j) &= E_m + E_j \text{ (intermediate state),} \\ E(g, i) &= E_g + E_i \text{ (initial state).} \end{aligned}$$

$$E_m - \frac{1}{2}(E_g + E_f) + E_j - \frac{1}{2}(E_i + E_k) = \Delta_e(g, m, f) + \Delta_v(i, j, k), \quad (85)$$

indexes  $g, m, f$  and  $i, j, k$  represent all the electronic and vibronic numbers in respective electronic states.

Two-photon transition dipole moment can be expressed in the following form:

$$C_{fk,gi} = \sum_{m,j} \frac{\vec{\mu}_{fk,mj} \vec{\mu}_{mj,gi}}{[E(m, j) - E(g, i)] - h\nu}. \quad (86)$$

Here we assume degeneracy, i.e., two absorbing photons have the same frequency  $\nu$  and vibronic matrix elements  $\vec{\mu}_{fk,mj}$  and  $\vec{\mu}_{mj,gi}$  are given with Equation (14) in part 1.1.4.

Two absorbing photons have a summed energy equal to the energy difference between the initial and final state, i.e.,  $2\hbar\omega = E(f, k) - E(g, i)$  and we can rewrite Equation (86):

$$C_{fk,gi} = \sum_{m,j} \frac{\vec{\mu}_{fk,mj} \vec{\mu}_{mj,gi}}{\Delta_e(n) + \Delta_v(i, j, k)}. \quad (87)$$

As state earlier, intermediate energy levels are assumed to be non-resonant i.e.,  $E(m, j) - E(g, i) \neq \hbar\omega$ . If the energy difference between electronic states is much larger than between vibronic states, then:  $(\Delta_e + \Delta_v)^{-1} \approx \Delta_e^{-1}(1 - \frac{\Delta_v}{\Delta_e})$  and we can again rewrite Equation (87)

$$C_{fk,gi} = \sum_{m,j} \frac{\vec{\mu}_{fk,mj} \vec{\mu}_{mj,gi} (1 - \Delta_v(i, j, k)/\Delta_e(n))}{\Delta_e(n)}. \quad (88)$$

Now we can write vibronic transition moment matrix elements in the form presented in Equation (18) in section 1.1.4. Where for simplicity we are looking molecules with only two atoms and dealing with only single normal coordinate  $Q$ :

$$\begin{aligned} \mu_{fk, mj}(Q) &= \mu_{fm}(0) \langle k|j\rangle + \left[ \frac{\partial \mu_{fm}}{\partial Q} \right] \langle k|Q|j\rangle, \\ &\text{and} \end{aligned} \quad (89)$$

$$\mu_{mj, gi}(Q) = \mu_{mg}(0)\langle j|i\rangle + \left[\frac{\partial\mu_{mg}}{\partial Q}\right]\langle j|Q|i\rangle,$$

where the indexes  $i, k, j$  represents individual quantum numbers. We can further shorten Equation (89) by writing,

$$\mu_{fk, mj}(Q) = \mu_{fm}(0)\langle k|j\rangle + \mu_{fm}(1)\langle k|Q|j\rangle, \quad \text{and} \quad (90)$$

$$\mu_{mj, gi}(Q) = \mu_{mg}(0)\langle j|i\rangle + \mu_{mg}(1)\langle j|Q|i\rangle,$$

Now inserting the terms into Equation (88) we get

$$C_{fk, gi} = \sum_{m,j} \frac{[\mu_{fm}(0)\langle k|j\rangle + \mu_{fm}(1)\langle k|Q|j\rangle][\mu_{mg}(0)\langle j|i\rangle + \mu_{mg}(1)\langle j|Q|i\rangle](1 - \Delta_v(i, j, k)/\Delta_e(n))}{\Delta_e(n)}, \quad (91)$$

$$C_{fk, gi} = \frac{\sum_{m,j} [\mu_{fm}(0)\mu_{mg}(0)\langle k|j\rangle\langle j|i\rangle + \mu_{mg}(1)\langle j|Q|i\rangle + \mu_{fm}(0)\mu_{fm}(1)\langle k|j\rangle\langle k|Q|j\rangle + \mu_{fm}(1)\mu_{mg}(0)\langle k|Q|j\rangle\langle j|i\rangle + \mu_{fm}(1)\mu_{mg}(1)\langle j|Q|i\rangle\langle k|Q|j\rangle](1 - \Delta_v(i, j, k)/\Delta_e(n))}{\Delta_e(n)}. \quad (92)$$

Discarding the  $\mu_{fm}(1)\mu_{mg}(1)$  (Taylor series first-order approximations) and then by first summarizing over  $j$  and then  $m$ . We can apply the quantum mechanical sum rule as a sum over  $j$  resembles a complete set of orthogonal vibrational wavefunctions, which are the eigenfunctions of the vibrational Hamiltonians:

$$\sum_j \langle k|F_1(Q)|j\rangle\langle j|F_2(Q)|i\rangle = \langle k|F_1(Q)F_2(Q)|i\rangle. \quad (93)$$

$F_1(Q)$  and  $F_2(Q)$  represent any continuous function or operators.

Following the same logic, we can write:

$$\sum_j \langle k|j\rangle\langle j|i\rangle = \langle k|i\rangle, \quad (94)$$

and

$$\sum_j \langle k|j\rangle\langle j|Q|i\rangle = \sum_j \langle k|Q''|j\rangle\langle j|i\rangle = \langle k|Q|i\rangle. \quad (95)$$

As  $\Delta_v$  was determined in Equation (85) and contains  $E_j$ , the summation over  $j$  takes the form

$$\sum_j \langle k|j\rangle\langle j|i\rangle E_j = \sum_j \langle k|j\rangle\langle j|H_j|j\rangle\langle j|i\rangle. \quad (96)$$

As the elements  $\langle s_m|H_j|j\rangle$  are only nonzero when  $s_m = j$  and zero terms would not affect the summation over  $j$ , we can write:

$$\sum_j \langle k|j\rangle\langle j|i\rangle E_j = \sum_j \langle k|s_m\rangle\langle s_m|H_j|j\rangle\langle j|i\rangle = \langle k|H_j|i\rangle. \quad (97)$$

The vibrational Hamiltonian of the intermediate state can be written through the potential vibrational functions of the intermediate and initial state:

$$H_j = H_i + V_j + V_i, \quad (98)$$

and

$$\langle k|H_j|i\rangle = \langle k|H_i + V_j + V_i|i\rangle = E_i\langle k|i\rangle + \langle k|V_j - V_i|i\rangle. \quad (99)$$

Using the same logic, we can write:

$$\sum_j \langle k|H_j|j\rangle\langle j|i\rangle E_j = E_i\langle k|Q|i\rangle + \langle k|Q|(V_j - V_i)|i\rangle, \quad (100)$$



$$\sum_j \langle k|j\rangle \langle j|Q_{(i)}|i\rangle E_j = \langle k|H_j Q_{(i)}|i\rangle, \quad (101)$$

and

$$\begin{aligned} \sum_t \langle k|H_{(j)}|t\rangle \langle t|Q_{(i)}|i\rangle &= \sum_t \langle k|H_i + V_j + V_i|t\rangle \langle t|Q_{(i)}|i\rangle = \\ &= \sum_t \langle k|H_{(i)}|t\rangle \langle t|Q_{(i)}|i\rangle + \sum_t \langle k|V_j - V_i|t\rangle \langle t|Q_{(i)}|i\rangle = \\ &= E_k \langle k|Q_{(i)}|i\rangle + \langle k|Q_{(i)}(V_j - V_i)|i\rangle. \end{aligned} \quad (102)$$

As  $\langle k|H_{(i)}|t\rangle = E_k \delta_{kt}$  and assuming potential harmonic functions

$$V = \frac{4\pi^2 \omega^2 c^2 Q^2}{2} = \frac{\lambda Q^2}{2}, \quad (103)$$

and  $Q_{(j)} = Q_{(i)} - d_{(j)}$  and  $Q_{(k)} = Q_{(i)} - d_{(k)}$  then  $Q_{(i)}(V_{(j)} - V_{(i)})$  has  $Q^3, Q^2$  and  $Q$ . Here we are only looking at matrix elements in  $Q$ ,

$$\langle k|Q_{(i)}(V_j - V_i)|i\rangle = \frac{\langle t|Q_{(i)}|i\rangle [\lambda_{(j)}(d_{(j)})^2 - \lambda_{(k)}(d_{(k)})^2]}{2}. \quad (104)$$

Now using predefined terms, we can finally write the two-photon transition moment:

$$\begin{aligned} C_{fk,gi} &= \langle k|i\rangle \sum_m \frac{\mu_{fm(0)} \mu_{mg(0)}}{\Delta_e(m)} \left[ 1 + \frac{(E_k - E_i)}{2\Delta_e(m)} \right] + \\ &+ \langle k|Q_{(i)}|i\rangle \sum_m \left\{ \frac{\mu_{fm(0)} \mu_{mg(1)}}{\Delta_e(m)} \left[ 1 + \frac{(E_k - E_i) - \lambda_{(j)}(d_{(j)})^2}{2\Delta_e(m)} \right] + \right. \\ &+ \left[ 1 + \frac{(E_i - E_k) + \lambda_{(k)}(d_{(k)})^2 - \lambda_{(j)}(d_{(j)})^2}{2\Delta_e(m)} \right] + \\ &\quad \left. + \frac{\mu_{fm(0)} \mu_{mg(0)}}{\Delta_e(m)} \left[ \frac{\lambda_{(j)} d_{(j)}}{\Delta_e(m)} \right] \right\} \end{aligned} \quad (105)$$

Due to the fact that summation over quantum numbers  $m$  includes vibrational energy terms  $E_i, E_j$  and  $E_k$ , there is no clear separation between the vibrational and electronic factors which determine the intensity distribution. Now if difference in vibrational energies i.e.  $E_i - E_k$  is much less than the difference in electronic energies  $\Delta_e(m)$ , then two-photon transition moment can be simplified as:

$$\begin{aligned} C_{fk,gi} &= \langle k|i\rangle \sum_m \frac{\mu_{fm(0)} \mu_{mg(0)}}{\Delta_e(m)} + \langle k|Q_{(i)}|i\rangle \times \\ &\quad \sum_m \left\{ \frac{\mu_{fm(0)} \mu_{mg(1)} + \mu_{fm(1)} \mu_{mg(0)}}{\Delta_e(m)} \right\}. \end{aligned} \quad (106)$$

Substituting latter equation to Equation (9) in section 1.1 and expressing the energy difference  $\Delta_e$  in terms of  $\omega$  we reach for the equation for 2PA cross-section that includes Herzberg-Teller description of vibrational modes.

$$\begin{aligned} \sigma_{2PA} &= \frac{\pi \omega^2}{\varepsilon_0^2 c^2 \hbar^2 n^2} \left\langle \left| \left( \langle k|i\rangle \sum_m \frac{\mu_{fm(0)} \mu_{mg(0)}}{(\omega_{mg} - \omega)} + \langle k|Q_{(i)}|i\rangle \times \right. \right. \right. \\ &\quad \left. \left. \sum_m \left\{ \frac{\mu_{fm(0)} \mu_{mg(1)} + \mu_{fm(1)} \mu_{mg(0)}}{(\omega_{mg} - \omega)} \right\} \right) \vec{e} \right|^2 \rangle g_M(2\omega). \end{aligned} \quad (107)$$

In the case of non-symmetric molecules where a two-level model may be applied, Equation 20 in part 1.1.5 can be abbreviated by summing over the initial and final level. The first sum in Equation (20) becomes the following:

$$\sum_m \frac{\mu_{fm}(0)\mu_{mg}(0)}{\Delta_e(m)} = \frac{\mu_{fg}\mu_{gg}}{\Delta_e(g)} + \frac{\mu_{ff}\mu_{fg}}{\Delta_e(f)}. \quad (108)$$

Where  $\Delta_e(m)$  is defined as:

$$\Delta_e(m) = E_m - \frac{1}{2}(E_g + E_f) \quad (109)$$

In the case of the two-level model intermediate level will be represented by the transition from the initial level to the initial level or final level to the final level and by denote  $E_f - E_g$  with  $\Delta E$ ,  $\Delta_e(m)$  become  $-1/2\Delta E$  and  $1/2\Delta E$  and Equation (20) can be rewritten:

$$\frac{\mu_{ff}\mu_{fg} - \mu_{fg}\mu_{gg}}{-\frac{1}{2}\Delta E} = \frac{\mu_{fg}(\mu_{ff} - \mu_{gg})}{\frac{1}{2}\Delta E}. \quad (110)$$

As term  $\mu_{ff} - \mu_{gg}$  represents the change in permanent dipole moment it is replaced with  $\Delta\mu$

$$\sum_m \frac{\mu_{fm}(0)\mu_{mg}(0)}{\Delta_e(m)} = \frac{2}{\Delta E} \mu_{fg} \Delta\mu. \quad (111)$$

Following the same logic, we can modify the second sum in Equation (20):

$$\begin{aligned} & \sum_m \left\{ \frac{\mu_{fm}(0)\mu_{mg}(1) + \mu_{fm}(1)\mu_{mg}(0)}{\Delta_e(m)} \right\} = \\ & = \frac{\mu_{fm} \frac{\partial \mu_{gg}}{\partial Q} + \mu_{gg} \frac{\partial \mu_{fg}}{\partial Q}}{-\frac{1}{2}\Delta E} + \frac{\mu_{ff} \frac{\partial \mu_{fg}}{\partial Q} + \mu_{fg} \frac{\partial \mu_{ff}}{\partial Q}}{\frac{1}{2}\Delta E} = \\ & = \frac{\mu_{fg} \frac{\partial(\mu_{ff} - \mu_{gg})}{\partial Q} + \frac{\partial \mu_{fg}}{\partial Q} (\mu_{ff} - \mu_{gg})}{\frac{1}{2}\Delta E} \\ & = \frac{2}{\Delta E} \left( \mu_{fg} \frac{\partial(\Delta\mu)}{\partial Q} + \frac{\partial \mu_{fg}}{\partial Q} (\Delta\mu) \right). \end{aligned} \quad (112)$$

Now we can add two sums back to Equation (20) and obtain a two-photon transition moment for a two-level model:

$$C_{fk,gi} = \langle k|i \rangle \frac{2}{\Delta E} \mu_{fg} \Delta\mu + \langle k|Q_{(i)}|i \rangle \times \frac{2}{\Delta E} \left( \mu_{fg} \frac{\partial(\Delta\mu)}{\partial Q} + \frac{\partial \mu_{fg}}{\partial Q} (\Delta\mu) \right). \quad (113)$$

To attain expression for a two-photon absorption cross-section that would involve vibronic contribution, we insert Equation (113) to Equation (9):

$$\begin{aligned} \sigma_{2PA}(\omega) &= \frac{\pi}{15 n^2 c^2 \epsilon_0^2 \hbar^2} (2 \cos^2(\beta) + 1) \left| \langle k|i \rangle \mu_{fg} \Delta\mu + \right. \\ & \left. \langle k|Q_{(i)}|i \rangle \left( \mu_{fg} \frac{\partial(\Delta\mu)}{\partial Q} + \frac{\partial \mu_{fg}}{\partial Q} (\Delta\mu) \right) \right|^2 g_M(2\omega). \end{aligned} \quad (114)$$

## Appendix 13

### One-photon spectral decompositions of PDP, HPDP and HPDPH

pH probe response was modeled with the Nernst equation [92],

$$pH = pH_0 - \frac{E}{k}. \quad (115)$$

Where pH is the actual pH of the solution,  $E$  is the reading from the probe,  $k$  is the practical slope factor, and  $pH_0$  is the pH which results in zero potential on the probe. Individual component concentrations can be expressed following  $K_a$  definition (Equation (32) in 2.3.5) for two acid-base reactions:

$$\begin{aligned} 10^{-pKa_1} &= \frac{10^{-pH}[\text{PDP}]}{[\text{HPDP}]}, \\ 10^{-pKa_2} &= \frac{10^{-pH}[\text{HPDP}]}{[\text{HPDPH}]}, \\ C_{tot} &= [\text{PDP}] + [\text{HPDP}] + [\text{HPDPH}]. \end{aligned} \quad (116)$$

Combining Equation (115) and Equation (116) concentration model for individual components can be established:

$$\begin{aligned} C_{\text{PDP}} &= \frac{C_{tot} \cdot 10^{-pKa_1 - pKa_2}}{10^{E/k_1 + E/k_2} + 10^{E/k_1 - pKa_2} + 10^{-pKa_1 - pKa_2}}, \\ C_{\text{HPDP}} &= \frac{C_{tot} \cdot 10^{E/k_1 - pKa_2}}{10^{E/k_1 + E/k_2} + 10^{E/k_1 - pKa_2} + 10^{-pKa_1 - pKa_2}}, \\ C_{\text{HPDPH}} &= \frac{C_{tot} \cdot 10^{E/k_1 + E/k_2}}{10^{E/k_1 + E/k_2} + 10^{E/k_1 - pKa_2} + 10^{-pKa_1 - pKa_2}}. \end{aligned} \quad (117)$$

There are two slope terms  $k_1$  and  $k_2$ , as the pH response is assumed to be linear near the buffered regions of  $pKa_1$  and  $pKa_2$ , but may deviate over larger pH range between them. The equilibrium parameters  $pKa_1$  and  $pKa_2$  are technically the difference,  $pKa - pH_0$ , but as the pH of zero potential was not measured, absolute  $pKa$  values are not achievable with this model. Measured pH-dependent absorption spectra matrix  $\mathbf{A}$  with dimensions ( $20_{\text{pH}} \times 600_{\lambda}$ ) is expressed as Beer-Lambert equation as:

$$\mathbf{A} = d \cdot \mathbf{C} \cdot \boldsymbol{\varepsilon}^T. \quad (118)$$

Where  $d$  is the optical path length of the cuvette,  $\mathbf{C}$  is the concentration matrix with the concentration of three individual components (PDP, HPDP and HPDPD) at each pH value.  $\boldsymbol{\varepsilon}$  is the corresponding molar absorption spectra matrix, again composing of individual components (PDP, HPDP and HPDPD)  $\boldsymbol{\varepsilon}$  values at every wavelength,  $\lambda$ . Using the MCR-ALS approach, the concentration model and the corresponding molar absorption spectra were alternately solved using the transformations:

$$\boldsymbol{\varepsilon}^T = (\mathbf{C}^T \cdot \mathbf{C})^{-1} (\mathbf{C}^T \cdot \mathbf{A}) \cdot \boldsymbol{\varepsilon}^T = (\mathbf{C}^T \cdot \mathbf{C})^{-1} \cdot \mathbf{C}^T \cdot \frac{\mathbf{A}}{d}, \quad (119)$$

$$\mathbf{C} = \mathbf{C} \cdot (\boldsymbol{\varepsilon}^T \cdot \boldsymbol{\varepsilon}) (\boldsymbol{\varepsilon}^T \cdot \boldsymbol{\varepsilon})^{-1} = \frac{\mathbf{A}}{d} \cdot \boldsymbol{\varepsilon} \cdot (\boldsymbol{\varepsilon}^T \cdot \boldsymbol{\varepsilon})^{-1}. \quad (120)$$

## Appendix 14

### Approximation of $\Delta\mu$ in the case of a two-level system

From Equation (11) in 1.1.2, where we consider isotropic averaging  $P(\beta)$ . For linearly polarized light  $P(\beta) = 2 \cos^2(\beta) + 1$  whereas for circularly polarized light  $P(\beta) = 1/2(\cos^2(\beta) + 3)$ .

$$\sigma_{2PA} = \frac{P(\beta)}{15} \frac{\pi}{\varepsilon_0^2 c^2 \hbar^2 n^2} |\mu_{fg}|^2 |\Delta\mu|^2 g_M\left(\frac{\omega}{2}\right), \quad (121)$$

from which we can extract delta  $\Delta\mu$ :

$$|\Delta\mu| = \sqrt{\frac{15 \varepsilon_0^2 c^2 \hbar^2 n^2 \sigma_{2PA}(\omega/2)}{P(\beta) \pi |\mu_{fg}|^2 g_M(\omega/2)}}. \quad (122)$$

Combining it with Equation (4)

$$\sigma_{1PA}(\omega) = \frac{\pi\omega}{3nc\varepsilon_0\hbar} |\vec{\mu}_{fg}|^2 g_M(\omega) \Rightarrow |\vec{\mu}_{fg}|^2 = \frac{3nc\varepsilon_0\hbar \sigma_{1PA}(\omega)}{\pi\omega g_M(\omega)}, \quad (123)$$

we arrive to

$$|\Delta\mu| = \sqrt{\frac{5nc\varepsilon_0\hbar \sigma_{2PA}(\omega/2)}{P(\beta) \sigma_{1PA}(\omega)}}. \quad (124)$$

We can modify the latter with the relation:

$$\varepsilon_M(\omega) = \frac{\sigma_{1PA}(\omega) N_a}{\ln(10)} \Rightarrow \sigma_{1PA}(\omega) = \frac{\varepsilon_M(\omega) \ln(10)}{N_a}, \quad (125)$$

to get:

$$|\Delta\mu| = \sqrt{\frac{5nc\varepsilon_0\hbar N_a \sigma_{2PA}(\omega/2) \omega}{P(\beta) \varepsilon_M(\omega) \ln(10)}}. \quad (126)$$

Considering that the electric field acting on the molecule in the solution often differs from the one applied. The optical local field correction factor  $L$  is introduced, and we arrive to the following equation for  $\Delta\mu$ :

$$|\Delta\mu| = \sqrt{\frac{5nc\varepsilon_0\hbar N_a \omega \sigma_{2PA(max)}}{P(\beta) \ln(10) L^2 \varepsilon_{M(max)}}}. \quad (127)$$

Here the terms  $\varepsilon_{M(max)}$  is the maximum molar extinction coefficient in the 0-0 band and the  $\sigma_{2PA(max)}$  is peak values for 2PA cross-sections at double the wavelength,

## Appendix 15

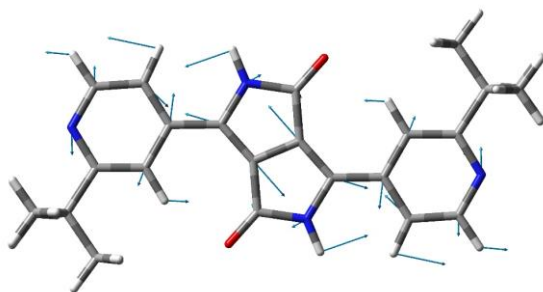
Table 9: Calculated electronic spectral properties of the  $C_2$  and  $C_s$  point group representations of PDP series in MeOH.

| Parameter  | PDP                           |                               |                               | HPDP                          |                               |                               | HPDPH                         |                               |                               |
|--|-------------------------------|-------------------------------|-------------------------------|-------------------------------|-------------------------------|-------------------------------|-------------------------------|-------------------------------|-------------------------------|
|  | $C_2$ (A)                     | $C_2$ (B)                     | $C_s$                         | $C_2$ -core (A)               | $C_2$ -core (B)               | $C_s$ -core                   | $C_2$ (A)                     | $C_2$ (B)                     | $C_s$                         |
| Relative ZPE-corrected energies, kJ/mol                        | 0.0                           | +0.9                          | +0.2                          | 0.0                           | +0.5                          | +0.2                          | 0.0                           | +1.8                          | +0.5                          |
| Aggregated Boltzmann probability, %                            | 64                            |                               | 36                            | 66                            |                               | 34                            | 64                            |                               | 36                            |
| $S_0 \rightarrow S_1$ transition, nm                           | 485                           | 486                           | 486                           | 556                           | 556                           | 557                           | 578                           | 577                           | 578                           |
| $f$ (oscillator strength)                                      | 0.449                         | 0.542                         | 0.494                         | 0.446                         | 0.537                         | 0.478                         | 0.418                         | 0.509                         | 0.461                         |
| $\epsilon_{\max}$ , $M^{-1}cm^{-1}$<br>( $\lambda_{1PA}$ , nm) | 34600 <sup>[b]</sup><br>(485) | 41800 <sup>[b]</sup><br>(486) | 38000 <sup>[b]</sup><br>(486) | 32500 <sup>[b]</sup><br>(556) | 39100 <sup>[b]</sup><br>(556) | 34800 <sup>[b]</sup><br>(557) | 31300 <sup>[b]</sup><br>(578) | 38100 <sup>[b]</sup><br>(577) | 34500 <sup>[b]</sup><br>(578) |
| $\delta_{2PA}$   | 0                             | 0                             | 8                             | 9837                          | 11000                         | 9732                          | 1                             | 5                             | 53                            |
| $\sigma_{2PA}$ , GM<br>( $\lambda_{2PA}$ )                     | 0 <sup>[c]</sup><br>(969)     | 0 <sup>[c]</sup> (968)        | 0 <sup>[c]</sup> (968)        | 16 <sup>[c]</sup><br>(1112)   | 18 <sup>[c]</sup><br>(1111)   | 16 <sup>[c]</sup><br>(1112)   | 0 <sup>[c]</sup><br>(1157)    | 0 <sup>[c]</sup><br>(1153)    | 0 <sup>[c]</sup><br>(1156)    |
| $\mu(S_0)$ , D   | 0.0                           | 0.0                           | 0.7                           | 23.2                          | 23.4                          | 23.5                          | 0.4                           | 0.2                           | 5.0                           |
| $\mu(S_1)$ , D   | 0.0                           | 0.0                           | 0.6                           | 18.3                          | 18.4                          | 18.7                          | 0.4                           | 0.3                           | 5.2                           |
| $\Delta\mu$ , D  | 0.0                           | 0.0                           | 0.1                           | 5.0                           | 5.0                           | 5.0                           | 0.1                           | 0.1                           | 0.2                           |

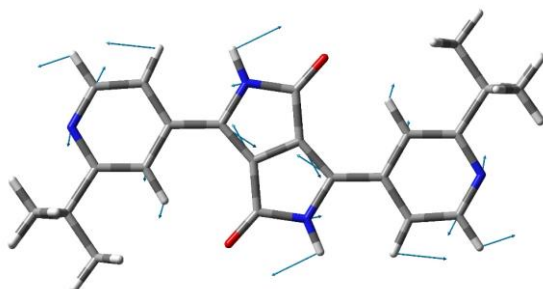
[a] For symmetric PDP the transition energies and oscillator strengths from PCM/mCAM-B3LYP ( $\alpha = 0.08$ ,  $\beta = 0.92$ ,  $\mu = 0.15$ ), for HPDP and for HPDPH from PCM/mCAM-B3LYP ( $\alpha = 0.08$ ,  $\beta = 0.92$ ,  $\mu = 0.135$ ) calculations at 6-311G(d,p) level. [b] 1PA FWHM 0.35, 0.37 and 0.36 eV for PDP, HPDP and HPDPH, respectively (Gaussian line shape) [c] 2PA FWHM 0.25, 0.22 and 0.27 eV for PDP, HPDP and HPDPH, respectively

## Appendix 16

Mode 129<sup>1</sup>  
(1567 cm<sup>-1</sup>)



Mode 131<sup>1</sup>  
(1606 cm<sup>-1</sup>)



Mode 133<sup>1</sup>  
(1631 cm<sup>-1</sup>)

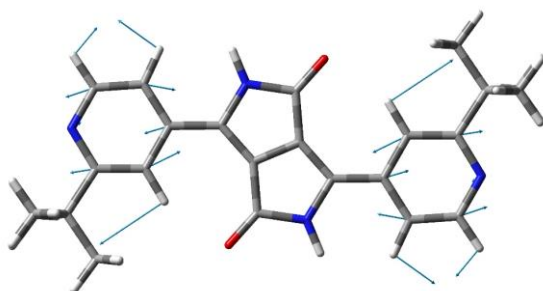
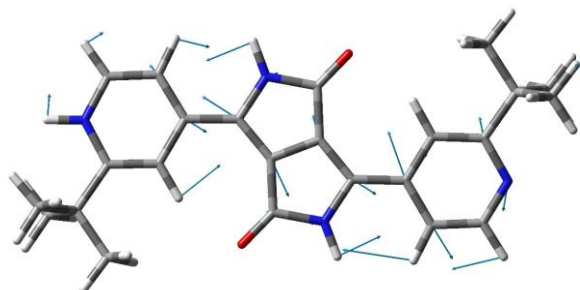


Figure 53: Average direction and magnitude of displacements for the selected 1PA-active ground-state normal modes for PDP from Figure 37.

Mode 132<sup>1</sup>  
(1595 cm<sup>-1</sup>)



Mode 136<sup>1</sup>  
(1663 cm<sup>-1</sup>)

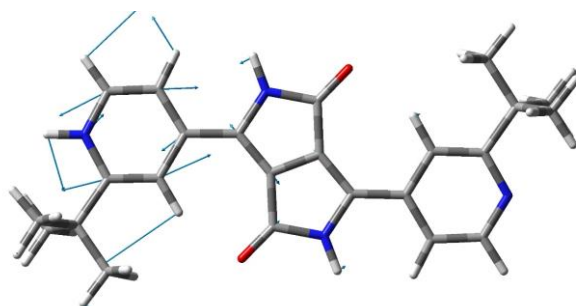


Figure 54: Average direction and magnitude of displacements for the selected 1PA-active ground-state normal modes for HPDP Figure 37.

Mode 133<sup>1</sup>  
(1591 cm<sup>-1</sup>)

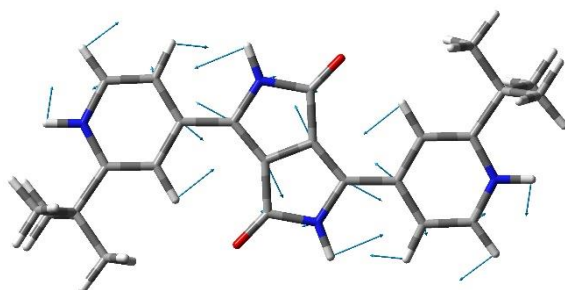


Figure 55: Average direction and magnitude of displacements for the selected 1PA-active ground-state normal mode for HPDPH from Figure 37.

## Appendix 17

Figure 56 shows the one photon absorbance and fluorescence emission of PDP in various solvents of changing polarity. While polar solvents indicate a redshift of absorption and emission maxima by 20 nm, the Stokes shift of emission stays nearly constant. An interesting solvation effect can be noted in the DMSO and weakly in the acetone solvent. The secondary absorption bands are visible at 580 nm and 620 nm. This effect may be caused by an association between  $sp^2$ -hybridized oxygen and the amide on the central diketopyrrolopyrrole, similar to interactions observed with fluoride ions [93]. However, a more in-depth study is needed to give a definite explanation.

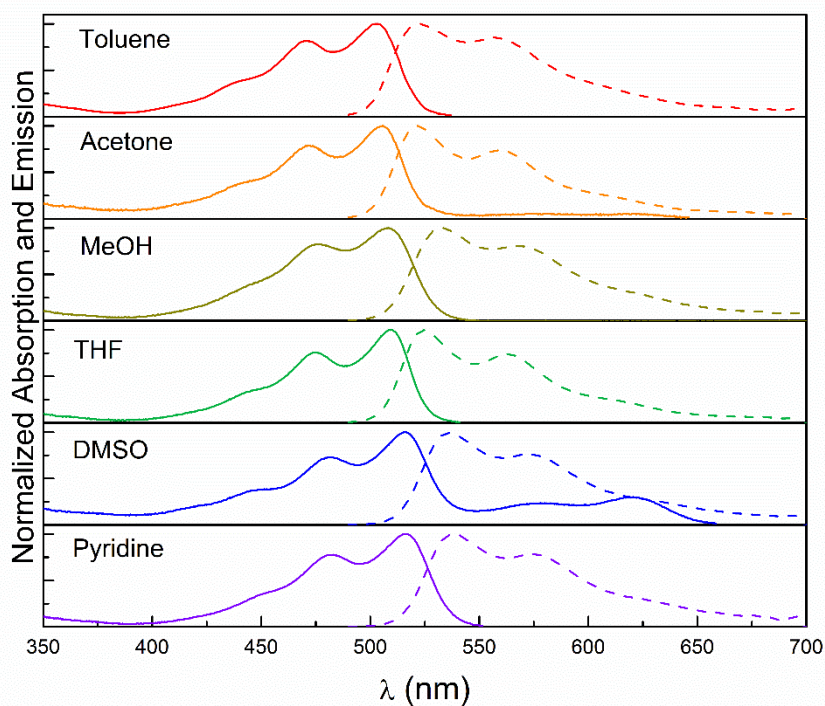


Figure 56: PDP Solvent dependence, one-photon absorption (solid lines), and fluorescence emission (dashed lines) profiles in variety of solvents.



## Curriculum vitae

Name: Matt Rammo  
Date of Birth: 11.04.1988  
Nationality: Estonian  
Email: rammomatt@gmail.com



### Education

15.09.2017– present      Doctoral studies (PhD), Physical Sciences, Tallinn University of Technology (TalTech)  
01.09.2014–25.01.2017      Master of Science (MSc), engineering physics, Tallinn University of Technology (TalTech)  
01.09.2009–29.01.2014      Bachelor of Science, engineering physics, Tallinn University of Technology (TalTech)

### Institutions and positions

15.09.2017–present      National Institute of Chemical Physics and Biophysics, Junior Researcher (1,00)

### Projects in progress

- PRG661 “Femtosecond multiphotonics: From quantitative spectroscopy to quantum optics” (1.01.2020–31.12.2024); Principal Investigator: Aleksander Rebane; National Institute of Chemical Physics and Biophysics; Financier: Estonian Research Council.
- PSG317 “Quantitative sensing of intramolecular electric fields by DNA-intercalating organometallic two-photon probes” (1.03.2019–31.12.2022); Principal Investigator: Charles William Stark; National Institute of Chemical Physics and Biophysics; Financier: Estonian Research Council.

### Publications

- Rammo, Matt; Trummal, Aleksander; Uudsemaa, Merle; Pahapill, Juri; Petritsenko, Katrin; Sildoja, Meelis-Mait; Stark, Charles W.; Selberg, Sigrid; Leito, Ivo; Palmi, Kirsti; Adamson, Jasper; Rebane, Aleksander (2022). Novel Lipophilic Fluorophores with Highly Acidity-Dependent Two-Photon Response. *Chemistry - A European Journal*, ARTN e202103707. DOI: 10.1002/chem.202103707.
- Rebane, Aleksander; Rammo, Matt; (2021). Going beyond the borders: pyrrolo[3,2-b]pyrroles with deep red emission. *Chemical Science*. DOI: 10.1039/D1SC05007A .

- Matt Rammo, Aleksander Trummal, Merle Uudsemaa, Juri Pahapill, Katrin Petritsenko, Meelis-Mait Sildoja, Charles Stark, Sigrid Selberg, Ivo Leito, Aleksander Rebane (2021). Novel pH-responsive highly fluorescent lipophilic coumarins as efficient two-photon sensors of acidic and basic environments. *Multiphoton Microscopy in the Biomedical Sciences XXI, 11648: Multiphoton Microscopy in the Biomedical Sciences XXI, SPIE BiOS*. Online Only: SPIE, 116481H-1–116481H-18. DOI: 10.1117/12.2584084.
- Lukasiewicz, Lukas; Rammo, Matt; Stark, Charlie; Krzeszewski, Maciej; Jacquemin, Denis; Gryko, Daniel (2020). Ground- and Excited-State Symmetry Breaking and Solvatofluorochromism in Centrosymmetric Pyrrolo[3,2-b]pyrroles Possessing two Nitro Groups. *ChemPhotoChem*, 4 (7), 508–519. DOI: 10.1002/cptc.202000013.
- Stark, Charles W.; Trummal, Aleksander; Uudsemaa, Merle; Pahapill, Juri; Rammo, Matt; Petritsenko, Katrin; Sildoja, Meelis-Mait; Rebane, Aleksander (2019). Solute-solvent electronic interaction is responsible for initial charge separation in ruthenium complexes  $[\text{Ru}(\text{bpy})_3]^{2+}$  and  $[\text{Ru}(\text{phen})_3]^{2+}$ . *Communications Chemistry*, 2 (1), 108. DOI: 10.1038/s42004-019-0213-5.
- Stark, C.; Rammo, M.; Pahapill, J.; Mikhaylov, A.; Rebane, A. (2018). Probing metal-to-ligand charge transfer transitions in ruthenium complexes by quantitative two-photon absorption spectroscopy. In: *Proceedings SPIE. (10529-1–10529-8). 21.02.2018 Proceedings SPIE. (Organic Photonic Materials and Devices XX)*.
- S. de Reguardati, J. Pahapill, M. Rammo, A. Rebane (2017). Improving the fidelity of two-photon absorption reference standards. *Proceedings of SPIE, 10094: SPIE Photonics West, San Francisco, California, USA, 28 January - 2 February 2017*. Ed. Alexander Heisterkamp; Peter R. Herman; Michel Meunier; Roberto Osellame. SPIE, 100941Q-1–100941Q-15. DOI: 10.1117/12.2250443.

## Elulookirjeldus

Nimi: Matt Rammo  
Sünniaeg: 11.04.1988  
Kodakondsus: Eesti  
Email: rammomatt@gmail.com

### Haridustee

15.09.2017–... Doktoriõpe Tallinna Tehnikaülikooli Füüsikaliste loodusteaduste erialal, Tallinn, Eesti.  
01.09.2014–25.01.2017 Loodusteaduste magistri kraad, tehniline füüsika, Tallinna Tehnikaülikool (TalTech)  
01.09.2009–29.01.2014 Loodusteaduste bakalaureuse kraad, tehniline füüsika, Tallinna Tehnikaülikool (TalTech)

### Keelteoskus

eesti keel emakeel  
inglise keel kõrgtase

### Töökohad

15.09.2017– Teadur, Keemilise ja Bioloogilise Füüsika Instituut (KBFI), Tallinn, Eesti;

### Teadustegevus

Teadusartiklite loetelu on toodud ingliskeelse elulookirjelduse juures

ISSN 2585-6901 (PDF)  
ISBN 978-9949-83-988-9 (PDF)